Accessibility

OSLO METROPOLITAN UNIVERSITY
STORBYUNIVERSITETET
Department of Civil Engineering and Energy Technology

Report for the course:
Master Program in Structural Engineering & Building Technology

MASTER THESIS

TITLE Modelling of crack initiation in fibre-reinforced injection moulded parts.	**DATE** 25/05/2022 **NUMBER OF PAGES** 138
AUTHOR Jenish Baniya Simon Berhane Tsegai	**SUPERVISOR** Aase Reyes Erik Andreassen (SINTEF) Frode Grytten (SINTEF)

SUMMARY

This study addresses the effects of injection moulding weld lines and fibre orientation distributions on the mechanical properties of short fibre-reinforced thermoplastics (SFT). In this thesis, a literature review, as well as numerical simulation, is carried out. The literature review presents the fibre orientation models and micromechanical models used to predict the stiffness of anisotropic materials. While a parametric study is conducted to study the influence of process parameters on the flow-induced fibre orientation for injection moulded fibre composites. The study found that fibre orientation process parameters have a significant impact on fibre orientation. Moreover, the mechanical properties of an injection moulded part are examined by simulating it in Moldex3D. And the results were transferred to structural analysis software ABAQUS to establish a model which can predict crack initiation at weld lines under quasi-static loading. According to the findings, optimising processing parameters and fibre orientation using experiments and simulations can improve the outcome of a moulded part.

KEYWORDS
Fibre-reinforced polymer
Injection moulding
Finite element analysis

Project assignment Spring 2022

Jenish Baniya & Silmon Berhane Tsegai

Modelling of crack initiation in fibre-reinforced injection moulded parts

Fibre-reinforced plastics are widely used in many sectors. With fibre-reinforced plastics, such as nylons, stiff and strong parts can be injection moulded. However, many parts have "weld lines" where flow fronts meet during moulding. These lines are weaknesses in the part, and the maximum load is limited by crack initiation along these lines. How can we better predict the crack initiation, in order to design lightweight parts that can withstand a certain loading? Is it possible to establish a numerical model that can predict crack initiation at the “weld lines”?

This topic will be studied further in the present project.

The project can consist of the following activities:

1. Theory and state-of-the art about the modelling of fibre-reinforced injection moulded parts, and the modelling of fracture.
2. Numerical modelling of fibre-reinforced injection moulded parts
    a. Establishing models of simple geometries in ABAQUS that can predict crack initiation at “weld lines” under quasi-static loading.
    b. Choosing suitable material models.
    c. Simulation of the injection moulding process, and using the results in the ABAQUS analyses.
    d. Establishing models of real industrial parts.
3. Calibration of the constitutive and/or failure model for the material.
4. Experimental work. The students can use available experimental data at SINTEF, and/or carry out their own experiments based on the numerical work.

The candidates can focus the work on specific parts of the assignment, or assess other aspects in consultation with the supervisors.

The form of the report will be as a scientific research report where emphasis is placed on a clear and well-arranged presentation.

Supervisors: Aase Reyes, Oslo Metropolitan University
Erik Andreassen & Frode Grytten, SINTEF

The report is due at the Department of Civil Engineering and Energy Technology at May 25 2022.

OsloMet, January 19 2022

Aase Reyes, Erik Andreassen & Frode Grytten
Supervisors

Acknowledgement

First and foremost, we are extremely grateful to our supervisor, Prof. Aase Reyes, for her invaluable advice, continuous support, and patience during our master thesis. We would like to thank Dr. Forde Grytten and Dr. Erik Andreassen for giving us the opportunity to write our master thesis with them and for providing us with invaluable guidance and time throughout study. We also extend our gratitude to them for helping us with the preliminary project and providing us with an essential overview of the project and its known parameters. We are also appreciative of all their technical support of our study. Their kind help and support have helped to fulfil the study. Additionally, we are also grateful for the invitation to the SINTEF office to get to know all the necessary equipment used for injection moulding processes.

We are very indebted for all the assistance; we have received from our external and internal supervisors. Their incredible knowledge and experience have encouraged us all the time to complete our master thesis. Besides our advisors, we would also like to extend our gratitude to Peer Guldbrandsen, who provided us with the Moldex3D license and guide under the installation process. We would also like to express our appreciation for his willingness to renew the license of Moldex3D after it expired. Last but not least, we would like to mention that we are grateful to the digital platforms such as zoom and teams for making it easier to hold meetings on our tutoring sessions.

Finally, our thanks go to our family for the continuous support, unconditional love, and constant prayers. All the people who have supported us to complete the research work directly or indirectly.

Abstract

Fibre-reinforced polymers are vital materials across different industries. The manufacturing processes of those materials have a typically strong impact on their final microstructure, which at the same time controls the mechanical performance of the part. Therefore, a reliable virtual engineering design of fibre-reinforced polymers requires considering the simulation of the process-induced microstructure. This thesis focuses on the modelling of fibre reinforced materials and presents a review of the different fibre orientation models and micromechanical models. In this study, different fibre orientation models such as the Folgar-Tucker, retarding principal rate (RPR), anisotropic rotary diffusion (ARD) and Moldflow rotary diffusion (MRD) model are described. Additionally, the micromechanical models that predict the stiffness of composite materials such as Mori-Tanaka, Halpin-Tsai and ruler-mixture are studied. Fibre-reinforced polymers dog-bone with and without weld lines are injection moulded in Moldex3D. The results from the Moldex3D and the process parameters that influence the alignment of fibres are briefly discussed. In order to conduct a structural analysis, the injection moulded part was mapped into ABAQUS by using the FEA interface. In ABAQUS, a tensile test simulation of the injection moulded specimen was conducted. After the stress-strain data set was created and compared to experimental results. The goal of this project is to provide a fundamental understanding to predict fibre orientation distribution in injection moulded parts using Moldex3D simulation and evaluate their structural and mechanical properties in structural software.

Table of Contents

List of figures

List of tables

Index Notation

This thesis is based on different theories in solid mechanics and fluid mechanics. These theories are presented in detail in the literature review chapter of the thesis. A standard convention of index notation is required to present the concepts and equations of theories based on linear algebra and matrices understandably and coherently. This chapter introduces a general explanation of the index notation used in this thesis. The most common index notation used in this thesis is vector notation for equations which involves matrices. This thesis presents the three spatial coordinates of matrices with notations i, j, and k. The general equations in this thesis are represented with subscripts and superscripts. For example, the plastic strain is defined as,

$$\varepsilon_{ij}^{el}$$

The subscript represents the spatial coordinates, while the superscript indicates that the strain is for the elastic region.

The theory of elasticity and micromechanical model is presented with the standard convention, the Einstein convention. The convention is also used to present such theories in this thesis. The Einstein convention generally applies 4 sets of rules. The set of rules states that any twice repeated index in a single term can be presented as the summation over that index. The convention allows the repeated index or dummy index to replace another index not presented in the product. However, the set of rules does not allow any index to occur 3 or more times in each term. In addition, the equation involving the Einstein convention requires the equilibrium of free indices on both sides of the equation. The vector with the Einstein convention can be written as,

$$v = v_i e_i = v_1 x_1 + \ v_2 e_2 + v_3 e_3$$

In addition, the introduction to the Kronecker Delta δ_{ij} and the permutation tensor ε_{ijk} is also essential for this thesis. The most general interpretation of the Kronecker delta is as the discrete version of the delta function. This form of Kronecker delta is defined as,

$$\delta_{ij} = \begin{cases} 1 & if\ i = j \\ 0 & if\ i \neq j \end{cases}$$

While the permutation tensor can be expressed as,

$$\varepsilon_{ijk} = \begin{cases} 1 & for\ even\ permutation\ of\ ijk \\ -1 & for\ odd\ permutation\ of\ ijk \\ 0 & for\ repeated\ indices \end{cases}$$

The Kronecker delta and the permutation tensor have a relationship expressed by $\varepsilon_{ijk}\varepsilon_{imn} = \delta_{jm}\delta_{kn} - \delta_{jn}\delta_{km}$. The Kronecker delta is essential for expressing vector dot products without using vector notation. For example, the dot product of $a \cdot b$ can be expressed as $a_i b_j \delta_{ij} = \ a_i b_i$. While the permutation tensor allows the cross product to be expressed as $a \times b = \varepsilon_{ijk} a_i b_j e_k$.

Abbreviation

ARD-RSC	Anisotropic Rotary Diffusion – Reduced Strain Closure
BLM	Boundary Layer Mesh
CAE	Computer-Aided Engineering
CFRP	Carbon Fibre Reinforced Polymer
F-T	Folgar-Tucker
FEM	Finite Element Analysis
FRP	Fibre Reinforced Polymer
FVM	Finite Volume Method
GFRP	Glass Fibre Reinforced Polymer
IBOF	Invariant Based Optimal Fitting
MRD	Moldflow rotational diffusion model
PVC	Polyvinyl Chloride
RSC	Reduced Strain Closure model
RTM	Resin Transfer Moulding
VCCT	Virtual Crack Closure Technique
iARD	Improved Anisotropic Rotary Diffusion
iARD-RPR	Improved ARD – Retarding Principal Rate Model

Nomenclature

η	Shear viscosity
σ	Stress
σ_{ij}	Principal stresses
α	Aspect ratio of the inclusion
τ	Shear stress tensor
$\dot{\gamma}$	Strain rate
∂	Partial derivative
ε	Strain
Ω	Control volume
γ	Shear strains
ρ	Fluid density
u	Velocity vector
C_p	Specific heat
F	Force
A_0	Initial cross-section area
L_0	Initial length
E_C	Modulus of composite
E_m	Modulus of matrix
V_f	Volume fraction
ξ	Reinforcing factor
Ψ	Factor to account fibre arrangement and fibre content
Φ	Packing fraction
η	Viscosity

λ	Eigenvalue of second orientation tensors
δ	Kronecker delta
β	Material characteristic pressure coefficient
v_0	Poisson's ratio
ζ	Shape factor of a particle
C_I	Fibre-fibre interaction
C_M	Fibre-matrix interaction
α	Slow down factor
e_i	Eigenvectors of the second-order orientation tensor
C_{ijkl}	Elastic modulus tensor in fourth order
K	Hardening parameter
V_0	Elastic homogenous material
ε_{ij}^T	Transformation strain
f_r	Volume fraction
C_r	Distinct moduli
D_r	Diffusion tensor
β_i	Polynomial expansions of the second tensor
E	Young's modulus
$\psi(p)$	Probability density function
p (α, θ)	Unit vector
C_r^f	Stiffness tensor of the inclusion
C_0^m	Matrix material respectively
V_R	Volume of the homogenous material
(T)	Traction force

P_f	Composite fibre material modulus
P_m	Composite matrix material modulus
G_{LT}	In-plane shear modulus

1 Introduction

The anthropogenic activities, which include decades of technological advancements, have accelerated the rise in global temperature. The annual rise in temperature has significantly increased the risk of climate-change-related impacts in the past decades. Today, climate-related disaster is considered the most significant threat humanity faces: a raging wildfire in the USA, melting the polar glaciers, or desertification of cultivatable land. As the hazardous event related to climate change intensifies, the ability humanity to adapt decreases. According to the synthesis report published by the International Panel of Climate Change, the vulnerability and exposure to climate-change impact have driven a significant fraction of species to extinction [1]. In Africa and Asia, access to clean drinking water and food scarcity due to climate change has emerged as the most significant concerns. The number of people facing such challenges increases annually.

The impact of climate change presents a global challenge to different economic sectors and the international community. Hence, collective mitigation and endeavours such as the 2015 Paris Agreement are required to reduce the overall embodied carbon. The Paris Agreement legally binds 196 signatory parties to reduce emissions to limit global warming below 2 degrees Celsius compared to the preindustrial level [2]. The environmental footprint of the construction industry is responsible for 39 % of the total global greenhouse gas emissions. The emission includes the embodied carbon from the manufacturing of materials, construction phase, and end of life phase. The potential to reduce the carbon emission from the building and construction sector is enormous compared to other industries. A recent report from the World Green Building Council has laid out a global roadmap to reduce 40 % of embodied carbon emissions by 2030 and 100 % net zero emissions by 2050 from building and infrastructure [3]. In addition, the report also estimates that the need for infrastructure will double by the year 2060, predominantly due to rapid economic growth and urbanisation in Asia. In the meantime, the report predicts that Europe will face different problems with maintaining the rapidly ageing infrastructure.

The future buildings and infrastructure must utilize optimised material with low embodied carbon. Therefore, low-cost composite material is considered as a viable option to replace traditional materials in the future construction industry. The combination of appropriate reinforcement and matrix material provides engineers to use composite in a wide range of applications. The demand for sustainable and durable materials that can replace traditional materials has increased due to climate change. The application of composite can increase the overall period of critical infrastructure while reducing the need for constant structural health monitoring. The European Commission has decided to fund projects regarding the research and development of durable and low-cost composite materials. These EU-funded projects aim to develop a composite material, particularly in large load-carrying structures such as bridges, buildings, wind-turbine blades, and offshore structures.

In addition, the composites are lightweight materials which can reduce the total weight of structures. With increasing oil prices and global effort to diversify the energy source, composite materials' lightweight and stiffness properties have a significant advantage in the automotive and aerospace industries. The emission from automobiles is considered the largest emitters of carbon dioxide. According to the report by The Norwegian Environment Agency, around 70 % of greenhouse gas emissions are emitted from energy use in Norway. Figure 1.1 from the report shows 34,5 % of the total emission of the total energy consumed by the transportation sector in 2019. Most of the emissions from transportation are contributed by carbon dioxide emissions from burning fossil fuels such as petroleum, natural gas, and coal. Therefore, the efficient fuel consumption by transportation industries can reduce the overall emission by enhancing the powertrain efficiency, reducing the aerodynamic drag, and using lighter vehicles. The composite material application provides higher stiffness while reducing the overall weight leading to better fuel consumption.

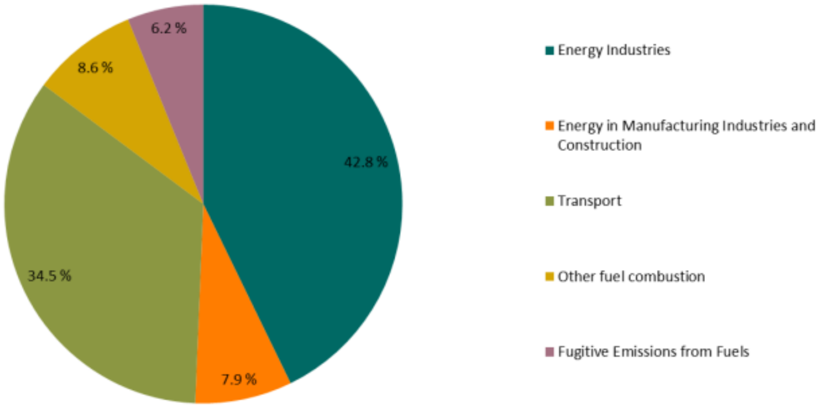

Figure 1.1: Greenhouse gas emissions in 2019 from the energy sector distributed among the different source categories [4].

1.1 Aims and research objectives

Thermoplastic polymer materials reinforced with discontinuous fibres are increasingly used in products requiring superior mechanical stiffness and strength, lightweight, chemical resistance, high operating temperatures, and dimensional tolerances. For such thermoplastic composites, injection moulding is the most applied manufacturing process. Injection moulding is a well-established method of producing plastic parts for engineering applications. This method is one of the most preferred manufacturing techniques due to its efficiency and low cost. Today, more than one-third of all thermoplastic materials are produced by injection moulding. The properties of discontinuous fibre-reinforced polymers material primarily depend on the fibre orientation, fibre length, and process parameters. Therefore, this thesis aims to study the different factors such as fibre orientation which affects the mechanical properties of short fibre reinforced polymers. In addition, the process conditions, and various micromechanical models for polymer composites is also included in the study.

The primary objective of this thesis is to study the mechanical properties of an injection moulded part. However, the mechanical properties of the final injection moulded part are dependent on the manufacturing process. Therefore, a study from injection moulding to nonlinear structural analysis will be conducted in this thesis. The general procedure of how this study is conducted is summarized in a flow chart presented in the Figure 1.2. The mechanical properties of fibre-reinforced composite can be enhanced with optimal injection moulding method. During injection moulding, the processing machinery, mould design, and process conditions must be carefully chosen and optimised for efficient industrial application. Although fibre-reinforced composite materials are not new, numerous challenges and unknown factors are associated with the development and production of components in these materials. As a result, the current situation is marked by a high degree of trial and error in the development process and specific challenges in the manufacturing process. Furthermore, poor material choices, mould designs, or process parameters can result in products that fail during installation or use. In this study, we will also look at one of the most common defects in injection moulding, known as weld lines.

Therefore, the injection moulding simulation based on the fibre orientation model and material data will be conducted with the help of software known as Moldex3D. In addition, a parametric study with different parameters will be conducted with Moldex3D to evaluate how these factor influences the orientation of fibres and mechanical properties. The simulation in Moldex3D provides the elastic constants based on the fibre orientation distribution. Thereafter, based on the results from the Moldex3D simulation a constitutive material model will be developed with the help of Python programming for nonlinear analysis. The material model will be developed initially for tensile bars with and without a weld line to determine the distinct model of weld line. The results from the tensile specimen will be developed with the help of experimental results in this study. However, we will also aim to apply the developed model in industrial part to determine the accuracy of the model. In addition, a constitutive damage model will be developed in ABAQUS to predict crack initiation at "weld lines" under quasi-static loading. Developing the material model which predicts the behaviour of composite material can replace the current practise trial and error which can be effective regarding cost and time.

The objectives of thesis can be summarised as:

1) Theory and state-of-the art about the modelling of fibre-reinforced injection moulded parts, and the modelling of fracture.
2) Injection moulding simulation of fibre-reinforced moulded parts in Moldex3D.

   a) To perform a parametric study to evaluate how the process parameters affect fibre orientations and the stiffness of the part.

3) Numerical modelling of fibre-reinforced injection moulded parts in ABAQUS.
   a) Analyse the mechanical behaviour of material based on the injection moulding simulation.
   b) Establishing models of simple geometries in ABAQUS that can predict crack initiation at "weld lines" under quasi-static loading.
   c) Establishing models of real industrial parts.
4) Calibration of the constitutive and/or failure model for the material.

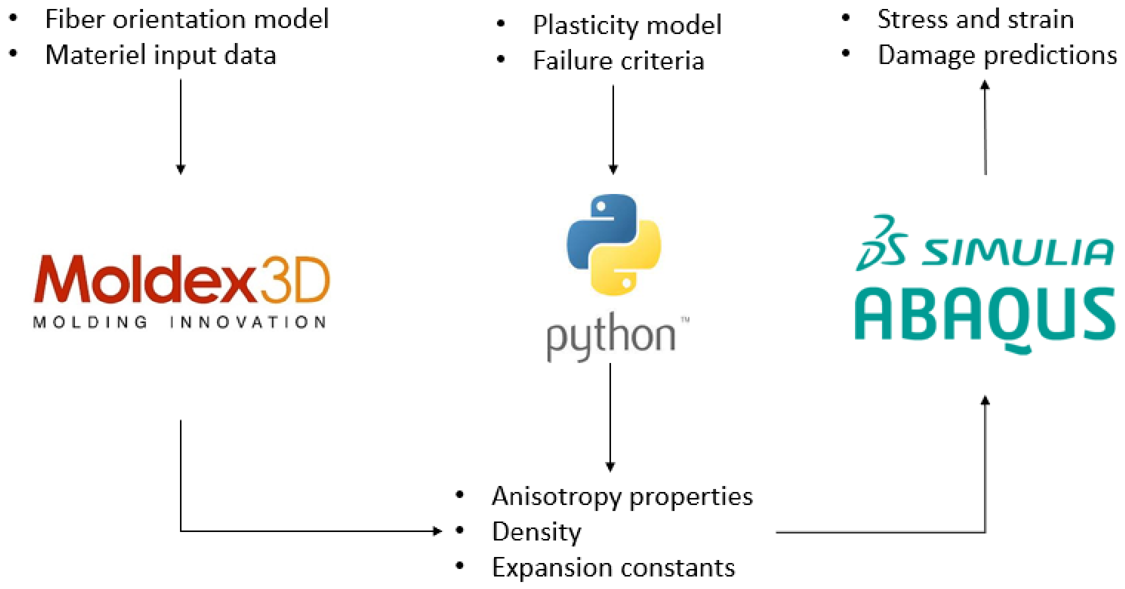

Figure 1.2: Flow chart which illustrates the procedure in which the study was conducted for this thesis.

1.2 Research scope and limitations

This study is a master's thesis for students at Oslo Metropolitan University. The thesis is written in collaboration with SINTEF also known as (Stiftelsen for industriell og teknisk forskning) which provided the topic for the master thesis. Since the study was constrained by time and considering the academic background of authors, we had to set clear limitations on the scope of the study. Due to the scope of the study and time limit, it was not possible to conduct any experiment to determine parameters or validate results. Therefore, the empirically based coefficient for the fibre orientation model is based on the previous studies. The experimental results used in this thesis was conducted prior to the study by SINTEF for their research project. However, the experimental results were provided for the study by the external supervisors to develop the material model. In addition, geometrical part needed for the numerical simulation was also provided by external supervisors from SINTEF.

In addition, there were limitation regarding the ABAQUS and Moldex3D licences. The academic licences in ABAQUS does not include the subroutines method. The user subroutine could allow us to define the material model customized specifically according to our problem. The plasticity model developed in this study will be based on the predefined model in ABAQUS. Additionally, in order to fix a mesh in Moldex3D, it is important to use an external program called Moldex3D CADdoctor. However, our licence was limited, and we could not access Moldex3D CADdoctor. During the Moldex3D simulation, a parametric study was conducted based on the fibre orientation parameters (C_i, C_m and α). However, the fibre flow coupling parameter effect on the injection moulded part has not been investigated due to lack of time.

1.3 Thesis outline

The thesis is organised in four sections:

- Section 1: includes chapter 1 and 2, which provides the introduction to the thesis and background knowledge about fibre-reinforced composite material.

- Section 2: compromise of chapter 3 which presents the literature review conducted for the thesis. This section provides essential knowledge and background needed to understand this thesis. In addition, this section is divided into four sub-sections based on the topic. The first sub-section of the literature review presents the basis knowledge regarding the hydrodynamic part of injection moulding. While the second sub-section summarise the in-detail knowledge of solid mechanics concerning fibre-reinforced polymer. The third and fourth sub-section focuses mainly on knowledge regarding the fibre orientation mathematical model and micromechanics model for simulation.

- Section 3: compromising of Chapters 4 and 5, focuses on the framework for modelling and numerical analysis of injection moulded part. The Chapter 4 starts with injection moulding simulation in Moldex3D. And the Chapter 5 presents the linear elastic analysis in ABAQUS. In addition, plasticity and damage model is developed further in the studies to predict nonlinear analysis and failure.

- Section 4: includes Chapter 6, 7, and 8, which consist the concluding portion of this thesis. The Chapter 6 discusses the various challenges faced during the analysis. While the Chapter 7 and 8 presents the concluding remarks and recommendation for further work.

2 Introduction to composites material

Breakthrough in science and technology has been a crucial factor for the advancement of humanity from palaeolithic to modern civilization. Humankind advanced from using stone during the palaeolithic age to melting metal during the bronze and iron age [4]. Throughout the history of mankind, the advancement of technology has occurred due to either new material or material properties being discovered. Today, materials can be considered a backbone of our modern industrialized civilization as more materials are being used today than ever. For example, materials are used to produce the smallest chip of our mobile device to the largest skyscraper, and from paper bags for daily use to the titanium shell of spacecraft. Researchers are developing different materials with distinct properties, today materials resistant to corrosion and heat are widely available for engineering application. The development of material with superior performance is crucial to sustaining human life on earth in near future.

Today mankind is experiencing new technological upheaval as compared to Industrial Revolution from 1760 to 1820 and again in 1840 [5]. Throughout history, we have enhanced technology by understanding the fundamental properties of material behaviour. I.e. on how the accidental discovery of the age-hardening properties of aluminium took the human race to the stratosphere [6]. Developing durable materials according to industrial standards is crucial to take a new leap in technology. Composite materials have emerged as one of the materials which have stiffer properties than metallic materials which are ideal for complex applications. Polymer or composite materials are engineered materials consisting of two or more elements with different properties. Materials with two or more components such as concrete date to ancient Rome in western civilization. While casted adobe brick made of a mixture of clay, sand or stones and natural fibres such as straw was also used as construction material in Guatemala for thousands of years [7].

But the discovery of modern polymer composites dates to the beginning of the 20th century. Leo Baekeland, a Belgian chemist who developed phenol-formaldehyde, the first synthetic plastic, and a polymer that is still in use today, as a reinforced and unreinforced plastic. Although the polymer material has been around since the 20th century, the application of polymer materials gained momentum only after the post-war era. Fibre-reinforced composite also known as fibre reinforced polymer is composed of a polymer matrix reinforced with fibres. The matrix and reinforcing fibres have substantially different properties where the fibres are strong and stiff embedded in a matrix that is weaker and less stiff. A combination of fibres based on carbon or glass embedded in a polymer matrix enhanced composite material properties. The performance and capabilities of the polymer material exceed the properties of the individual components [7].

Composite materials are widely applied for structural applications due to high strength and stiffness, combined with low density which reduced the overall weight of the material [8]. In modern technologies, composite materials are applicable in different fields such as aerospace and aeronautics, automotive, civil, and structural engineering, biomedical applications etc. However today composite materials are widely applied to build critical civil structures such as bridges and buildings due to higher resistance against environmental conditions. Due to the higher performance to weight ratio, the application of polymer materials has contributed to the enhancement and innovation of sustainable energy technologies and energy-efficient processes. For example, in the early years of aviation aircraft propellers cracked easily causing catastrophic failures. A stiff phenolic-cloth polymer propeller replaced wooden due to the toughness and weight which reduced failures in aircraft [7].

In contrast to traditional materials, fibre reinforced polymer provides higher specific strength and modulus. The application of polymer materials presents clear advantages over traditional materials such as steel, aluminium, wood, and performance plastics. But the application of fibre reinforced material is significantly limited due to the high cost of fibre reinforced polymer. Fibre-reinforced polymer is expensive due to the costs of raw materials and manufacturing defects leading to structural failure. The progressive damage of composite material is an ongoing research topic that aims to optimize the application of composites. However, innovation in manufacturing industries has reduced the cost of composites and improved performance in recent years. In addition, fibre-reinforced materials require less processing energy compared to metallic during manufacturing [9]. The application of fibre reinforced polymer is increasing due to their weight to strength ratio and recent development in manufacturing which has reduced the cost of the material in recent years.

2.1 Classification of fibre-reinforced polymer

2.1.1 Types of polymer matrix

The matrix phase of fibres can be a metal, polymer, or ceramic. In general, metals and polymers are used as matrix materials because some ductility is desirable for matrix composites, the reinforcing component is added to improve fracture toughness. For fibre-reinforced composites, the matrix phase serves several functions. First, it binds the fibres together and acts as the medium by which an externally applied stress is transmitted and distributed to the fibres; only a very small proportion of an applied load is sustained by the matrix phase. Furthermore, the matrix material should be ductile. In addition, the elastic modulus of the fibre should be much higher than that of the matrix. The second function of the matrix is to protect the individual fibres from surface damage as a result pf mechanical abrasion or chemical reactions with the environments. Such interactions may introduce surface flaws capable of forming cracks, which may lead to failure at low tensile stress levels. Finally, the matrix separates the fibres and by virtue of its relative softness and plasticity, prevents the propagation of brittle cracks from fibre to fibre, which could result in catastrophic failure. In other words, the matrix phase serves as a barrier to crack propagation [10].

The polymer structure of a molecular chain is determined by the detailed arrangement of individual repeating units at the atomic level. This affects the overall properties of plastic products. Polymeric materials can be linear, branched, or crosslinked, depending on the intermolecular bonds between each chain. In linear polymers, repeating units are linked end-to-end with a single flexible chain. The polymer chains are held together by physical attraction. Linear polymers are usually made from single-ended monomers. In linear polymers, repeating units are linked end-to-end with a single flexible chain. The polymer chains are held together by physical attraction. Linear polymers are usually made from single-ended monomers[11].

Polymer's matrix composite consists of a polymer resin as the matrix, with fibres as the reinforcement medium. These materials are used in the greatest diversity of composite applications, as well as in the largest quantities, in light of their room-temperatures properties, ease of fabrication, and cost. A polymer matrix reinforced with fibres contains a good resistance and interfacial bonding between them helps to maintain their mechanical and chemical identities. In general, the fibre is the carrier of charge, while the matrix keeps them in position at the desired orientation, it acts as a means of protecting them from environmental damage and transferring the charge between the fibre. Polymer matrix composites have several advantages, such as low density, low cost, and less abrasiveness. Depending on the constituents used, the property of the resulting composite material could be changed. We can improve the strength, reduce the weight, and make cost-effective composite materials by altering the constituents. Polymeric matrix composites can be classified as thermosets and thermoplastics [12].

The response of a polymer to mechanical forces at elevated temperature is related to its dominant structure. In fact, one classification scheme for these materials is according to behaviour with rising temperature. Thermoplastic polymers and thermosetting polymers are the two subdivisions. Thermoplastics soften when heated and harden when cooled. On a molecular level, as the temperature is raised, secondary bonding forces are diminished so that the relative movement of adjacent chains is facilitated when a stress is applied. Irreversible degradation results when molten thermoplastic polymer is raised to too high of a temperature. In addition, thermoplastics are relatively soft. Most linear polymers and those having some branched structures with flexible chains are thermoplastic. These materials are normally fabricated by the simultaneous application of heat and pressure. Most linear polymers are thermoplastic. Examples of common thermoplastic polymers include polyethylene, polystyrene, polyethylene and polyvinyl [10].

Thermosetting polymers are network polymers. They become permanently hard during their formation, and do not soften upon heating. Network polymers have covalent crosslinks between adjacent molecular chains. During heat treatments, these bonds anchor the chains together to resist the vibration and rotational chain motions at high temperatures. Thus, the materials do not soften when heated. Crosslinking is usually extensive, in that 10 to 50% of the chain repeat units are crosslinked. Only heating to excessive temperatures will cause severance of these crosslink bonds and polymers degradation. Thermoset polymers are generally harder and stronger than thermoplastics and have better dimensional stability. Most of the crosslinked and network polymers, which include vulcanized rubbers, epoxies, and phenolics and some polyester resins, are thermosetting [10].

2.1.2 Fibre material

The reinforcing phase provides the strength and stiffness. In most cases, the reinforcement is harder, stronger, and stiffer than the matrix. Reinforcement fibre materials are either natural fibres such as animal, mineral, or cellulose fibres or synthetic manmade fibres such as glass, carbon, or other polymers such as aramid fibres. Typical fibre reinforcement that is widely used are glass fibre, carbon fibre, and polyaramid fibres. Glass fibres are one of the most widely used polymer reinforcements with nearly 90% of all fibre reinforced polymers made of glass fibres. Glass fibre is popular for large volume, lower performance applications due to its low cost and ready availability and chemical inertness. On the contrary Carbon fibre, typically made from polyacrylonitrile is the most commonly used reinforcement for advanced high-performance applications due to its very high specific modulus and specific strength, and excellent elevated temperature performance [13, 14].

A fibre has a length that is much greater than its diameter. The length-to-diameter (l/d) ratio is known as the aspect ratio and can vary greatly. Composite materials may include continuous fibres such as glass, carbon, aramid, basalt, or short fibres such as chopped glass fibres or chopped carbon fibres. Continuous fibres have long aspect ratios, while discontinuous fibres have short aspect ratios. Continuous-fibre composites normally have a preferred orientation, while discontinuous fibres generally have a random orientation [15].

The first commercial production of glass fibres was in 1936. In 1938, Owens-Illinois Glass Company and Corning Glass Works joined to form the Owens-Corning Fibreglass Corporation. Glass fibres are the materials made from extremely fine fibre of glass which is a non-crystalline material with a short-range network structure. As such it has no distinctive microstructure and the mechanical properties which are determined mainly by composition and surface finish are isotropic. Glass fibres are formed from melts and manufactured in various compositions by changing the number of raw materials like sand for silica, clay for alumina, calcite for calcium oxide, and colemanite for boron oxide. Therefore, different types of glass fibres show different performances like alkali resistance or high mechanical properties using various amounts of silica or other sources [16].

Glass fibre products are classified according to the type of composite at which they are utilized. Moreover, chopped strands, direct draw roving, assembled roving, and mats are the most important products that are used in the injection moulding, filament winding, pultrusion, sheet moulding, and hand layup processes to form glass fibre-reinforced composites. Protection of the glass fibre filaments from breakage or disintegration is an important issue either during manufacturing of glass fibre or during composite production. The types of glass fibres most commonly used are mainly E-glass an aluminon-borosilicate glass with less than 1 wt.% alkali oxides mainly used for glass-reinforced plastics, but also A-glass, E-CR-glass, C-glass, D-glass, R-glass and S-glass [16].

2.1.3 Classification by fibre length

Fibre-reinforced composites (FRP) are classified into continuous and discontinuous fibre-reinforced composites. The classification of fibre-reinforced composites depends on the aspect ratio of fibres. Aspect ratio is the length-to-diameter (l/d) ratio of fibres reinforcing matrix in the composite material. Generally, fibres have a length that is much larger than their diameter and varies significantly. Continuous fibre reinforced composites have a long aspect ratio while the discontinuous fibres have short aspect ratios [8]. The aspect ratio of reinforcements influences the elastic properties of composite material such as Young's modulus and yield strength [17].

2.1.3.1 Continuous fibre-reinforced composites

Continuous fibres reinforced material has preferred fibre orientation which can be produced in many forms such as woven, knitted also as laminated composites. Usually, continuous fibre composites are composed as laminates by stacking sheets of continuous fibre in various directions. According to Campbell, (2010) study, the orientation of fibres provide desired strength and stiffness of composites with fibre volumes as high as 60-70 % [8]. Additionally, there is the woven composite of fibre fabric material produced with infused resin. Resin transfer moulding (RTM) and vacuum-assisted resin infusion (VARI) are the most known processes to infuse resin in woven fabric. During the RTM process, thermoset resin is infused throughout the fibre layout or woven fabric in a closed cavity. Whereas VARI utilizes a vacuum bag and infuses laid fibres using vacuum ports [18]. Continuous fibre reinforced composite materials are widely applied in the space and aeronautical industries due to their high specific stiffness and low weight. Boeing 787 and Falcon Spacecraft by SpaceX are some examples of where continuous-reinforced fibre materials are applied. Falcon Spacecraft has an interstage component with continuous Carbon fibre skin to cover the Aluminium core [19]. However, the application of continuous fibre composites is limited in the automotive industry because of the high manufacturing cost [20].

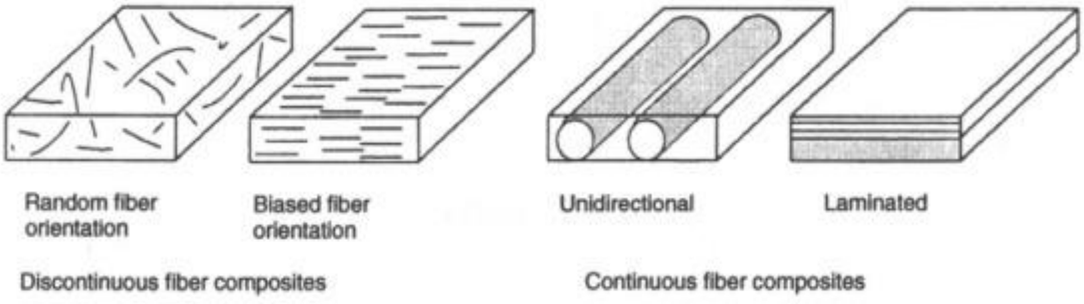

Figure 2.1: Schematic representation of continuous and discontinuous fibre-reinforced composites [21].

2.1.3.2 Discontinuous fibre-reinforced composites

Compared to continuous fibres which have preferred orientation, discontinuous fibre reinforced composites have random orientation. The random orientation of fibres reduces their strength and elastic modulus drastically [8]. However, the material properties of discontinuous fibre reinforced material are a lot higher compared to traditional materials such as steel and concrete. Additionally, the cost of manufacturing discontinuous composite is relatively lower than continuous fibre and is easier to produce in high-volume for industrial use. Generally, discontinuous fibre-reinforced polymer consists of thermoset or thermoplastic matrix material. The most known engineering thermoplastic are polyamide (PA) and polypropylene (PP). Thermoplastic materials are typical plastic material used in our daily life, but has superior properties compared. Generally, thermoplastic material is preferred as matrix material for due to the low cost. While glass fibres are preferred as reinforcing material in discontinuous fibre reinforced for general industrial application. In comparison the application of carbon fibre provides superior mechanical performance. But the usage of carbon fibre as a reinforcing material in discontinuous fibre-reinforced is limited due to higher costs. However, the price of carbon fibre is falling in recent year as the interest in application in discontinuous fibre reinforced, is increasing.

Discontinuous fibre-reinforced composites can be further classified as short fibre-reinforced polymer and long fibre-reinforced polymer. Short fibre-reinforced polymers have fibre lengths less than 5 mm. While the long fibre-reinforced composites have a fibre length between 10-30 mm. Since the fibres in long fibre-reinforced composite is longer they have more interaction with each other during manufacturing [7]. The classification of discontinuous fibre-reinforced composite is illustrated in the Figure 2.2. Due to anisotropic development of fibre orientation determines the regional and overall material properties of the discontinuous fibre-reinforced composite. Preferential alignment of fibres is dependent on the processing parameters and flow conditions during mould filling.

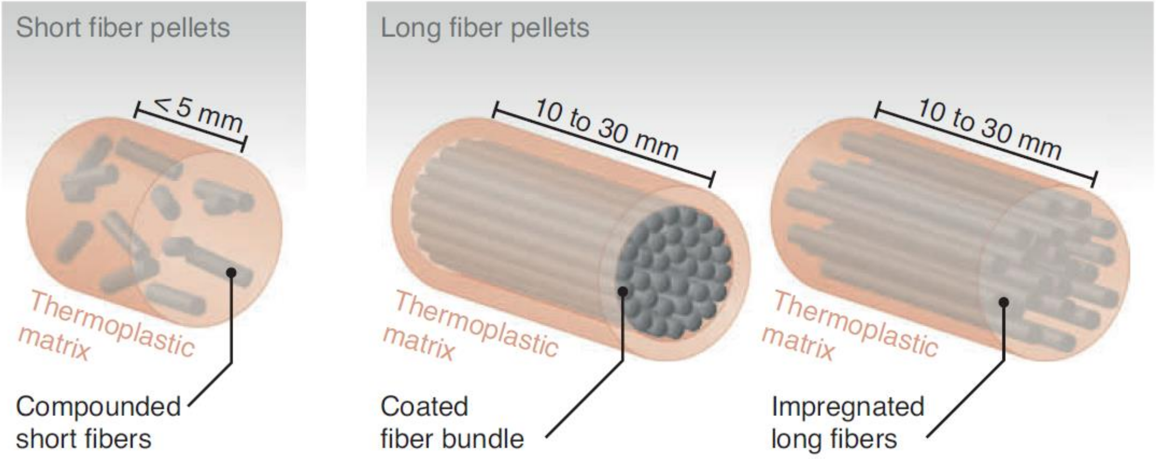

Figure 2.2: Short fibre and long fibre pellets of discontinuous fibre-reinforced composite based on aspect ratio of fibres presented in (U. Gandhi et al., 2020).

2.2 Application of polymer materials

Polymer Matrix Composites have been well-known materials in advanced applications for many years. They are valuable materials and easy to be moulded into any required application. Advanced composite materials have expanded use in aerospace, marine and automobile industries during the past few decades due to their good engineering properties such as high specific strength and stiffness, lower density, high fatigue endurance, high damping, low thermal coefficient, etc. However, there are a few aspects in the field of polymer to consider well. A polymer alone cannot meet the requirements in advanced applications. Therefore, polymers reinforced with fibres attracted the attention of the world. Civil engineers and the construction industry have recently begun to realize the potential of composites as strengthening material for many problems associated with the deterioration of infrastructures. Nowadays, many industries focus on replacing of traditionally used metal alloys with polymer composites, thermosets or temperature resistant and high-strength thermoplastics [22].

In addition to the aerospace and automotive industry, composite materials, especially glass fibre composite materials get a wider range of applications in other economic areas because of the advantages of their price and performance. For instance, in the construction industry, composite materials are widely used in a variety of lighthouses, large building structures, architectural features, and sculptures. Additionally, composite materials are used in the production of a variety of workboats, fishing boats, transport boats, motorboats, cruises, military minesweepers, and submarines in the shipbuilding industry. Composite materials are also applied in anti-corrosion equipment made by glass fibre reinforced plastics that include large tanks, containers, various pipes in mass transfer, elbow, three links, and so on. In the production of anti-corrosion equipment's glass fibre is used as reinforcement since glass fibre reinforced plastics are highly resistant to corrosive chemicals and provide new chemical anti-corrosion materials.

2.2.1 Automotive industry

Within the last few decades, polymers and polymer composites have become more important in the automotive industry. Since the requirement for energy saving in the automotive industry started to rise dramatically over the years. Reduction of weight was one of the options to reduce energy consumption. To reduce weight, an invention technology material was introduced with polymeric-based composite materials in the automotive industry, which offer high specific stiffness, low weight, corrosion-free, and the ability to produce complex shapes. The substitution of metals with polymeric-based composite material in automotive components was beneficial for fuel and weight reduction. The use of structural composites in the automotive industry began in the 1950s. Composites have proven to be a seemingly attractive metal alternative from their early days. However, there has been no comprehensive conversion from metals to composites in the automotive sector. This is because there are still some technical issues related to composite materials that have not yet been resolved, such as accurate material characterization, manufacturing, and bonding [23].

Chevrolet Corvette in1953 started using fibreglass body which was the first application of PMC in the field of the automotive industry. Around the globe, in the auto-mobile field, 24% of thermoset and 50% of thermoplastic are utilized due to their ability to facilitate parts integration, fast cycling time, and low cost. A commonly used composite in the automotive industry is polymer matrix reinforced with fibre. The glass fibre reinforced thermoplastic polymer is a promising one in the automobile sector for weight reduction and specific strength properties with a weight saving of 20–40%. For example, the replacement of steel structures with stronger and lighter PMCs has been estimated to reduce vehicle weight by 30%–50%. Such weight savings in the primary structure from composite materials enable power train size reduction while maintaining performance, which results in very significant fuel efficiency improvements [14].

As shown in Figure 2.3, composite materials can be applied in different parts of a car such as electrical/light, under the hood, exterior, and interior. Typical interior applications are seats, instrument panels, steering wheels, and interior linings. Exterior applications include bumpers, roof modules, exterior mirror housings, and car body panels whereas applications under the hood describe parts like engine covers, air ducts, tubes, water tanks, and hydraulic hoses. Electrical and light applications are found in headlamp front lenses, headlamp casings, electrical wire isolators, and fastening clips. Currently, there are about 30,000 parts in a vehicle, out of which 1/3 are made of plastic. In total, about 39 different types of basic plastics and polymers are used to make an automobile. More than 70% of the plastic used in automobiles comes from four polymers: polypropylene, polyurethane, polyamides, and PVC. Fig. below shows examples of polymers used in automobiles [24].

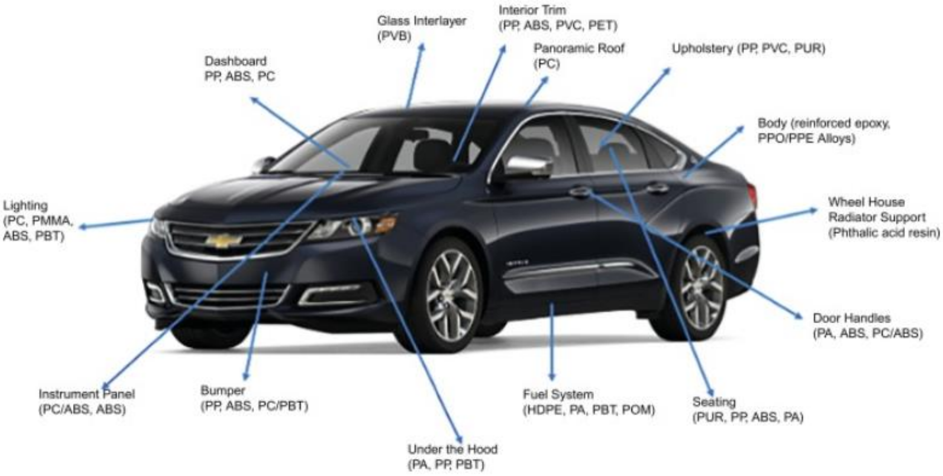

Figure 2.3: Plastic applications in the automotive industry [24].

2.2.2 Aerospace industry

The aerospace industry demands sophisticated equipment and structural and propulsive systems with almost guaranteed safety levels as the loss are often great, costly, and sometimes even catastrophic. Therefore, there is a need for lighter, cheaper, and more reliable technologies in day-to-day demands. The need for high performance and capability to design material characteristics to meet specific requirements has made polymeric materials the first choice for many aerospace applications. Polymer materials are widely used for many aerospace applications due to their many engineering designable advantages such as specific strength properties with a weight saving of 20-40%, potential for rapid process cycles, ability to meet stringent dimensional stability, lower thermal expansion properties, and excellent fatigue and fracture resistance over other materials like metals and ceramics [25].

The application of polymer materials has contributed for development of sustainable energy technologies and energy efficient processes. For example, in the early years of aviation aircraft propellers cracked easily causing catastrophic failures. A stiff phenolic-cloth polymer propellers replaced wooden due to the toughness and weight which reduced failures in aircraft [7]. As stated nowadays, composite materials are used in large volumes in various engineering structures including sports equipment, space crafts, aeroplanes, boats, bridges, automobiles, and buildings. Examples in aeronautical applications can be the Airbus A380, which has 25% of the weight of its parts made of composites, and the Boeing 787 Dreamliner, which has 50% composites by weight. The widespread use of composite materials in the industry is due to the good characteristics of their strength to density and hardness to density. The aerospace industry in many countries has benefited from the abilities and characteristics of these advanced materials. Along with the progress in technology, metallic aerospace parts are replaced by composite ones [12, 22].

Another most known example is the application of Graphite Epoxy polymer in aerospace industry. The Falcon Spacecraft by SpaceX uses carbon fibre in payload firing and interstage. The interstage component in Falcon Spacecraft uses Carbon fibre skin to cover the Aluminium core [19]. Application of polymer material contributed to increase the strength of aircraft component. In addition, material is lighter and shrinks less compared with metal alloys used for cryogenic fuel tank. The reduction of mass reduces the amount of fuel use even though construction cost is considerably high. However, the project was later scraped due to huge fire risk in the fuselage due to the carbon fibre skin.

As it is pointed out composite materials are obtaining a wide range of applications in various economic fields, the amount of usage is still small. However, there is a big gap between developing and developed countries in the application of composites both in quantity and quality. To promote the development of composite materials, the following main issues should be solved: reduce the price of composite materials based on quality assurance, improve the effectiveness of their application, develop new types of the more effective moulding process, and further promote the field of application of composite materials [26].

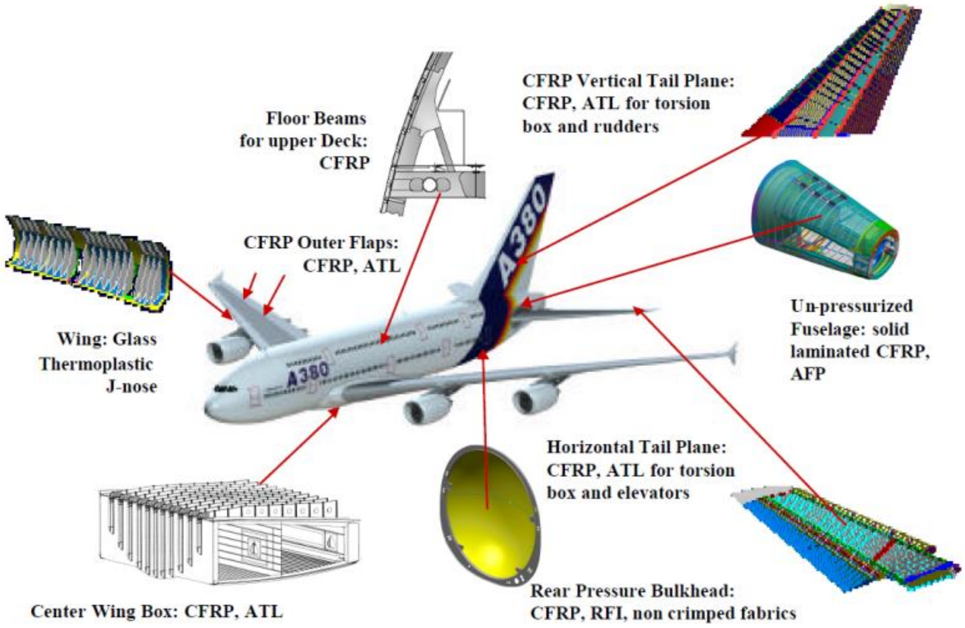

Figure 2.4: The application of polymer material in the Boeing 387 Dreamliner [7].

2.2.3 Construction industry

The history of polymers and composites in the construction industry began during the Second World War when instant progress was made with the manufacture of house electronic radar equipment. The key growth interest and technology in glass fibre composite in the building and construction industry began in the 1960s. Two structures were built made of GFRP, the dome structure in Benghazi built in 1968 and the roof structure at Dubai airport built-in 1972. The need for infrastructure repair and renewal has increased since the early 1990s, and simultaneously the interest in the use of fibre reinforced polymers materials for structures has also increased steadily. There are currently hundreds of field applications of FRPs in structures worldwide. For instance, The Ibach bridge, located in the Canton of Lucerne in Switzerland, was repaired in 1991 with three CFRP strips, making it the first CFRP reinforced concrete bridge globally. Some of the more common fibre reinforced polymers applications in civil engineering structures and design rules are externally bonded FRP plates, sheets, and wraps for the strengthening of reinforced concrete, steel, aluminium, and timber structural members and FRP bars for the internal reinforcement of concrete [27].

Additionally, practical applications in recent years have shown that FRPs can be used as an alternative strengthening material for masonry structures, especially those of considerable historical importance. Some of the first research within this field worldwide was conducted at the Swiss Federal Laboratories for Materials Science and Technology. FRP strips and fabrics were used for the masonry shear walls in the laboratory using epoxy adhesives. The walls were then examined under static cyclic loading. It was shown that the in-plane deformation capacity of the masonry shear walls after strengthening could be increased up to 300%. Many historical buildings, especially in Italy, Greece, and Portugal, were retrofitted by applying FRP composites. For instance, the Basilica of St Francis of Assisi in Italy was severely damaged by earthquakes and aftershocks in 1997 where glass FRP was applied for restoring the building [27].

The composite material of glass fibre can be utilized as a glass fibre reinforced polymer deck in bridge construction. It is possible to create a bridge span consisting of steel main beams and a GFRP deck. GFRP bridge deck is the alternative to the heavy popular concrete deck, which has poor durability, for bridges where there are steel main beams. A bridge deck made of fibre-reinforced polymers (FRP) is beneficial for maintenance purposes. A composite bridge deck also provides greater durability and reduced maintenance costs over the life of the bridge. Compared to concrete and steel that have been used as bridge deck material in the past, FRP material has the advantage of being lightweight and non-corrosive. GFRP bridge decks have been thoroughly tested in both laboratory and field settings. Static tests typically indicate an extremely high factor of safety for strength, while fatigue tests show little to no degradation after millions of load cycles [28].

The glass fibre-reinforced polymers deck has great potential in bridge construction. Many steel footbridges with light GFRP decks were built in Denmark and Nederland as shown in fig 2.4. For example, in the 2011 Karrebæksminde Bridge in Denmark, a GFRP deck and main steel structure of a moving span were constructed. Traditional bridge decks are heavy and have poor durability. But effective connection systems and better durability of pavement, which covered the GFRP deck. On the other hand, GFRP deck is a good alternative for old steel bridges, which need to exchange heavy old decks. Imposing stress and fatigue parameters of glass fibre polymer give possibilities of the modern shape of bridge structures using long-life material and coexistence of traditional main part of the bridge – steel girders with light, anticorrosion deck [28].

Figure 2.5: Fly-over Waarderpolder bridge in Netherland with FRP edge elements [29].

2.3 Manufacturing process - *Injection moulding*

When it comes to the mechanical behaviour of inhomogeneous materials such as polymer material it depends mainly on the relation between fibre and matrix. The type of matrix used to reinforce the fibre also affects the processing procedure. Figure 2.6 shows major processing routes for polymer matrix composites. Typically, there are two types of polymer matrices known as thermosets and thermoplastics. A thermosets matrix is a low-viscosity resin that reacts and cures during processing, forming an intractable solid. While thermoplastic is a high-viscosity resin that is processed by heating it above its melting temperature [8].

Injection moulding is a highly preferred polymer processing technique in the polymer industry even various manufacturing processes have been developed over the last decades. Applied manufacturing processes and techniques depend on the type of matrix in polymer materials. Discontinuous fibre-reinforced composite material with thermosets matrix can be produced by sheet moulding compounds (SMC) and injection-compression moulding. While fibre-reinforced thermoplastics have been used in injection or compression moulding. According to Khosravani, Nasiri, & Reinicke, (2021) almost one-third of all thermoplastic materials are produced by injection moulding [30]. The injection moulding method is appropriate to manufacture mass-produced parts of complicated structures with precise dimensions. The efficiency of the injection moulding process depends on factors such as machine parameters, in-mould parameters, and parts quality control [30].

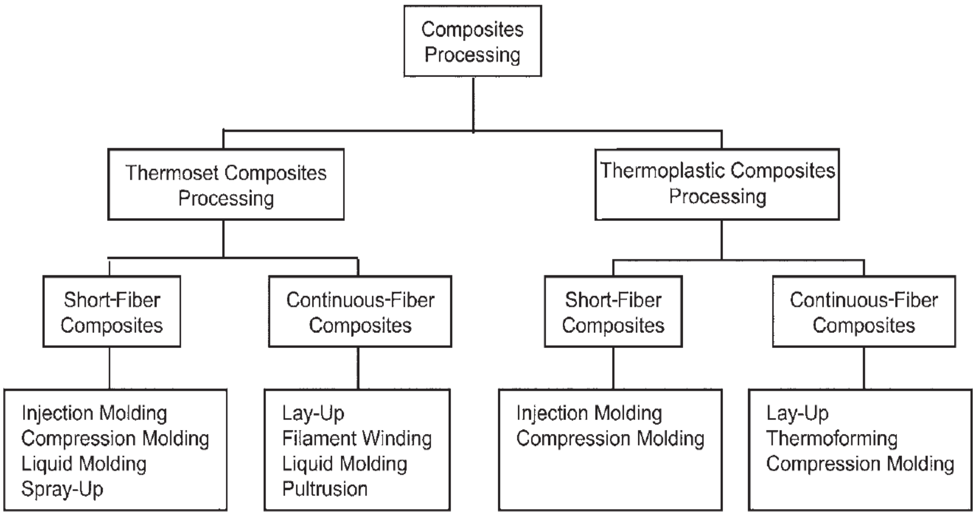

Figure 2.6: The major polymer matrix composite fabrication processes according to [8].

2.3.1 Injection moulding cycle

Polymer injection moulding technique is a process of melting plastic pellets either made of thermosets or thermoplastic. The process is conducted in an injection moulding machine which is divided into 2 units, known as clamping unit and injecting unit. The function of injecting unit is to melt pellets into molten polymers by heat. The main function of the clamping unit is to open and close mould, and to ejects products after moulding. The clamping unit’s configuration can differ from a toggle type and a straight hydraulic type. In the hydraulic injection clamping unit, the mould is directly opened and closed with a hydraulic cylinder. Polymer pellets are melted by a rotating screw to plastic in the injection unit. After the pellets are melted into molten plastic, the accumulated molten material is injected into a clamping unit. When the molten plastic flows into a mould the clamping unit is opened after the cooling process. The whole process of injection moulding is classified into the following steps by [31].

- Clamping
- Injection
- Dwelling
- Cooling
- Mould opening
- Removal of products

The injection moulding cycle starts when the mould cavity closes as the injection polymer melt flows into the mould cavity. During the filling of the mould cavity, a holding pressure is maintained to counteract the material shrinkage. Then the screw starts to turn as the polymer melt is accumulated at the front of the screw for the next shot. The screw starts to withdraw as the polymer melt is ready to be injected to melt to prepare the next shot. The injection moulding process is completed when the mould opens, and the part is ejected. The mould opens when the temperature of the moulded part is sufficiently cool [32].

The time at closing and ejection is dependent on the injection moulding machine and the size of the mould. During the process, the machine controls the moving speed of the screw or the injection speed. While other moulding conditions such as cylinder temperature, back pressure, mould temperature etc are also regulated during the injection process. Moulding factors or conditions determine cured polymer materials' appearances, dimensions, and mechanical properties. Ghandi et al. [7] states that the hold pressure is constrained by a low pressure that leads to excessive shrinkage, while the melt temperature is constrained by a low temperature that results in the void cavity and a high temperature that leads to material degradation. While the hold pressure is bound by low pressure resulting in excessive shrinkage and cavity pressure exceeding the machine clamping force leads to melt flowing across the mould part line. Material shrinkage during cooling and residual stresses can lead to environmental stress cracking under certain conditions in a final moulded part.

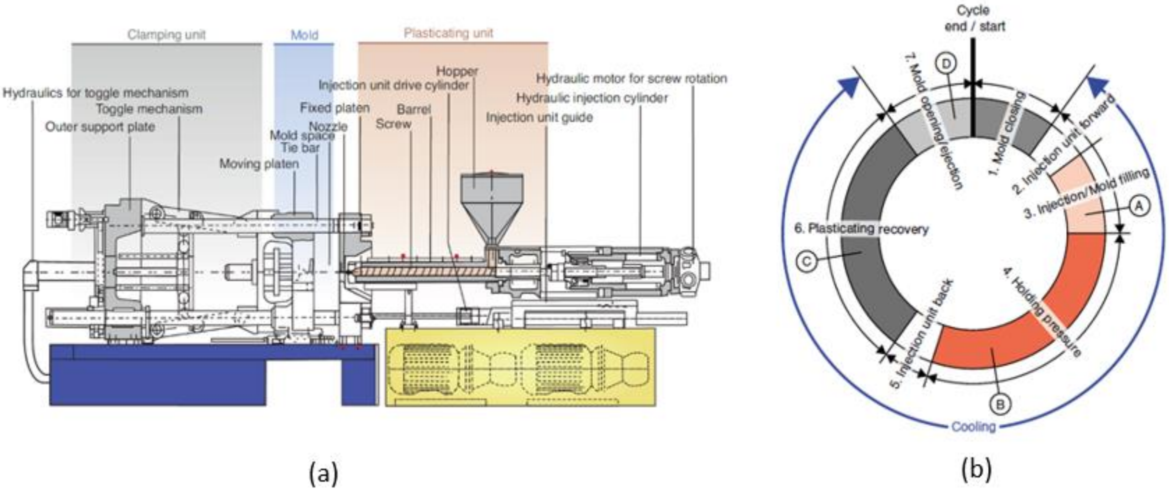

Figure 2.7: An injection moulding machine used to manufacture typical polymer materials in Figure (a) and an injection moulding cycle in Figure (b) (Gandhi et al., 2020).

3 State of the art- *Literature review*

In this section, a literature review on a specific subject area which provides an overview of current knowledge, allowing us to identify relevant theories, methods, and gaps in the existing research in the study regarding micromechanical material models for polymer composites, fibre alignment and theories of mechanics of material for fibre-reinforced composite is conducted. The reviewed literature involves relevant publications such as books and journal articles. The obtained findings from the literature review are analysed, synthesized, and evaluated to provide a holistic picture of the state of knowledge on the subject.

3.1 Rheology of polymer melt

Natural phenomena behave according to the fundamental principle of physics. Professor Bingham of Lafayette College, Indiana quoted a term called "Rheology" describing the study of deformation and flow of matter. The definition was accepted when the American Society of Rheology was founded in 1929. The fundamental work for describing the flow was already initiated by Sir Isaac Newton in his work "Principia" published in 1687s [33].The rheological study of the polymer melt is complex because of shear-thinning, viscoelastic, and their flow properties which are dependent on temperature. During processing, the polymer viscosity is a widely used material parameter to simulate the behaviour of polymers. The viscosity of polymer melt is generally measured using shear deformation measurement devices since most polymer processes are shear rate dominated. The properties of polymer melt during processing determine the development of injection moulded fibre-reinforced polymer material. Therefore, a brief introduction to polymer and properties and flow kinematic during manufacturing is introduced in the following chapter.

3.1.1 Viscosity

The intuitive understanding of viscosity can be defined with the help of equation 3.1. The viscosity of material governs the physical behaviour of materials such as heat flow due to temperature difference, electric current through wire etc. The phenomenon of viscosity influences various daily events for examples when an object slides on a frozen surface such as ice cubes, sledges, or hockey shoes. According to the equation of viscosity, the objects slide on frozen surfaces due to interference of thin film of liquid water. In these phenomena, the thin film forms due to excessive concentration of pressure or normal stress. Where the flow in the direction of motion is caused by the shear stress which must overcome certain resistance. Similarly, the fluid flow of material result from the application of external shear stress, τ_0 [34].

$$\begin{pmatrix} result, or \\ flux \end{pmatrix} = \begin{pmatrix} transfer\ coefficient, \\ or\ inverse\ resistance \end{pmatrix} \begin{pmatrix} cause, \\ or\ gradient \end{pmatrix} \tag{3.1}$$

According to equation 3.1, fluid flow is an effect of shear stress applied by ice weight in the example of sliding on ice. While the transfer coefficient or fluidity which is a characteristic property of the fluid is identical to its inverse resistance of flow. The resistance of a fluid to change shape or flow relative to one another is known as viscosity. The greater a fluid can withstand flow, its viscosity is greater [34].

Viscosity in the polymeric material

The flow of polymer is defined by viscosity during the production that determines the mechanical properties. The viscosity of polymer melts depends significantly on matrix composition. The most common matrix used for the manufacturing of polymer materials is thermosets and thermoplastics. Thermoplastics are traditional plastic material used in our typical daily life. The molecules in thermoplastic are held together by smaller molecular forces. Thermoplastic material is formed by repetition of identical molecule chain known as monomer. Most typical thermoplastic are polypropylene and polyamide. Whereas thermoset plastics are fundamentally distinct due to their chemical composition. The fundamental behaviour of thermoplastic and thermoset differ during application as matrix in polymer material. Thermoset polymer matrix are materials like phenolics, epoxy resins, polyurethanes, etc.

Initial viscosity of thermoset matrix is lower compared to thermoplastic due to their lower molecular mass. Therefore, the application of thermosets in the composite material has a major advantage. Low molecular weight results in low initial viscosity which leads to easy and fast impregnation of the fibres [7]. But thermoset materials tend to solidify when the molecules crosslink due to carbon molecules and epoxy rings. The carbon molecule and epoxy rings allow the molecules to crosslink which increases the viscosity. The crosslinking of thermoset polymer materials is avoided by increasing the polymer melt temperature which reduces the viscosity. Since the solidification of thermoset is initiated typically by heat, increase in temperature accelerates the solidification process which increases viscosity rapidly. The relationship between viscosity and temperature is explained in detail in the following chapter.

Effect of temperature and shear rate

Polymer molecules undergo small and random fluctuation known as Brownian motion where they move constantly past each other and rotate during flow. Brownian motion of polymer material increases when the temperature of the melt is increased. Thus, providing the polymer molecules free volume making the flow of material effortless, and decreasing the viscosity [35]. Generally, the viscosity of liquids decreases rapidly with an increase in temperature. But the viscosity of gases increases when the temperature increases. The accuracy of injection moulding simulation is dependent on the ability of the viscosity model to predict the flow behaviour. The major factor influencing the viscosity during manufacturing of polymer materials is temperature. There are different injection moulding parameters based on temperature such as “melt temperature”, “holding temperature” and “mould temperature” which influences viscosity.

Generally, the thermoplastic polymer hardens when the temperature decreases from the molten state. When the thermoplastics are cooled, the long molecules are no longer allowed to move easily. If the cooled thermoplastics are reheated, then they will regain the ability to “flow” and the molecules can slide past each other freely. Thermoplastics are characterized into two different categories amorphous and semi-crystalline thermoplastics. Amorphous thermoplastics have molecules that remain in disorder when the temperature cools. Fall in temperature leads to materials obtaining random molecular structures. An amorphous polymer hardens, or vitrifies, as it is cooled below its glass transition temperature. While semi-crystalline thermoplastics solidify which forms a crystalline structure. The molecules begin to arrange in a regular order when the material is cooled, and the temperature drops below the melting temperature [7].

Compared to thermoplastics, thermosets are harder, more rigid and brittle, and their mechanical properties are less temperature dependent. The curing of fibre-reinforced thermoset is dominated by an exothermic reaction. During the reaction, the cross-linking of molecules solidifies the polymer material. The exothermic reaction increases the temperature of the thermosetting resin. Temperature rise results in the melting of resin and the mobility of the molecules are increased. Subsequently, reducing the viscosity of polymeric fluid which facilitates fibre impregnation. However, since the solidification process is a chemical curing reaction, thermosets typically have a longer processing time compared to thermoplastics. Simultaneously, high temperature accelerates the reaction and growth of molecules. As the temperature rises higher, the cross-linking reaction causes the viscosity to increase rapidly. During this transition, the viscosity increases until the resin ceases to flow, a stage known as the gel point. At the gel point, the resin gels transform from a liquid to a rubbery state. At the gel point, all the molecules are interconnected and become so large that fluid is not capable to flow. Viscosity at the gel point often reaches a value of 1000 poise. Regulating the temperature during the manufacturing of polymer is essential to avoid the degradation of fibres [8].

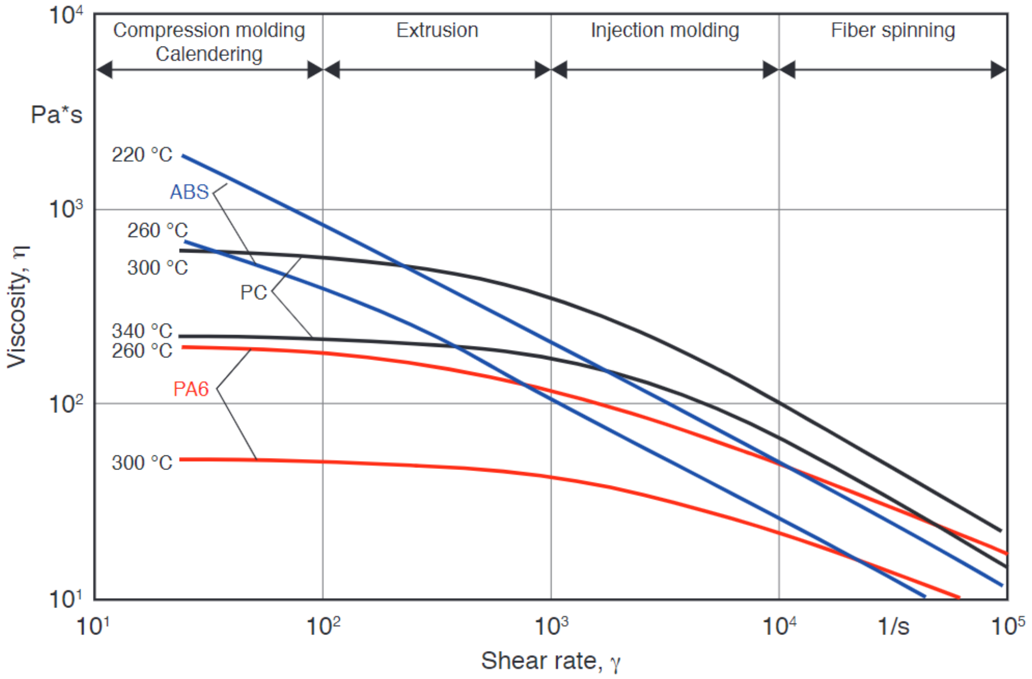

Figure 3.1: Viscosity curves for a selected number of thermoplastics with temperature and shear rate according to [36].

Pressure dependency on viscosity

Generally, fluids such as polymer melts are considered incompressible. But during processing, polymer melts are subjected to high pressure which affects the viscosity of flow. The dependency of polymer viscosity increases with the hydrostatic pressure. When the hydrostatic pressure during manufacturing is high the polymer melts exhibit small compressibility. Usually, it occurs during manufacturing processes such as Resin Transfer Moulding (RTM) and Reactive Injection Moulding (RIM). The dependency of viscosity on pressure is significant during manufacturing with injection moulding because the pressure frequently exceeds 100 MPa. According to the equation, the viscosity follows pressure exponentially, but with an inverse effect. The free volume between the molecules decreases when the pressure increases [35]. The effect of pressure on viscosity can be described with the following equation:

$$\eta_{0,p} = \eta_{0,np} e^{\beta p} \tag{3.2}$$

Where the $\eta_{0,np}$ is zero-shear viscosity at atmospheric pressure, p is pressure, and β is material-characteristic pressure coefficient. Therefore, an increase in pressure also increases viscosity, but the effects of pressure on viscosity are not effective as temperature [35].

The injection pressure varies with the permeability of fibre mat, geometry, and injection rate. Manufacturing process such as Resin Transfer Moulding (RTM) and Reactive Injection Moulding (RIM) has a major advantage due to low injection pressure. A low injection rate requires injection pressures between 70 kPa and 140 kPa, and fibre content of 10% to 20% by volume. A rapid mould filling requires injection pressures between 700 kPa and 1400 kPa, and higher fibre contents can be reached, varying from 30% to 50% by volume. In addition, RTM and RIM employ closed moulds, which reduces or eliminate the emission of hazardous vapour. Other advantages include more repeatable part thickness and minimal trimming and de-flashing of the final part. Therefore, RTM and RIM processes are applied to manufacture high-strength and lightweight parts for both the aerospace and automotive industry [7].

Aspect ratio and polymer concentration

Fibre aspect ratio is the ratio of length to diameter of a fibre. The viscosity of typical fibre-reinforced thermoplastic composites increases with the length of fibres. The movement of polymer molecule is hindered more when the fibre length is longer. Therefore, the complex viscosity of composites increases with an increase in the length of the original fibre [37]. A study by [38] was conducted to identify the rheological properties of a material according to squeeze flow between two parallel disks. Results from the study indicated that the viscosity of polymer is dependent on aspect ratio of fibre. The study concluded that at constant volume, fibres with a longer aspect ratio made the material more viscous [31].

The polymer concentration has a direct relationship with the polymer viscosity. The polymer viscosity increases when the polymer concentration increases. In the Figure 3.2, polymer materials AP-P3 and MO-400 have different salinities in ppm are shown as 10 000, 30 000, and 100 000 at 80 degrees Celsius. The Figure 3.2 shows that the viscosity of polymer material varies with the polymer concentration. The polymer solution with higher concentration has larger molecules that exert drag and interact with each other. Thus, leading to a higher viscosity with higher concentration. However, at higher salinities the viscosity of material increases and decreases with lower salinity when the polymer concentrations is constant [39]. An experimental study conducted by Goris, (2017) concluded that the viscosity is dependent on fibre concentration [40]. The study showed that the viscosity of polymer melts increases with fibre concentration. The experiment also concluded that higher fibre concentration increases the interaction of fibres which can accelerate fibre breakage.

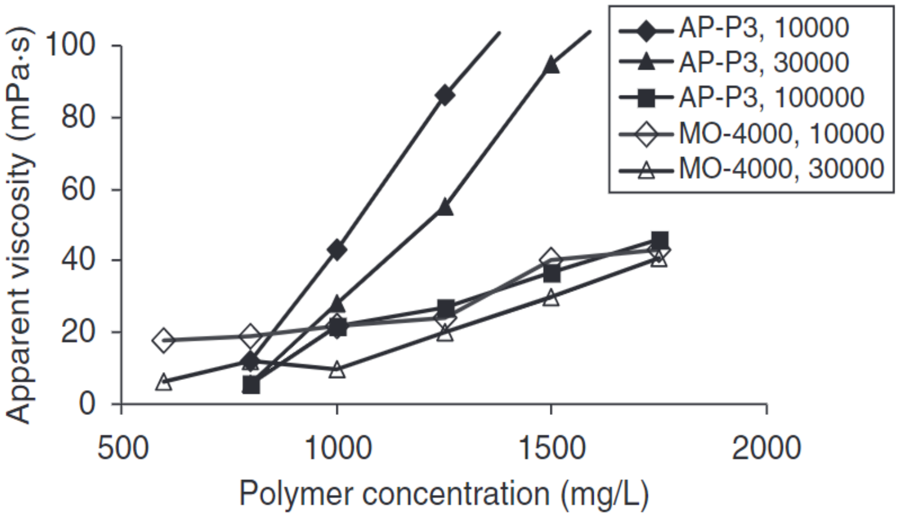

Figure 3.2: Viscosity of polymer compared with the concentration for AP-P3 and MO-4000 [39].

3.1.2 The generalized Newtonian fluids

Three hundred years ago the laws' derived by Hooke and Newton was considered universal. But the advancement of science in the 19th century established that Newtonian fluid and Hookean solid laws' application were invariably limited. For example, helium-4 is an isotope form of element helium that behaves like a fluid with zero viscosity. Therefore, these forms of helium are characterized as superfluid. Properties such as rigidity modulus and viscosity of materials that defy the linear laws of Newton and Hooke vary significantly relative to small stress [41]. Newton's postulated that the force per unit area required to produce the motion is F/A also known as stress and is denoted by σ. According to Newton, stresses are proportional to the velocity gradient U/d or shear rate. Shear rate is usually written as $\dot{\gamma}$ instead of U/d. The postulate claims that if we double the force on the object, then we will also double the shear rate. The constant of proportionality η is called the coefficient of viscosity [33].

Thus,

$$\sigma = \eta \frac{U}{d} = \eta\dot{\gamma} \tag{3.3}$$

Fluids that obey Newton's postulate are known as Newtonian fluids. Fluids, where viscosity depends on shear rate, are characterized as non-Newtonian fluid, e.g., blood, synovial fluid, mucus etc. [42]. Glycerine and water are common Newtonian fluids characterized by their viscosity (the ratio between shear stress and shear rate). The viscosity for glycerine in SI units is 1 Pa.s, whereas the viscosity of water is about 1 mPa.s or 1 centipoise. This says that water is one thousand times less viscous than glycerine. Newtonian fluids display a linear relationship between shear stress and shear rate. Thus, the only parameter to describe these fluids is the slope of the shear stress-shear rate relationship, η (Pa.s). Fluids are characterized as Newtonian by constant viscosity independent of shear rate. Polymer materials that have linear dependency between shear stress and shear rate are Newtonian polymer fluids [43].

3.1.3 Shear thinning behaviour of polymers

Fluids that defy the Newtonian law of fluid are characterized as non-linear behaviour of material as shown in the Figure 3.3a and 3.3b. The most common nonlinearity of fluid is known as shear thinning which is illustrated in the Figure 3.3a. For shear-thinning materials, the viscosity is reduced when the shear rate is increased in a steady flow. The toothpaste which sits apparently on the toothbrush is easily squeezed from the tube is a familiar example of shear-thinning material. Shear-thinning is just one type of non-linear behaviour, there are others such as shear-thickening which is the opposite phenomenon of shear-thinning [42]. And Bingham plastics flow only when the material is subjected to shear stress bigger than characteristic stress, the yield stress [34].

Generally, polymer melts are considered as shear-thinning fluids whereas shear-thickening properties are also rarely observed. Therefore, polymers exhibiting shear thinning are considered pseudoplastic materials. The shear-thinning effect of the material is the reduction in viscosity at a high rate of deformation. Shear-thinning occurs due to low rates of deformation which allows the polymer molecules to be entangled. While the molecules are stretched out and disentangled at high rates of deformation. The disentangled of molecules allows to move more freely which reduces the melt viscosity of polymer [36]. The degree of disentanglement of polymer material differs on the shear rate. At a high shear rate, the polymer molecules will behave like a Newtonian fluid. Polymer materials disentangle entirely at a high shear rate where the viscosity of a fluid is determined independently of the shear rate. The polymer also begins to exhibit Newtonian behaviour at a very low shear rate where the polymer molecules move slowly that the entanglement does not occur.

A model proposed by Ostwald and de Waale based on the power law can accurately represent the shear-thinning properties of polymer material. The proposed power-law model is [36]:

$$\tau = m(T)\left(\frac{d\gamma}{dt}\right)^{n} = m(T)\,\dot{\gamma}^{n} \tag{3.4}$$

The equation 3.4 can be rewritten in logarithmic form,

$$log(\tau) = log(m) + n * log\,(\dot{\gamma}) \tag{3.5}$$

With the definition of viscosity and Oswald equation, we obtain,

$$\eta = m(T)\dot{\gamma}^{n-1} \tag{3.6}$$

Where m represents the consistency index and n, the power-law index.

The shear thinning of the polymer occurs due to the significant orientation of the segments between entanglements under the shear flow. The small-angle neutron scattering (SANS) method which studies the polymer melts under steady-state flow simulates the flow behaviour at a molecular scale. Different results from the Rheo-SANS studies conducted in Japan and France is published in a book by [44]. Studies concluded that the polymer chains remain largely undeformed under steady-state shear flow conditions for which extensive shear thinning was present. Studies observed that, as the polymer is sheared in the non-Newtonian region the macromolecular dimensions of melt remained unaffected. Observation by these studies were directly contradicting the accepted understanding of shear-thinning in the polymer.

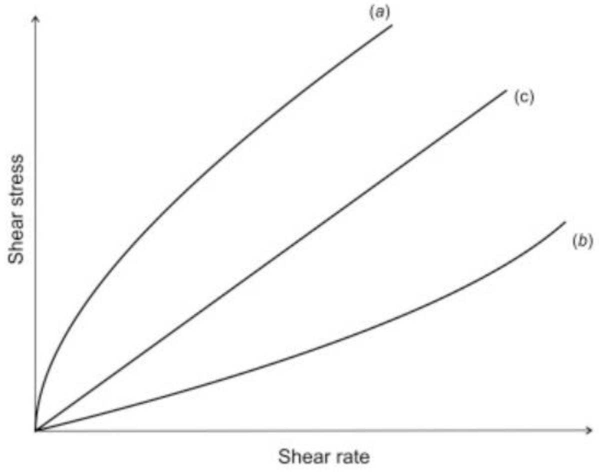

Figure 3.3: Non-Newtonian flow: (a) shear-thinning fluid, (b) shear-thickening fluid, and (c) Newtonian fluid [42].

3.1.4 Flow kinematics during injection moulding

The principles of fluid mechanics need to obey the law of conservation of mass, Newton's laws of motion, the laws of thermodynamics and certain boundary conditions. The fluid flow must satisfy these laws and conditions that form the essence of fluid mechanics. The term kinematics of fluid flow is the rate of displacement or velocities of fluid [45]. During the filling phase, the polymer melt can be considered as a generalized Newtonian fluid (GNF). Thus, the flow of fluid can be described mathematically where u, v, and w denote the velocity along the x, y, and z spatial coordinates [7].

$$\frac{\partial \rho}{\partial t} + \bar{V} * \rho u = 0 \tag{3.7}$$

$$\frac{\partial}{\partial t}(\rho u) + \bar{V} * (\rho u u - \sigma) = \rho g \tag{3.8}$$

$$\sigma = -pI + \eta(\bar{V}u + \bar{V}u^T) \tag{3.9}$$

$$\sigma = -pI + \eta(\bar{V}u + \bar{V}u^T) \tag{3.10}$$

$$\rho C_p\left(\frac{\partial T}{\partial t} + u * \bar{V}T\right) = \bar{V} * (k\bar{V}T) + \eta\,\dot{\gamma}^2 \tag{3.11}$$

Here u is the velocity of flow, T is temperature, p is the pressure σ the total stress tensor, ρ the density, η is the viscosity, k is the thermal conductivity, C_p is the specific heat, and $\dot{\gamma}$ is the rate of deformation tensor.

Fountain flow and particle orientation

Generally, polymer fluids are considered viscous fluids during injection moulding. During modelling of injection moulding, the polymer melts can define as a fountain type flow. When the molten fluid flows through the mould cavity there is a resistance to the flow and the temperature of melts cools which results in fountain flow. In a fountain flow, the flow rate is faster at the middle of the flow and slower at the top and bottom of the flows [7]. The illustration of the fountain flow of polymer melts during injection moulding is depicted in the Figure 3.4. Fountain flow during injection moulding results in fibre orient along the parallel direction of the flow at the top and bottom surfaces. While this also causes the polymer to have a random orientation in the middle of the flow. The parallel orientation of polymer forms a skin-core phenomenon during injection moulding. Skin formed at the walls can have different properties compared with the core properties of the fluid. While the thickness of the skin is determined by the polymer type and viscosity. During injection moulding, the thickness can be regulated with the processing condition [46].

The development of anisotropy is one of the major factors that determine the mechanical properties and the dimensional stability of a moulded part. The anisotropic properties of the moulded part are a consequence of preferential fibre alignment based on the flow conditions during mould filling. The main challenge with injection moulded polymer material is the high amount of fibre alignment distribution throughout the moulded part. Fibre alignment throughout the moulded part depends on the high shear rates and long flow paths during mould filling. The main reason for high degrees of orientation in injection moulded parts is due to the flow kinetic such as fountain flow and radial flow.

The fountain flow effect is caused by the no-slip condition on the mould walls which considers the velocity at mould walls to be zero. This forces material from the centre of the part to flow outward to the mould surfaces at the flow front as shown in the Figure 3.4 [7].

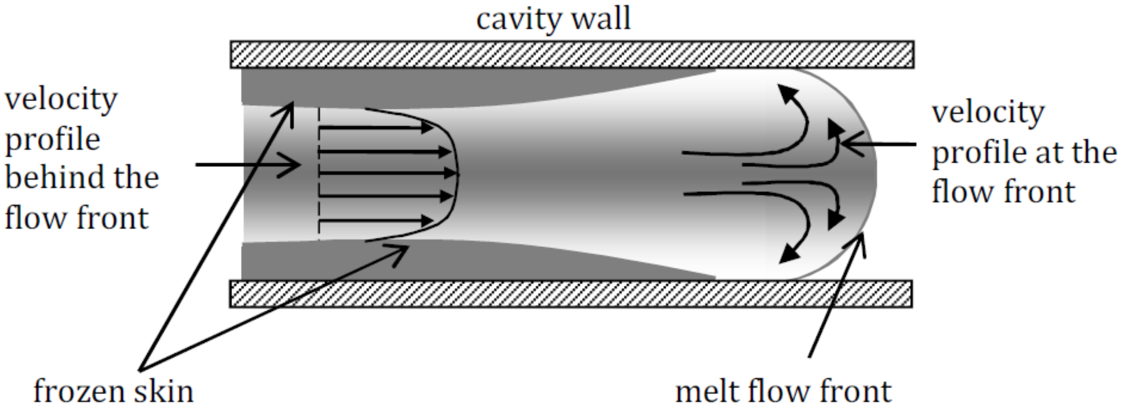

Figure 3.4: Fountain-flow and solidification mechanisms through the part thickness during injection moulding [35].

Radial flow

The second flow kinematics that often influences the parameter of fibre reinforced polymer during injection moulding is radial flow. Radial flows are unidirectional flows where a unique nonzero velocity component is dependent on one direction. The velocity of the components forces the flow of fluid to flow in a unidirectional manner. Where the velocity profile is determined by the mass balance on an appropriate control volume with surfaces orthogonal to the radial streamlines. Usually, the pressure of radial flow can be calculated by Bernoulli's equation. Since there is no loss in mechanical energy along streamlines. Bernoulli's equations emphasise that the pressure is reduced near sinks and sources to provide for the high velocity may cause cavitation of fluid [34].

Due to the radial flow, the fibres in polymer material start to orientate perpendicular to the flow direction. Often the orientation is concentrated in the central layer of an injection moulded part. The effects of radial flow during polymer processing are depicted in the Figure 3.5. This mechanism is illustrated by U. Gandhi, (2020) suggests that the polymer flowing through the gate is stretched transversely [7]. While the material flowing throughout the surface as it flows away from the gate is radially expanding. This leads to high degrees of orientation in injection moulded polymer materials. The flow is well represented in different mould filling software such as Moldex3D today [47].

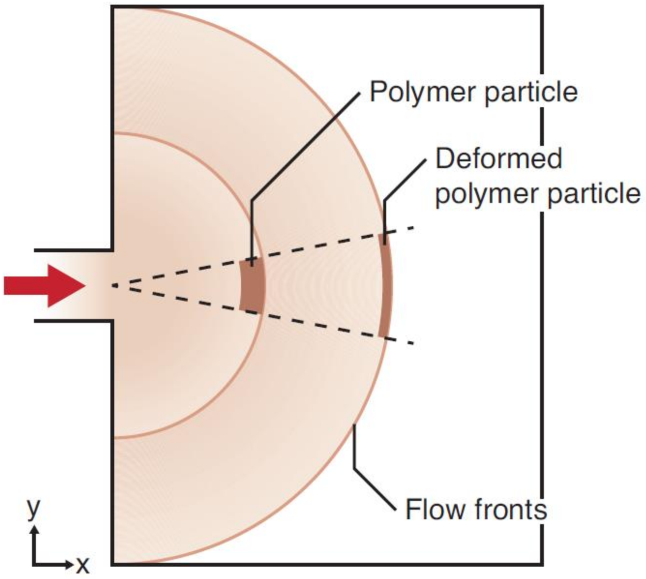

Figure 3.5: Deformation of the polymer during injection moulding due to radial flow [7].

Formation of weld line

In many products manufactured by injection moulding, weld lines occur. Weld lines are also called knit lines or simply welds. The term" weld line" is common to everyone working in plastics fabrication. The line which can be seen on a product surface is just the optical defect of this phenomenon. The correct term would be weld region, weld zone, or weld plane. One of the most commonly seen defects in injection moulding is weld lines. A weld line is formed when two or more flow paths meet in the injection filling process. If the flow fronts did not inter-diffuse well enough before they cooled, a line, notch and colour change will occur, which is generally referred to as a weld line or a knit line. The properties of the weld line strongly depend on the shape of the three-dimensional area, which is formed when two melt streams reunite [48].

Weld lines can be divided into two groups called meld lines and frontal weld lines. Frontal weld lines are formed by the frontal collision of two flow fronts and streaming weld lines, or meld lines are formed by two flow fronts moving parallel. Roughly, the meeting angle can be used to differentiate weld lines and meld lines. A meeting angle smaller than 135° produces a weld line, while greater than 135° produces a meld line. Typically, weld lines are considered to be of lower quality than meld lines. The meeting angle influences weld lines' properties significantly since it affects the degree of molecular fusion, entwisting, and diffusion across a weld line after it is formed. The larger the meeting angle, the higher the properties of weld lines [49]. In this study, two different simulations are conducted with dog-bone specimen and water pipe, which are presented in chapters four and five and in both cases, frontal weld lines are formed.

Weld lines result from multiple flow fronts. They can be caused by multiple injection gates, the usage of inserts in the moulding, the existence of holes, and other specific part geometric characteristics that may cause melt flow to split and then merge again [50]. The consequences of weld lines composite materials lead to a weak structure at weld lines, especially when they are close to snap fits, screw holes, etc. Moreover, weld lines are visually undesirable, causing an appearance issue. According to a report published by John W. Bozzelli (2008), a weld line can have as little as 20 % of the nominal strength of the part. Weakness is caused when polymer chains are only partially entangled across the weld line. The strength or weakness of the weld line depends on material design, tooling, and processing [51].

The best solution to reduce the effect of weld lines is to eliminate the weld line, which is not possible. But several different approaches can be taken to minimise the impact of weld lines. For instance, the part design can be modified such as by increasing the part thicknesses to facilitate the transmission of pressure; flow deflectors and flow leaders can be used to relocate the weld lines and holes, and other geometric features that may cause melt to split and merge again can be avoided. Moreover, many studies indicate that other methods, including modifying the mould design and setting up appropriate moulding process parameters, can be implemented to minimise the effect of weld lines. For mould design, one may increase or adjust the size of runners and gate, place vents in the area where the weld lines may appear or enlarge the existing vents to eliminate the entrapped air. Factors such as the gate location, injection time, melt temperature, and mould temperature are among the most influential factors that cause the occurrence of weld lines. These process parameters can be set to a specific range to improve the inter-diffusion of flow fronts, thus reducing the possibility of weld lines

Additionally, Zhai (2008) proposed a method for relocating weld lines to specific positions by dividing the moulding into sub-mouldings, determining the optimal gate location for each sub-moulding, and resizing runner dimensions to reduce the impact of weld lines. Zhai (2008) also proposed a Taguchi experimental method for reducing the effect of weld lines on the appearance of plastic parts. This method allows for analysing a wide range of parameters without requiring excessive experimentation. They used an image processing method to identify weld lines on the parts for the experiment. The research revealed that the severity of weld lines is relevant to the injection speed, injection pressure, and melt temperature. By adjusting these parameters, weld lines may be reduced to a certain degree. This is an experimental approach, and it did not consider one of the most influential factors for weld lines, which is the gate location [50].

Furthermore, John W. Bozzelli (2008) proposed in his study that the gate be placed so that the weld line location is not in an area of the part that will be subjected to high stress during use. Changing the gate location to relocate the wild line to less-stressed areas is one solution. It is also essential to properly vent the area around weld lines. It may be worthwhile to include a flow tab that allows the flow fronts to knit more tightly and serves as a vent for trapped air where the flow fronts meet. The paper also emphasises that while processing can affect the strength and cosmetics of weld lines, it cannot eliminate the underlying causes. It is also vital to avoid low pressure as low pressure at the flow front does not promote molecular chain entanglement, resulting in poor impact strength during the injection moulding process. Another solution is to increase the injection velocity, decrease the fill time and increase the shear rate, which can lower the viscosity of the polymer during fill, thereby allowing for better chain entanglement and better packing [51].

3.2 Theories of mechanics of material for fibre-reinforced composite

On the other hand, Robert Hooke derived the “True Theory of Elasticity” in 1678. Robert Hooke developed a principle for Hookean solid, where the relationship between deformation and stress is directly proportional. Understanding both Hookean and rheological properties of polymer materials is essential to predicting moulded polymer material's mechanical performance for industrial applications [33]. Composites are usually described as multiphase material which consists of different materials to obtain desired mechanical properties [52]. The fibre and matrix composition of composites provides significantly complicated micro and macrostructures compared to traditional materials such as metals, concrete etc. Micro and macrostructures make it difficult to predict the mechanical behaviour of composite material. Particularly composite material reinforced with short fibres makes the structures far more complex. Theories describing micromechanics of the short fibre reinforced composite is presented in the chapter. Even with distinctive micro and macrostructures of composites material the mechanical properties and behaviour is governed by the same general laws and principles of mechanics [53]. A brief description of the general material properties and mechanics of composite is given below.

3.2.1 Classical stress and strain

The classical method to define stress and strain is based on the notion that an object is subjected to small deformation. The small deformation approach is based on the infinitesimal strain theory to describe the deformation of a solid body. The infinitesimal strain theory is derived by considering the geometric changes during the loading of a body are small [54]. This means that the displacement of each material point (a location that is fixed in a body under deformation) is assumed to be linear. The geometric changes can be represented using a first-order linear representation with only one stress and strain.

Uniaxial loading

In the classical approach, stress and strain of material are defined in a uniaxial deformation which is illustrated in Figure 3.6. The figure illustrates an elastic body with a cylinder with an initial length L_0

and cross - sectional area A_0. The cylinder is loaded uniaxially with a force F and is fixed at the bottom. The cylindrical body is displaced at the top with a distance u due to the applied force F. Generally, the length of the cylinder L can be represented with a nonlinear function of the applied force $L = L(F)$ [55].

The relationship of the function $L = L(F)$ can be represented as a Taylor series expansion expressed as,

$$L = L_0 + \frac{dL(F)}{dF} F + \cdots \tag{3.12}$$

According to the infinitesimal strain theory, only the linear term or the first derivation of $L(F)$ is included [55]. Thus, the displacement of the cylinder $u = L - L_0$ and stiffness of the body $k = dF/dL$. This gives the classical linear elastic relationship of force and displacement also known as Hooke's law. The relationship shows that force at an object is directly proportional to the stiffness and displacement.

$$F = ku \tag{3.13}$$

The stress of the body is equal to the force divided by the cross-sectional area of the body. The stress of an object is proportional to the applied force and inversely proportional to the cross-sectional area.

$$\sigma = \frac{F}{A_0} \tag{3.14}$$

And the strain is defined as the deformation of a body due to stress. The strain is given by the normalized displacement,

$$\varepsilon = \frac{u}{L_0} = \frac{L - L_0}{L_0} \tag{3.15}$$

In addition, the engineering stress-strain curve which is also known as the nominal stress-strain curve, is obtained from the uniaxial tensile test. The engineering strain ε_e is defined by the uniaxial deformation relative to the initial gauge length L_0. While the true stress σ_t and the true strain ε_t are defined in terms of the initial specimen geometric parameters, without considering the change in cross-section.

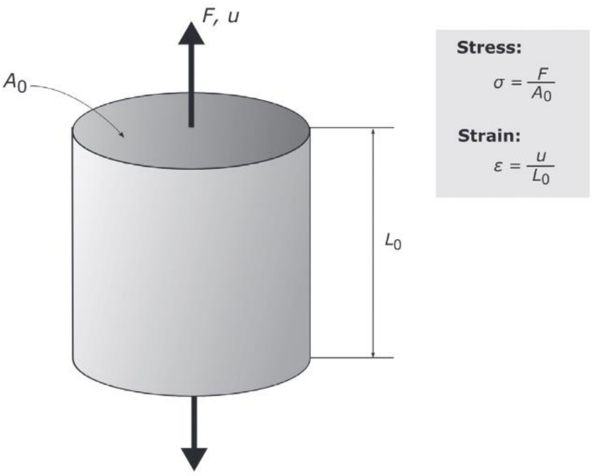

Figure 3.6: Classical definition of stress and strain for uniaxial loading with small deformations [55].

Multiaxial loading

Figure 3.7 shows the classical approach the stress and strain of material is defined in a multiaxial deformation. Stress and strain of the object can be characterized by normal and shear stresses on a small cubical volume element, as illustrated in the Figure 3.7. The shear stress on the surface in the cube has two perpendicular components aligned with two axes parallel to the edges of the face. Therefore, there are nine stress components consisting of three normal components and six shear components on a cubic element [54]. Each surface of the cube consists of single normal stress and two shear components. The shear stress matrix is symmetric where $\sigma_{xy} = \sigma_{yx}$, $\sigma_{xz} = \sigma_{zx}$, and $\sigma_{yz} = \sigma_{zy}$, because the force equilibrium is satisfied [55]. In multiaxial loading, the stress and strain at each point of the body are characterized by six components for stress and strain. The six components of stress and strain in multiaxial loading can be represented by symmetric 3x3 matrices. Thus, the stress tensor can be represented as follows,

$$\sigma_{ij} = \begin{matrix} \sigma_{xx} & \sigma_{xy} & \sigma_{xz} \\ \sigma_{yx} & \sigma_{yy} & \sigma_{yz} \\ \sigma_{zx} & \sigma_{zy} & \sigma_{zz} \end{matrix} \tag{3.16}$$

The strain in the multiaxial loading is calculated with the same principle as in uniaxial loading. The displacement vector $U = (u_x, u_{y,} u_z)$ of the object which differs with the position $X = (x, y, z)$ in the object. Displacement of an object is given by the following equation,

$$U(X) = x(X) - X \tag{3.17}$$

Where, X is the initial position of the material point and x is the deformed state in the equation. The normal strain in the three-dimensional domain is given as,

$$\varepsilon_x = \frac{\partial u_x}{\partial x}, \qquad \varepsilon_y = \frac{\partial u_y}{\partial y}, \qquad \varepsilon_z = \frac{\partial u_z}{\partial x} \tag{3.18}$$

Where the normal strains are denoted as ε_{xx}, ε_{yy}, and ε_{zz} in a spatial coordinates x, y, and z. And the displacement in x, y and z-direction is given by u_x, u_y, and u_z respectively. The shear strains in each direction can be expressed by,

$$\gamma_{xy} = \gamma_{xy} = \frac{\partial u_x}{\partial x} + \frac{\partial u_y}{\partial x} \tag{3.19}$$

$$\gamma_{yz} = \gamma_{zy} = \frac{\partial u_y}{\partial z} + \frac{\partial u_z}{\partial y} \tag{3.20}$$

$$\gamma_{zx} = \gamma_{xz} = \frac{\partial u_z}{\partial x} + \frac{\partial u_z}{\partial z} \tag{3.21}$$

And the tensorial normal and shear strain components of the infinitesimal strain tensor can be represented as given,

$$\varepsilon_{ij} = \begin{matrix} \varepsilon_{xx} & \varepsilon_{xy} & \varepsilon_{xz} \\ \varepsilon_{yx} & \varepsilon_{yy} & \varepsilon_{yz} \\ \varepsilon_{zx} & \varepsilon_{zy} & \varepsilon_{zz} \end{matrix} = \begin{matrix} \varepsilon_x & 0{,}5\gamma_{xy} & 0{,}5\gamma_{xz} \\ 0{,}5\gamma_{yx} & \varepsilon_y & 0{,}5\gamma_{yz} \\ 0{,}5\gamma_{zx} & 0{,}5\gamma_{zy} & \varepsilon_z \end{matrix} \tag{3.22}$$

In both stress and strain matrix the first subscript of i represents the normal direction of the cube surface. And the second subscript j represents the direction of the stress or strain quantity.

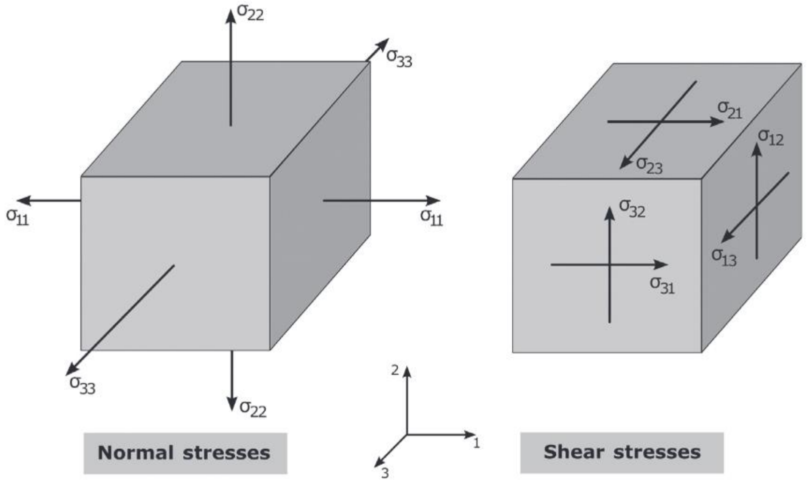

Figure 3.7: Classical definition of stress and strain for multiaxial loading with small deformation and shows shear and normal stress components [55].

3.2.2 Large Strain Kinematic

Polymer mechanics and solid mechanics are theories regarding the evolution of stresses and strains under extreme loading condition in form of forces, displacement, and temperatures. The classical definition of stress and strain are accurate to study object with small deformation. However, the calculation becomes complicated when the applied deformation of an objects is significantly large. The large deformation on an object changes shape and size significantly compared to before applying deformation [55]. The theory of large strain deformation can be addressed by defining a few basic physical quantities (motion and deformation) and the corresponding mathematical relationship. The applied loads acting on a body make it move from one position to another. This motion can be defined by studying a position vector in the "deformed" and "undeformed" configuration. The configuration of deformed and undeformed position in large strain deformation is illustrated in the Figure 3.8.

Large or finite strain theory is widely applied to establish the governing equation for large deformation problem. According to the finite strain theory or large strain theory the body consist of a collection of small volume elements. These volume elements are also referred as a material point. Kinematics is a subject that defines the movement of material point when the object is applied with deformation. In finite strain theory the deformations are finite, implying that the object can undergo changes to size and shape under loading. In contrast to small strain theory where the displacements are small which does not change that shape and size of object during deformation.

The lagrangian and Eulerian approaches are examples of such kinematic formulations to determine the motion of a deforming body. The kinematic formulation describes stress and strain in the object with one material point at original position P and the deformed configuration p with time t as shown in the Figure 3.8. At time $t = 0$, the region of three-dimensional (3D) Euclidean space is called the initial or undeformed configuration (Ω_0). And when the region of 3D Euclidean space occupied at time t is called current or deformed configuration (Ω). The position of a material point in the initial configuration is given by [56] as,

$$X = X_i \, e_i = \sum_{i=1}^{n_{sd}} X_i \, e_i \tag{3.23}$$

where, X_i are the components of the position vector in the undeformed configuration and e_i denotes the unit base vectors. The initial position vector X of the material point P does not change with time [57]. The coordinated X_i are called the material coordinates or Lagrangian coordinates. Whereas the position vector x of the object in the current configuration is given by,

$$x = x_i\, e_i = \sum_{i=1}^{n_{sd}} x_i\, e_i \tag{3.24}$$

where, e_i is the unit vector that defines the basis of the spatial coordinate system and x_i are the coordinated of the object in the spatial coordinate system. The coordinated x_i describes the spatial position of the material point. Therefore, it is referred to as spatial coordinates or Eulerian coordinates. The Eulerian description is focused on deformation at a specific coordinate in space with time. This approach is widely applied in fluid mechanics where it is not required to define motion with respect to an initial configuration. Whereas in the Lagrangian description the body changes in the position and physical properties as the body moves in space and time [57]. Approaches to define the deformation of an object with material and spatial coordinates is called Lagrangian or material description and spatial or Eulerian description respectively. The motion of the body is defined in terms of Lagrangian description as $x = x(X, t)$ and with Eulerian description as $X = X(x, t)$. Thus, the Lagrangian description expresses the displacement field which is the difference between the initial position to current position as,

$$u = x(X, t) - X \tag{3.25}$$

In the Eulerian description the displacement is defined in terms of spatial coordinates as,

$$u = x - X(x, t) \tag{3.26}$$

The velocity of the position vector for a material point is the rate of change of its position with time and holding X constant. The partial derivative of body moving with respect to time is called the material derivative of quantity [56]. Where the velocity is expressed as,

$$v = \frac{\partial x(X, t)}{\partial t} = \frac{\partial u(X, t)}{\partial t} \tag{3.27}$$

And the material derivatives in Eulerian coordinates is obtained by applying chain rule and $x = x(X, t)$ as,

$$\frac{Dv_i(x, t)}{Dt} = \frac{\partial v_i(x, t)}{\partial t} + \frac{\partial v_i(x, t)}{\partial x_j} * \frac{\partial \phi_i(X, t)}{\partial t} = \frac{\partial v_i}{\partial t} + \frac{\partial v_i}{\partial x_j} v_j \tag{3.28}$$

Where the first term on the right-hand side is the Eulerian derivative. The Eulerian derivation yields the local rate of change of the quantity occurring at the position x. And the second term of the right-hand side is the convective derivative defining the rate of change of quantity [57].

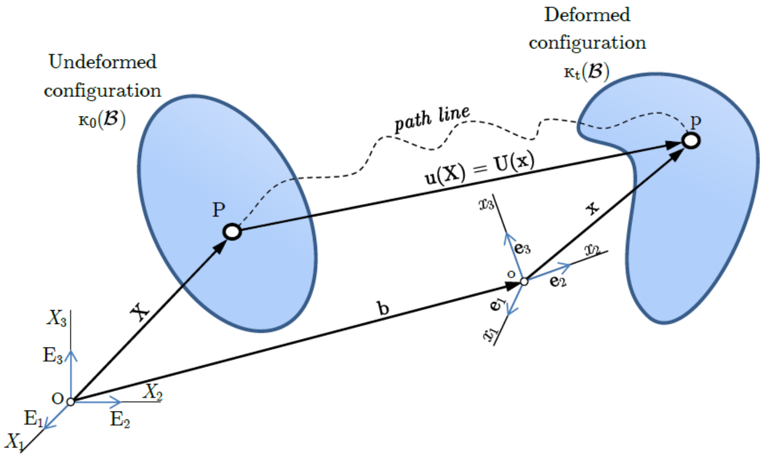

Figure 3.8: Undeformed (initial) and deformed (current) configuration of the 3D Euclidean space with time [58].

3.2.3 Anisotropy

The development of material properties under applied load is dependent on microstructure of a solid material from nano to macro scale. However, the isotropy of material should not be mistaken with homogeneity which characterizes properties as being independent of position. When a material exhibits identical strength under loading irrespective of direction is known as isotropic material. Common examples of material exhibiting isotropic properties are metal, glass and plastics. Even though metallic materials are inhomogeneous they are isotropic because the constituents are distributed sufficiently. The distribution of metal constituents provides same material properties (stiffness, strength, conductivity, etc) in all orientations. Isotropic materials differ from anisotropic material, which exhibits material properties dependent of the direction. Anisotropy must be considered for various material, such as fibre reinforced composite and wood. These material displays superior strength when the force is applied along the fibre direction compared to orthogonal to fibre direction. Additionally, failure of materials with anisotropic properties is unique compared to isotropic material, and usually cannot be categorized as brittle or ductile [59].

Anisotropy of material is further distinguished as orthotropic, a material is orthotopic when the mechanical or thermal properties in different direction varies with direction. Wooden materials are considered as orthotopic material which has different properties in longitudinal, radial, and tangential direction. Additionally, composite material with continuous fibres with laminated structures are also considered to be orthotropic. However, fibre-reinforced composite material consists of discontinuous fibres which are embedded inside a polymer matrix during manufacturing does not exhibit orthotopic property. The discontinuous fibres rotate during processing, which gives a preferential alignment and concentration based on the flow condition. The fibre alignment of fibres develops anisotropy in moulded composites which determines the mechanical properties and the dimensional stability. The mechanical properties of the discontinuous fibre-reinforced composites are determined with process of homogenization according to micromechanics model presented later in the thesis.

Anisotropic stress and strain relation

Fibre-reinforced composite filled with fibres gives anisotropic inhomogeneous material. Therefore, the traditional stress-strain assumptions do not give accurate results due to the development of anisotropy. The anisotropic strain-stress relation in a three-dimensional coordinate system is derived by [7] as,

$$\mathrm{\varepsilon}_{11} = \frac{1}{\mathrm{E}_{11}}\sigma_{11} - \frac{\mathrm{v}_{21}}{\mathrm{E}_{22}}\sigma_{22} - \frac{\mathrm{v}_{31}}{\mathrm{E}_{33}}\sigma_{33} \tag{3.29}$$

$$\mathrm{\varepsilon}_{22} = -\frac{\mathrm{v}_{12}}{\mathrm{E}_{11}}\sigma_{11} + \frac{1}{\mathrm{E}_{22}}\sigma_{22} - \frac{\mathrm{v}_{32}}{\mathrm{E}_{33}} \tag{3.30}$$

$$\mathrm{\varepsilon}_{33} = -\frac{\mathrm{v}_{13}}{\mathrm{E}_{11}}\sigma_{11} - \frac{\mathrm{v}_{23}}{\mathrm{E}_{22}}\sigma_{22} + \frac{1}{\mathrm{E}_{33}}\sigma_{33} \tag{3.31}$$

$$\gamma_{12} = -\frac{1}{\mathrm{G}_{12}}\tau_{12} \tag{3.32}$$

$$\gamma_{23} = -\frac{1}{G_{23}}\tau_{23} \tag{3.33}$$

$$\gamma_{31} = -\frac{1}{G_{31}}\tau_{31} \tag{3.34}$$

where the strain and stress are second-order tensors, thus the remaining terms are symmetric. Thus, the strain can be represented by the equation,

$$\varepsilon = \begin{pmatrix} \varepsilon_{11} & \gamma_{12} & \gamma_{13} \\ \gamma_{21} & \varepsilon_{22} & \gamma_{23} \\ \gamma_{31} & \gamma_{32} & \varepsilon_{33} \end{pmatrix} \rightarrow \left\{ \begin{matrix} \varepsilon_{11} \\ \varepsilon_{22} \\ \varepsilon_{33} \\ \gamma_{12} \\ \gamma_{23} \\ \gamma_{31} \end{matrix} \right\} \tag{3.35}$$

The strain-stress relationship in fourth order tensor can be represented as,

$$\begin{Bmatrix} \varepsilon_{11} \\ \varepsilon_{22} \\ \varepsilon_{33} \\ \gamma_{12} \\ \gamma_{23} \\ \gamma_{31} \end{Bmatrix} = \begin{bmatrix} C_{11} & C_{12} & C_{13} & C_{14} & C_{15} & C_{16} \\ C_{21} & C_{22} & C_{23} & C_{24} & C_{25} & C_{26} \\ C_{31} & C_{32} & C_{33} & C_{34} & C_{35} & C_{36} \\ C_{41} & C_{42} & C_{43} & C_{44} & C_{45} & C_{46} \\ C_{51} & C_{52} & C_{53} & C_{54} & C_{55} & C_{56} \\ C_{61} & C_{62} & C_{63} & C_{64} & C_{65} & C_{66} \end{bmatrix} \begin{Bmatrix} \sigma_{11} \\ \sigma_{22} \\ \sigma_{33} \\ \sigma_{12} \\ \sigma_{23} \\ \sigma_{31} \end{Bmatrix} \tag{3.36}$$

Equation of general anisotropic elasticity

Hooke's constitutive equation states that the stress is linearly proportional to strain. Thus, the equation giving the relation between stress and strain can be given as,

$$\sigma_{ij} = C_{ijkl}\varepsilon_{kl} \tag{3.37}$$

Where, C_{ijkl} denotes the elastic modulus tensor in fourth order which gives the relationship between stress and strain with 6x6 matrix. The components of the C_{ijkl} depend on location within an elastic body as well as time and temperature. In total there are 81 components of C_{ijkl}, however the symmetry of the stress and strain gives only 36 independent components. Furthermore, the resulting symmetry by describing the elastic body with a strain energy function reduces the elastic constants to 21 [60].

$$C_{ijkl} = C_{klij} \tag{3.38}$$

The maximum number of independent elastic constant for any material symmetry is 21. An elastic modulus tensor with 21 constants defines the material property for most type of anisotropy. Orthotropic symmetry relating the stresses and strains of the material can be established, coupled with the invariance of C gives orthotropic stiffness matrix by [60] as,

$$C = \begin{bmatrix} C_{11} & C_{12} & C_{13} & 0 & 0 & 0 \\ C_{12} & C_{22} & C_{23} & 0 & 0 & 0 \\ C_{13} & C_{23} & C_{33} & 0 & 0 & 0 \\ 0 & 0 & 0 & C_{44} & 0 & 0 \\ 0 & 0 & 0 & 0 & C_{55} & 0 \\ 0 & 0 & 0 & 0 & 0 & C_{66} \end{bmatrix} \tag{3.39}$$

With 9 independent elastic constants associated with an orthotropic material and a total of 12 non-zero terms. Compared to an isotropic material which have 2 independent elastic constants associated with an isotropic material. And a total of 12 non-zero terms in the stiffness matrix. Resulting in matrix for an isotropic material as,

$$C = \begin{bmatrix} C_{11} & C_{12} & C_{12} & 0 & 0 & 0 \\ C_{12} & C_{22} & C_{12} & 0 & 0 & 0 \\ C_{12} & C_{12} & C_{33} & 0 & 0 & 0 \\ 0 & 0 & 0 & C_{44} & 0 & 0 \\ 0 & 0 & 0 & 0 & C_{44} & 0 \\ 0 & 0 & 0 & 0 & 0 & C_{44} \end{bmatrix} \tag{3.40}$$

where,

$$C_{44} = \frac{C_{11} - C_{12}}{2} \tag{3.41}$$

3.2.4 Theory of Plasticity

The previous chapter presented some constitutive equations for the linear elasticity problem. Linear elasticity is the most straightforward representation of the behaviour of a solid. The theory of linear elasticity represents the small-strain mechanical behaviour of materials [61]. The deformation under the elastic limit is reversible and independent of time. In addition, a reversible deformation dependent on time is regarded as a viscoelastic material [62]. The process of increasing the stress on the material is known as loading. The deformed material returns to the original configuration when the load is removed from the material. The linear elastic model is used to determine the material properties until their elastic limit. Under linear elasticity, the strains in the material are small, and strains are proportional to the stress. However, the elastic model has a significant limitation since the material obtains permanent strains once the loading exceeds the initial yield value of the material. The development of permanent strains in a material is generally referred to as plastic strains.

The phenomenon of plastic deformation can be easily observed in our day-to-day activities. For example, stretching copper wire beyond the elastic limit gives the wire a permanently elongated wire after the load is removed due to the plastic deformation limit. The experimental stress-strain curve for copper is illustrated in the Figure 3.9. In the figure, the initial yielding occurs at A, which is the material's elastic. The stress at the yield point of the material is referred to as the yield stress, which is denoted by σ_y. The region OA in the Figure 3.9 is the elastic region where Hooke's law is applicable [63]. After the material reaches the initial yielding, it obtains an irreversible strain known as plastic strain. The linear strain and plastic strain can be determined by equation 3.42 for ductile metals where only small deformations are considered.

$$\varepsilon_{ij} = \varepsilon_{ij}^{el} + \varepsilon_{ij}^{pl} \tag{3.42}$$

Where the following equation gives the elastic strain,

$$\varepsilon_{ij}^{el} = \varepsilon_{ij} - \varepsilon_{ij}^{pl} \tag{3.43}$$

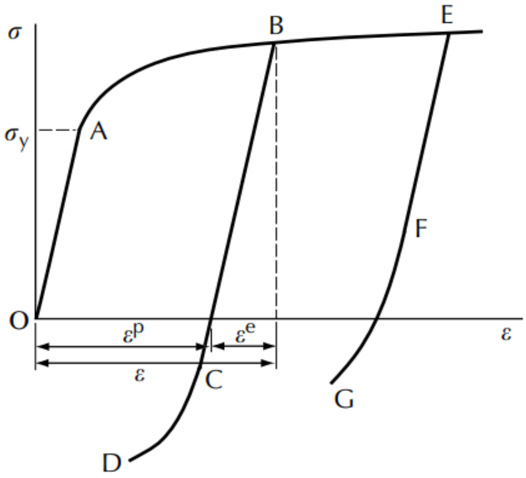

Figure 3.9: The stress–strain curve for metallic materials under monotonic loading [57].

Yield criterion

A yield condition or yield criterion describes a material failure in structural plasticity. It defines the threshold state of material between elastic and plastic or brittle failure deformations [64]. It is essential to adopt a proper yield criterion in designing a structure. The estimated load-bearing capacity of structures may be significantly affected by different yield criteria. Great efforts have been devoted to the formulation of yield criteria. Many other yield criteria have been proposed during the past 100 years. In engineering applications, various yield criteria are available, such as the Tresca, von Mises, Mohr-Coulomb, and Drucker-Prager criteria. The Tresca criterion is also known as the Maximum shear stress theory, and the von Mises yield criterion is known as the distortion energy criterion. The selection of each criterion is primarily determined by the material to be used.

As considered in this work, pressure-insensitive criteria, like von Mises, are used for the material. For materials like soil, rock or concrete, which are compressible, pressure-sensitive criteria are necessary. The Mohr-Coulomb and Drucker-Prager criteria are two examples of this. The von Mises criteria, introduced by Mises in 1913, are the focus of this research. By assuming that the material behavior is isotropic, the yield function can be expressed in terms of the stress tensor invariants, or the principal stresses captured by the von Mises assumption. The yield criteria von mises are detailed in the following section.

Von Mises yield criterion

The von Mises criterion is determined by calculating the distortion energy associated with changes in shape in a given material instead of the energy associated with changes in volume in the same material. This criterion states that a given structural material is safe as long as the maximum value of the distortion energy per unit volume in that material remains less than the distortion energy per unit volume required to cause yield in the same material's specified tensile test.

In material science and engineering, the Von Mises yield criterion can also be expressed in terms of the Von Mises stress or equivalent tensile stress, which is a scalar stress value computed from the stress tensor. When a material's Von Mises stress reaches a critical value known as the yield strength, it is said to begin yielding. Von Mises also discovered that, even if none of the principal stresses exceeds the material yield stress, yielding is still possible due to the combination of the stresses. The Von Mises criteria is a formula for combining the three principal stresses into equivalent stress, which is then compared to the material's yield stress to determine the material's failure conditions. The equivalent stress is often called the Von Mises Stress [65].

Von Mises states that yielding will occur in a body if the components of stress acting on it are more significant than the criterion

$$(\sigma_1 - \sigma_2)^2 + (\sigma_2 - \sigma_3)^2 + (\sigma_3 - \sigma_1)^2 = 2Y^2 = 6k^2 \tag{3.44}$$

For plane strain condition, we have: $\sigma_2 = (\sigma_1 - \sigma_3)/2$

Hence, from distortion energy criterion, we have $\sigma_1 - \sigma_3 = \frac{2}{\sqrt{3}}Y$= Here, $\frac{2}{\sqrt{3}}Y$ is called plane strain strength. Von Mises criterion can also be interpreted as the yield criterion, which states that shear stress reaches a critical value when octahedral. A certain yield criterion has been proposed based on the Von Mises criterion. For instance, the Hill criterion developed by Rodney Hill (1948) is an extension of the Von Mises yield criterion to account for the anisotropic yield of the material. It can be used to model material in which the microstructure influences the macroscopic behaviour of the material, such as composites [66].

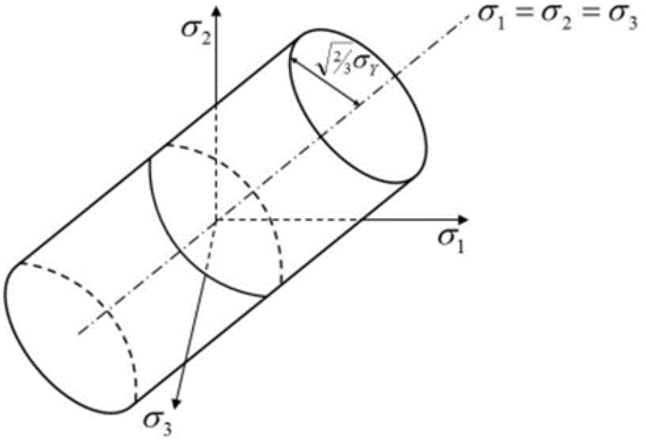

Figure 3.10: Von Mises yield surface in 3-D stress space [67].

Hardening Laws

The hardening rule represents the difference in material strength depicted by material constants in the yield function during plastic yielding. In addition, the difference in material strength can also be represented by a change in the geometry or the location of the yield surface. The hardening law defines how the shape, size, and position of yield surface changess under plastic deformation. In hardening law mathematics, the yielding surface change is considered by additional terms in the yield function [68]. Generally, the hardening of material can be classified into three different types. The hardening material, such as the perfect plasticity, isotropic and kinematic hardening, is represented in the following subsection.

Perfect plasticity

The notion of perfect plasticity is associated with material properties that, while yielding, do not exhibit a further increase in stress and strain. The perfectly plastic materials do not display hardening properties under plastic deformation [68]. Therefore, the yield surface of material regarded as perfectly plastic has a fixed size and shape under plastic defomation. In perfectly plastic material, the yield function f is only a function of the stress state which can be expressed by $f = f(a_{ij}) = 0$ [69]. The Figure 3.11 shows the behaviour of perfectly plastic material. In perfectly plastic material, the yield surface, and the yield stress σ_y remain constant under the plastic deformation process. The concept of perfect plastic is often applied in metal forming technology and stabilization of geotechnical issues [69]. However, materials which exhibit perfectly plastic behaviour are yet to be discovered.

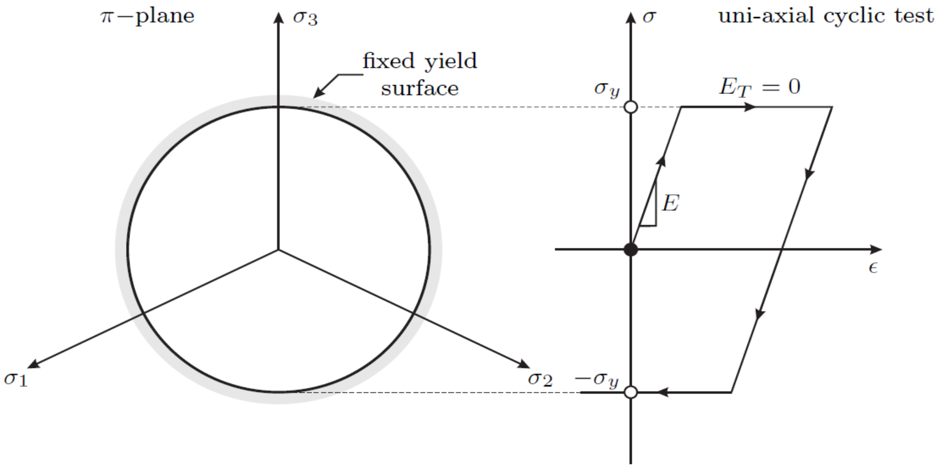

Figure 3.11: The yield surface and stress-strain curve of perfectly plastic material under cyclic loading [68].

Isotropic Hardening

Isotropic hardening is the simplest method available to model strain hardening. The isotropic hardening behaviour describes the plasticity behaviour of material where the yield surface expands in size with an identical shape in the hydrostatic axis. Under isotropic hardening, the yield surface evolves with respect to the initial yield surface and without any translation of the yield surface [68]. The isotropic hardening behaviour is depicted in Figure 3.12, which shows that the change in the yield surface's size increases with an increase in stress. The figure also shows that the yield surface expands uniformly in all directions with the plastic flow. However, the Bauschinger effect, where the yield strength of the material in compression compared to the prior tension deformation, is not considered in the isotropic hardening [70]. The value of isotropic hardening is directly related to the amount of strain.

The yield function in isotropic hardening can be represented with the following equation,

$$f(a_{ij},K_i) = f_0(a_{ij}) - K = 0 \tag{3.45}$$

Where the initial yield function specifies the shape. And the size of the yield function changes with the hardening parameter K. For example, considering the yield surface based on Von Mises accumulated plastic strain. The material behaviour at initial yield can be determined with by equation,

$$f_0(a_{ij}) = \frac{1}{\sqrt{2}}\sqrt{(\sigma_1-\sigma_2)^2+(\sigma_2-\sigma_3)^2+(\sigma_3-\sigma_1)^2} - Y = \sqrt{\frac{3}{2}s_{ij}s_{ij}} - Y \tag{3.46}$$

Where Y denotes the yield stress in uniaxial tension. The isotropic hardening with Von Mises function provided in the equation 3.46 gives,

$$f\left(a_{ij},K_i\right) = \sqrt{3J_2} - Y - K = 0 \tag{3.47}$$

The solution shows that the radius of the initial yield surface increases from $\sqrt{\frac{2}{3}}Y$ in equation 3.47 to a radius of $\sqrt{\frac{2}{3}}(Y+K)$ in equation 3.47. It indicates how the hardening parameter K changes under plastic deformation with the Von Mises criterion. Another criterion such as the Drucker-Pager criterion provides a different solution for the isotropic hardening.

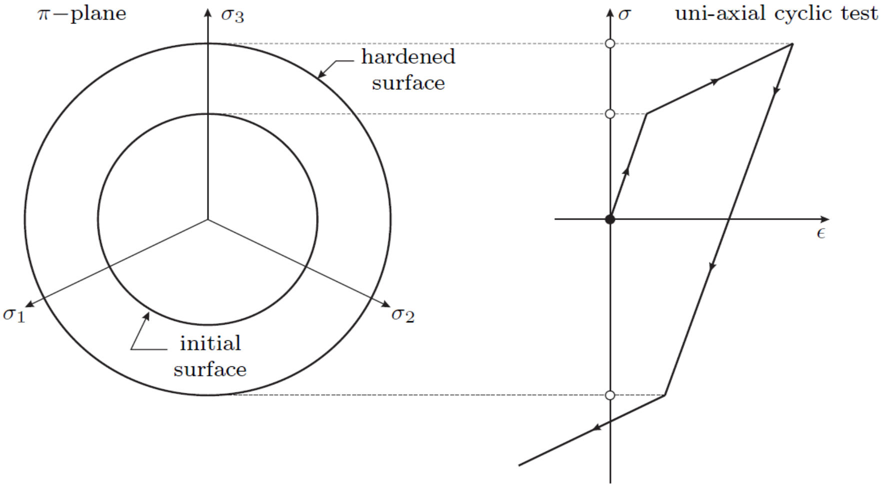

Figure 3.12: The uniform expansion of yield surface in every principle direction and stress-strain curve of isotropic hardening under cyclic test [68].

Kinematic hardening

In the isotropic hardening model, the yield strength in tension and compression are initially equal. It implies that the yield surface is symmetric along the stress axes, and the yield surface remains constant as the plastic strain develops. The application of the isotropic hardening model for many metallic materials provides an inaccurate stress-strain response under cyclic loading [71]. Therefore, the theory of plasticity provides a hardening model based on the motion of the yield surface in the stress space, known as kinematic hardening. During the kinematic hardening, the shape and size of the yield surface remain constant, but the centre of the yield surface translates along the hydrostatic axes. Figure 3.13 illustrates the translation of yield surface in kinematic hardening is shown in the Figure 3.13. In addition, the translation of the yield surface leads to a reduction of yield stress in the opposite direction of the loading direction, denoted as the Bauschinger effect [68]. The kinematic hardening model takes the Bauschinger effect into account, where a hardening in tension leads to a softening in a subsequent compression. The yield function according to the kinematic hardening is represented by,

$$f(a_{ij},K_i) = f_0(a_{ij} - \alpha_{ij}) = 0 \tag{3.48}$$

The hardening parameter is the s, representing α_{ij} which means the total translation of the centre of the initial yield surface. The kinematic hardening with the Von Mises criterion can be written as,

$$f(a_{ij,}\, K_i) = \sqrt{\frac{3}{2}(s_{ij} - \alpha_{ij}^d)(s_{ij} - \alpha_{ij}^d)} - Y = 0 \tag{3.49}$$

Here, α_{ij}^d denotes the deviatoric part of α_{ij}. The translation of yield surface is defined by α_{ij} and the expansion by a change in the value of K.

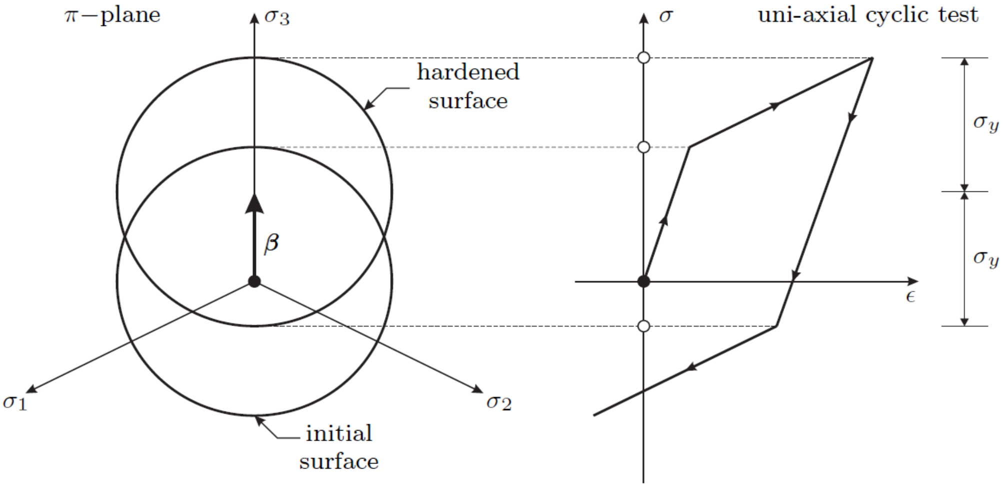

Figure 3.13: The translation of yield surface according to the stress and stress-strain curve of kinematic hardening with uniaxial cyclic test [68].

3.2.5 Fracture mechanics

Materials such as glass and rock fail in a brittle manner. However, failure in ductile material such as structural steel can also occur in a brittle manner when it contains a crack in a region of tensile stress. Generally, the crack initiates at a stress raiser and increases gradually from cyclic loading or corrosion under steady loading [59]. The crack in ductile material crack reaches a “critical length” then the brittle crack is propagated as a brittle fracture and the material part or structure breaks further. The separation of material is mitigated by the propagation of crack into a “crack arrester”. The formation of crack arresters can arise from an existing hole or deformation that stops the propagation of crack [59]. The field of studying the propagation of cracks in materials is known as fracture mechanics. Fracture mechanics employ analytical solid mechanics methods to calculate the driving force on a crack and experimental solid mechanics methods to characterise the material's resistance to fracture.

In modern materials science, fracture mechanics is an important tool for improving the mechanical performance of mechanical parts. It applies the physics of stress and strain, particularly the theories of elasticity and plasticity, to the microscopic crystallographic defects found in real materials to predict the macroscopic mechanical failure of bodies. There are several methods of applying a force to enable a crack to propagate: mode I fracture, mode II fracture, and mode III fracture. Mode I fracture – refers to tensile stress normal to the plane of the crack) while Mode II fracture refers to shear stress acting parallel to the plane of the crack and perpendicular to the crack front). And Mode III refers to shear stress acting parallel to the plane of the crack and parallel to the crack front [67]. The illustration of these three different crack modes is presented in the Figure 3.14.

Most engineering materials show some nonlinear elastic and inelastic behaviour under operating conditions that involve large loads. In such materials, the assumptions of linear elastic fracture mechanics may not hold. Therefore, more general crack growth is needed for elastic-plastic materials that can account for the local conditions for initial crack growth and a global energy balance criterion for further crack growth and unstable fracture [67]. Related to Fracture Mechanics, there are different options available in ABAQUS that can be used user to study the initiation and propagation of cracks along surfaces. ABAQUS software allows for five types of fracture criteria: critical stress at a certain distance ahead of the crack tip, critical crack opening displacement, crack length versus time, and VCCT (the Virtual Crack Closure Technique) and the low-cycle fatigue criterion based on the Paris law etc.

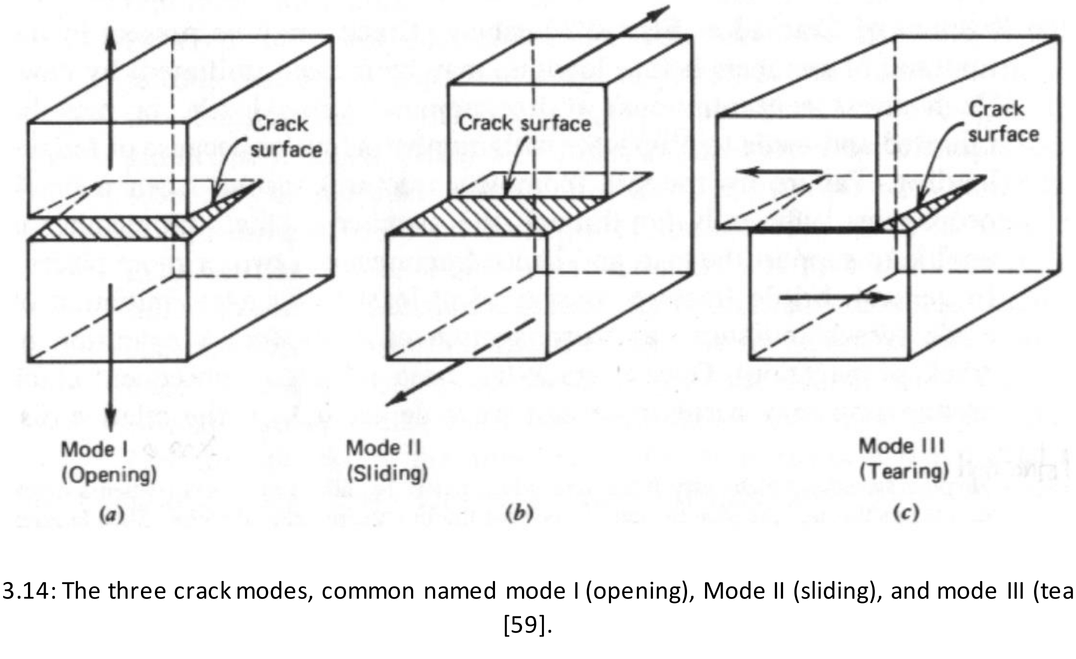

Figure 3.14: The three crack modes, common named mode I (opening), Mode II (sliding), and mode III (tearing) [59].

Fracture in composite material

In this study, the behaviour of composite material is studied. Therefore, it is vital to explain the relationship between fracture mechanics and composite materials. The cracks in fibre reinforced composite material appears to be a substantial amount of slow crack growth prior to unstable fracture under increasing load or displacement conditions. The crack in the composite material can be classified into three phases, crack initiation, crack propagation and complete failure. Crack initiation is distinguished by the balance of energy dW with the energy dQ which is essential for crack tip propagation [72]. It can be expressed as,

$$dW \geq dQ = Rdc \tag{3.50}$$

The corresponding expression for the effective fracture toughness K_c can be expressed in terms of the single values K_{ic}. The term K_{ic} for the different phases (i) and their volume fractions, v_i of multiphase material can be derived as equation 3.51 for composite material [72]. The equation of effective fracture toughness for the special case of two different constituents can be expressed as,

$$K_c = (K_{1c} - K_{2c})\,(1 - v_1)^{1/2} + K_{2c} \tag{3.51}$$

However, the equation for effective fracture toughness is derived considering the principle of superposition of stresses. Therefore, the equation is only valid in linear elastic theory where the total force in a cross section is equal to the sum of its parts. In addition, an approach for fracture mechanics is developed by considering structural aspects known as a laminate analogy. The approach is based on the combination of micro and micromechanical consideration of composite material. The structural parameter such as fibre orientation can distinguish the composite material into different layers with distinct elastic constants for each layer [72]. The fracture toughness, K_c of composites can be evaluated by the following bimodal equation:

$$K_c = \frac{2S}{B}\,K_{c,skin} + \frac{C_0}{B}\,K_{c,core} \tag{3.52}$$

Where $K_{c,skin}$ is the fracture toughness of the skin layers while $K_{c,core}$ denotes the fracture toughness of the core layer.

The fracture behaviour in composite materials is related to the interplay of crack growth in the matrix material and the reinforcements and the delamination of interfaces between the constituents. The spatial distribution and orientations of the reinforcements, in general, induce anisotropic elastic and fracture mechanical properties in composites, as stated previously. Since the elastic properties of composites are anisotropic, thus, their elastic behaviour depends on the loading direction concerning the material orientation. The fracture behaviour of composite materials is related to the effects of fibre, local delamination at the interfaces between matrix and fibre and growing cracks in the matrix material. Therefore, a complex system of interacting damage and energy-consuming processes must be considered for an appropriate description of the fracture process [73]. Various criteria have been proposed to predict the fracture behaviour of composite materials. Most of these criteria which predict mode I, Mode II and Mode III are stress-based and are experimental curve fitting. Therefore, they are only applicable to certain composite materials with specific constituent ratios [74].

3.3 Micromechanical material models for polymer composites

The material properties of inhomogeneous material are measured according to Young’s modulus and Poisson’s ratio. The linear elastic parameter of inhomogeneous material is obtained from simple tensile and compression load tests. Obtained stress and strain from the test are the averages for the specimen and the results are the effective properties of the material. The material is considered homogenous, while there is no such material that is homogeneous. Homogenisation of material is considered always for obtaining material properties whether it is from empirical, analytical, semi-analytical or numerical FEM-based methods [75]. The study of deformation and motions of material under the applied external forces comes under the branch of physics known as continuum mechanics.

The material area and surrounding area considered uniform in classical continuum mechanics. Theories of polymer mechanics are formulated on basis of continuum mechanics. The foundation of classical continuum mechanics was laid around two centuries ago by Augustin Cauchy. It is based on Cauchy’s oral presentation at Académie des Sciences in 1822 [76]. Continuum mechanics unifies the discrete theories of solid mechanics, fluid mechanics, thermodynamics, and heat transfer which are fundamental subjects for the field of engineering [55]. A general notion of continuum mechanics is that the mass, stress and strain are considered as essentially uniform within an infinitesimal surface area and its surrounding area. Since continuum mechanics is well researched and applied field of physics, it is beneficial to apply concepts of continuum mechanics to study non-homogeneous material [77]. Several researchers have taken the approach to estimate the elastic properties of inhomogeneous material such as discontinuous short fibre polymer. Here in this chapter, we have provided some of the methods which have been used extensively to calculate the elastic properties of inhomogeneous material.

Estimating elastic moduli of composite material is essential in the early design stages. The theoretical model for determining the modulus of elasticity of a short fibre composite may deviate from the actual properties due to the simplification of the assumptions. However, the model chosen should incorporate the main parameters influencing the elastic moduli of short fibre composites, such as the volume fraction of fibres, fibre aspect ratio, fibre orientation distribution, matrix properties, etc. This study explores the applicability of these models to fibre-reinforced composites through a literature review. The main objective of the conducted literature review is to find an appropriate theoretical model for fibre composites produced using a high production rate injection moulding process. The literature review briefly introduces the theoretical models to determine elastic moduli of short fibre composites. Various theoretical models like the Halpin-Tsai model, Mori-Tanaka model, rule-of-mixtures, and Nielsen Elastic Model, along with the Eshelby method, are presented that can be employed to obtain elastic properties of composites as shown in Table 3.1. Additionally, from the mentioned theoretical models, the Halpin-Tsai model and Mori-Tanaka model are employed in this study to predict the elastic moduli by using FEM software.

Table 3.1: Summary of theoretical models used for homogenisation of fibres and matrix to determine the elastic moduli for short fibre composites.

Micromechanical material models	**Equations**
Rule of mixture	$E_C = E_f V_f + E_m(1 - V_f)$
	$\frac{1}{E_C} = \frac{V_f}{E_f} + \frac{V_m}{E_m}$
Halpin- Tsai	$E_L = E_m \frac{1 + 2(\frac{l_f}{d_f})\eta_L V_f}{1 - \eta_L V_f}$
	$E_T = E_m \frac{1 + 2\eta_T V_f}{1 - \eta_T V_f}$
Nielsen Elastic Model	$\frac{P}{P_m} = \frac{1 + \zeta\eta V_f}{1 - \eta\Psi V_f}$
Mori-Tanaka model	$C = \left(f_0 C_0 + \sum_{r=1}^{N-1} f_r\{C_r A_r^{dil}\}\right)\left(f_0 I + \sum_{r=1}^{N-1} f_r\{A_r^{dil}\}\right)^{-1}$

3.3.1 Rule of mixture

The mechanical characterization of a short fibre composite was first approached analytically by the implementation of micromechanical models. An innovative work was released in 1889 by Voigt and in 1929 by Reuss. Both Voigt and Reuss models were reference models, since the earlier developed models were mainly based on the Voigt model, known later as the Rule of Mixtures. Rule of Mixture is one of the methods to find the stiffness of the composite material and its constituents. It is the weighted mean method to evaluate the various properties of composite materials. Currently, the Rule of mixtures is the simplest available micromechanical analysis model that can be used to predict the elastic properties of a composite material. The parameters that matter in the prediction of properties using Rule of Mixture is the volume fraction and Young's modulus of the constituents in the composite material. Composites consist of generally two phases, where the continuous phase is called matrix and the discontinuous phase is termed as reinforcements. Therefore, the formulae generated for Rule of Mixture is generally made for two phases which are fibre and matrix. The rule of mixtures predicts longitudinal modulus, transverse modulus, and Poisson's ratio assuming unidirectional fibres and predicts young's modulus in fibre direction.

Additionally, the rule of mixtures describes the macro-mechanical properties of short-fibre composites based on the assumption that the fibres are randomly oriented. The overall material properties can be expressed by some weighted sum of the material properties of the constituents of the composite material which are the fibres and the matrix. As an application of the rule of mixtures approach, Equation 3.55 and 3.56 show how to estimate the modulus of elasticity E_{11} and E_{22} of the composite, as a function of the properties of the fibres and matrix materials and volume fractions, considering the direction of fibre alignment.

where, E_m, E_f, Vm, and V_f represents the moduli and volume fractions of the matrix and fibre respectively and E_c represents the modulus of the composite. Fibre and matrix volume fractions of the material, Vf and Vm are known from the manufacture of fibre-reinforced composite materials. The equation 3.57 requires the assumption that strains in the fibre are equal to those in the matrix [78].

The equation for two phases of the composite for longitudinal direction can be written as:

E_{11} = Longitudinal Stiffness

$$E_C = E_f V_f + E_m \left(1 - V_f\right) \tag{3.53}$$

The equation for two phases of the composite for transverse direction can be written as:

E_{22}= Transverse Stiffness

$$\frac{1}{E_C} = \frac{V_f}{E_f} + \frac{V_m}{E_m} \tag{3.54}$$

V_{12}= Poisson's ratio

The equation for two phases of the composite for Poisson's ratio can be written as:

$$V_{12} = v_f V_f + v_m(1 - V_f) \tag{3.55}$$

The equation for two phases of the composite for in-plane shear modulus can be written as:

G_{12}= In-plane shear modulus

$$\frac{1}{G_{12}} = \frac{V_f}{G_f} + \frac{(1 - V_f)}{G_m} \tag{3.56}$$

$$\frac{1}{G_{12}} = \frac{V_f}{G_f} + \frac{(1 - V_f)}{G_m} \tag{3.57}$$

Based on the presented equations of the Rule of Mixtures for the volume fraction and Young's modulus of the constituents, the prediction of composite material properties can be provided. The rule of mixture assumes a perfect bonded interface between matrix and reinforcement. This assumption may be unrealistic for the majority of real manufactured composites, and therefore it is useful to adopt semi-empirical models like the Halpin-Tsai one, which compensates for non-perfect interface conditions [79].

3.3.2 Halpin–Tsai

The short natural fibre-reinforced polymer matrix composite is a cost-effective option in various structural applications. Therefore, estimating accurate elastic moduli of such composites is vital during the initial design phase. Halpin and Tsai developed the equations for aligned fibre-reinforced composite materials and predicted the elastic modulus based on Herman's and Hill's equations. The model is one of the most popular homogenization theories developed by Halpin and Tsai, using generalised and straightforward equations to approximate the results of more precise micromechanical techniques to describe the composite material easily.

Similar to the other micromechanical models, the Halpin-Tsai model attempts to estimate the composite modulus based on the moduli of the reinforcement, matrix materials, and the shape and volume fraction of the aligned inclusion phase. Assuming a completely aligned distribution of fibres, longitudinal and transverse elastic moduli can be estimated, where E_L and E_T are the longitudinal and transverse modulus of an aligned short-fibre composite [80].

The moduli can be expressed mathematically as:

$$E_L = E_m \frac{1 + 2(\frac{l_f}{d_f})\eta_L V_f}{1 - \eta_L V_f} \tag{3.58}$$

$$E_T = E_m \frac{1 + 2\eta_T V_f}{1 - \eta_T V_f} \tag{3.59}$$

For composites with aligned short fibres, the Halpin–Tsai model describes the modulus of elasticity as shown in equations 3.62 and 3.63. In the above expressions, V_f is the fibre volume fraction, E_f is the elastic modulus of the fibres, E_m is the elastic modulus of the matrix, l is the fibre length, and d is the fibre diameter. The aspect ratio is defined as the fibre length divided by the fibre diameter (l/d). For the randomly oriented short-fibre composite under consideration, the fibre aspect ratio and fibre volume fraction is the same as in the corresponding aligned short-fibre composite [81].

The Halpin–Tsai equation for the in-plane shear modulus of a unidirectional is similar to that for the transverse modulus and it is given by

$$G_{LT} = G_m \frac{1 + 2\eta_G V_f}{1 - \eta_G V_f} \tag{3.60}$$

Furthermore, from assuming an isotropic, linear elastic material, the Poisson ratio is given in ().

$$V_{LT} = V_f V_f + V_m V_m \tag{3.61}$$

Where η_L, η_T, and η_G are given by following,

$$\eta_L = \frac{\frac{E_f}{E_m} - 1}{\frac{E_f}{E_m} + 2(\frac{lf}{df})} \qquad \eta_T = \frac{\frac{E_f}{E_m} - 1}{\frac{E_f}{E_m} + 2} \qquad \eta_G = \frac{\frac{G_f}{G_m} - 1}{\frac{G_f}{G_m} + 2} \tag{3.62}$$

The term ξ is called the reinforcing factor and it depends on the fibre geometry, packing geometry, and loading conditions. Halpin–Tsai equations are very simple to apply; however, their accuracy depends on the choice of the parameter ξ. It is determined by a procedure of curve fitting and comparing equations and with elasticity solutions or reliable experimental data. The only difficulty of using the Halpin Tsai equations would thus appear to be in the determination of a suitable value for ξ. Halpin and Tsai developed empirical generalized equations that readily give quite satisfactory approximation of more complicated micromechanics results. These equations are quite accurate at low fibre volume fraction. They are also useful in determining the properties of composites that contain discontinuous fibres oriented in the loading direction [82].

The reinforcing factor ξ is given by s

$$\zeta = 2\left(\frac{L}{D}\right) for\ E_1 \tag{3.63}$$

$$\zeta = 2\ \ for\ E_2 \tag{3.64}$$

$$\zeta = 1\, for\ G_{12} \tag{3.65}$$

$$\zeta = 2\left(\frac{1}{4-3v_m}\right) for\ G_{23} \tag{3.66}$$

3.3.2.1 Nielsen Elastic Model

Nielsen elastic model is another method to find the stiffness of the composite material and its constituents. Nilsen modified the Halpin-Tsai model further by Nielsen taking into consideration a factor to account fibre arrangement as well as fibre content, ψ to enable a better prediction [83].

The equation can be written as:

$$\frac{P}{P_m} = \frac{1+\zeta\eta V_f}{1-\eta\Psi V_f} \tag{3.67}$$

$$\eta = \frac{\frac{P_f}{P_m}-1}{\frac{P_f}{P_m}+\zeta} \tag{3.68}$$

in which,

P = Composite material modulus E_2, G_{12}

P_f = Composite fibre material modulus E_f, G_f and v_f

P_m = Composite matrix material modulus E_m, G_m and v_m

ζ is an empirical factor as stated earlir the this parameter measures fibre reinforcement of the composite material that depends on the loading and boundary condition of the fibre geometry.

And

$$\Psi = 1 + \frac{(1 + \Phi_{max})}{\Phi_{max}^2} V_f \tag{3.69}$$

The Nielsen elastic model modified based on Halpin-Tsai equation also includes a maximum packing fraction ϕmax for the relevant fibre arrangement which depends on geometry of the model.

For a square array of fibres, ϕmax = 0.785

For a hexagonal arrangement of fibres, ϕmax = 0.907

For value in between above two extremes and near the random packing, ϕmax = 0.82.

3.3.3 The Eshelby method

When it comes to the micromechanical model for heterogeneous materials such as composite material homogenization is a vital concept. Theories are typically based on classical solutions for a single solid material in an infinite medium with different assumptions. The deformation of an isotropic elastic solid material undertakes a spontaneous change of form. When the surrounding material is absent then the material undergoes a homogenous deformation. Due to the existence of material around the solid, stresses obtained in the material will be distributed between the inside and outside regions. The consistency of the material is disturbed by the solids within the material medium. The problem with inhomogeneity can be solved for a region of the random shape while some solution requires some form of ellipsoidal shape. In 1957 at the University of Birmingham John Douglas Eshelby published a solution to incorporate the uniformity due to different materials [84].

The solution presented by [84] found the elastic field of the inhomogeneous material based on a simple procedure with an imaginary cutting, straining and welding. To explain the procedure Eshelby conducted a virtual experiment where a region (the inclusion) was embedded in an infinite homogeneous isotropic linear elastic medium. An illustration of the elastic body with the inclusion is shown in the Figure 3.15. The volume of homogenous material is V and the surface area S, which has an elastic constant of C_{ijkl}. And the inclusion of the volume is V_0, whereas the material surrounding the inclusion is referred to as a matrix. According to [84] the virtual experiment followed the 4 steps to derive the solution,

I. Removed the inclusion region (V_0) from the matrix. This allows unrestricted transformation since force is neither applied to inclusion nor the matrix.

$$p_{ij}^T = \lambda e^T \delta_{ij} + 2\mu e_{ij}^T \tag{3.70}$$

The stress-free strain (e_{ij}^T) is derived by Hooke's law.

II. Apply the surface tractions ($T = -p_{ij}^T n_j$) to surface S_0, which restores the shape of the inclusion to the original shape. Therefore, the sum of the elastic strain and eigenstrain of the inclusion is zero, i.e., $e_{ij}^{el} = -e_{ij}^*$.

III. Insert the inclusion back to the matrix. As the traction force (T) is applied to the internal surface, there is no deformation either in the inclusion or the matrix.

IV. Remove the traction force in the inclusion by applying an equal and opposite body force ($F = -T$. Due to the force (F) at the internal surface (S_0) of the body the inclusion will return to the original shape.

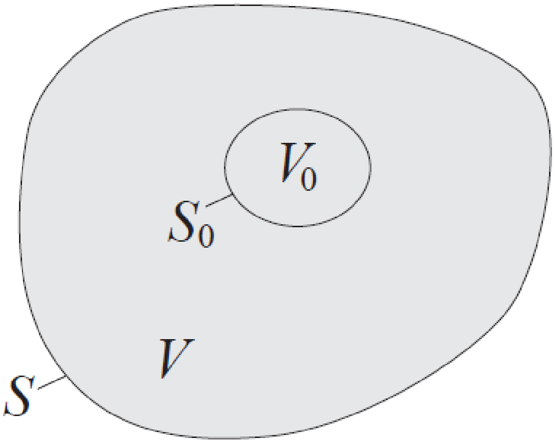

Figure 3.15: A homogenous linear elastic solid (matrix) with volume V and surface S. and inclusion with a sub-volume V0 with surface S0 depicted by Eshelby for his virtual experiment [85].

3.3.3.1 The ellipsoidal inclusion

Considering the displacement field $u_i^c(x)$ in reaction to the body force F_j on the inclusion surface S_0. Where the displacement field is also referred as constrained displacement field. The elastic field for the constrained displacement field is derived according to Green's function of the elastic body by [85].

$$u_i^c(x) = \int F_j\,(x')G_{ij}(x,x')dS(x') = \int \sigma_{lk}^*\,n_k(x')G_{ij}(x,x')dS(x') \tag{3.71}$$

Where the displacement gradient, strain and stress of the constrained field is given as,

$$u_i^c(x) = \int \sigma_{lk}^* n_k(x')G_{ij}(x,x')dS(x') \tag{3.72}$$

$$e_{ij}^c(x) = \frac{1}{2}(u_{i,j}^c + u_{i,j}^c) = \frac{1}{2}\int \sigma_{lk}^* n_k(x')(G_{il,j}(x,x') + G_{il,j}(x,x'))dS(x') \tag{3.73}$$

$$\sigma_{ij}^c(x) = C_{ijkl}e_{kl}^c(x) \tag{3.74}$$

The expression for stress and stains at any location of the material is obtained by determining the constrained field. Both the inside and outside of the inclusion is considered as constrained. Thus, a fourth order tensor S_{ijkl} is defined. This tensor gives the relationship between the constrained strain inside the inclusion and the stress-free strain (eigenstrain). [85] expressed the relationship as,

$$e_{ij}^c = S_{ijkl}\, e_{kl}^* \tag{3.75}$$

where the S_{ijkl} is known as Eshelby's tensor. This satisfies minor symmetry condition since the fourth order tensor S_{ijkl} relates two symmetric strain tensors. Thus, $S_{ijkl} = S_{jikl} = S_{ijlk}$, but in general does not satisfies the major symmetry. Where S_{ijkl} is not equal to S_{klij}. The Eshelby's tensor differs according to the shape of the inclusion. According to the [86] the spheroidal inclusions where the volume V_0 occupies the inclusion is expressed as,

$$\gamma_{xy} = \gamma_{xy} = \frac{\partial u_x}{\partial x} + \frac{\partial u_y}{\partial x} \tag{3.76}$$

$$\left(\frac{x'}{a}\right)^2 + \left(\frac{y'}{b}\right)^2 + \left(\frac{z'}{x}\right)^2 \leq 1 \tag{3.77}$$

Here a, b and c are coordinates to specify the geometric configuration of the spheroid in a spatial coordinate system x', y' and z' respectively. The expressions of the Eshelby tensor differs on the size of the inclusion. Eshelby tensor for shapes such as elliptic cylinder, flat ellipsoid, and penny shaped inclusion is presented by [85]. For spherical inclusion where semi-axes ($a = b = c$), the Eshelby tensor can be expressed as elliptic integrals,

$$S_{ijkl} = \frac{5v_0 - 1}{15(1 - v_0)}\delta_{ij}\delta_{kl} + \frac{4 - 5v_0}{15(1 - v_0)}(\delta_{ik}\delta_{jl} + \delta_{il}\delta_{jk}) \tag{3.78}$$

Where δ_{jl} denotes the Kronecker delta, and v_0 is the Poisson's ratio of the elastic continuous matrix. [87] has derived the out for the (non-zero) coefficients as,

$$S_{1111} = S_{2222} = S_{3333} = \frac{7 - 5v_0}{15(1 - v_0)} \tag{3.79}$$

$$S_{1122} = S_{1133} = S_{2211} = S_{2233} = S_{3311} = S_{3322} = \frac{5v_0 - 1}{15(1 - v_0)} \tag{3.80}$$

$$S_{1212} = S_{2323} = S_{3131} = \frac{4 - 5v_0}{15(1 - v_0)} \tag{3.81}$$

For fibre-like spheroidal inclusions, [87] derived the Eshelby tensor as following,

$$S_{1111} = \frac{1}{2(1 - v_0)}\left\{1 - 2v_0 + \frac{3\alpha^2 - 1}{\alpha^2 - 1} - \left[1 - 2v_0 + \frac{3\alpha^2}{\alpha^2 - 1}\right] g\right\} \tag{3.82}$$

$$S_{2222} = S_{3333} = \frac{3}{8(1 - v_0)}\frac{3\alpha^2}{\alpha^2 - 1} + \frac{1}{4(1 - v_0)}\left[1 - 2v_0 + \frac{9}{4(\alpha^2 - 1)}\right] g \tag{3.83}$$

$$S_{2233} = S_{3322} = \frac{1}{4(1 - v_0)}\left\{\frac{\alpha^2}{2(\alpha^2 - 1)} - \left[1 - 2v_0 + \frac{9}{4(\alpha^2 - 1)}\right] g\right\} \tag{3.84}$$

$$S_{1122} = S_{1133} = \frac{1}{2(1 - v_0)}\left[1 - 2v_0 + \frac{1}{\alpha^2 - 1}\right] + \frac{1}{2(1 - v_0)}\left[1 - 2v_0 + \frac{3}{2(\alpha^2 - 1)}\right] g \tag{3.85}$$

$$S_{2323} = S_{3232} = \frac{1}{4(1 - v_0)}\left\{\frac{\alpha^2}{2(\alpha^2 - 1)} + \left[1 - 2v_0 - \frac{3}{4(\alpha^2 - 1)}\right] g\right\} \tag{3.86}$$

$$S_{1212} = S_{1313} = \frac{1}{4(1 - v_0)}\left\{1 - 2v_0 - \frac{\alpha^2 + 1}{\alpha^2 - 1} - \frac{1}{2}\left[1 - 2v_0 + \frac{3(\alpha^2 - 1)}{\alpha^2 - 1}\right] g\right\} \tag{3.87}$$

where g is given by the following equation,

$$g = \frac{\alpha}{(\alpha^2 - 1)^{\frac{3}{2}}}\left\{\alpha(\alpha^2 - 1)^{\frac{1}{2}} - \cosh^{-1}\alpha\right\} \tag{3.88}$$

where, α is the aspect ratio of the inclusion (fibres). Aspect ratio is ratio of the length l of the fibres with the diameter of the fibre d. Thus, the aspect ratio which indicates the size of fibres is given as $\alpha = \frac{l}{d}$.

3.3.4 Mori-Tanaka model

During the modelling composite the inclusions are assumed to be either aligned or randomly distributed in the matrix. But the fibres are neither aligned nor dispersed at random directions. During manufacturing of short fibre composite with injection moulding the fibres are governed by the nature of the complicated fluid flow field of matrix. The elastic property of the composite material is highly dependent on the fibre orientation. The method proposed by Mori& Tanaka, (1973) is based on considering the average internal stress in matrix [88]. Where the elastic constant C_{ijkl} are uniform throughout a volume of the elastic homogenous material V_0 is considered. The material obtains total strain ε_{ij}^{*} when an inclusion acquires uniform transformation strain ε_{ij}^{T}. Mori& Tanaka, (1973) distinguished the total strain into constrained strain $\varepsilon_{ij}^{\infty}$ and image strain ε_{ij}^{im}. The image strain in the elastic body is introduced due to the presence of the free boundary. The constrained strain $\varepsilon_{ij}^{\infty}$ of the material is given by,

$$\varepsilon_{ij}^{\infty} = \varepsilon_{mn}^{T} \int_{V}^{\cdot} \left\{ -\frac{C_{mnkl}\left[G_{ki,lj}(x,x') + G_{kj,li}(x,x')\right]}{2} \right\} dD(x') \tag{3.89}$$

where the green's function is applied to an infinite homogenous material. When the inclusion acquires transformation strain ε_{ij}^{T} the elastic homogenous material undergoes shape change. The average strain that illustrates the shape change is given by the following equation,

$$(\varepsilon_{ij}^{F})_{V_0} = f\varepsilon_{ij}^{T} \tag{3.90}$$

The equation 3.92 shows that the average stain $(\varepsilon_{ij}^{F})_{V_0}$ is directly proportional to the volume fraction of the inclusion f and the transformation strain ε_{ij}^{T}. Solution proposed by Mori & Tanaka, (1973) is based on the assumption where the average total strains in an representative volume V_R of the homogenous material is equal to $f\varepsilon_{ij}^{T}$ [88]. In addition, considering the identical shape of the inclusion in the representative volume. The average elastic strain which is independent of size of representative volume and size is derived as,

$$(\varepsilon_{ij}^{\cdot})_{V_R} = -f(S_{ijmn}{e_{mn}}^{T} - {e_{ij}}^{T}) \tag{3.91}$$

where S_{ijmn} denotes the Eshelby's tensor. The average internal stress $({\sigma_{ij}}^{0})_{V_R}$ is the average in representative volume of the sum of the image stresses. Since the inclusion is in the infinite volume the sum includes the stresses of all the inclusions inside and outside of the representative volume. It is given by the following equation,

$$({\sigma_{ij}}^{0})_{V_R} = C_{ijkl}(\varepsilon_{kl}^{\cdot})_{V_R} \tag{3.92}$$

The average internal stress of the material is also independent of the position and the size of the representative volume. The method based on Mori & Tanaka, (1973), is presented as below by [89]. In the derivation by Fisher and Brinson the main concept is the tensor based on the dilute strain concentration A_r^{dil}. The dilute strain concentration is related to average strain in the inclusion $\bar{\varepsilon_r}$ with the field strain $\bar{\varepsilon}$. Thus, the dilute strain concentration tensor,

$$\bar{\varepsilon_r} = A_r^{dil}\,\bar{\varepsilon} \tag{3.93}$$

$$A_r^{dil} = \left[I + S_{ijkl}(C_0^m)^{-1}(C_r^f - C_0^m)\right]^{-1} \tag{3.94}$$

Where, A_r^{dil} is the quantity of inclusion according to the Eshelby tensor, which depends on shape of the inclusion [86]. C_r^f and C_0^m are the stiffness tensor of the inclusion and matrix material respectively, and I is the fourth order identity tensor. The approach presented above is for the “dilute” case which considers small enough volume fraction of the inclusion to neglect the interaction between inclusions. The elastic modulus for the dilute case is given by Fisher & Brinson, (2006) [89] as,

$$C = C_0^m + f_r(C_r^f - C_0^m)A_r^{dil} \tag{3.95}$$

where f_r represents the volume fraction of the inclusion. But for the non-dilute concentrations approach the method presented by Fisher & Brinson, (2006) takes the interaction of the inclusion into account [89]. The non-dilute concentration requires the volume-weighted average phase strain and the far-field applied strain to be in equilibrium. Considering the equilibrium condition, [86] the strain-concentration factor for non-dilute concentration is derived as,

$$\bar{\varepsilon_0} = \left(f_0 I + \sum_{r=1}^{N-1} f_r\,A_r^{dil}\right)^{-1} \tag{3.96}$$

$$\bar{\varepsilon_r} = A_r^{dil}\,\bar{\varepsilon_0} \tag{3.97}$$

The approach based on Mori-Tanaka considers the average matrix strain $\bar{\varepsilon_0}$ contrary to the far field applied strain. Thus, the elastic modulus for unidirectionally aligned inclusion is derived by, the following equation,

$$C = \left(f_0 C_0 + \sum_{r=1}^{N-1} f_r C_r A_r^{dil}\right)\left(f_0 I + \sum_{r=1}^{N-1} f_r\,A_r^{dil}\right)^{-1} \tag{3.98}$$

where N represents the different types of inclusion within the volume fraction f_r and distinct moduli C_r. The derivation of the approach based on Mori-Tanaka is presented by Fisher & Brinson, (2006) [89]. To employ the equation for random orientation of the inclusion, the equation above needs to include other orientation distributions by averaging the inclusion orientation. The equation for random orientation of inclusion is obtained by,

$$C = \left(f_0 C_0 + \sum_{r=1}^{N-1} f_r \{ C_r \, A_r^{dil} \} \right) \left(f_0 I + \sum_{r=1}^{N-1} f_r \{ \, A_r^{dil} \} \right)^{-1} \tag{3.99}$$

where $\{C_r \, A_r^{dil}\}$ and $\{A_r^{dil}\}$ represents the average of inclusion in homogenous material over all potential orientation. When it comes to estimating mechanical properties of the short fibre composite, the method based on the work of Mori & Tanaka, (1973) is widely applied. Throughout the years the model has demonstrated high reliability to predict the effective properties of different material with either random orientation or total alignment of the reinforcing phases. But for composite material comprising of different shapes of inclusions or orientation, the model might violate the symmetry requirement of $C_{ijkl} = C_{klij}$ [77].

3.4 Fibre alignment and theoretical model

The theories regarding fibre reinforced polymer materials in the injection moulding process are classified into polymer fluid mechanics, the fibre orientation kinetics, and the evolution of viscosity by Flow–Fibre Coupling. During the injection moulding processing, the orientation of the fibre inside the FRP composite is affected by the polymer fluid mechanics. In general, the orientation of a single fibre can be in an arbitrary direction, or at one of the three principal directions. Since there are hundreds of thousands of fibres inside the polymer matrix in injection moulding, it is too difficult to observe manually. Instead, to predict the fibre orientation kinetics. In the upcoming section, the orientation of a single fibre defined by an orientation vector is presented.

3.4.1 Fibre alignment

The injection moulding process of short-fibre reinforced polymers generates various fibre alignments or orientations. The orientations of fibres during injection moulding are determined based on the flow of injection mould filling [90]. Discontinuous fibres embedded in the melt thermoplastic matrix rotate and translate due to suspension deformation during processing. On the other hand, the moulded product has anisotropic properties and causes fibre orientation as a consequence of internal shear stress and tensile stress. Processing parameters such as cavity design, and material properties are key factors in determining fibre orientation. The mechanical properties of anisotropy depend on the fibre orientation distribution.

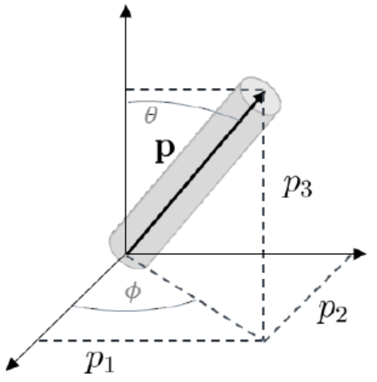

Figure 3.16: The fibre orientation of a single rigid fibre **p** [91].

Mathematically, the fibre orientation of a single rigid fibre can be represented in 3D spatial coordinates. Three-dimensional space is represented by either a pair of angles (α, θ) or a unit vector p (α, θ) along the fibre axis shown above. The unit vector p (α, θ) according to [7] is descried as:

$$P = \begin{pmatrix} p_1 \\ p_2 \\ p_3 \end{pmatrix} = \begin{pmatrix} cos\alpha\ sin\theta \\ sin\alpha\ cos\theta \\ cos\theta \end{pmatrix} \tag{3.100}$$

Where the fibre orientation of a single fibre is described as a unit vector p along its axis direction. The orientation state of fibres in a polymer is depicted in [91] by a second moment tensor,

$$A_{ij} = \int \psi(p)\, p_i\, p_j\, dp \tag{3.101}$$

The n-rank tensor in m dimensions has n indices and m to the n components and follows specific transformation rules mathematically. The second moment tensor expresses p as a unit vector with Cartesian components p_i along a single fibre axis. Whereas $\psi(p)$is the probability density function integrated over orientation space for fibre orientation. The Advani and Trucker model, which uses the second-order orientation tensor to define fibre orientation, is the most well-known theoretical model.

$$A = \int \psi(p)\, p\, p\, dp = \begin{pmatrix} A_{11} & A_{12} & A_{13} \\ A_{12} & A_{22} & A_{23} \\ A_{13} & A_{23} & A_{33} \end{pmatrix} \tag{3.102}$$

Since the orientation tensor A is represented as a symmetric matrix, the sum of $A_{11} + A_{22} + A_{33} = 1$. The isotropic orientation state is denoted by A = I/3, where I is the tensor's identity matrix. A fibre orientation tensor's off-diagonal components correspond to the number of orientations that differ from the spatial coordinate system. And are set to zero when the coordinate axes coincide with the orientation tensor's principal directions [92]. The orientation state of the fibres in the polymer is represented by tensor A, whether they are perfectly aligned or randomly aligned. The relative orientation of fibres is also described by the orientation tensor A. The tensor can be expanded to fourth-order orientation tensor or n dimension tensor, which is defined as,

$$A_{ijkl} = \int \psi(p)\, p_i\, p_j\, p_k\, p_l\, dp \tag{3.103}$$

$$A_{i\ldots n} = \int \psi(p)\, p_i \ldots\ldots p_n\, dp \tag{3.104}$$

When compared to the polymer matrix, fibres with a diameter of 5–10 μm have superior mechanical strength. As a result, fibres are brittle materials in which cracks form without plastic deformation. Thus, when fibres are embedded in the polymer matrix, the polymer composition exhibits exceptional toughness and strength properties. According to Abdelbary & Mohamed, (2021) the reinforcement polymer fibres are distributed in the following orientations [93]:

- Short randomly or aligned fibres.
- Continuous randomly or aligned fibres.
- Woven or unidirectional continuous fibres.

3.4.2 Fibre orientation model

During the injection moulding process of discontinuous fibre composites, the flow creates a fibre orientation that controls the mechanical properties of the part. During those processes, the fibres orient themselves due to the flow and interactions between n fibres and cavity walls. This orientation is anisotropic in general, which causes an anisotropic property of final products. Thus, an accurate prediction of this fibre orientation is vital to the design and production of high-quality parts. The Folgar-Tucker, iARD model, and Jeffery's hydrodynamic model, along with other accurate closure approximations make fibre alignment predictions practical in commercial software such as Moldesx3D[94]. These models employ a probabilistic approach to obtain the fibre configuration evolution during processing which is based on the input parameters, such as fibre characteristics and flow conditions. The Folgar–Tucker model and the other models have been incorporated into the state-of-the-art software of injection moulding simulation. In this study, several fibre orientation models are presented, in order to assist readers both in understanding and in applying them effectively.

3.4.2.1 Jeffery's Hydrodynamic model

G.B. Jeffery, a fellow at University College London, published his work on Ellipsoidal Particles Immersed in Viscous Fluid in 1922. He studied the motion of ellipsoidal particles immersed in a viscous fluid. (Jefery,1922) main goal was to determine how the presence of particles affects the fluid's properties. As a result, the viscosity of the immersed Newtonian fluid increases. The research was an extension of Einstein's work, which presented the mathematical formulation. However, the equation took into account the case of spherical particles for an increase in viscosity [95]. The model considering the Jeffery orbit is defined by the following equation,

$$\frac{DA}{Dt} = (W * A - A * W) + \zeta(D * A + A * D - 2A_4 : D) \tag{3.105}$$

$$W = \frac{(\bar{V}v)^t - \bar{V}v}{2} \tag{3.106}$$

For the study, used a small dimension single rigid ellipsoidal particle. The rate of deformation around the particle can be assumed as identical on the particle in a Newtonian fluid. As a result of the model's o symmetry, the orientation tensors are defined by only even moments. As shown in the equation above, the second-order orientation tensor of the unit vector determines the orientation with respect to the particle axis. W denotes the vorticity tensor, which describes the particle shape factor [96].

3.4.2.2 Folgar–Tucker model

The classical Jeffery model predicts the flow-induced orientation in diluted fibre suspensions. However, the application of classical model for prediction of orientation for most of industrial application is inadequate. The fibre suspension is concentrated and the interaction between fibre-fibre cannot be neglected. Therefore, (Folger & Tucker,1984) [97] proposed the new model by combining Jeffery's model, rotary diffusion and the concept of orientation tensors which is the most used model for the evaluation of the second order orientation tensor. The Folgar-Trucker model considers the rotary Brownian diffusion of the fibre interaction. This model is statistical in nature and predicts the probability distribution of fibre orientation.

Regarding the fibre orientation, models by Folgar and Tucker and their successors are available to predict the fibre rotation and alignment during flow. The general principle of fibre rotation is based on Jeffery's model as stated, which describes the rotation of an ellipsoidal, rigid body immersed in viscous flow. Folgar and Tucker equation extended this model for concentrated fibre suspensions by implementing the fibre orientation tensor and adding the fibre interaction term. The Folgar-Trucker model is defined by Huang-Chang (2018), where the Jeffery hydrodynamic effect is represented by $\dot{A}^{HD}$ and the IRD effect as $\dot{A}^{IRD}$[92]. Thus, the model is characterized as the following equation,

$$\frac{DA}{Dt} = \dot{A}^{HD} + \dot{A}^{IRD} \tag{3.107}$$

$$\frac{DA}{Dt} = (W * A - A * W) + \zeta(D * A + A * D - 2A_4 : D) + 2\dot{\gamma}C_1(I - 3A) \tag{3.108}$$

where, the $\dot{\gamma}$ is the strain rate, $\dot{\gamma} = (2D{:}D)^{\frac{1}{2}}$ and C_1 represents the fibre - fibre interaction in fluid. $\zeta = \frac{a_r^2-1}{(a_r^2+1)}$ is a shape factor of a particle; a fibre's aspect ratio (a_r) is the ratio of its length l to its diameter d, a_r = l/d. The factor ζ equals 1.0, 0.0, and 1.0, which indicates a thin rod, a spherical molecule, and a thin disc of a particle, respectively. Tseng, (2020) emphasize that the concept introduced by Folgar and Tucker offers advantages in the prediction of fibre orientation but is difficult to solve numerically and can only be solved with high computational effort [94]. It is also interesting to note the values of the interaction coefficient C_i used in the calculations. Folgar found that C_i, increases as either the fibre volume fraction or aspect ratio increases, and suggested that one value of C_i should characterize any given suspension.

Kugler, Kech & Osswald, (2020) study specifies that the famous Folgar–Tucker equation of fibre orientation has previously been used to predict the skin–shell–core structure of fibre orientation patterns for injection-moulded fibre composites [98]. However, this model results in inaccurate predictions regarding the thinner core width. Jørgesen, Andreassen & salaberger, (2019) study also indicates that that the predictions with the FT model still deviate from experimental observations. A slower rate of orientation development and a thicker core layer with a more gradual transition is noted in experiments when compared to the FT model predictions[99].

Additionally, the study conducted by Kugler, (2020) informs that the Folgar–Tucker equation, which describes the evolution of the second-order fibre orientation tensor in terms of the velocity gradient is valid under the following additional assumptions: the fibres are rigid cylinders and uniform in length and diameter [98]. Moreover, the fibres are sufficient large such that Brownian motion is negligible. The matrix is incompressible and sufficient viscous, such that particle inertia and buoyancy is negligible. The centre of mass of the fibres are randomly distributed and no external forces act on the suspension.

3.4.2.3 Reduced Strain Closure (RSC) model

The Folgar-Tucker model is the most popular mathematical model, widely applied in commercial software packages and research program. Generally, the fibre orientation of polymer fluid in injection-moulded part is predicted by the F-T model. However, as it is stated by Wang & Jin (2010) the Folgar-Tucker model overestimates the change rate of the orientation tensor in concentrated suspensions [100]. Hence, the reduced strain closure (RSC) models were developed as empirical modifications to the Folgar–Tucker model to better reflect slower orientation kinetics observed experimentally.

Wang & Tucker, (2008) modified the Folgar-Tucker model by reducing the growth rates of the eigenvalues of the fibre orientation tensor by a constant scalar factor but keeping the rotation rates of the eigenvectors unchanged and developed the reduced strain closure (RSC) model [101]. The RSC model exhibits slower orientation kinetics than the Folgar-Tucker model but exhibits a similar steady-state orientation and provides excellent agreement with experimental data. Further adaptation of the RSC model has been employed by Phelps to include anisotropic rotary diffusion to account for fibre interactions that are dependent on the fibre orientation state and flow deformation.

The kinetics of fibre orientation is represented by the eigenvalue λ and eigenvector e decomposition. Reduced Strain Closure (RSC) model is illustrated by Susanne & Kugler, (2020) [91] as following,

$$\begin{aligned}\frac{DA}{Dt} = (W * A - A * W) + \zeta(D * A + A * D - 2(A_4 + (1-\kappa)(L_4 - M_4{:}A_4){:}D) \\ + 2\kappa\dot{\gamma}C_1(I - 3A)\end{aligned} \tag{3.109}$$

In the model the factor κ constrained between the value of 0 and 1. The value of κ determined by empirical studies to be map the slow-down factor of fibre in polymer melt. This is referred to as strain reduction factor by D. V. Peumal, (2020) which ensures unaffected eigenvector kinetics [96].

$$L_4 = \sum_{i=1}^{3} \lambda_i \, e_i e_i e_i e_i \tag{3.110}$$

$$M_4 = \sum_{i=1}^{3} e_i e_i e_i e_i \tag{3.111}$$

where, M_4 and L_4 are fourth-order orientation tensors dependent of eigenvalues λ_i and eigenvectors e_i of the second-order orientation tensor A.

Wang, (2016) demonstrate that the RSC model yields good agreement of fibre orientation with experimental measurements in shell element simulations using the Hele-Shaw flow approximation [102]. Additionally, the study indicates that the RSC model is able to capture the orientation distribution through the part thickness and the average orientation trends along the flow length without the need to tailor the inlet orientation condition to pre-existing data. Recently RSC, was successfully implemented in a research version of Autodesk Moldflow Insight software used for fibre orientation analysis. The program reasonably predicts the fibre orientation, and the prediction agrees well with the measured orientation data for a short fibre material using the RSC model. Wang, (2016) claims that the RSC model is superior to the commonly used Folgar-Tucker model and the default Moldflow's model implemented in Autodesk Moldflow Insight software available commercially.

3.4.2.4 Anisotropic Rotary Diffusion – Reduced Strain Closure (ARD-RSC) Model

Many studies have confirmed that the RSC model accurately predicts fibre orientation for short glass fibre polymers. However, when isotropic diffusion is taken into account, the model is less precise for long glass fibres. Ohan, Tanner & Zheng, (2002) proposed an isotropic rotary diffusion model using the Folgar-Tucker model [103].

$$\frac{DA}{Dt} = \dot{\gamma}(2C - 2tr(C)A - 3(C * A + A * C) + 6A{:}C) \tag{3.112}$$

The rotary diffusion portion of the fibre orientation tensor derived by [104]. In general form the ARD model is proposed by the equation below,

$$\begin{aligned}\frac{DA}{Dt} = {} & \dot{\gamma}(a_1 + a_1 trC + a_3 trC^2)(2I - 6A) + a_4\dot{\gamma}(2(A{:}C)I + 2(C * A + A * C) - \\ & 10A{:}C) + a_5\dot{\gamma}(2(A{:}C^2)I + 2(C^2 * A + A * C^2) - 10A{:}C^2) + \dot{\gamma}(a_6 + \\ & a_7 trC)(2C - 2(trC)A - 5(C * A + A * C) + 10A{:}C) + a_8\dot{\gamma}(2Ctr(A * C) + \\ & 2(C^2 * A + A * C^2) - 2(trC)(A{:}C) - 4A{:}C^2 - 7(C * (A{:}C) + (A{:}C) * C) + \\ & 14C{:}A{:}C) + a_9\dot{\gamma}(2C^2 - 2(trC^2)A - 5(C^2 * A + A * C^2) + 10A{:}C^2)\end{aligned} \tag{3.113}$$

The hydrodynamic term of the orientation tensor is identical to the Folgar-Trucker model. When we consider the $a_4 = C_1$and $a_{2-9} = 0$, then we can derive back to the F-T model. And considering $a_6 = 1$ and $a_{1-5,7-9} = 0$, then the [103] proposed rotary diffusion model is obtained.

Numerical experiments proposed by [104] demonstrated that all a_i parameters from the equation were not needed to predict fibre orientation. Therefore, a new parameter was developed by adjusting a4 and a6 to describe for anisotropic rotary diffusion. The proposed isotropic model replaces the second-order tensor C in F-T model with scalar interaction coefficient C_1. The substitution considers the anisotropic properties in the rotary diffusion model.

$$C = b_1 I + b_2 A + b_3 A^2 + \frac{b_4}{\dot{\gamma}} D + \frac{b_5}{\dot{\gamma}^2} D^2 \tag{3.114}$$

Equation 3.117 ensures the objectivity of C or anisotropic rotary tensor and gives a proportional relation between $\dot{A}^d$ and shear rate. The ARD model for fibre orientation is adjusted just the parameter C. The use of C tensor simplifies the ARD model for general application. Here the isotropic terms are replaced with anisotropic terms in the equation. The ARD model is simplified by Phelps & Tucker, (2009) [104] as following,

$$\begin{aligned}\frac{DA^{ARD}}{Dt} = {} & (W * A - A * W) + \zeta(D * A + A * D - 2A{:}D) + \dot{\gamma}(2C - 2(tr\ C)A - \\ & 5(C * A + A * C) + 10A{:}C)\end{aligned} \tag{3.115}$$

Identical to the RSC model to reduce the orientation kinetics of the Folgar-Trucker model. The ARD-RSC equation model is derived to slow the kinetics of ARD model. The following equation 3.118 is developed when the RSC model is combined with ARD model.

$$\frac{DA}{Dt}^{ARD,RSC} = (W * A - A * W) + \zeta(D * A + A * D - 2(A + (1-\kappa)(L - M{:}A){:}D) + \dot{\gamma}(2(C - (1-\kappa)M{:}C) - 2\kappa(tr\, C)A - 5(C * A + A * C) + 10(A + (1-\kappa)(L - M{:}A){:}C) \tag{3.116}$$

When the value of κ is 1, the ARD-RSC equation is reduced to only ARD model. According to Huan & chang Tseng, (2018) both RSC and ARD-RSC models are incorporated into various injection moulding software [92].

3.4.2.5 Improved ARD – Retarding Principal Rate (iARD-RPR) Model

Despite the fact that ARD-RSC model is generally applied in various commercial simulation software. The ARD-RSC model above shows it requires experimental fitting of 6 coefficients. Consequently, this model is challenging to implement in software application because of its complexity. However, Tseng, Chang & Hsu, (2013) developed a new orientation model based on previous models [105]. Based on the Folgar-Trucker model as a basis, Tseng, Chang & Hsu, (2013) attempted to obtain an objective equation for strain reduction factor and anisotropic rotary diffusion. The iARD-RPR model obtained the strain reduction factor similar to that obtained using the RSC model. The Retarding Principal Rate (RPR) model expressed fibre orientation evolution with eigenvectors and eigenvalues [96]. The new model developed by Tseng, Chang & Hsu, (2013) is given by following equation,

$$\frac{DA}{Dt} = \frac{DA}{Dt}^{HD} + \frac{DA}{Dt}^{iARD}(C_I, C_M) + \frac{DA}{Dt}^{RPR}(\alpha) \tag{3.117}$$

Where, the parameters C_I denotes the fibre-fibre interaction or Folger-Trucker coefficient and C_M denote the fibre-matrix interaction parameter in improved Anisotropic Rotary Diffusion. The parameter α signifies the slow down factor of the fibre orientation in RPR model. The new model included three terms, where the first was Jeffery Hydrodynamics $\frac{DA}{Dt}^{HD}$, improved Anisotropic Rotary Diffusion $\frac{DA}{Dt}^{iARD}$ and the newly developed Retarding Principal Rate $\frac{DA}{Dt}^{RPR}$. The equation for Jeffery Hydrodynamics is presented above in equation 3.107. The second term of the equation according to Huan-Chang Tseng , (2018) is based on diffusion tensor D_r [92]. The diffusion tensor is derived according to the rate of deformation tensor D to define the improved Anisotropic Rotary diffusion (iARD) model, as below:

$$\frac{DA^{iARD}}{Dt} = \dot{\gamma}(2D_r - 2tr(D_r)A - 5D_rA - 5A * D_r + 10\, A_4 \colon D_r) \tag{3.118}$$

$$D_r = C_I(I - \frac{C_M D^2}{\|D^2\|} \tag{3.119}$$

According to Tseng, (2013) [105], the Retarding Principal Rate is determined with the material derivation $\dot{\Lambda}^{IOK}$ of the tensor which considers Intrinsic Orientation Kinetics (IOK) [105]. The RPR model given as following equation:

$$\frac{DA^{RPR}}{Dt} = -R * \dot{\Lambda}^{IOK} * R^T \tag{3.120}$$

$$\dot{\Lambda}^{IOK} = \alpha\lambda_i \tag{3.121}$$

Here the symbol α denote a dimensionless constant and λ is the eigenvalue of second orientation tensors. RPR model calculates the orientation according to two stepped methods. where the orientation is described as the function which determines the isotropic model [96].

The iARD-RPR model is implemented in the commercial CAE software and Moldex3D to provide the fibre orientation predictions in injection moulding and compression moulding simulation. Tseng, Chang & Hsu, (2018) shows that the iARD-RPR model has only the three physical parameters: a fibre-fibre interaction parameter C_I, a fibre matrix interaction parameter C_M and a slow-down parameter α [106]. The available region of these parameters, $0 < C_I < 0.1$, $0 < C_M < 1$, and $0 < \alpha < 1$. Additionally, the study enlightened that the shell-orientation layer depends on the iARD parameters, while the core width is controlled by the RPR parameter. The value of fibre orientation in the shell increases with increasing C_I and decreasing C_M. The core width increases with increasing α. According to these criteria, we could fine-tune three parameters to obtain an accurate orientation prediction compared with experimental data by determining optimal parameters set.

3.4.2.6 Moldflow rotational diffusion (MRD) model

Moldflow rotational diffusion (MRD) was developed in order to improve the accuracy of 3-D orientation predictions for Autodesk Moldflow. The new model Moldflow rotational diffusion was proposed by Bakharev & Wang (2018) based on both the Folgar–Tucker model and the ARD model

[107]. The MRD model, has a structure similar to the FT model, but it involves three additional parameters to fine-tune the orientation alignment rate with the current orientation tensor.

$$\dot{A} = \dot{A}^{HD} + \dot{A}^{MRD} \tag{3.122}$$

$$\dot{A}^{MRD} = 2\dot{\gamma} C_I (D - tr(D)A) \tag{3.123}$$

$$D = \begin{pmatrix} D_1 & 0 & 0 \\ 0 & D_2 & 0 \\ 0 & 0 & D_3 \end{pmatrix} \tag{3.124}$$

The model is characterized by four parameters C_I D_1 D_2 D_3 where the tensor D is an anisotropy factor tensor accounting for anisotropy of fibre–fibre interactions. Fibre interaction coefficient Ci corresponds to the magnitude of the rotational diffusion. The coefficients of asymmetry D1, D2 and D3 show how the rotational diffusion is biased towards the direction of the principal vectors of fibre orientation tensor. The higher the value of the corresponding D coefficient, the more the rotational diffusion is biased in the direction of the corresponding principal vector. [94] states that the MRD model contains four parameters and region of these parameters are: $0 < D^1 < 10^6$, $0 < D^2 < 10^6$, $0 < D^3 < 1$, and $0 < C_I < 1$. When setting $D_1 = D_2 = D_3 = 1$ the MRD model becomes a classic Folgar–Tucker model. The default values for the D_i coefficients are D_1=1.0, D_2=0.8, D_3=0.15. However, Bakharev & Wang (2018) have found that the best fibre orientation results are obtained for $D_1 = 1.0$, $D_2 = 0.5$, and $D_3 = 0.3$ in the commercial injection moulding simulation software, Autodesk Moldflow Insight [107].

3.4.3 Closure approximations

The fibre orientation model uses a fourth-order orientation tensor to predict the fibre behaviour in submerged suspensions. Application of any orientation models derived by Folgar-Tucker requires the fourth-order orientation tensor to be represented as a function of the second-order orientation.
The closure approximations are needed to obtain higher-order polynomial by decoupling the fourth-order orientation tensor [92]. Different suitable closure approximations are developed to transform fourth-order tensors to second-order tensors. Some of the most known closure approximations are eigenvalue-based optimal fitting (EBOF), linear closure, quadratic closure, hybrid closure, etc.

3.4.3.1 Linear closure model

The closure based on linear approximation was proposed by Hand, (2018) [108]. The linear closure approximation for planar orientation is given by,

$$\hat{a}_{ijkl} = -\frac{1}{24}(\delta_{ij}\delta_{kl} + \delta_{ik}\delta_{jl} + \delta_{il}\delta_{jk}) + \frac{1}{6}(a_{ij}\delta_{kl} + a_{ik}\delta_{jl} + a_{il}\delta_{jk} + a_{kl}\delta_{ij} + a_{jl}\delta_{ik} + a_{jk}\delta_{il}) \quad (3.125)$$

Here $\hat{a}_{ijkl}$ and δ_{ij} represents the modelled a_{ijkl} and Kronecker delta respectively. According to Hand, (2018) [108], the following equation is more suitable for flows with a small rate of strain where the fibres are distributed randomly. But the accuracy of the model decreases when the fibres orientations are highly aligned.

3.4.3.2 Eigenvalue based closures

Eigenvalue based closures are one of the several orthotropic closures of the fourth-order orientation tensor. The principal axis of the fourth and second-order tensors must be identical, which gives an orthotropic fourth-order orientation tensor [109]. This assumption provides symmetry where many components are neglected. Therefore, orthotropic closures are required to satisfy the condition where the tensor components contributing to the shear-extensional coupling terms are zero [110]. The fourth-order orientation tensor is represented as a second-order tensor by the following equation,

$$A_{mn} = \begin{pmatrix} A_{11} & A_{12} & A_{13} & 0 & 0 & 0 \\ A_{12} & A_{22} & A_{23} & 0 & 0 & 0 \\ A_{13} & A_{23} & A_{33} & 0 & 0 & 0 \\ 0 & 0 & 0 & A_{44} & 0 & 0 \\ 0 & 0 & 0 & 0 & A_{55} & 0 \\ 0 & 0 & 0 & 0 & 0 & A_{66} \end{pmatrix} \quad (3.126)$$

Application of symmetries in the function of six independent components of the fourth-order tensor gives $A_{12} = A_{66}$, $A_{13} = A_{55}$, and $A_{23} = A_{44}$.

3.4.3.3 Invariant based closures

Invariant based optimal fitting closure approximation (IBOF) is a widely applied orthotropic closure approximation in polymer simulation. IBOF is derived by [111] starts with a general expression of a full symmetric fourth-order tensor as below,

$$a_{ijkl} = \beta_1 S(\delta_{ij}\delta_{kl}) + \beta_2 S(\delta_{ij}a_{kl}) + \beta_3 S(a_{ij}a_{kl}) + \beta_4 S(\delta_{ij}a_{km}a_{ml}) + \beta_5 S(a_{ij}a_{km}a_{ml}) + \beta_6 S(a_{im}a_{mj}a_{kn}a_{nl}) \quad (3.127)$$

Where β_i are the function of the invariants of the second-order orientation tensor a_{ij}. IBOF assumes that the coefficients β_i are polynomial expansions of the second and third invariants of a_{ij} [111]. And S denotes the symmetric operator which forms the invariant closures given by,

$$S(T_{ijlk}) = \frac{1}{24}(T_{ijlk} + T_{jikl} + \cdots (24\ total\ terms) \tag{3.128}$$

Where the eigenvalue and invariant-based optimal fitting are fitted closure. In these closures, the representation of the approximation depends on invariants or eigenvalues of orientation tensor [91]. The closure approximation for the injection moulding simulation was considered invariant-based optimal fitting (IBOF). Generally, the fitted closure approximation based on invariant reduces the simulation period.

4 Numerical simulation of the injection moulding process

The injection moulding process is one of the essential techniques for producing plastic parts. Competition has pushed the industry to increase parts quality at the lowest possible cost. There is several software on the commercial market today which enable the analysis of the injection moulding process. One of them is the software Moldex3D by core tech system. Moldex3D is the world-leading CAE product for the plastic injection moulding industry with the best-in-class analysis technology [47].

A typical scenario continues to occur in part and mould designs; in many cases, a manufacturer must modify the design again and again because the optimal result is too difficult to reach when using the traditional trial-and-error approach, in which case the mould verification can be done only when the mould is fully finished. Hence, Moldex3D can be employed to predict the behaviour of the system. Moldex3D solutions assist users in simulating and validating their part and mould designs before putting mould trials and fixes into practice, and it can avoid countless trial-and-errors. Therefore, much can be gained since the software allows one to make most of the tedious and cost-consuming trial and errors in the virtual world. Additionally, Moldex3D assists in saving time, energy, and money more efficiently during the mould-making process.

4.1 Geometry description

A dog-bone specimen was simulated according to ISO 527 for the injection moulding process in this project [112]. The standard dog-bone sample based on ISO 527 is demonstrated in the Figure 4.1. The specimen has a total length L_3 of 150 mm, which is a minimum. The length of parallel edges at the narrow zone L_1 and the radius R of the specimen are 60 mm. The sample has two widths, one at the end $b_2$and the other at the narrow zone b_1, with a span of 20 mm and 10 mm, respectively. At the same time, the specimen designed for injection moulding simulation has a thickness h of 4 mm. Our external supervisors from SINTEF modelled the part geometry of the dog-bone specimen utilized in this specific project. To start model preparation, the geometry file of the model was imported from the external resource.

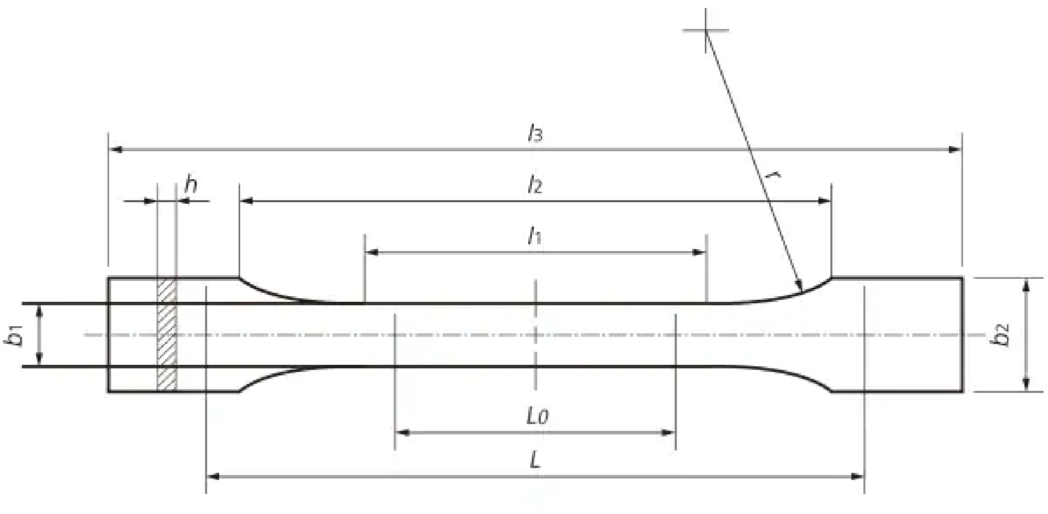

Figure 4.1: Geometry of dog bone specimen used in this thesis for simulation according to the ISO 527 [113].

4.2 Material and process parameters

Process parameters play an important role in improving result accuracy, mechanical properties, and simulation time. Additionally, it is essential to prepare the moulding model and mesh it to the desired target. Good simulation results depend on several important factors, and material is one of them. Polymer material behaviour is very complicated during injection moulding, so good simulation results are influenced by the material's nature and selection. Moldex3D Material Wizard provides accurate and comprehensive material data for users to select a suitable material. The polymer matrix selected for the simulation is Polyamide (PA) 12, also known as Nylon 12. The fibre material is considered glass fibre material of LV-65H with a weight percentage of 60. The shear viscosity flow curve of the material (30wt%-SGF/PA6) used in Moldex3D is shown in Figure 4.2. The aspect ratio or the ratio of length to fibres diameter of the fibre materials is assumed to be 20 during simulation.

Improper process parameters lead to an unreasonable simulation result, so the user must select reasonable parameters. In the Moldex3D process wizard, melt temperature, mould temperature, and injection pressure can be set. For the simulation, the temperature of molten polymer is assumed to be 280° C and mould temperature as 90° C. Moldex3D also allow the user to modify the computation parameter to fit different circumstances. Computation parameters include solver type, advanced analysis option, extra data output and calculation step. In the advanced analysis option, fibre orientation models can be specified. The fibre orientation model is included to predict the positioning of the fibres in the finished moulded part. The orientation model applied in this simulation was the improved Anisotropic Rotary diffusion (iARD) model and Folgar-Tucker. Additionally, the values of coefficient C_i, C_m and α can be determined in the advanced analysis option. The default values of fibre-matrix interaction, fibre-matrix interaction and alpha are set as 0,005, 0 and 0.7, respectively.

These three parameters have a value in the range of (0-0,1) for fibre-fibre interaction, (0-1) for fibre-matrix interaction, and (0-1) for alpha factor.

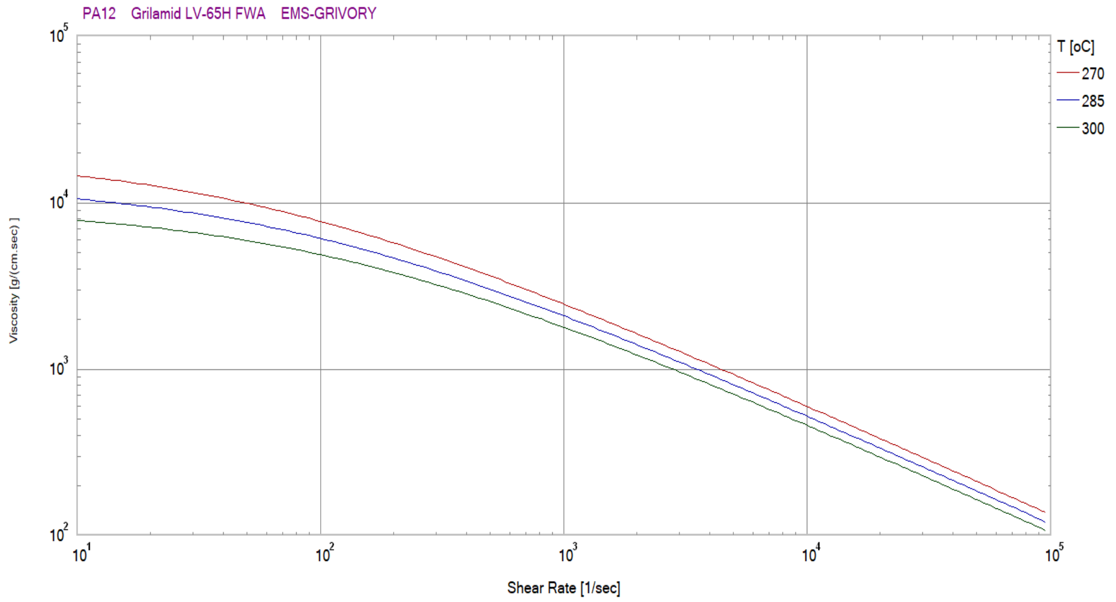

Figure 4.2: Viscosity flow curve of Polyamide (PA) 12 from the Moldex3D database.

4.3 Meshing strategy

When the runner valve gate in the geometry was specified, the mesh was generated for the specimen. A refined mesh and efficient mesh strategy is required to simulate the injection moulding process in Moldex3D with high accuracy and reliable results. In addition, the meshing strategy is influenced by the CPU processing power and the computational time depends on the complexity of the CAE simulation. Moldex3D provides various options to create the mesh model depending on the simulation requirement. The main meshing techniques provided by Moldex3D are Automatic 3D Meshing Engine (eDesign), high-resolution 3d mesh technology (BLM) and hybrid mesh technology. Since we are conducting an injection moulding process for short fibre composites in a dog bone specimen, the following mesh strategy is applied for the simulation to increase accuracy and reduce computational time.

In the simulation of the specimen, the polymer melt is injected with two valve gates set at the opposite end of the specimen. Due to the polymer melt flowing from the opposite direction, the melt front meets at the centre of the specimen with complex polymer melt behaviour. The phenomenon where polymer melt fronts meet during injection moulding cause locally weak areas in the moulded part known as weld lines. To predict the behaviour of fibre orientation at weld lines, a comprehensive strategy for mesh distribution based on seeding was developed. The specimen geometry was divided into 6 zones to distribute mesh to reduce the seeding size gradually to the location where flow fronts meet, where areas A1 and a1 have a seeding size of 0,8 and A2 and a2 has a size of 0,6. The mesh seed size of 0,4 is applied in areas A3 and a3. In addition, the mesh size of 0,2 was used at the centre of the specimen to obtain finer mesh where the flow fronts meet the accurate behaviour of the simulation. Furthermore, a linear biasing method in the longitudinal direction was applied to increase the transition smoothness of the mesh size between two different zones. The biasing factor for A1, A2 and A3 was 0,6, 0,4 and 0,2, while the biasing factor at a1, a2 and a3 was negative 0,6, 0,4 and 0,2 to make the mesh fine with a seed of 0,2 at the centre of the specimen.

The mesh chosen for the injection moulding simulation was solid with high-resolution 3d mesh technology Boundary Layer Mesh (BLM). Furthermore, Moldex3D allows users to adjust solid mesh parameters for geometry meshing, curve meshing and hybrid meshing. The attribute of the mould part was applied with geometry meshing, and 11 layers of boundary layer mesh were applied as mesh type with an automatic boundary layer offset ratio. Application of (BLM) allows Moldex3D to generate an injection flow of multiple layers with prismatic meshes out of triangular surface mesh. Additionally, the internal space is filled with quality-controlled tetrahedral mesh. An illustration of the boundary layer mesh for the specimen is shown in the Figure 4.3. The valve runner system for the simulation was applied with the curving mesh of 4 inner and 5 outer layers illustrated in the Figure 4.4. Additionally, the mesh type of pure tetrahedral shapes is used in the compression zone as hybrid meshing.

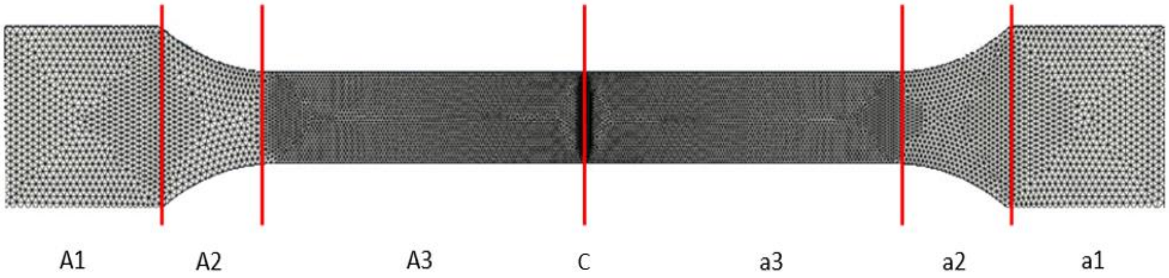

Figure 4.3: Division of specimen area in the longitudinal direction to distribute mesh with red lines and final surface mesh applied in the Moldex3D simulation.

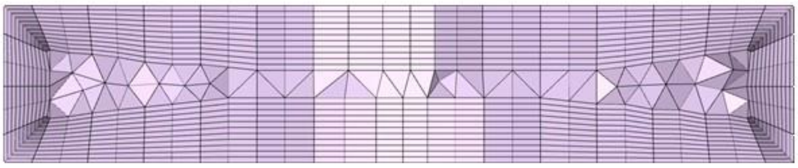

Figure 4.4: Cross-section of the specimen after applying 11-layer boundary layer mesh to generate a flow in multiple layers.

4.4 Melt front filling simulation

Short fibre reinforced composite is produced by injection of melted polymer pellets (thermosetting/ thermoplastic polymers) with fibres inside a mould cavity with given injection pressure. When the mould cavity is filled, the material is hardened to produce the solid final part for industrial application. Understanding how the mould fills is important for designing efficient polymer parts. Moldex3D simulates the injection moulding process with different materials and flow conditions inside the mould cavity and gives appropriate fibre orientation. Flow simulation in Moldex3D provides an enhanced understanding of polymer flow behaviours under the injection moulding process. The effect of temperature, viscosity, acceleration vector of gravity, and inertia forces are also included in the flow governing equation of flow simulation. These parameters are employed to solve the transient flow field in a 3D geometry according to the 3D Finite Volume Method (FVM) in Moldex3D simulation.

Injection moulding simulation of a dog bone specimens with and without a weld line is performed with a single and double valve gate. The formation of weld lines during injection moulding is the most common defect in injection moulded parts. The development of weld lines is a significant challenge regarding the mechanical properties of polymer material produced with injection moulding. A weld line is formed when different melt flow fronts and plastic welds meet during the mould filling process. Accordingly, two various valve gates at the end of the specimen were employed to create a melt front collision. The collision due to the additional valve gate will produce a moulded part with a weld line at the centre of the specimen where the melt fronts collide. These welds lines created by simulation can be studied to determine mechanical weakness and imperfection of polymer parts. The simulation conducted for the dog bone specimen has a total fill time of 0,4 seconds. The fill time indicates the polymer's total amount of to fill the mould cavity. The Figure 4.5 and 4.6 shows the simulation process of polymer taken from Moldex3D in four different time steps.

Figure 4.5 shows the simulation process for the model without a weld line, whereas Figure 4.5 (a) illustrates the polymer simulation at 0,037 seconds. At a fill time of 0,037 seconds, the mould is filled with 8,92 % of the total volume. The simulation shows that the mould volume closer to the valve gate is filled primarily with polymer. At a fill time of 0,182, almost half of the mould volume, specifically

45,4 %, is filled with polymer material. 81,8% of the mould volume is packed with polymer melts at a fill time of 0,328 seconds, illustrated in Figure 4.5 (c). Figure 4.5 (d) depicts the final simulation phase with an entirely packed mould at a fill time of 0,405 seconds. The simulation demonstrates that the volume at the opposite end of the valve gate is filled at the end of fill time. Additionally, Figure 4.6 displays the simulation process with two parallel valves in Moldex3D at four different time steps. The simulation with parallel valves results in melt front collision at the centre of the specimen. Figure 4.6 (a) demonstrates the polymer simulation where 8,73 % of the mould cavity is filled with polymer at a fill time of 0,037 seconds. Identical to the previous simulation, Figures 4.6 (b) and (c) illustrate the melt fill simulation at a fill time of 0,183 and 0,328 seconds. Where 45,4 % and 80,81 % of the mould volume is filled with polymer material at respective fill times. And Figure 4.6 (d) illustrates an entirely packed mould cavity at a fill time of 0,405 seconds at the final simulation stage. According to the simulation, the volume near the valve gates is filled at the beginning of the fill time, gradually increasing towards the centre of the specimen. The centre area where the flow fronts meet is filled at the end of the fill time in contrast to the simulation without a weld line.

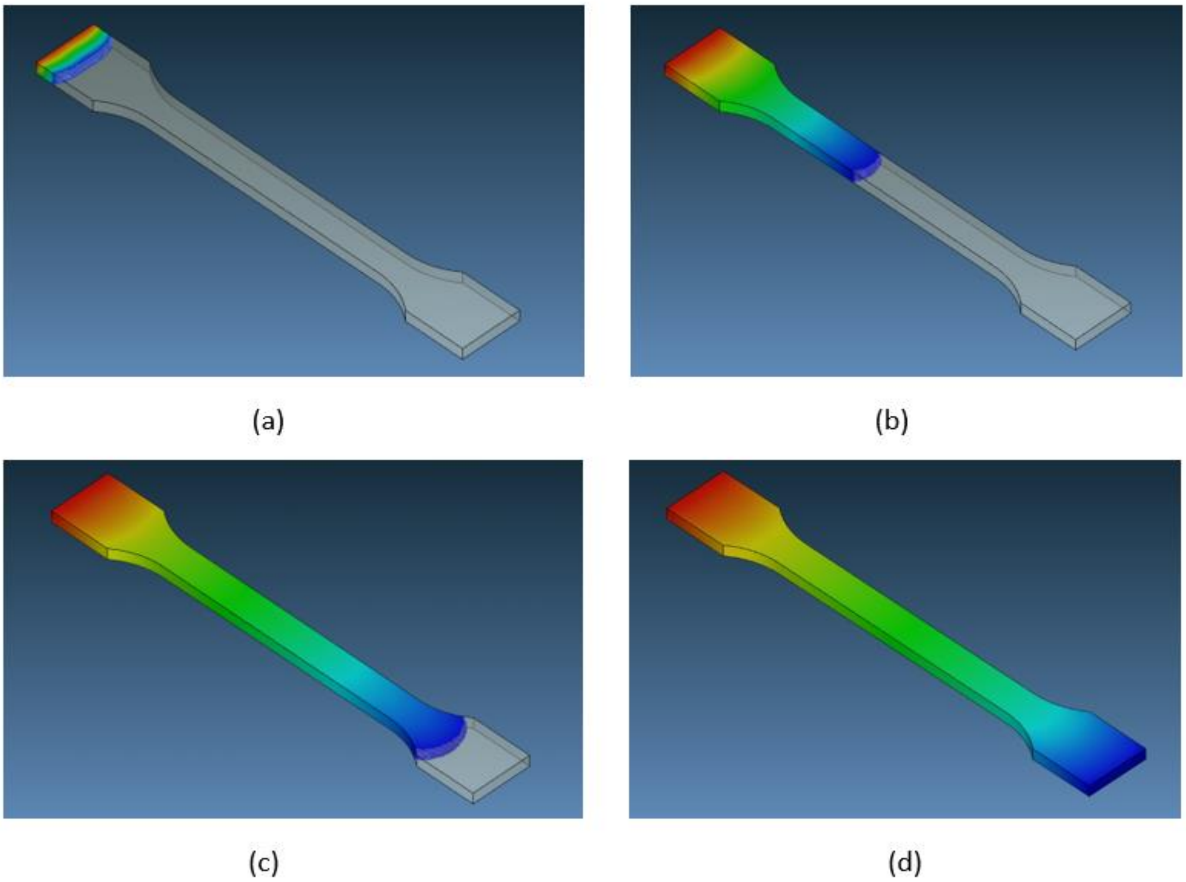

Figure 4.5: Filling phase simulation of injection moulding from Modlex3D with single polymer valve gate at different fill times for (a) 0,037 s, (b) 0,182 s, (c) 0,328 s, and (d) 0,405 s.

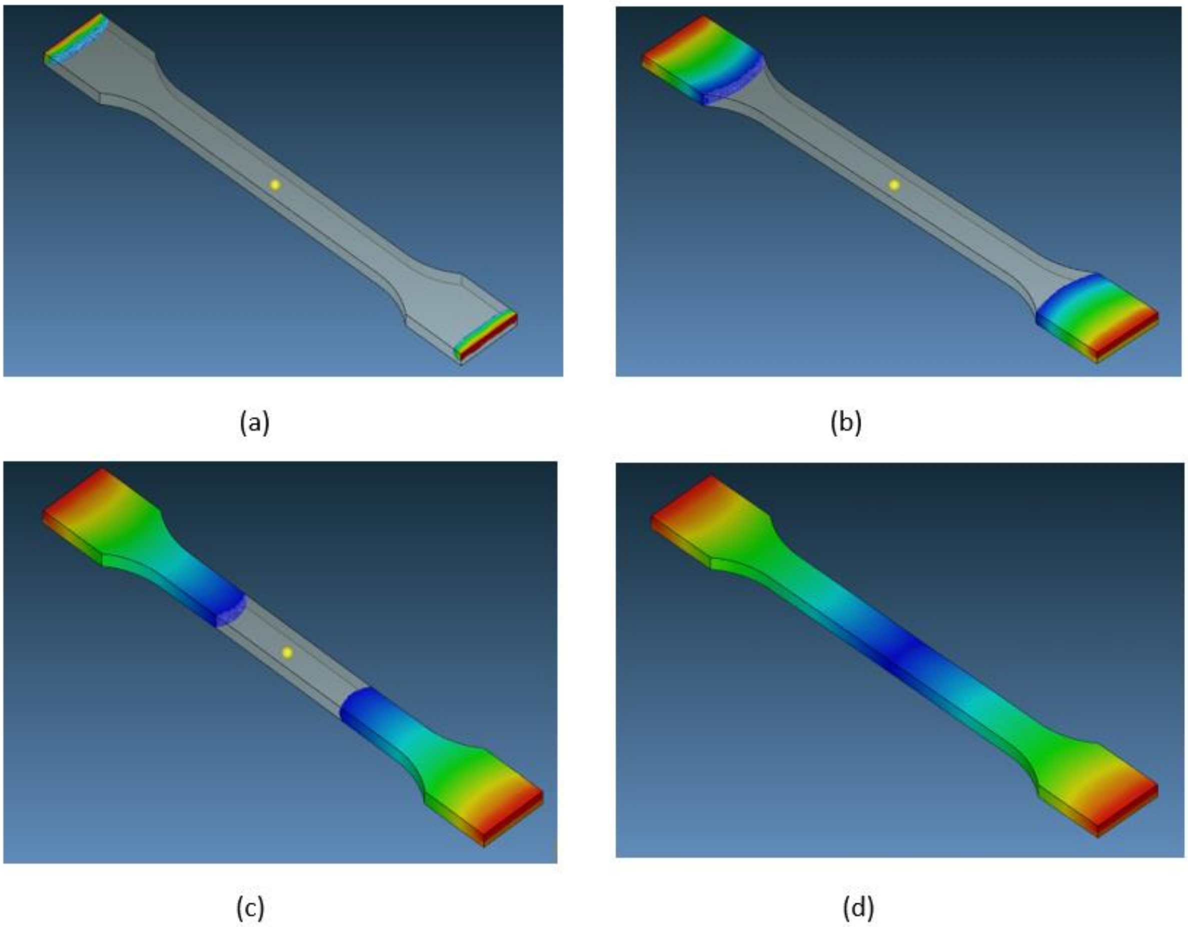

Figure 4.6: Moldex3D simulation of injection moulding at different fill times for (a) 0,037 s, (b) 0,183 s, (c) 0,328 s, and (d) 0,405 s with two polymer valve gates at the opposite end.

4.5 Temperature

The temperature distribution expresses temperatures in all three dimensional for the full cavity. From the temperature results obtained from Moldex3D, it can be determined which region has high frictional heating. Moreover, it is possible to check if the temperature variation corresponds to the process condition from the temperature outcomes. The higher temperature typically indicates a less severe weld line. This happens because the melt flow fronts will entangle much more efficiently for high temperatures, which helps reduce both the visual appearance and potential mechanical weakness. On the other side, when the temperature is lower, the melt will be more viscous, and so it will be more challenging to mix the independent flow fronts, with the consequent problems for the appearance and mechanical behaviour.

Figure 4.7 shows that the temperature on the part's surface and the external walls have a similar variation. In addition, the figure displays the position and the temperature at which the melt flow front meets, as predicted by Moldex3D. Furthermore, it indicates that the temperature near the weld line is higher. The lowest and highest temperature values are 108 °C and 282 °C, respectively. Additionally, the temperature results at different cross-sections are presented. The results obtained in different areas across the yz-component cross-sections are generally similar and show constant temperature. However, the graphics analysis demonstrates that the temperature next to the walls and skin layers is lower than the weld line's cross-section. Generally, the temperature inside the part is much higher than the temperature experienced on the surface.

The Figure 4.8 shows the temperature distribution for the part without a weld line. The lowest and highest temperature registered is about 103 °C and 290 °C. The temperature on the surface of the part is almost evenly distributed throughout the skin layer and walls of the part. However, hotter spots are observed at the edge of the part near the end fill. According to the figure, it is observed that the temperature increases as the flow go further away from the gate and near the end fill, the temperature appears to be higher. The distribution of temperature inside the part at the cross-section is presented. The temperature inside the part is homogeneously distributed, as shown in Figure 4.8, which is good for eliminating product defects caused by poor temperature control. A significant difference can be seen between the internal and surface temperatures. The temperature is cooler on the part surface, as demonstrated by the graphical cross-sections of the part without a weld line.

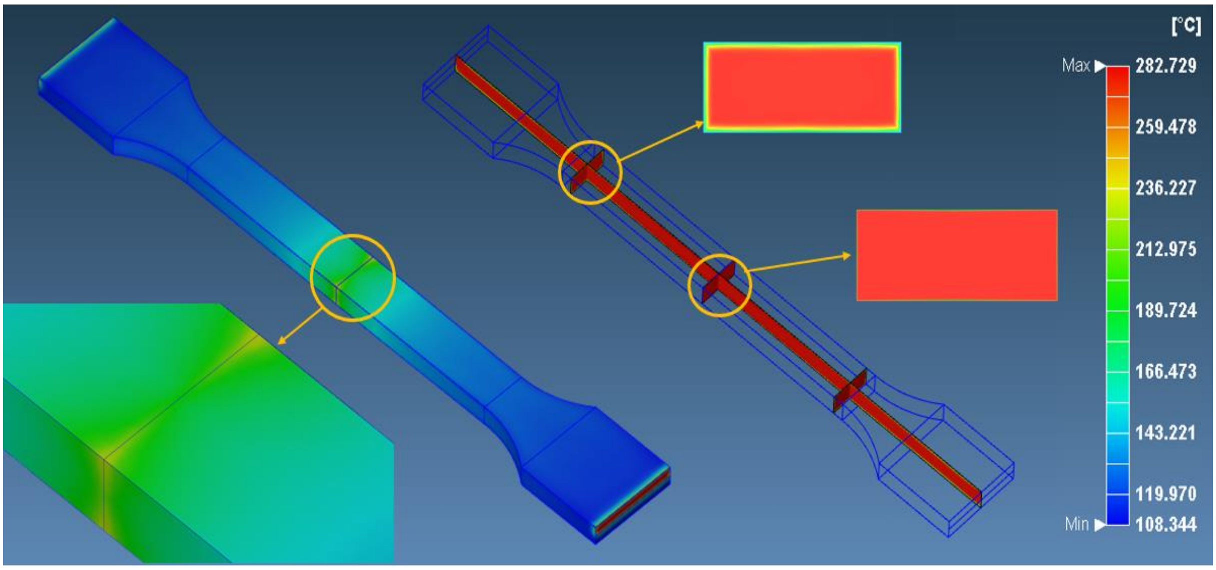

Figure 4.7: The internal and external filling temperature of the injection moulded part in Moldex3D with weld line.

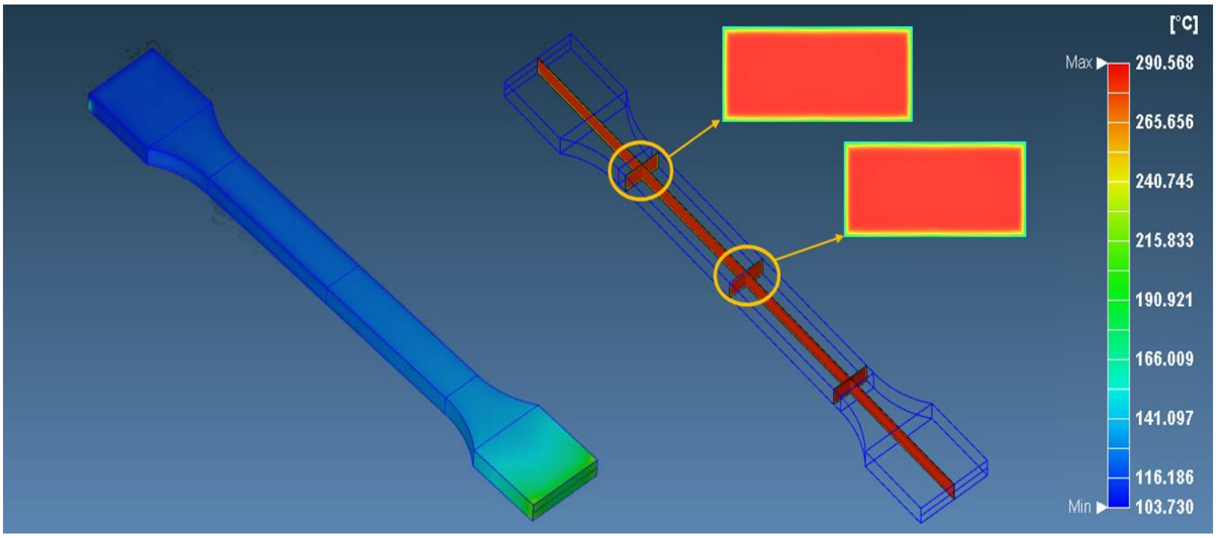

Figure 4.8: The internal and external filling temperature of the injection moulded part in Moldex3D without weld line.

4.6 Shear stress

Shear stress measures the tension created between plastic molecules caused by shear flow during the moulding process. Shear stress increases with higher viscosity, shear rate and gradient of velocity. Shear rate is the rate change in velocity at which one layer of fluid passes over an adjacent layer. So when the moulding process is performed fast, it often increases the shear rate resulting in a higher shear of stress during the process. During the filling stage, the polymer is subjected to shear stresses and shear rates, both responsible for the orientation of the material in the flow direction. Non-uniform shear stress distribution might cause a warping in the finished part. Therefore, the shear stress should be distributed consistently in optimised conditions to obtain an improved product.

In Moldex3D, shear stress predictions are shown in a few different plots, which display how much stress is in a particular region of the part geometry. The shear stress results in Figure 4.9 indicate the shear stress distribution of plastic melt. Figure 4.9 shows that high shear stresses are found near the gate on the part's surface, while the region near the weld line has quite a low share stress. On the contrary, the shear stress inside the part of the cross-sectional area is homogeneously distributed, indicating that most regions of the part are undergoing less than 0.013 MPa of stress. Based on the result, the lowest and highest temperature value found are about 8.533 MPa and 0.013 MPa, respectively.

Figure 4.10 shows shear stress on the part's surface without a weld line. According to the obtained results, the minimum and maximum shear stress are 12.3 MPa and 0.015 MPa. The results demonstrates that share stresses near the gate are higher with uneven distribution of shear stress, while the region near the end fill of the part has lower shear stress. In addition, the results show the distribution of share stress inside the part. The graphical demonstration of a cross-section through the part indicates that the shear stress inside the part is homogeneously distributed. Generally, the shear stress inside the part is much lower than the detected share stress on the part's surface.

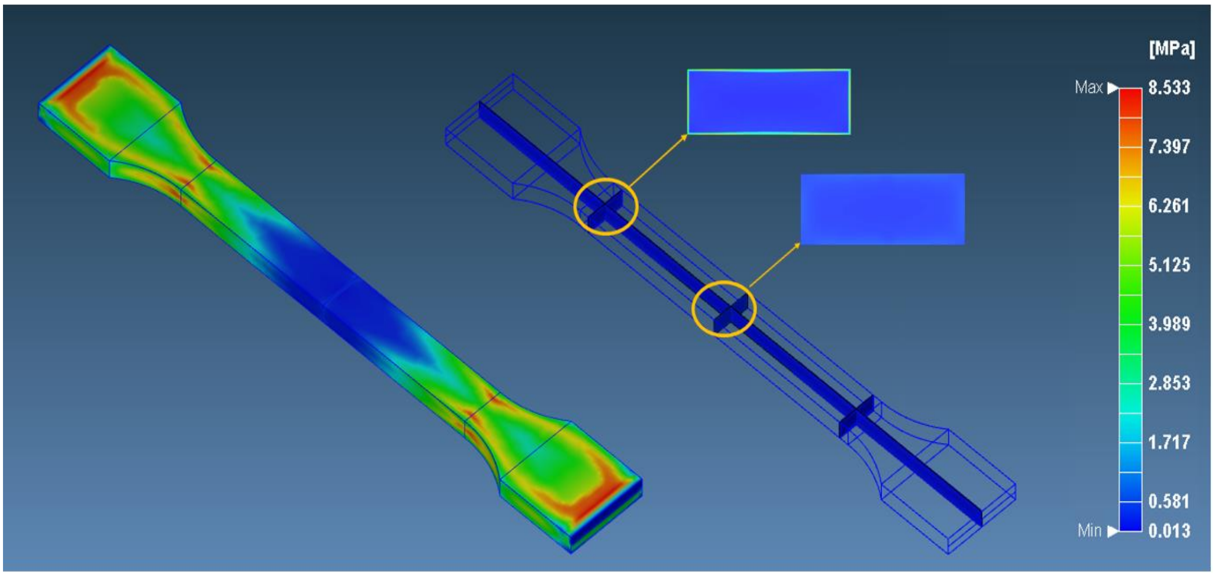

Figure 4.9: The share stress of the injection moulded part in Moldex3D with weld line.

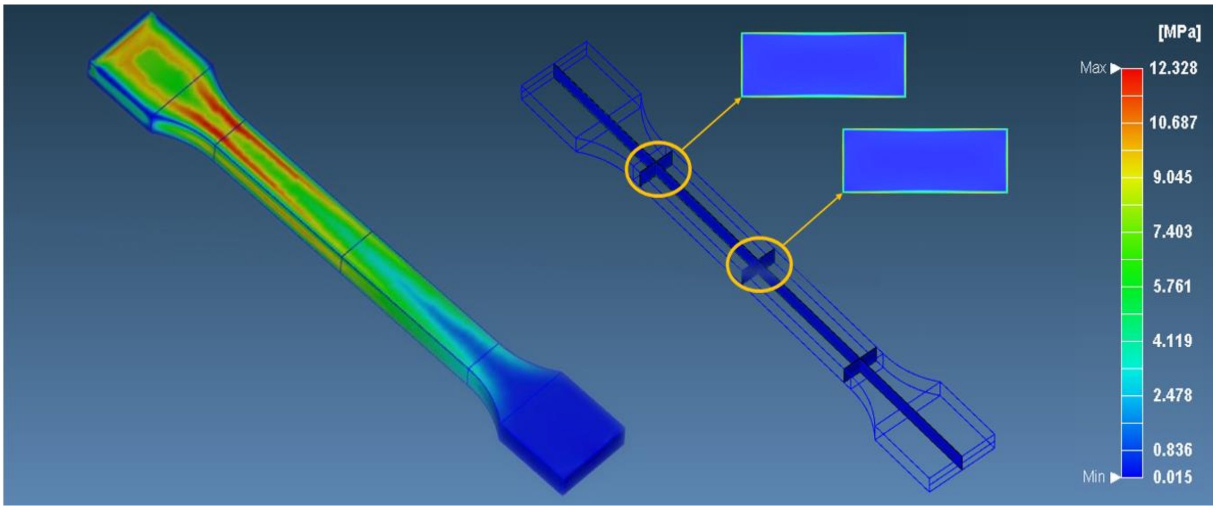

Figure 4.10: The share stress of the injection moulded part in Moldex3D without weld line.

4.7 Viscosity

Viscosity measures a fluid's resistance to flow, which depends on temperature, shear rate and pressure. The viscosity of thermoplastics shows a strong temperature dependence. Typically, viscosity drops dramatically when temperature increases. The simulation output analysis obtained from Moldex3D indicates that the viscosity of the part varies throughout the part geometry, where the minimum and maximum viscosity are 2.773 Poise (P) and 9 Poise (P). The poise is the unit of dynamic viscosity (absolute viscosity) in the centimetre–gram–second system of units. According to the contour plots for viscosity in Figure 4.11, it can be observed that the viscosity on the surface of the part is low at the end of the fill near the weld line positioned at the centre of the part. On the other hand, the viscosity is seen to be high near the gate; this might be due to the reduction in temperature on the surface. Generally, the result specifies that the viscosity decreases as the melt flow approaches the weld line.

In addition, the viscosity inside the part is presented in Figure 4.11. The cross-section in the yz-xz component specifies that the viscosity variations in the yz- xz component appearances are consistent. However, the internal viscosity is lower at which the melt flow front meets. The graphical analysis of the cross-sectional area demonstrates that the viscosity next to the wall and skin layer is much higher. The viscosity inside the part is realised to be more homogenous than viscosity on the part’s surface. Additionally, the internal viscosity observed through the iso-contour lines is lower than the surface’s viscosity.

Figure 4.12 shows viscosity on the part’s surface without a weld line. The outcome analysis achieved from Moldex3D indicates that the magnitude of viscosity changes throughout the part where the minimum and maximum viscosity are 3.2 Poise(P) and 9 Poise (P). According to the visual observation, the magnitude of the viscosity decrease as the flow moves further away from the gate and approaches the end fill. Additionally, the result indicates that the lowest viscosity is detected at the edge of the part at the end fill. Figure 4.12 shows also the viscosity distribution inside the part across the thickness direction, including the yz and xz components. The results imply that the viscosity inside the part is uniformly distributed, but the presented cross-section shows that the skin layer and the walls have higher viscosity. The viscosity of the polymer inner layer of the part is much lower than the viscosity experienced on the part's surface. The result was as expected due to the lower temperature on the surface, which leads to higher viscosity.

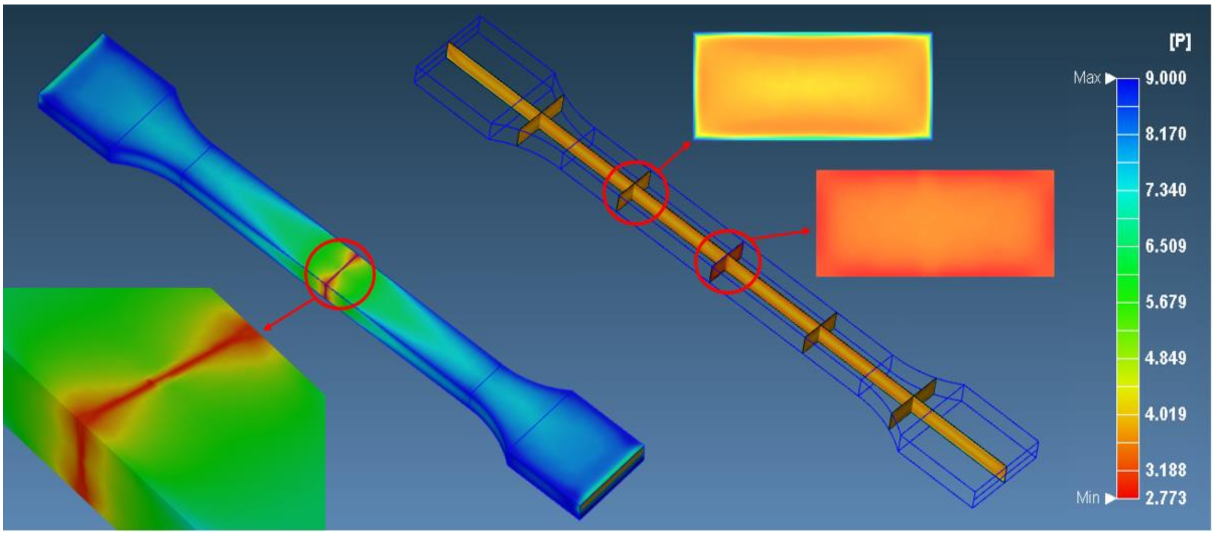

Figure 4.11: Viscosity of the injection moulded part in Moldex3D with weld line on the surface and exterior part.

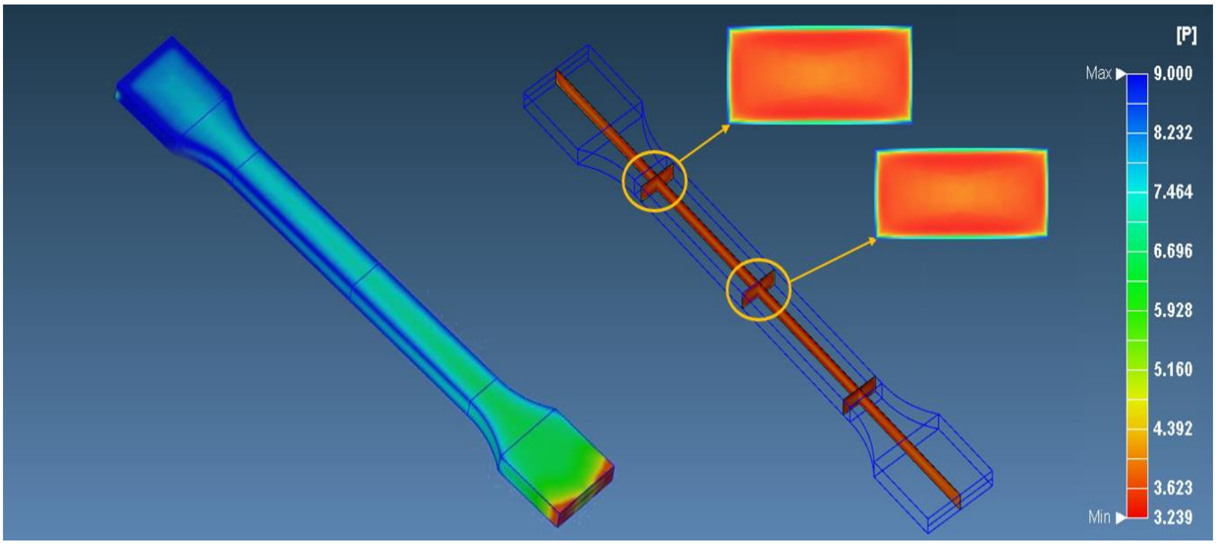

Figure 4.12: Viscosity of the injection moulded part in Moldex3D without weld line on the surface and exterior part.

4.8 Fibre concentration

Figure 4.13 demonstrates the fibre concentration distribution in the part. An appropriate level of fibre concentration is essential to increase product structure. Furthermore, non-uniform distribution of fibre concentration can cause defects such as warpage and bad appearance. Figure 4.13 displays the distribution of fibre content (66%) using weight percentage. According to the obtained results, the minimum and maximum concentrations are 58.5 w/v % and 65.01 w/v %, respectively.

Based on the results, it is clear that the fibre concentration on the surface of the part is distributed uniformly. However, the concentration is relatively high near the centre of the part at which the flow fronts merge. The highly accumulated fibres at the weld line where the flow front merges may influence the fibre configuration. Additionally, the fibre concentration near the gate is lower. In contrast, the fibre concentration is nearly constant throughout the part according to the vast majority of the analyses undergoing less than 66.281 w/v % fibre concentration. Based on the cross-sectional result, the fibre concentration inside the part appears to be constant throughout the entire part in all directions, as the iso-contour lines demonstrate. The fibre concentration is higher inside the part than the fibre concentration viewed on the surface.

Figure 4.14 shows the concentration distribution of the part without a weld line. The minimum and maximum registered fibre concentrations are 57.1 w/v % and 65.12 w/v %, respectively. According to the result, it is clearly shown that the fibre concentration is distributed consistently throughout the part. However, higher fibre concentration is seen at the edges of the end fill. The figure similarly illustrates the distribution of fibre concentration inside the part. And the distribution of fibre concentration inside the part appears to have homogenous distribution. Additionally, yz and xz cross-sections of the part indicate that the skin layer and walls have lower fibre concentration than the magnitude of fibre concentration inside the part. Generally, the fibre concentration is higher inside the part.

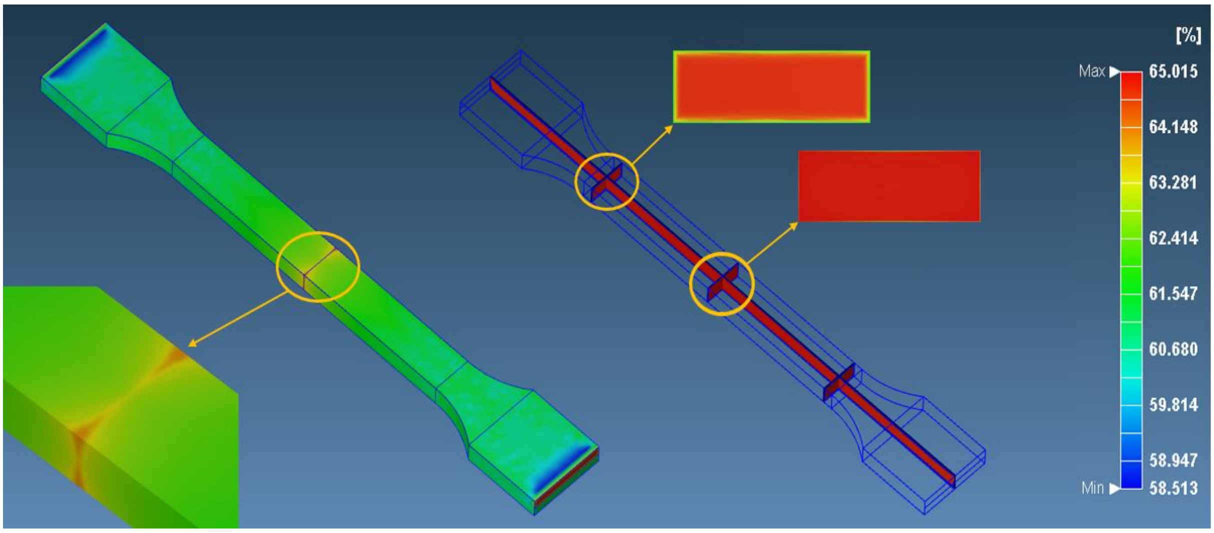

Figure 4.13: The magnitude of fibre concentration of the part simulated on Moldex3D with weld line.

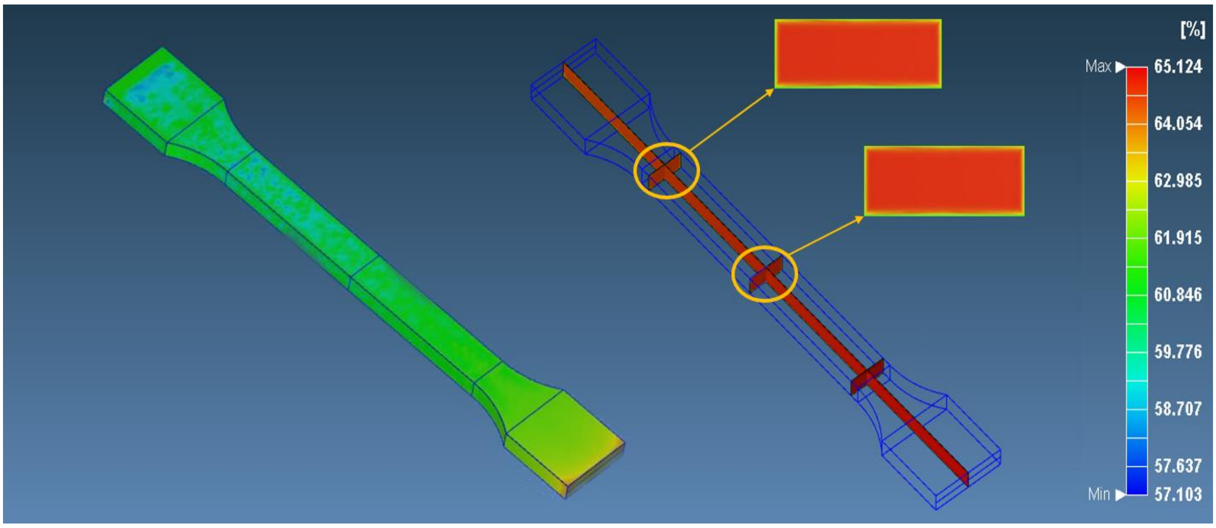

Figure 4.14: The magnitude of fibre concentration of the part simulated on Moldex3D without weld line.

4.9 Fibre orientation

The Moldex3D software is compatible with Folger Tucker and the iARD-RPR model to predict fibre orientation in an injection moulded part. The injection moulding simulation was conducted with an applied iARD-RPR model with three parameters (C_I, C_M, and α). Different parameters in the model can be optimised to increase the accuracy of predicting fibre orientation for any given material. For the simulation, the fibre-matrix interaction (C_M) was considered 0, but the fibre-fibre interaction (C_I) was set as 0,005. The diffusion tensor is directly proportional to the fibre-fibre interaction (C_I) and the unit tensor (I). The slow down factor or the dimensionless constant α for the simulation was 0,7. The Moldex3D simulation provides orientation corresponding to the flow direction, crossflow direction, and thickness direction. The orientation of fibres differs significantly with the formation of the weld line. In this thesis, the classic five-layers orientation distribution based on [114] is applied to make it simple to describe the distribution in the thickness direction. The five-layers structure is distributed in two skin layers, two shell layers, and one core layer between the skin and core regions in the specimen. Skin layers are located at the surface of the specimen, and the shell layers are the regions between the skin and core layer. Additionally, the sum of the fibre orientation value at each point is 1 since the fibre orientation is defined as a tensor. Figure 4.15 illustrates the five layers of structure components for fibre distribution through the thickness.

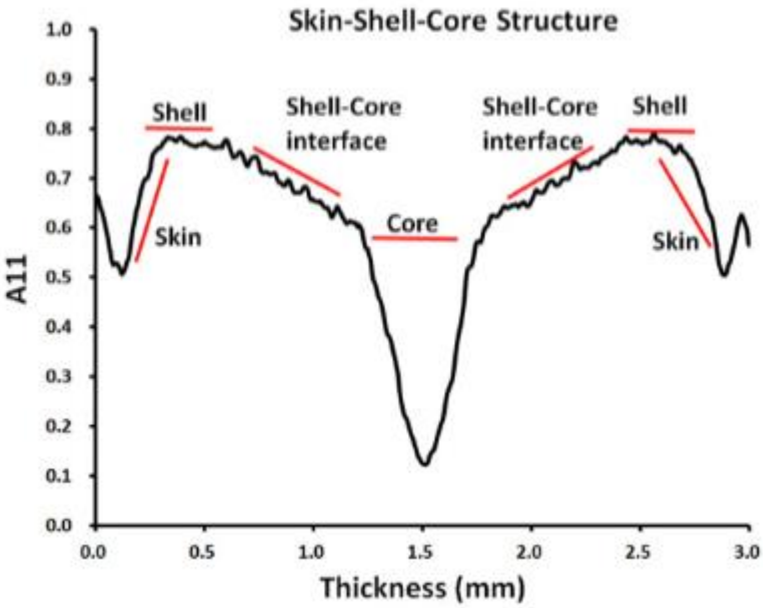

Figure 4.15: The flow orientation component A11 distribution according to the five layers structure [94].

4.9.1 Sensor node

The results from Moldex3D were extracted from 4 different sensor nodes, which are defined in Figure 4.16. The nodes along the thickness of the specimen are classified as group 1, group 2, group 3 and group 4. Group 1 and group 3 are placed 40 mm from the sensor group 2, which is located at the centre of the specimen. In addition, sensor group 4 extracts the results from the middle of the specimen. Sensor group 4 extracts the fibre orientation throughout the specimen at 20 mm from the centre in both directions along the flow direction. The flow direction in injection moulding simulation is considered in the x-direction. The accuracy of fibre orientation during the injection moulding simulation is significant in predicting the mechanical properties of the final moulded parts. Therefore, the predicted fibre orientation from Moldex3D was studied in this thesis. The fibre orientation distribution from the sensor nodes were imported to Excel, where the orientation distribution was illustrated graphically according to the direction.

The orientation results from the Moldex3D simulation are presented according to direction illustrated the figure 4.16. Here the A11 direction corresponds to flow direction, A22 to crossflow direction and A33 to thickness direction A high rate of tensor in the A11-direction indicates, that most fibres are oriented in the flow direction. A low tensor rate close to zero in the A33-direction indicates small or no orientation in the thickness direction. Usually, polymer materials are applied loading in the flow direction. Therefore, the orientation in the flow direction has a significant impact on the development of mechanical properties. Figure 4.16 shows the corresponding directions along with flow (A11), cross flow (A22), and thickness (A33) of the specimen.

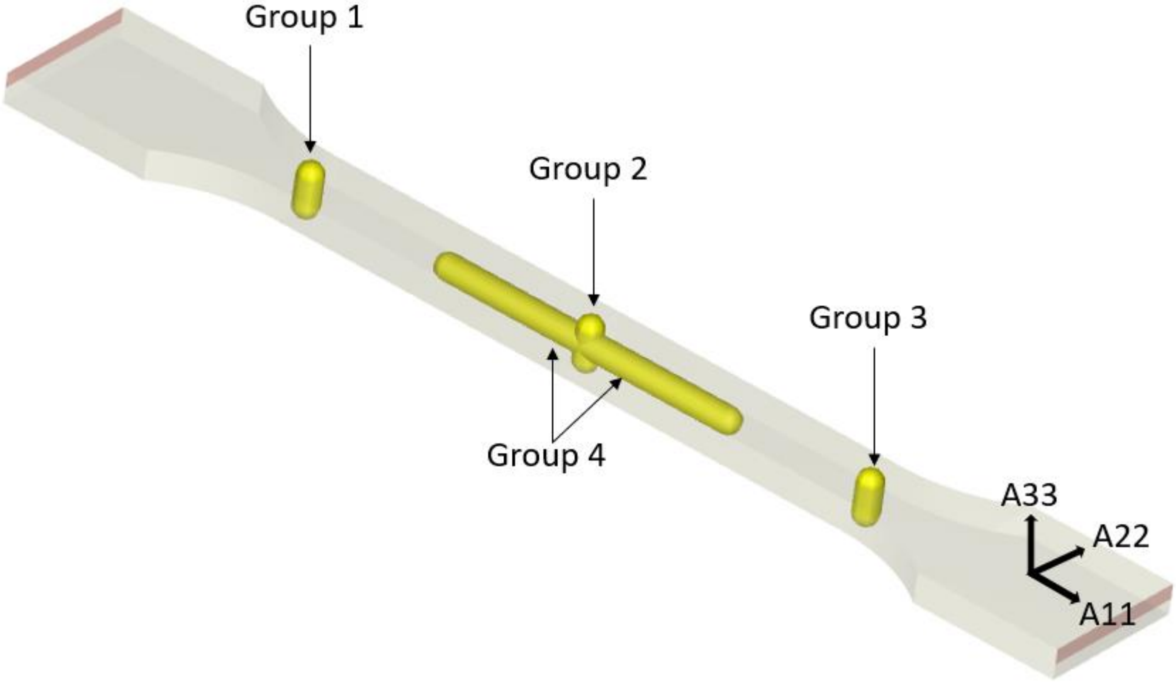

Figure 4.16: Different nodes described in the specimen to take results from the Moldex3D simulation.

4.9.2 Fibre orientation for simulation with weld line

During the production of polymer composite, the formation of a weld line is almost inevitable. As mentioned previously, weld lines are created when separate polymer flow fronts meet during manufacturing with injection moulding. Multiple flow fronts can appear due to multiple injection gates, which can be specified into two types of weld lines, Frontal and Flowing weld lines. During the Frontal weld line, the melt fronts meet and stagnate simultaneously in contrast to the flow through the mould in the Flowing weld line. The formation of a Frontal weld line in short fibre composites can reduce the mechanical properties up to 50 %. The fibre orientation at the weld line is orientated preferentially parallel to the weld line surface. During loading, the orientation of fibre reduces the fibre strengthening of composite material. Therefore, fibre orientation at weld line is studied in this thesis.

4.9.2.1 Fibre orientation at centre along the thickness direction

The Moldex3D simulation from the weld line shows that most of the fibres are orientated along the thickness direction. The results of predicted fibre orientation in the thickness direction of the specimen with weld line are provided in the Figure 4.17. The results from the injection moulding simulation indicate that the flow front collision results in high numbers of fibres being orientated along the thickness direction. At the skin of the specimen, fibres are orientated with a rate of 0,6 in the thickness direction (A33). And the results show that fibres in the flow direction (A11) and crossflow direction

(A22) are orientated with a rate of 0,11 and 0,29 respectively. However, fibre orientation in the skin layer increases drastically to a value of 0,8 towards the shell area in the flow direction. In contrast, the number of fibres orientated in the crossflow and thickness direction decreases at the skin layer to a value of 0,06 and 0,17, respectively. At the shell layer, the number of fibres orientated in the flow direction decreases and increases in the thickness and crossflow direction. At the same time, the number of fibres aligned in the flow, thickness and crossflow direction remains constant towards the specimen's core region.

4.9.2.2 Fibre orientation in thickness direction at a distance of 40 mm

The predicted fibre orientation at the length of the (x=40) from the centre of the specimen is presented in the Figure 4.18. The simulation results show that the orientation of fibres varies in small quantities throughout the thickness of the specimen. The injection moulding simulation predicts that most of the fibres are aligned in the flow direction at sensor group 1. At the skin layer, the number of fibres in the flow direction increases, whereas the fibres in the crossflow and thickness direction decrease. In the shell region, the fibres aligned in the flow direction increase to a maximum value of 0,87, while the quantity of fibres in the flow direction decreases to a minimum value of 0,8 at the core region. In addition, the number of fibres in the crossflow direction decreases throughout the thickness due to the fountain flow effect. However, the number of fibres aligned in the thickness direction increased to a value of 0,15 in the core region. In the core region, the number of fibres orientated in the thickness direction is higher than the orientation in the crossflow direction.

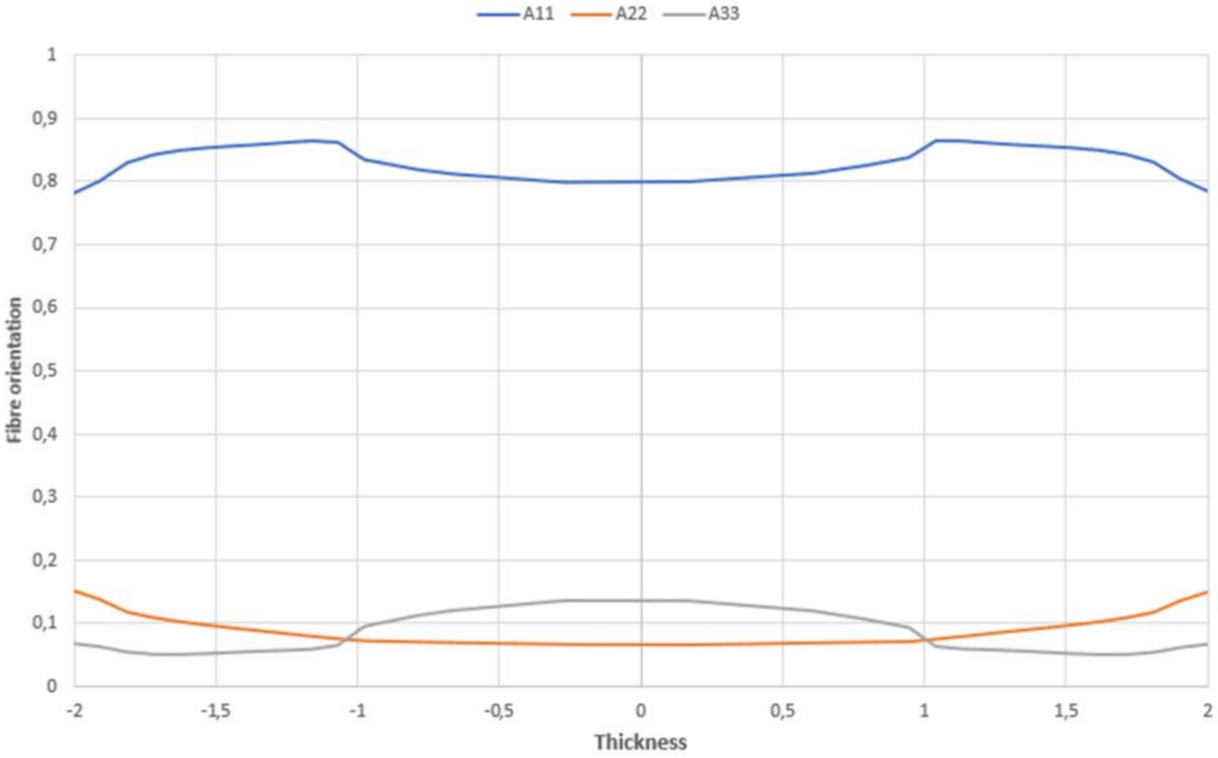

Figure 4.17: Fibre orientation distribution in every direction from Moldex3D simulation with weld line from a sensor node at 40 mm from the centre of the specimen.

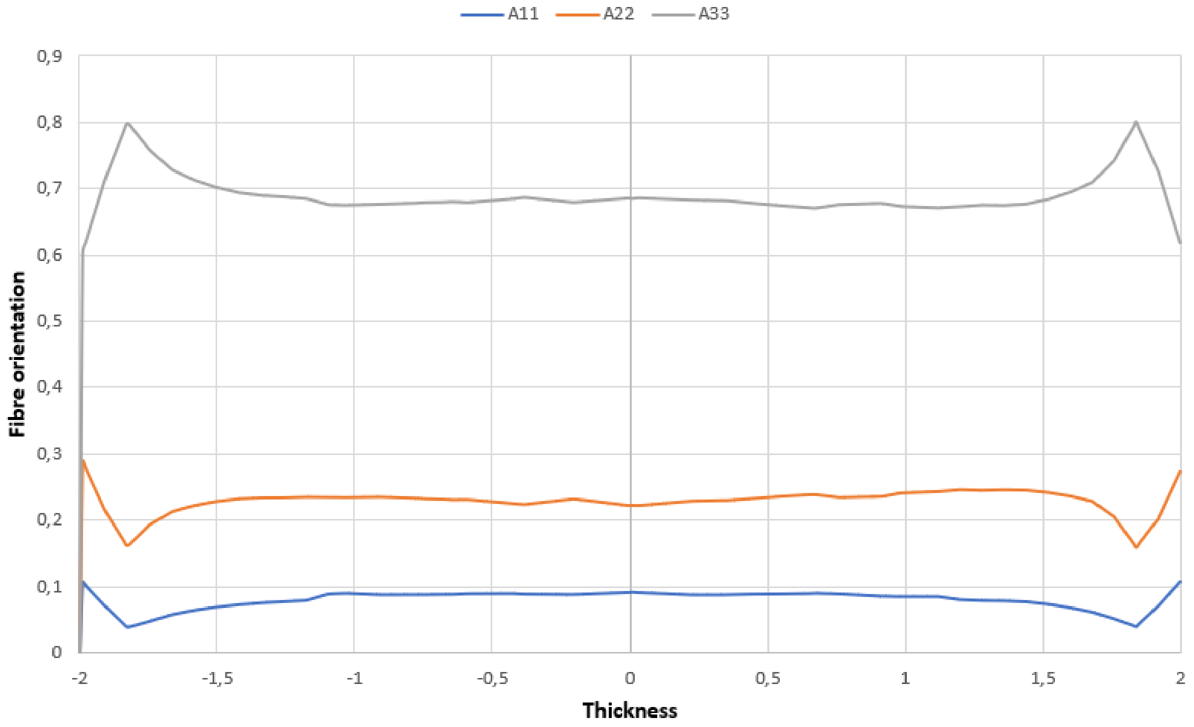

Figure 4.18: The predicted fibre orientation obtained from Moldex3D simulation with weld line along with the thickness at the centre of the specimen.

4.9.2.3 Fibre orientation along x-direction

The fibre orientation in the middle of the specimen along the x-direction is presented in the Figure 4.19. The amount of fibres orientated in the flow direction (A11) reduces steadily towards the centre from a max orientation value of 0,77. The quantity of fibres aligned in the flow direction gradually declines towards the centre of the specimen. In addition, the number of fibres in the flow direction decreases significantly from 5 mm to the centre of the specimen. At the centre of the specimen where the flow fronts meet, the least number of fibres are orientated in the flow direction (A11) to the value of 0,1. In contrast, the fibre alignment in the thickness and crossflow direction increases towards the centre of the specimen. The simulation results predict that fibres aligned in the thickness and crossflow direction increase towards the centre of the specimen. But the fibres aligned in the thickness direction increase significantly to the value of 0,68 at the centre of the specimen. However, the results show that the fibres are aligned more in the thickness direction than the crossflow near the area where the melt front meets. At the same time, the fibre orientation in the crossflow direction decreases to the value of 0,22 towards the centre where the melt front meets. The orientation in the flow direction decreases due to the fountain flow effect and collision of melt front during injection moulding

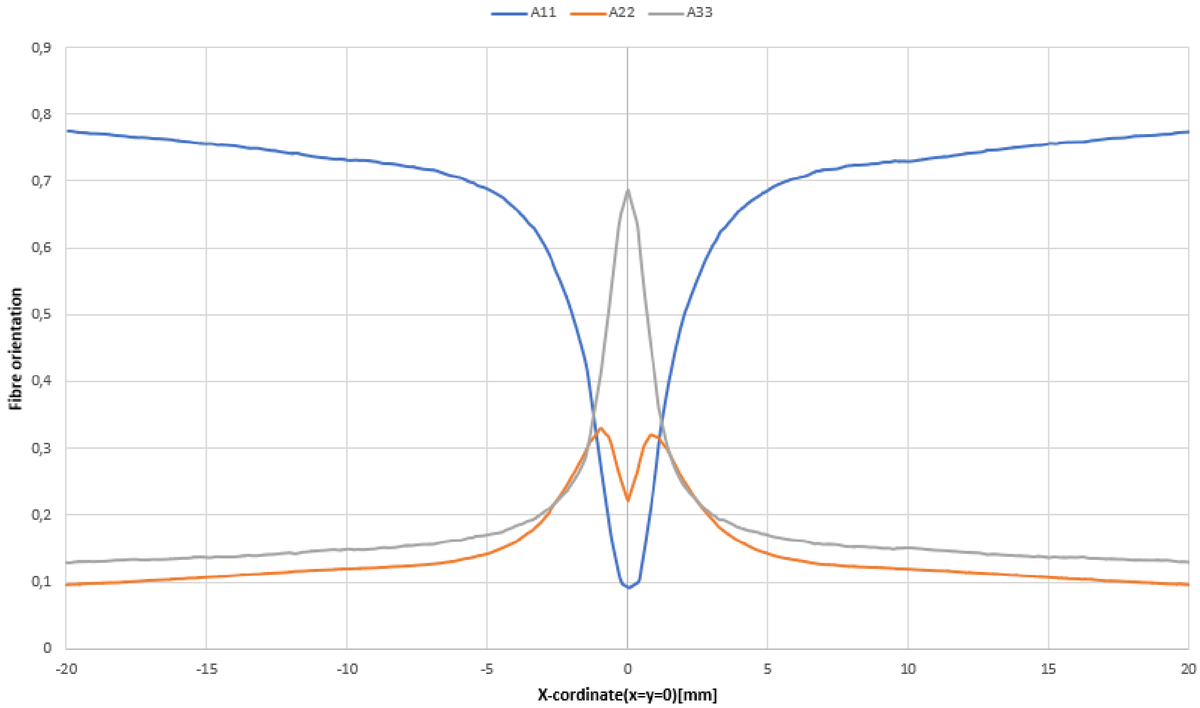

Figure 4.19: The predicted fibre alignment in every direction from Moldex3D simulation with weld line at the middle of thickness along the x-direction.

4.9.3 Fibre orientation for simulation without weld line

Weld lines in injection moulded parts form due to various circumstances and conditions such as low temperature and pressure. But usually, the weld lines in injected moulded parts are formed at the region where the melt fronts meet. To study the effect of the weld line, an injection moulding simulation without a weld line is conducted with a singular valve avoiding the melt front collision. As presented in the previous section, the melt flows from a single valve to avoid the melt front collision. The collision of melt fronts during injection moulding leads to the formation of a weld line in the final moulded parts. The results from the simulation with a single valve gate are presented in this section.

4.9.3.1 Fibre orientation at centre along the thickness

Along the z-direction in the centre of the specimen, the simulation results in Figure 4.20 show that most of the fibres are aligned in the flow direction. The number of fibres in the flow direction increases from a value of 0,78 at the skin of the specimen. In shell region, the fibre orientation in the flow direction increase to a maximum value of 0,85, whereas the number of fibres aligned in the flow direction decreases to a value of 0,8 at the core region. In addition, the fibres aligned in the thickness (A33) and crossflow (A22) directions reduce at the skin layer from a value of 0,05 and 0,16 respectively. The distribution of fibres orientation in the crossflow (A22) direction remains constant at a value of 0,8 in the shell and core region. However, the number of fibres aligned in the thickness direction increases gradually in the shell region. At the core region, the number of fibres orientated in the thickness direction rises to a maximum value of 0,052. The number of fibres orientated in the thickness direction is higher than the crossflow direction at the core region.

4.9.3.2 Fibre orientation in thickness direction at a distance of 40 mm

Figure 4.21 shows the fibre orientation distribution along with the thickness of the specimen without a weld line. The results at the length of the (x=40) from the centre are identical to previous results from simulation with weld line. Throughout the thickness of the specimen, most fibres are aligned in the flow direction according to the injection moulding simulation in Moldex3D. The number of fibres in the flow direction increases at the skin layer from a value of 0,8. The quantity of fibres in the crossflow and thickness direction decreases from a value of 0,15 and 0,05, respectively. And at the shell region, the fibres aligned in the flow direction increase to a maximum value of 0,87. While the fibres distribution in the crossflow direction decreases throughout the skin, shell, and core region. The fibres in the thickness direction remain constant at a value of 0,05 in the skin and shell region. At the skin and the shell region, the quantity of fibres orientated in the crossflow direction is higher compared to the thickness direction. However, the fibre distribution increases to a maximum value of 0,12 at the core region. At the core region, the quantity of fibres orientated in the thickness direction is higher than the distribution in the crossflow direction.

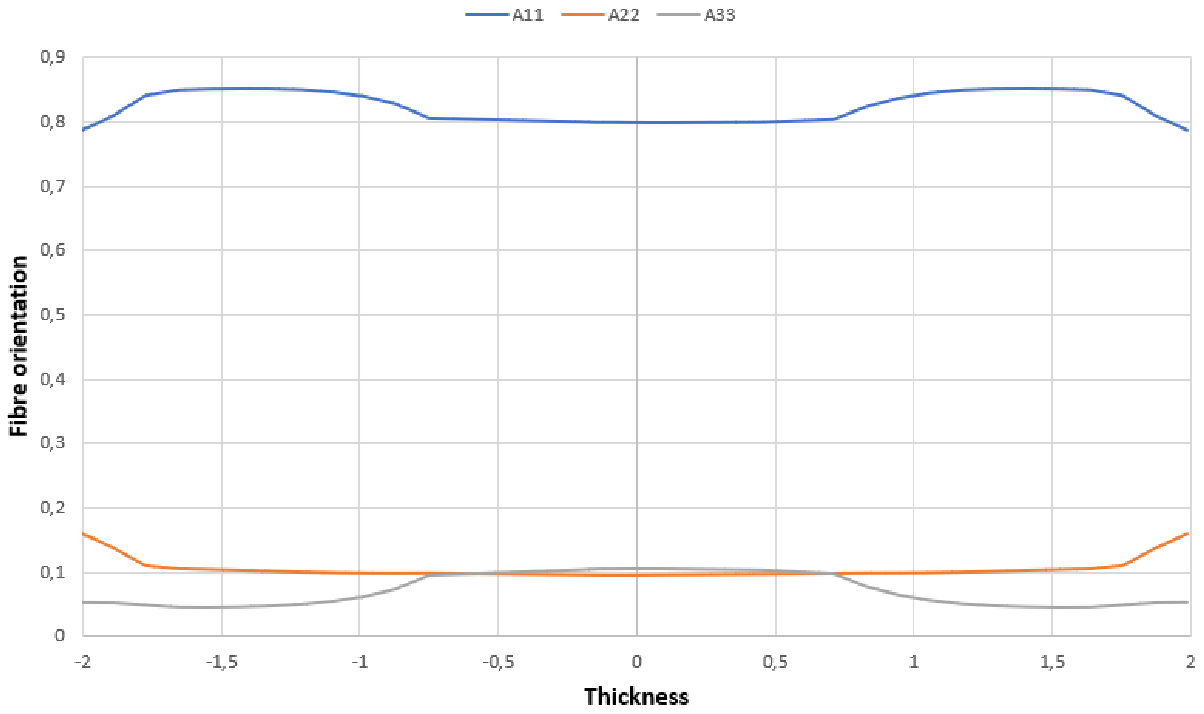

Figure 4.20: Fibre orientation distribution in every direction from Moldex3D simulation with weld line along the z-direction in the centre of the specimen.

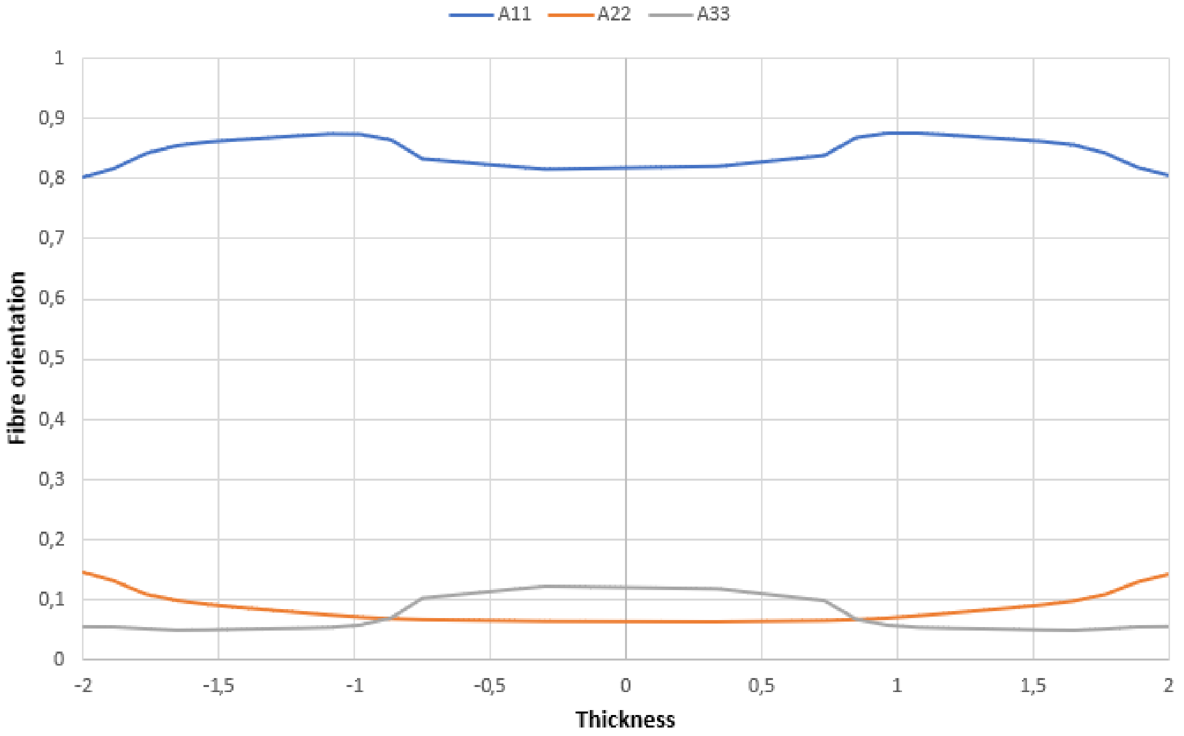

Figure 4.21: Fibre orientation distribution in every direction from Moldex3D simulation without weld line along the thickness.

4.9.3.3 Fibres orientation along the x-direction

The fibre orientation results for the simulation without the weld line along the x-direction from the centre of the specimen are illustrated in the Figure 4.22. The results show that the fibre orientation distribution is constant along the x-direction. The simulation predicts most fibres are orientated in the flow directions (A11) along the x-direction. At -20 mm, the prediction from the simulation shows that the orientation value in the flow direction is at 0,79. The corresponding orientation value in the thickness and crossflow direction is 0,10 and 0,11, respectively. The number of fibre orientations in the flow direction increases slightly to a value of 0,81 at 20 mm from the centre. However, the fibre orientation in the thickness direction rises to 0,11, the orientation value in the crossflow direction declines slightly to a value of 0,081 from 0,11. The fibre orientation distribution obtained from the simulation without a weld line is distinct from the simulation with the weld line. It can be observed that the melt front collision during injection moulding reduces orientation in the flow region where a weld line forms.

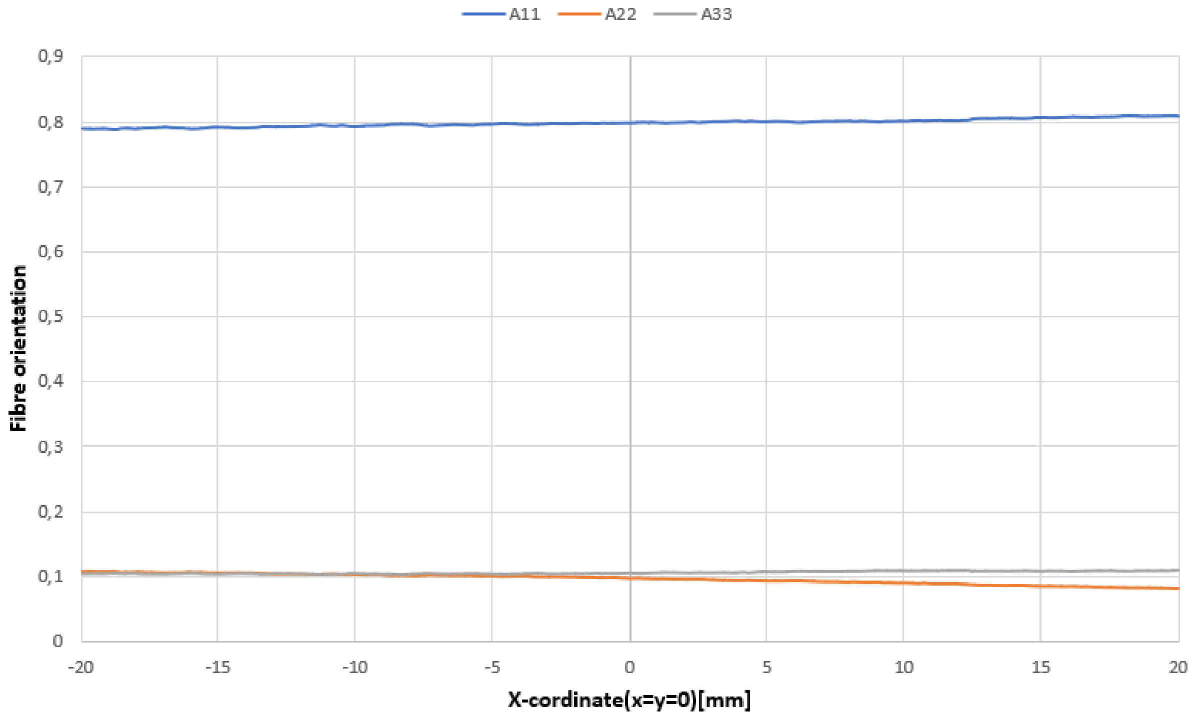

Figure 4.22: Fibre orientation distribution in every direction from Moldex3D simulation with weld line from sensor nodes along x-direction from the centre of the specimen.

4.10 Parametric study of fibre interaction coefficient

In order to manufacture high-quality products more efficiently, using software tools to assist product development has become a standard practice in today's product design and manufacturing world. Identifying the optimal parameters quickly to run a productive analysis and shorten the overall simulation time is the key to improving efficiency. In this project, parametric analysis is carried out to study the effects of melt temperature, aspect ratio, fibre-fibre interaction, and fibre-matrix interaction (within the range of input) to find their influence on the prediction of fibre orientation in plastic injection moulded components using Moldex3D. Generally, the final orientation in the x-direction or flow direction significantly affects the injection moulded part's local mechanical and physical properties. Most of the fibre orientation in injection moulded parts are aligned in the flow direction, which develops stronger and stiffer properties in the direction with most fibres oriented. Therefore, in this section, how the parameters of the mathematical fibre alignment model influence the orientation of fibre in the x-direction is studied.

In this analysis, a data set is generated by the varying value of one input parameter within the input range and keeping other parameters constant, as shown in Table 4.1. In this parametric study, the importance of melt temperature, aspect ratio, C_i, C_m and α are tested. The simulation results can then be verified with a preliminary experiment conducted by other researchers. The best possible applied parameters can be evaluated by comparing the simulation results. With the help of this parametric study, it is possible to optimise the processing conditions and investigate the accuracy of these fibre orientation models. Additionally, the outcomes of this parametric study can be applied as a guideline and recommendations to the mould designers for their future injection mould designs.

Tabell 4.1:Presents the different parameters and fibre orientation models used during the parametric study.

Simulation test group	**Fill - time**	**Closure**	**Fibre orientation - model**	**Aspect ratio**	**Fibre-fibre interaction (C_i)**	**Fibre-matrix interaction (C_m)**	**Alpha**
1	0.4	IBOF	Folgar-Tucker	20	0.01 0.005 0.0007	0	0
2	0.4	IBOF	iARD	20	0.005	0	0.0 0.7 0.9
3	0.4	IBOF	iARD	20	0.005	0.0 0.6 0.9	0.7
4	0.4	IBOF	iARD	20 40 80	0.005	0	0.7

4.10.1 Folgar-Tucker model

It is imperative to adjust parameters to obtain an accurate orientation prediction. The fibre orientation in the different regions of a part depends on the parameters C_I and C_M; the regions are also controlled by the RPR parameter (α). The standard Folgar–Tucker equation has only the fibre–fibre interaction parameter, and the fibre-matrix interaction parameter is neglected. The fibre-fibre interaction contains the factors determining the rate and strength of the interaction between two fibres. Folger and Trucker assumed that the interaction between two fibres occurs when the centre of one fibre passes the fibre length of another fibre. The assumption is that the occurrence of the fibre-fibre interaction is proportional to the strain rate [94].

In this parametric study, various values of C_I were used to predict fibre orientation. The Figure 4.23 displays the flow-direction (x-axis) orientation tensor component A11 along the longitudinal direction of the part. Figure 4.23 presents the flow-direction orientation at different values of parameter C_I = 0.01, 0.0007 and 0.005. The representation of the fibre orientation over the specimen cross-section shows that the parameters significantly influence the fibre orientation. When C_I is set to 0.001 results in a lower degree of fibre orientation in the range -5 – (-20) mm and 5-20 mm and broader in the centre region. When parameter C_I is decreased from 0.001 to 0.005, the centre width is narrow, and the height of regions found in the range -5 – (-20) mm and 5-20 mm is seen to increase. Additionally, when C_I is set to 0.0007, the graph clearly shows that the centre region gets narrower while the rest of the regions get a higher degree. This means that more fibres are oriented approximately in the flow direction in the range -5 – (-20) mm and 5-20 mm when C_I is set to 0.0007.

Based on a general observation, the fibres in the region -20-(-5) mm and 5-20 mm are more aligned with the flow direction, whereas the region in the centre was quite wide. Additionally, it can be observed that the fibre orientation is at its lowest degree near the weld line of the part. Therefore, to find out whether the Folgar–Tucker model provides a satisfactory result, the results need to be compared with experimental data. At this point, it must be pointed out that it cannot be excluded that the changed process parameters cause the differences in fibre orientation. Based on the results, it can be assumed that the variation of the process parameters influences the regions in the range -5 – (-20) mm and 5-20 mm significantly, while the regions very close to the centre where the flow front merges can be considered very similar in all cases.

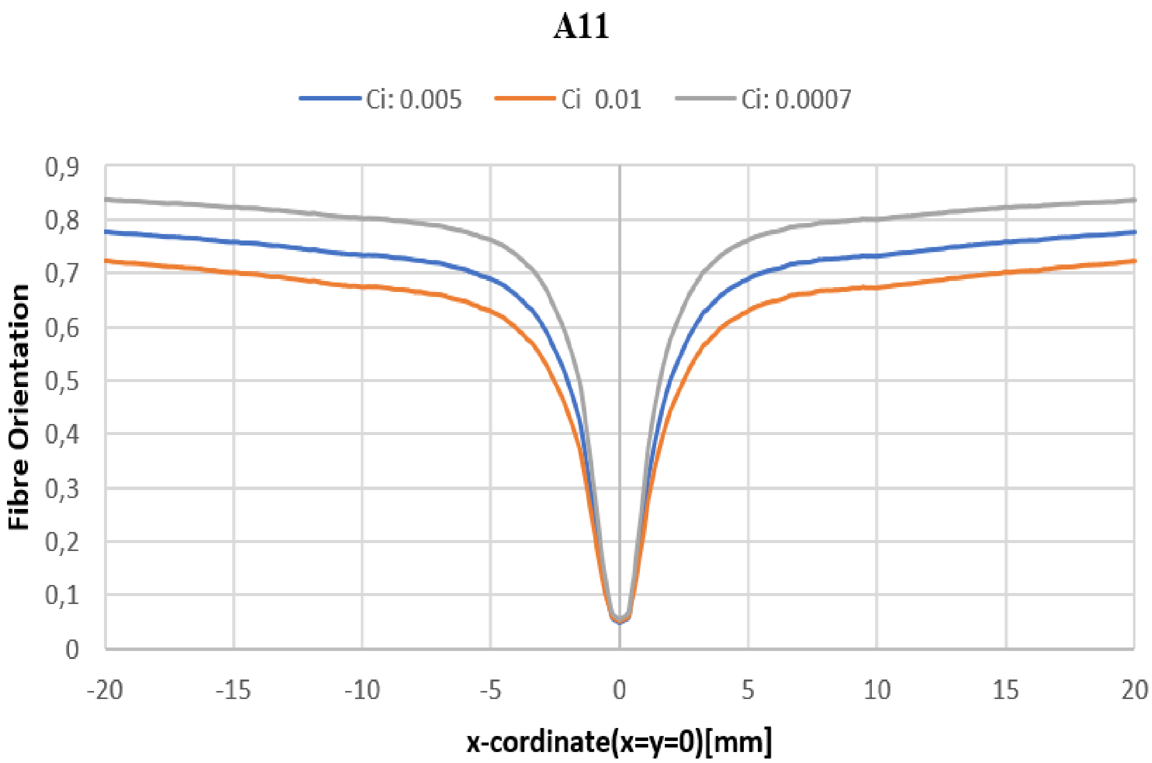

Figure 4.23: Using the Folgar–Tucker model to obtain the fibre orientation distribution of flow orientation component A11 through the longitudinal part for various Ci Values.

4.10.2 iARD-RPR model

The accuracy of the flow-induced fibre orientation determines the prediction of structural properties. The fibre orientation model is based on Jeffery's equation 3.107 as presented in chapter three "Literature review" under "theoretical mathematical model". As mentioned in the previous chapter, the standard fibre orientation model is derived from the motion of a single ellipsoidal inclusion in an infinite Newtonian matrix. Furthermore, the fibre orientation model has been improved by incorporating an isotropic rotary diffusion term to account for fibre-fibre interaction by Tucker and associates. Based on their work Tseng developed the iARD-RPR model, which contains three physical parameters: a slowdown factor, fibre to fibre and fibre to matrix interaction. The iARD-RPR mathematical model uses an interaction coefficient between fibre-fibre and fibre, which actions are determined empirically to determine the fibre orientation. During the application of the iARD-RPR model in Moldex3D, these parameters could be adjusted to obtain acceptable results.

The Brownian motion, which describes the random and uncontrolled movement of particles caused by molecules of a dilute suspension. However, the Brownian motion is not solely responsible for the orientation of fibres. Interaction between fibres reorients and gives random final orientation in a dilute suspension. The fibre-fibre interaction depicts the diffusivity in rotary Brownian motion dependent on the strain rate. According to (Tseng et al., 2013), the fibre-fibre interaction has a value between (0-0,1). Therefore, three simulations with fibre-fibre interaction with 0,01, 0,005 and 0,0007 are conducted to study the effect of C_I. The simulation results with different fibre-fibre interaction coefficients shows that most of the fibres are orientated along the flow direction away from the centre of the specimen. The number of fibres oriented in the flow direction decreases toward the centre. The phenomenon is expected as the melt fronts collision reduces the orientation in the flow direction. However, the quantity of fibre orientated along the flow direction varies with the fibre-fibre interaction coefficient. The results from the simulation show that when C_I has a value of 0,01, fibres are orientated less in the flow direction compared to $C_I = \ 005$ and $C_I = \ 0{,}07$. This study shows that the orientation in the flow direction increases when the value of fibre-fibre interaction is reduced. In addition, the fall of orientation distribution in flow direction where flow fronts meet decreases when the value of coefficient increases. Therefore, the width of the weld line region increases with the fibre-fibre interaction coefficient. However, the number of fibres oriented in the flow direction is identical to where the flow front meets.

The second coefficient in the iARD-RPR model examined is the interaction between fibres and matrix. The orientation of fibres in a diluted suspension or matrix is also influenced by the flow kinematic of the matrix. Generally, the fibre-matrix coefficient lies between 0 and 1, according to (Tseng et al., 2013). The effect of the fibre-matrix coefficient in the iARD-RPR model for orientation in the flow direction is presented in the Figure 4.24 from the Moldex3D simulation. The figure shows the fibre orientation in flow direction with fibre-matrix coefficients at 0, 0,6, and 0,9. The quantity of fibres orientated along the flow direction deforms with the fibre-matrix interaction coefficient away from the region where the flow front collides. The quantity of fibre orientation increases when the fibre-matrix coefficient is gradually increased. But at the collision region, the quantity of fibres oriented in the flow direction is identical with different fibre-matrix coefficients. In addition, the fall in orientation at the collision region is identical, which gives distinct slopes of reduction rate. It can be concluded that the parameter C_m influences the fibre orientation distribution away from the collision region while the effect is insignificant at the collision region.

In addition, the RPR model, which slows down the transient orientation rate distribution, is added to the iARD model. The parameter alpha in the RPR model can slow down the rate of fibre orientation development during the flow. The available value for the RPR parameter is suggested as less than 1 and higher than 0. Therefore, a value of 0, 0,7 and 0,9 was preferred for injection moulding simulation in Moldex3D. Figure 4.25 shows the effect of the different RPR parameters during the injection moulding simulation as the figure illustrates that the slow down factor is related to the amount of fibre orientation in the flow direction at the collision region. The simulation with a slowdown factor of 0 has the lowest number of fibres aligned in the flow direction at the collision region. The simulation with a slowdown factor of 0,9 has the most fibres orientated in the flow direction. The simulation results show that the number of fibre orientations decreases when the slow down factor is higher. However, the fibre orientation distribution away from the collision region is identical with different slowdown factors.

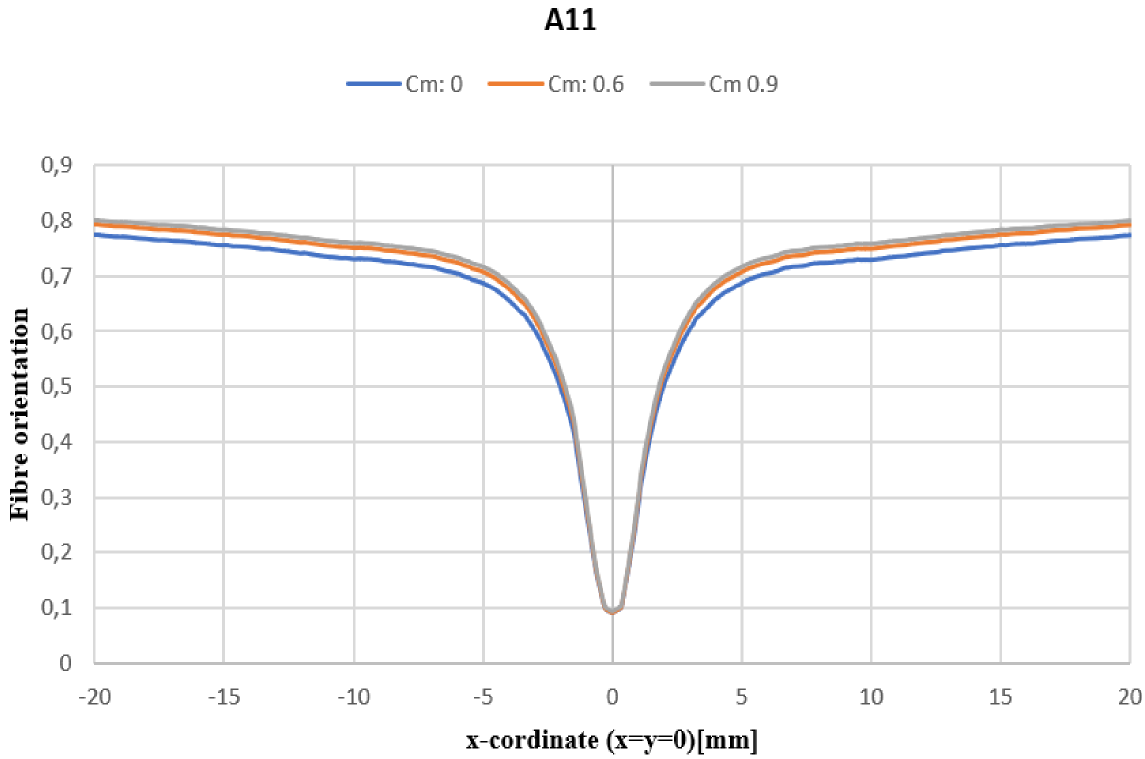

Figure 4.24: The fibre orientation distribution of flow orientation component A11 along the x-direction for simulation with different fibre-matrix interaction coefficient values.

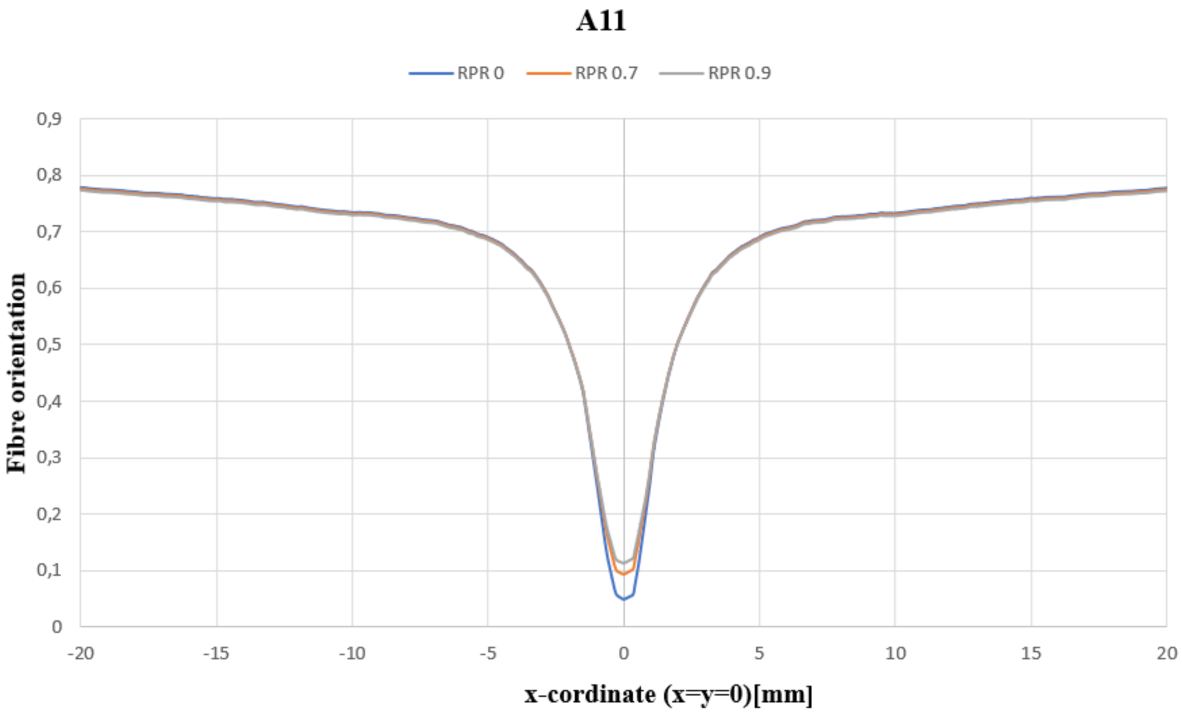

Figure 4.25: The fibre orientation distribution of flow orientation component A11 through the longitudinal direction with slow down factor of 0, 0.7, and 0.9.

4.10.3 Aspect ratio

Reinforcing fibres and the matrix are two major discontinuous components in fibre reinforced composite. As previously mentioned, fibre-reinforced composite materials are produced by embedding fibres in a surrounding matrix. Generally, the fibres are brittle with high strength, which reinforces the surrounding matrix with an elastic property. The fibres in the composite materials are classified based on the aspect ratio (defined as a ratio of the length of a single fibre to its diameter). In general, the aspect ratio and shape of the reinforcing fibres have a huge impact on the development of the mechanical properties of the composite. In addition, the aspect ratio of fibre influences the viscosity of polymer melt during injection moulding. The viscosity of polymer melt determines the distribution of fibre orientation which again influences the strength of the final moulded part. Therefore, simulations with aspect ratios of 5, 40 and 80 were conducted to study the influence of aspect ratios on fibre orientation.

Figure 4.26 shows simulated fibre orientation distributions with different aspect ratios through the longitudinal direction. The important orientation descriptors are the orientation tensor components. A11 is the flow direction along the x-axis. The graph clearly shows the influence of the various aspect ratio on the results of the simulated fibre orientation. The representation of the fibre orientation of the specimen shows that the curves are very similar for the aspect ratios 20 and 80. When the aspect ratio is set to 5 results in a lower degree of fibre orientation in the range -5 – (-20) mm and 5-20 mm and broader in the centre region where the flow melt merges. The graph indicates that the higher aspect ratio gives a higher degree of fibre orientation. This means that more fibres are oriented approximately in the flow direction when the aspect ratio increases. However, when the aspect ratio is set to 20, and 80, there are no differences in fibre orientations, and the curves are the same in all cases. The graph illustrates that fewer fibres are oriented in the flow direction at the regions close to the centre where the flow front merges.

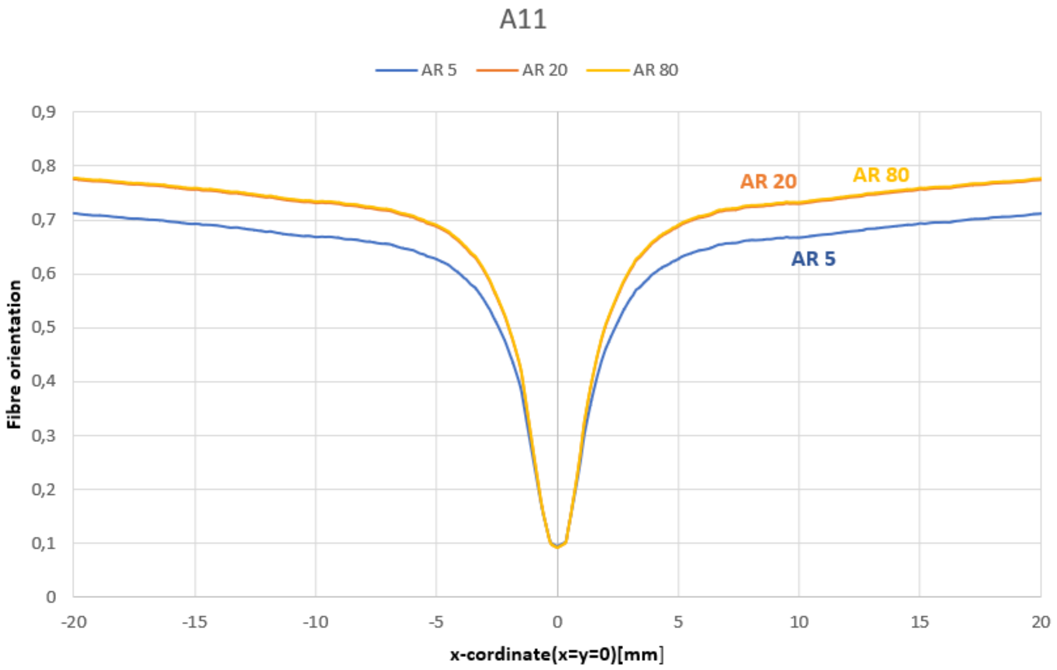

Figure 4.26: The fibre orientation distribution of flow orientation component A11 through the longitudinal direction with aspect ratio of 5, 20, and 80.

5 Finite element modelling in ABAQUS

In recent years application of finite element analysis of injection-moulded plastic parts has become more relevant. The finite element method (FEM) is widely applied to solve linear and nonlinear transient problems and applies a numerical solution to solve various engineering problems from biomedical to civil engineering. A field problem requires the user to determine the spatial distribution of one or more dependent variables. Mathematically, a field problem can be illustrated as partial differential equations that use the weighted residual or integral expression [115]. The concept of the FEM is to discretise the spatial domain into simple geometric elements during application. Generally, geometric elements such as triangles and quadrilaterals are applied regarding the scope of the problem. At each finite element domain, the weighted residual concept is applied to calculate the approximate solution of function. The solution is calculated for each element by transforming the partial differential equation into sets of ordinary differential equations in time [116].

The partial differential equations are solved by using computational software. There are various commercial suppliers of FEM software widely available for industrial applications. Different commercial software packages differ from each other according to the terms of their features. This thesis uses ABAQUS developed by Dassault Systemes SIMULIA as finite element software to analyse injection-moulded plastic parts [117]. Originally ABAQUS was released in 1978; however newer version with different features has been updated every year. The ABAQUS product provides options for scripting and customization simulation using the open-source scripting language Python. ABAQUS/CAE uses the fox-toolkit for Graphical User Interface development. Today ABAQUS is applied in various engineering applications, which provides high performance and accurate solutions for challenging linear and nonlinear problems. In addition, ABAQUS provides a robust solution for large-scale linear dynamics applications and contact simulation. The simulation can be conducted with two distinct solvers provided by ABAQUS for structural analysis problems: Standard and Explicit solvers. The application of solvers is determined according to the type of analysis. Generally, a Standard solver is used to find the natural frequency, mode shape and simple static analysis, while the Explicit solver is applied in Coupled Eulerian-Lagrangian (CEL) analysis.

Moldex3D FEA Interface modules provide a bridge between injection moulding CAE and ABAQUS. After injection moulding simulation in Moldex3D is conducted, Moldex3D data can be translated to ABAQUS. The exported data could include the original mesh and material properties. The exported material properties are material stiffness, thermal expansion coefficient, density, etc. In this study, a simulation of the injection moulding process for a dog-bone specimen is performed, and the model was exported to ABAQUS. In ABAQUS, the dog-bone specimen was analysed based on the exported Moldex3D data such as material stiffness, thermal expansion coefficient and density.

5.1 Homogenisation approach

The discontinuous fibre-reinforced composite consists of short fibres embedded inside an elastic medium referred to as a matrix. The individual components of composite have significantly different mechanical and chemical properties. Generally, fibres have much greater strength compared to the matrix, but fibres are brittle whereas the matrix has a greater elastic property. The combination of individual properties of fibres and matrix gives discontinuous fibre-reinforced composite material superior mechanical properties. In addition, the distribution of fibre orientation in the matrix also significantly influences the development of properties in the final product. Moldex3D simulation shows that the fibre orientation varies throughout the parts of the injection-moulded short-fibre composite. The orientation is distributed according to the flow condition during injection moulding, which significantly influences the development of mechanical properties. Therefore, the homogenisation method is required to bridge the length scales to describe the anisotropic properties of fibre-reinforced composite material. The homogenisation method calculates the effective properties considering the response of the microstructure.

The method of homogenisation with micromechanics of materials is vital to analysing the properties of inhomogeneous materials such as composite materials. Micromechanics can be defined as a process of bridging the meso or micro scale to a larger scale where the behaviour on a smaller scale is applied to upscale the effective material properties of heterogeneous material. The purpose of homogenisation is to define an equivalent homogenous media which can replace the composite medium with homogeneous material. In general, in heterogeneous material homogenisation according to micromechanics of material analyse the material is at the level of the individual constituent. This will solve the problem of inhomogeneous characterisation of composite material by applying a global approach. During the homogenisation of heterogeneous material, the microstructure of the material is related to the overall response of the material through a representative volume element. Today there are various alternative methods to homogenise composite material based on the analytical and computational methods. Predominantly, computational homogenisation is getting traction in recent years due to the accessibility of higher computational power.

The most common computational homogenisation approaches are the asymptotic homogenisation method, volume average homogenisation and the reaction force approach. The asymptotic homogenisation approach is efficient to model physical phenomena on media with periodic microstructure. In addition, the asymptotic homogenisation technique applies to studying the mechanical behaviour of structural components built with composite materials. The major advantage of the asymptotic method is the reduction of several degrees of freedom. Additionally, it can discover the stress and strain microstructural fields associated with a given macrostructural equilibrium state [118]. The volume average homogenisation obtains the overall homogenised properties of a heterogeneous material by calculating the volume average properties of the medium. The volume average method is based on the stress and strain field on the representative volume. The homogenisation process with volume average requires information for the micro-scale which can be calculated through the finite element analysis. While the reaction force approach applies the notion of classical terms of mechanical stress which is the division of applied force with the cross-section area.

However, in the early years when the computational method was not widely available the homogenisation method was mainly based on analytical approaches. Eshelby's inclusion presented in the literature review chapter is one example of the analytical homogenisation method. The analytical method is based on two steps. According to [119], the first step includes the approximation of a local problem with single inclusion embedded in an infinite elastic medium. And the second step requires the response of the single inclusion to be averaged throughout the local field. The analytical method is still a widely preferred method to homogenise short fibre composite material. However, analytical methods cannot provide accurate results. Homogenisation based on micromechanics considers the microstructure of composite material on the micro-level to a material point on the macro level. An analytical method based on the Rule of the mixture, Mori-Tanaka and Halpin-Tsai are presented in the literature review chapter. As previously mentioned, the main disadvantage of applying the analytical method is the assumption of the material property of elastic medium and inclusion distribution. The injection moulding software Moldex3D provides an analytical method for the homogenisation of moulded parts with an FEA interface. The procedure for homogenisation with the FEA interface is presented later in the study.

5.1.1 FEA interface in Moldex3D

The Finite Element Interface module is available in Moldex3D, which integrates the injection moulding CAE with finite element method software for structural analysis. The FEA interface in Moldex3D can reduce the anisotropy scale by homogenising similar anisotropic properties. The homogenisation of the injection moulded part improves overall computational efficiency. The FEA interface allows the data output such as residual stress, temperature distribution, pressure distribution and fibre orientation results to structural analysis software. Moldex3D output data can be interpreted to software such as ABAQUS, Ansys, MSC Nastran, NASTRAN, LS-Dyna, MSC Marc, NX Nastran, OptiStruct, etc. The Moldex3D simulation data can be exported with the original mesh, warpage mesh and material properties. According to the Moldex3D user manual, the original mesh describes the geometry before the moulding process, and the warpage mesh describes the geometry of the moulded part. In addition, the interface module allows the users to choose the element type and type of mesh associated with the output data.

Homogenisation of composite is required to transfer the injection moulding results to structural analysis software. The FEA interface applies a homogenisation approach based on the analytical method. The homogenisation approach is based on the micromechanics model developed by Mori-Tanaka and Halpin-Tsai is available in the FEA interface. Predominantly, the homogenisation approach selected for this study is based on the Mori-Tanaka. However, a comparative study is also conducted between Mori-Tanaka and Halpin-Tsai micromechanics model. The FEA function option in the micromechanics interface allows the user to export weld line output, fibre length output, and fibre concentration output from the simulation. In addition, Moldex3D FEA Interface allows the strength to be transferred into the structural analysis software. The function options weld line according to the angle range in the FEA interface considers the reduction of mechanical strength from weld lines. In this study, the weld line with max weld line angle (0-135), fibre concentration output, fibre length and fibre orientation output were included for the FEA analysis. The weld line output based on angle range was ignored for the analysis in ABAQUS.

The original mesh provided by Moldex3D for flow simulation, which is based on tetrahedral geometry, is not ideal for FE analysis. Therefore, the mapped option provided by the FEA interface is selected as the output mesh for the FEA analysis. Moldex3D FEA also supports fibre orientation of 3D mesh results that can be mapped to 2D shell mesh. The mesh with hexahedral elements is considered suitable for the finite element method regarding the geometry of the specimen. The selection of mesh type for analysis in ABAQUS will be presented in detail in the study later. The mesh with hex elements is defined in ABAQUS prior to map the output result from an original tetrahedral mesh. In this way the preferred mesh of hex element will be used for structural analysis. The material output data is transferred from the elements in Moldex3D to elements in mapped file. Therefore, the geometry for Moldex3D simulation and input mesh file needs to have the same spatial coordinates to transfer the output data correctly. The meshed file was uploaded in the FEA interface as input file format from ABAQUS.

The homogenisation with the micromechanical model is based on the micromechanical model provided in the FEA interface. The number of material cards can be controlled by selecting the appropriate reduction level. FEA interface in Moldex3D provides different levels of material reduction, a medium level reduction for material reduction of fibre orientation is considered in this thesis. The material reduction of fibre orientation at a medium level reduction has generated more than 5600 material cards for structural simulation in ABAQUS. The material properties such as elastic constants, thermal expansion coefficient, and density are exported at each material card. The FEA interface provided 21 independent constants at each material card. According to the constitutive law of linear elasticity, the fourth-order elasticity tensor has 81 material constants. However, due the symmetry the constants are reduced to 21. In addition, the homogenisation with FEA interface in

Moldex3D provides same density with uniform distribution at each material cards. And 6-expansion coefficient is also provided by the FEA interface as material properties in each material card.

5.1.2 Mesh

The Finite Element Analysis software solves the Partial Differential Equations (PDEs) for engineering applications. Real-world objects have infinite degrees of freedom, but mesh discretizes the domain into a finite number of elements to simplify the calculation. Meshing is one of the vital concepts to obtain accurate results during the FE simulations. The mesh used for FEA analysis of the mapped specimen is shown in the Figure 5.1. The finite element mesh consists of hexahedral geometry with C3D8R elements of dimensions 1 mm × 1 mm throughout the geometry. These dimensions of the mesh generated 8236 elements distributed uniformly throughout the geometry for FEA analysis. Generally, the mesh with hexahedral elements produces better and more accurate results during FEA analysis compared to other elements. In addition, hexahedral elements are also preferred for simulation with simple geometry. The C3D8R elements uses reduced integration with linear elements to use fewer integration points in each direction than the fully integrated elements. The linear element used by C3D8R elements has a single integration point which lies at the centroid of the element.

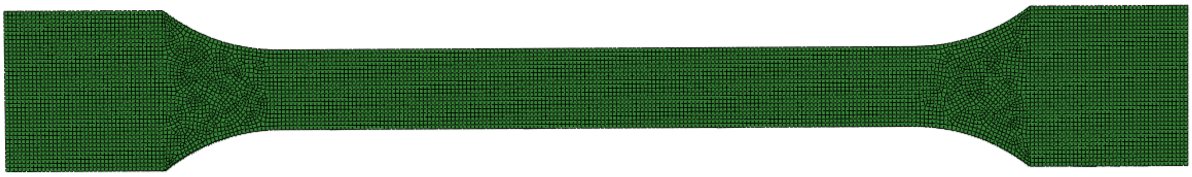

Figure 5.1: Mesh tensile specimen with hexahedral geometry with C3D8R elements applied for the simulation of injection moulded part in ABAQUS.

5.1.3 Boundary condition

It is important to define reasonable boundary and force application conditions because they can significantly affect the results. The specimen is fully fixed on one side in this analysis, preventing rotations and translations in all directions. On the other side, a longitudinal displacement is applied as shown in the Figure 5.2. The displacement changes incrementally while the reaction force results from the stiffness of the structure.

When a force is used instead of displacement during a simulation, the model can easily become unstable when the ultimate load is suddenly reached. Therefore, in this simulation, a displacement of 10 mm is applied to the other side of the specimen in the longitudinal direction. When assigning the displacement boundary condition, it’s also necessary to define at which amplitude the displacement is applied. In this analysis, all the displacement is applied in a ramp format. An extensometer measures the distance at the specimen centre. An extensometer's gauge length is the distance between the extensometer's initial measuring points on the test specimen. Based on the extensometer, two sets were created in the model to extract the total elongation ΔL utilised to calculate the strain. To find the total reaction force acting on the upper body of the specimen, the body was coupled to a point during the model setup stage in the interaction module. After the analysis, the reaction force was checked at this node, giving the total reaction force.

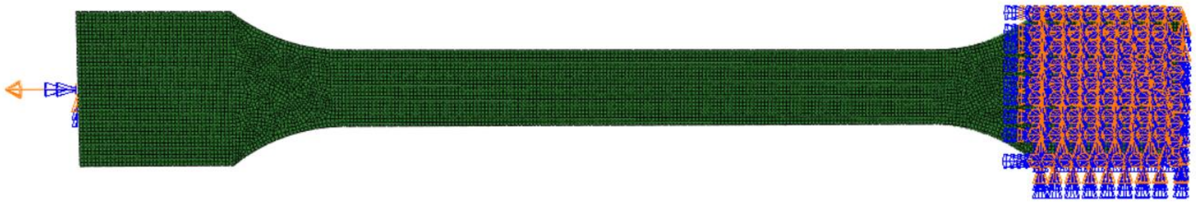

Figure 5.2: Boundary condition and applied displacement for the simulation of injection moulded part in ABAQUS.

5.2 Linear elastic analysis and strength calculation

The general theory of elasticity is a simplification of the more general (nonlinear) theory of elasticity. Generally, linear elasticity requires only two material parameters determined empirically: Young's modulus (E) and Poisson's ratio (v). Young's modulus for injection moulded parts can be is determined from the uniaxial tensile or compression test, while Poisson's ratio can be determined by measuring the transverse strain during the tensile or compression test [120]. The present work implemented the mechanical testing of the stress-strain response for the tensile-bar specimens composite in the ABAQUS finite element. The predicted stress-strain responses are based on our data on predicted fibre orientation. The following sections present the stiffness calculations with different values of aspect ratios, micromechanics models, C_m, C_m and α. So far, most studies on the structural analysis of fibre composites have been limited to investigating the effect of fibre orientation distributions on mechanical properties. However, the effect of coefficients or fibre aspect ratio has not yet been attempted in theoretical predictions.

The tensile test is the most commonly used mechanical testing method for obtaining stress-strain data. During tensile testing, the test specimen is lambed at each end. By stretching the test specimen at a constant rate, the test specimen is gradually deformed. Typically, the test is performed until fracture, with a constant elongation exerted in a uniaxial direction along the axis of the test specimen. During the test, the obtained force as a function of displacement is measured, and the global result of stress-strain data is obtained. Moreover, tensile test can help to identify the stiffness of materials and to evaluate the elasticity of different materials. This type of identification mainly categorises elastic or plastic behaviour. However, anisotropic materials have different strengths in different directions, meaning that they fail at different stress levels depending on the direction of the stress. Especially for short fibre composites, this issue is more complicated as the failure properties, like the mechanical properties, vary over the entire volume of the component.

In the present study, a tensile test simulation on the glass-fibre reinforced polymer specimen using ABAQUS was carried out. The finite element model of the composite specimen by applying displacement was modelled, and stress analysis was carried out. ABAQUS was used as a solver (ABAQUS/Standard) because of its interface with Moldex3D. First, the model was mapped and preprocessed in the ABAQUS CAE environment, where all loads and boundary conditions were applied as stated in order to perform a tensile test simulation.

The results generated from the tensile test can tell whether the obtained Young’s modulus from the simulation correlates well with the obtained Young’s modulus from the experiment. Additionally, the tensile test can help to determine if the fibre orientation-dependent material properties obtained from Moldex3D are reliable. In this thesis, the global stiffness properties of the composite constituents have been roughly estimated. However, the strength of the composite will have to be investigated further. As suggested in the previous sections of this report, the ultimate longitudinal strength of a composite can be estimated using the rule of mixtures for the longitudinal strength and the matrix strength for the transverse strength.

5.2.1 Calculation of Young’s modulus

Young's modulus is a critical material property because of its influence on material underload strains and, as a result, structure displacement. Engineers must be aware of the value of this parameter in order to run a computer simulation of structural behaviour. The Young's modulus (E or Y) of a solid is a measurement of its stiffness or resistance to elastic deformation under load. It describes the relationship between stress (force per unit area) and strain (proportional deformation) along an axis. When a material is compressed or extended, it undergoes elastic deformation and returns to its original shape when the load is removed. A stiff material will have a high module of elasticity, while a flexible material will have a low module of elasticity. In other words, a solid with a low Young's modulus value is elastic, and a solid with a high Young's modulus value is stiff [121].

Composite materials have various values in each direction, for example, in the parallel direction and the perpendicular direction. The elastic modulus of short fibre reinforced polymers is critically dependent on fibre length distribution and orientation in the final composite product. The composite elastic modulus is affected not only by the mean fibre length and the mean fibre orientation angle but also by the fibre orientation coefficient, density of fibres and the accumulated fibre orientation distribution. It is also affected by the loading direction, as the SFRP exhibits modulus anisotropy [122].

The stress and strain of the studied tensile specimen were calculated based on the results of force and elongation obtained from the tensile test simulation. The largest stress and strain experienced by the element were also registered. After the stress and strain of the material were obtained depending on the applied force concerning the cross-sectional area, the change in length of a material and the area of the material. It was possible to calculate Young's modulus of the specimen with the following formula:

$$E = \frac{\sigma}{\varepsilon} \tag{5.1}$$

5.2.2 Effect of fibre distribution coefficient

An injection moulding simulation with various parameters of melt temperature, aspect ratio and coefficients were carried out to evaluate the effect of the various parameters on the stiffness of the material. The parametric study conducted based on the varying parameter input range is presented in chapter 1.10. All the injection moulding simulation with various parameters were exported to ABAQUS in order to conduct a FEM analysis. Based on the FEM analysis in ABAQUS, the effect of the various parameters on the stiffness of the material is analysed and the results are presented in this section.

Figure 5.3 shows the stiffness of the specimen with different values of Cm: 0, 0.6 and 0.9, respectively. As seen in the bar chart, the calculated stiffnesses are very close to each other, but as the Cm value is decreased, the difference between the graphs intensifies. The bar chart indicates that the maximum and minimum stiffnesses are 13091.92 N/mm^2 and 12706.92 N/mm^2. According to the column graphs, the maximum stiffness is obtained when the value of Cm is equal to 0.9. On the contrary, the lowest stress (1211,3) is registered when the value Cm is reduced to 0. Figure 5.3 displays the stiffness response of the specimen as well in the bar chart with various values of Ci: 0.0007, 0.005 and 0.01. The Figure 5.3 shows that the stiffness is high when Ci is set equal to 0.0007. On the other hand, the form of stiffness is at its minimum level when Ci is set to 0.01, indicating that the stiffness decreases when the Ci increases. According to the figure, the parameter Ci might significantly impact the stiffness response of the part. When the value Ci increases, the stiffnesses fall slightly from 14035.8 N/mm^2 to 12632.53 N/mm^2. It is also observed that the lowest value of Ci gives the highest stress and strain, which are 1356,86 and 0,096672.

Additionally, Figure 5.3 shows the stiffness of the specimen with various values of alpha: 0, 0.7 and 0.09. The predicted stiffness with different alpha values pretty much matches each other. Although there is a minimal difference, the results are pretty similar compared to the column graphs with varying values of Ci. The different alpha values provide similar stress and strains, whereas the highest and lowest registered stress-strain are 1238,827 - 0,0964 and 1211,336 - 0,095852.

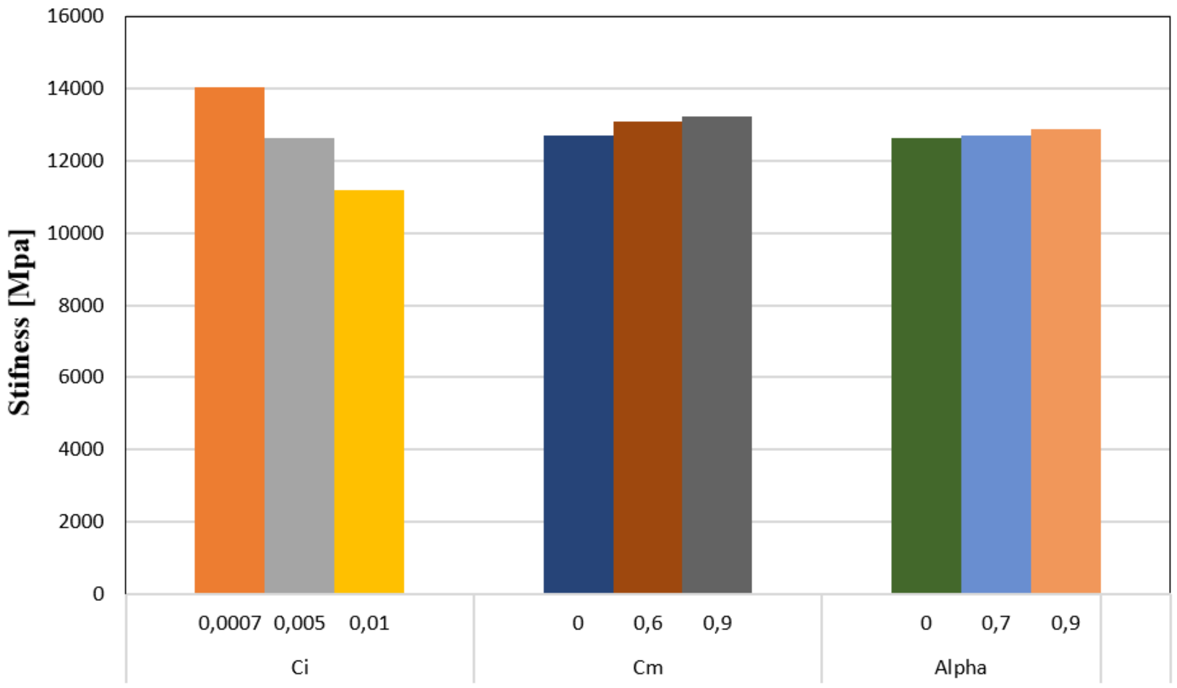

Figure 5.3: Column graphs representing values of stiffness for the simulated material (PA12 Grilamid LV-65H) with different values of fibre-matrix interactions, fibre-fibre interactions, and alpha factor.

5.2.3 Study of a weld line in strength calculation

As previously mentioned, the formation of the weld line is caused by the frontal collision of two melt fronts in the mould. At the collision region, the fibre orientation remains aligned perpendicular to the flow direction. The phenomenon of fibre orientation at the weld line showed that most fibres are oriented in the thickness direction. Injection moulded parts have higher strength and stiffness when the fibres are orientated parallel to the load direction. The strength is reduced when the fibres are oriented perpendicularly due to the external stresses which are transferred by the matrix material [123]. The fibres which reinforce the matrix to improve the mechanical properties disturb the stress transmission when the fibres are oriented parallel to the load direction. The subsequent solidification of injection moulded parts with fibre orientation perpendicular to the load direction leads to the weakening of the moulded part.

Various studies have shown that the formation of weld lines during injection moulding can reduce the strength of the final part significantly [48]. Therefore, a study of stiffness with and without weld lines is conducted in this thesis. The stiffness of the injection moulded part is based on the FEM analysis in ABAQUS. The results from the stiffness calculation of parts with and without weld lines are presented in the Figure 5.4. The linear elastic study indicates the moulded specimen without a weld line has maximum stress of 1344,71 MPa, while the maximum stress for the moulded part with weld line is lower compared to with weld line at a value of 1228,27 MPa. In addition, the ABAQUS simulation provides a strain value of 0,097097 and 0,09666 for the final part without and with the weld line, respectively. The strain value is calculated from the displacement of the extensometer divided by the original length. The simulation provides slightly smaller strain and stress for the part with a weld line. However, the overall stiffness or Young's modulus for the part without a weld line is higher than for the part with a weld line. The calculation provides Young's modulus of 13849,045 MPa for the part without a weld line. And the part with a weld line has Young's modulus of 12706,53 MPa.

5.2.4 Micromechanics model

The combination of individual constituents with isotropic properties makes the final fibre-reinforced composite material heterogenous. Therefore, the combination individual material needs to be homogenised to calculate the strength development of final composite material. The homogenisation of material is based on the approximation of micromechanical model. Various micromechanical model which is applied for the homogenisation of short fibre composite is presented in the chapter literature review. In this thesis models based on the Mori-Tanaka and Halpin Tsai applied for the structural analysis of injection moulded parts. Mori-Tanaka model is based on the approximation of effective field derived by Eshelby's inclusion in an infinite medium. While the Halpin-Tsai is a semi-empirical model based on the self-consistent field method. The micromechanics models are available for linear elastic analysis with high accuracy. Therefore, the analytical homogenisation based on the work of Mori-Tanaka and Halpin-Tsai is studied and compared in this study.

The study shows that the stiffness of the injection moulded part provides a similar Young's modulus with both micromechanics models. However, the analysis results with homogenisation based on Halpin-Tsai predicts a slightly higher Young's modulus at a value of 12850,91 MPa. Whereas the micromechanics model based on Mori-Tanaka predicts Young's modulus of 12706,53 MPa for the moulded specimen. The analysis indicates maximum stress of 1238,83 MPa and strain value of 0,0964 for homogenisation of injection moulded part based on Halpin-Tsai. While the homogenisation based on Mori-Tanaka predicts maximum stress of 1228,27 MPa and the strain value of 0,0967. According to the study, the simulation with Mori-Tanaka provides slightly higher stress for the moulded part. In contrast, the linear elastic analysis based on Halpin-Tsai predicts a higher strain value compared to Mori-Tanaka.

5.2.5 Aspect ratio

The combination of fibres and polymer matrix in the discontinuous fibre-reinforced composite provides superior mechanical behaviour compared to traditional material. The development of strength in composite material is dependent in the aspect ratio of fibres. The aspect ratio defines the ratio of fibre length to the diameter that influences. Generally, the composite material produced with a longer fibre length has greater strength since the stresses are transferred easily under loading. Therefore, simulation with aspect ratios 5, 20, and 80 was conducted to study the influence of aspect ratios on the development of strength. The result from the study is illustrated in the Figure 5.4.

The study indicates that fibre length has a significant effect on the development of strength in fibre-reinforced composite material. According to the ABAQUS simulation of injection moulded parts, the strength of material increases with the fibre aspect ratios. The obtained results shows that the fibres with an aspect ratio of 5 have maximum stress of 1055,92 MPa and a strain of 0,0994 based on linear elastic analysis. Whereas the specimen with an aspect ratio of 20 and 80 has maximum stress of 1228,27 MPa and 1227,044 MPa, respectively. The strain of 0,0967, and 0,0958 is calculated for specimen with aspect ratios of 20 and 80 at the extensometer of 75 mm from the ABAQUS simulation. According to the obtained results, the aspect ratio of 5 has relatively small stiffness at a value of 10625,07 MPa. While the specimen with aspect ratios of 20 and 80 stiffness of 12706,53 MPa and 12814,73 MPa according to the calculated stress and strain. The overall stiffness or Young's modulus of the injection moulded is superior for simulation with a larger aspect ratio. The stiffness of the specimen increases with the aspect ratio since the specimen with small aspect ratio has smaller fibre length. However, the obtained stiffness for simulation with aspect ratio of 20 and 80 is identical since the calculated strain and stress for both simulations are identical. The stiffness increases by 19,6 % from aspect ratio 5 to 20. Whereas Young's modulus for an aspect ratio of 80 increases with a value of 0,8 % from an aspect ratio of 20. The obtained stiffness of the specimen increases with a higher rate from an aspect ratio of 5 to 20. Whereas the stiffness for specimen aspect ratios of 20 and 80 with a significantly smaller rate.

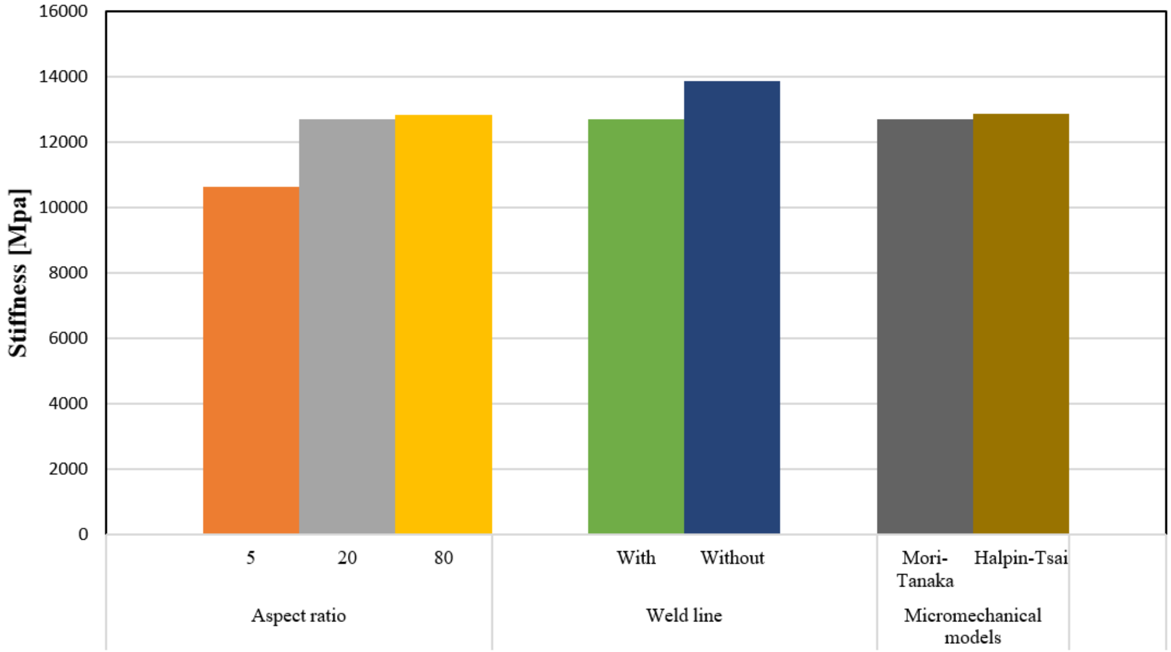

Figure 5.4: Column graphs representing values of stiffness for the simulated material (PA12 Grilamid LV-65H) with different values of aspect ratio, micromechanics model and with and without weld line.

5.3 Development of constitutive material model

The elastic properties which define the anisotropic behaviour of the specimen are provided by injection moulding simulation in Moldex3D. The homogenisation of fibres and matrix based on micromechanics models in Moldex3D is available for linear elastic analysis with high accuracy. The linear models cannot simulate the behaviour of the short fibre composite in the plastic region during structural analysis. The results from the linear elastic analysis continue where the stress remains proportional to the strain. Therefore, the analysis follows Hooke's law without any upper-stress limit. But the strain value in the linear elastic analysis is significantly low. Thus, the linear elastic model can only represent the solid material when they are subjected to sufficiently small stresses. The linear elastic constitutive equations are widely applied to solve different solid mechanics problems. This model is generally used because they are relatively easy to solve and provides a satisfactory approximation for many issues.

Generally, the uniaxial tensile experiment is time consuming and expensive process. In order to reduce the time and cost associated with the experiment, simulation in finite element software is widely practised. Thus, the primary objective of this subsection is to develop the material model to estimate the plastic behaviour of the specimen with and without a weld line. The developed constitutive material model can predict the plastic behaviour of short fibre composite. In addition, the plastic model can be applied to simulate the behaviour of an industrial product to validate the model.

5.3.1 Experimental background

The engineering tension test is widely used to provide basic design information on the strength of materials. In order to test the strength and compare the material properties with the simulation results, a tensile test was performed on the test specimen with a type of specimens ISO 527-2 1A dumb Bells. The test was performed with test standard ISO 527-1. The experiment was conducted for polymer matrix material of Grilamid LV-65H (PA12-GF65) with a glass fibre content of 65 %. During the test, the specimens are placed in the grips of the universal tester at a specified grip separation and pulled until failure. To ensure that the specimens elongated plastically and finally fractured, a load cell of 50kN was applied at a uniform velocity during the experiment. For ISO 527, the test speed is typically 5 or 50 mm/min for strength and elongation and 1 mm/min for modulus. The test speed is set to 2 mm/min in this test. An extensometer is used to determine elongation and tensile modulus. The test data file records the displacement and the corresponding force applied at every time step of a given second.

From the tensile test results, tensile strength, tensile modulus, strain and elongation and percent elongation at yield can be calculated. The tensile test generated a series of data to analyse. For the specimen, a Stress vs Strain and Force vs Displacement curve can be plotted based on the generated data from the tensile test. The results from the uniaxial simulation in ABAQUS are compared with the stress-strain curve obtained from the experiment in this section.

5.3.2 ABAQUS settings

The nonlinear analysis for the injection moulded part is also conducted with ABAQUS/standard solver with static general. The objective of the analysis is to determine the plastic model which can accurately predict plastic behaviour. However, the nonlinear analysis cannot simulate the material's behaviour with a single linear equation system as in linear analysis. The standard solver predicts the nonlinear behaviour of the material with a combination of incremental and iterative procedures. A nonlinear analysis with a standard solver splits the simulation into small time increments and uses the Newton method with many iterations to predict the solution at each time increment [124]. The standard solver provides solutions for problems based on the static or dynamic implicit algorithm. The static and dynamic implicit algorithm was applied to predict the behaviour of the material. Therefore, incrementation and mesh elements applied for the simulation to solve the nonlinear problem are presented in this chapter.

Both implicit and explicit algorithms are based on dynamic equilibrium. The dynamic solver provided by ABAQUS defines the time integration procedure based on the dynamic equilibrium of motion. The equilibrium is defined in terms of externally applied forces (P), the internal element forces (I), and the nodal accelerations [124]. Thus, the dynamic equilibrium of motion can be explained with the following equation,

$$M\ddot{u} = P - I$$

Here M is the mass matrix, and $\ddot{u}$ is the acceleration. The implicit solver finds a solution for nodal acceleration and uses the same calculation to determine the internal element forces identical to the explicit analysis. However, the algorithm for implicit solver requires a coupled system of equations to be solved. Therefore, implicit solver in ABAQUS/standard uses non-linear solution method such as Newton-Raphson iterative solution method with automatic incrementation. Thus, this approach needs to satisfy the dynamic equilibrium at the end of each increment at the time $(t + \Delta t)$ and calculate displacement simultaneously. The solution for a nonlinear problem is solved through several iterations in each increment since the implicit solver is unconditionally stable. At the same time, the explicit algorithm can find a new solution based on the extrapolation of data available in the current state. The time increment for the explicit algorithm is relatively large compared to the implicit algorithm during analysis. Subsequently, the computational cost for solving the set of equations is higher with an implicit solver. However, the explicit solver was not applicable for anisotropic elastic constants from Moldex3D with a ductile plasticity material model. Therefore, the implicit solver instead of the explicit solver was used in this study.

Step and incrementation

An increment in ABAQUS is a part of the step where the load condition is applied [124]. In plastic analysis, the total load applied in the specimen is distributed further into smaller increments to follow the nonlinear solution path. ABAQUS allows users to select automatic or fixed time incrementation. The default setting provides a maximum number of increments of 100. When the step exceeds the maximum number of increments, the analysis stops. The default increments of 100 are not sufficient for the nonlinear analysis of the specimen. Therefore, the maximum number of increments for the analysis is increased to a very high number of 10 000 to avoid unwanted completion of analysis. Generally, the standard solver requires the user intervention for the size of the initial increment while it automatically selects the subsequent increments. The initial increment size at which the step starts the analysis is chosen as 0,001 for the ABAQUS analysis. In addition, for automatic time incrementation, ABAQUS uses the minimum and maximum increments sizes of 1e-0010 and 1, respectively. The general solution controls associated with each step are altered for the nonlinear analysis. The analysis uses a value of 20 for several equilibrium iterations (I_0) and the number of consecutive equilibrium iterations (I_R) 40. And a maximum number of attempts allowed for an increment (I_A) is selected as 10. According to the ABAQUS manual, these settings can avoid premature cutbacks of the time increment [124].

Additionally, the nonlinear analysis with a standard solver is not conditionally stable during simulation. The nonlinear problem has instabilities that occurred of a geometrical nature, such as buckling or material nature, such as material softening. Therefore, the analysis with a standard solver requires automatic stabilisation. The activation of automatic stabilisation introduces virtual viscous damping forces in the material. The analysis conducted in this thesis applied automatic stabilisation with a dissipated energy fraction of 0,0002. In addition, the analysis uses adaptive stabilisation with a max ratio of stabilisation to stain energy of 0,05. In comparison, the explicit solver has fully automatic default time incrementation and does not require intervention from an external user. The plastic analysis is conducted with a standard solver. Therefore, the nonlinear geometry must be active in the ABAQUS step module in the step where the load is applied. The ABAQUS include the nonlinear effects of large displacement and affects subsequent steps when the nonlinear geometry is included during the simulation. In addition, it allows the ABAQUS to solve the nonlinear problem of the specimen with a static solver.

Mesh strategy

The general structure and the geometry of the mesh are not changed for the nonlinear analysis. However, the mesh element settings in ABAQUS are critical to obtaining accurate and reliable results from the nonlinear analysis. The nonlinear analysis and damage criteria require the mesh adjustment from the prior settings presented in the Chapter 5.1.2. It is conducted with hex elements with linear geometric order and reduced integration. The hourglassing problem can occur by applying first-order reduced integration elements (C3D8R) with a single integration point for analysis [124]. Therefore, an enhanced hourglass control provides improved coarse mesh accuracy for nonlinear material response at high strain levels. In addition, the distortion control with a length ratio of 0,1 is applied for the analysis. However, distortion control is generally applied for C3D10HS mesh elements. The distortion control activates a limitation that prevents negative element volumes or excessive distortion for crushable materials. But the second-order accuracy for the analysis is implemented for the damage simulation. According to the ABAQUS manual, the second-order accuracy applies second-order formulation for solid or shell elements suitable to analyse a large number of revolutions [124].

In addition, damage initiation criteria based on ductile failure are implemented to simulate the fracture in the material during the analysis. The analysis in ABAQUS simulates the plastic behaviour post ultimate strength according to the damage initiation criteria and damage evolution. To simulate the damage in the element mesh must be deleted when the analysis reaches the maximum degradation and the damage criteria [124]. ABAQUS provides mesh settings with the “element deletion” technique to equally apply damage to every stiffness component for elements eventually deleted according to the equation 5.2.

$$\sigma = (a - D)\bar{\sigma} \tag{5.2}$$

The elements are deleted from the mesh when the value of D reaches a maximum value of D_{max} at all the section points at all integration locations [124]. The method of element deletion is generally used to study the collapse of steel material through finite element models, which consider a constant critical strain. During the analysis, the implemented algorithm in ABAQUS deletes the mesh to simulate a fracture in the material. This strategy provides an essential value equivalent to plastic strain to delete an element without implementing any softening behaviour. Max degradation value which initiates the element mesh deletion for the analysis is selected as $D_{max} = 0.999$.

5.3.3 Inverse modelling procedure

The Moldex3D simulation presented in the Chapter 4 distributes the elastic properties in the different material cards, representing a specific specimen volume. The specimen without a weld line has 5 368-material cards with specific elastic properties, while the model with a weld line has 5 835 material cards. Inserting plastic data and damage parameter manually is a tedious and time-consuming procedure for every material card. However, ABAQUS allows programming languages such as Matlab and Python to accomplish time consuming or practically impossible tasks. The plastic data and damage parameter for the specimen is inserted with the help of simple Python scripts developed for the specific task. The Python script is used to program the repetitive task of inserting parameters in every material card with a for loop.

A plasticity model is required to represent the non-linear behaviour of the specimen with and without weld lines. The most common method to describe the mechanical material properties in the plastic domain of short-fibre composite material is applying a plasticity model for metal [125]. This thesis develops the material model for short fibre composite material to simulate the plastic behaviour of short fibre reinforced composite. Generally, the material model is based on calibration from experiment results also known as inverse modelling. The method of calibrating the material models with experiments has been used for a long time to solve problems in the domain of science and engineering. Based on this method, the simulation was conducted iteratively with optimised input parameters which can be fitted to the results obtained from the uniaxial tensile test. The results from the simulation were considered adequate when the plastic parameters provided results that were identical to the results from the experiment. SINTEF conducted the experimental data to fit the simulation results, which were provided by the external supervisors for this study. In addition, the Python scripts used for inserting plasticity data for specimen without weld lines is presented in Appendix I.

But determining the plastic behaviour of the simulation with a weld line is more complex. The formation of a weld line in the simulation leads to weakness in injection moulded material. The effects of the weld line are considered for the linear elastic analysis based on the final fibre alignment distribution from the injection moulding simulation. However, the weld line effect on the plastic region needs to be considered to achieve reliable simulation results. The Moldex3D simulation of injection moulding presented in Chapter 4 shows the formation of a weld line in the middle of the specimen. Therefore, a weld line region at the centre of the specimen is selected to determine the plastic properties of the weld line. The region for weld line is modelled as 2 mm wide with 4 mesh elements along with the thickness of the specimen. The weld line region selected for the simulation is illustrated in Figure 5.5.

The same calibration principle determines the plasticity data for the weld lines region with experimental results. Since the plastic behaviour outside the weld line region is defined in the previous simulation, which provides highly accurate results. The same plastic data of the previous simulation is applied to the specimen region outside the weld line. At the same time, the plastic behaviour for the weld line is determined from iterative simulation and tuning of the plastic data to fit the results from the experiment. The material elements provided from the Moldex3D simulation in the weld line regions need to be determined by applying the plastic data. And the plasticity data in the material elements are implemented with the help of the Python script presented in Appendix II.

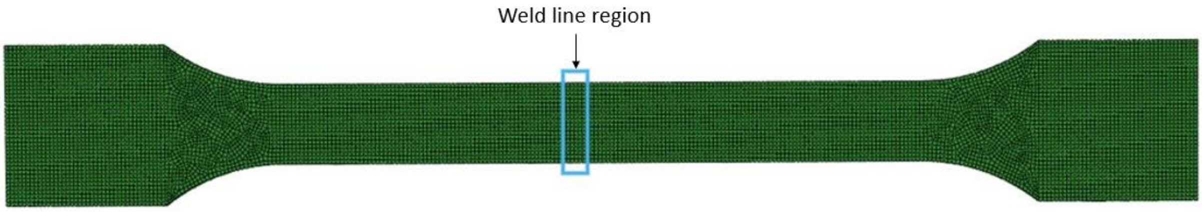

Figure 5.5: The weld line region at the centre of the specimen was used in the study to determine the plasticity model for the weld line.

5.3.4 Plasticity model

In this thesis, the classical metal plasticity model available in ABAQUS, which defines the post-yield behaviour of most metals, is applied to represent the plastic behaviour of short fibre composite material. ABAQUS approximates the smoothness of stress-strain behaviour of the model with a series of straight lines connecting the given data points. The different data points were selected from the experiments to simulate the plastic behaviour of short fibre composite material. The initially selected data points were calibrated with the experimental results to provide accurate results. After many simulations, the data points presented in the Table 5.1 and 5.2 were obtained to simulate the accurate plastic behaviour. The data points were further applied in the study to simulate the plastic behaviour of the injection moulded part without a weld line. The specimen without a weld line has an initial yield stress of 134 Pa is obtained for the model without a weld line. The input plasticity data defines the true yield stress of the material as a function of true plastic strain. At the initial yield stress, the material does not exhibit any form of plastic behaviour. Therefore, the initial input data defines the material's initial yield stress and has a plastic strain value of zero. The plastic strain is obtained by subtracting the elastic strain.

The global plastic behaviour of the simulation is determined by the plasticity data of the weld line. After many simulations and a curve fitting process, the data points to describe the post-yielding behaviour of the weld line region are determined. ABAQUS can simulate the actual material behaviour with any number of points. Therefore, the effect of the weld line region in the simulation is described with the 3 data points presented in the Table 5.2. While the post yielding of the material cards outside the weld line region was defined according to the previous data points presented in the Table 5.1. The yield stress at the weld line region is significantly lower than for material cards outside the weld line region. Since the weld line formation decreases the global stiffness of injection moulded material, the obtained yield stress at the weld line region was drastically reduced during the simulation. Therefore, the yield stress or the elastic limit for the material cards region outside the weld line is 134 MPa. While the yield stress of the material card in the region is 26 MPa. In addition, the initial yield stress has a plastic strain value of zero since the material does not exhibit plastic behaviour identical to the simulation without a weld line.

Table 5.1: The 4 data points obtained from the uniaxial tensile simulation to describe the plastic behaviour for injection moulded parts without weld lines.

Yield stress	**Plastic strain**
134	0
164	0.003957654
175	0.010245708
186	0.02474255

Table 5.2: The final plastic data obtained from the ABAQUS simulation describes the plastic behaviour for weld lines in injection moulded parts.

Yield stress	**Plastic strain**
24	0
30	0.003957654
36	0.007525465

Comparison of constitutive model with experimental results

To develop the material model for the specimen, different experimental results were provided by external supervisors. The test was conducted four times to increase the reliability of results and reduce the external impact on results. The simulation of the specimen with weld line is compared with results from the uniaxial tensile test. Figure 5.6 shows the comparison of the stress-strain curve obtained by simulation and experimental results for dog-bone specimens with weld lines. The results show a good agreement with the result obtained by the experiments. However, the ultimate strength obtained from the simulation is approximately 55 MPa and differs slightly from the experimental results. According to the Figure 5.8, the stress starts to drop after the necking region and keeps dropping even after the specimen reaches the fracture point. In the necking region, the cross-sectional area begins to decrease, which causes the stress to decrease and the strain to increase. In this analysis, a fracture criterion was not applied; therefore, the curve from ABAQUS keeps falling.

Figure 5.6 compares the stress-strain curves obtained by simulation and experiments. After FE simulation in ABAQUS, stress and strain for the specimen without weld line are obtained. These data are plotted together with the experimental ones. As shown in Figure 5.6, the uniaxial tensile test simulation using the proposed material model showed a good agreement with the result obtained by the experiment. The stress-strain plot for the specimens in Figure 5.6 illustrates the elastic and plastic region before fracture. The graph shows roughly that the stress achieved from the experiment is higher in the strain hardening region. However, both the simulation and experiment results show a good fit, especially in hardening slopes and overall flow stress evolution. In both cases, the ultimate strength is approximately 180 MPa. But the result from ABAQUS shows that the stress remains almost constant after the upper yield point while the strain keeps increasing.

Figure 5.7 shows a comparison of the stress-strain curves obtained from the simulation with dynamic implicit and static general analysis with the result from the experiment. However, in this analysis, the simulation is conducted with a nonlinear geometric setting turned ON, which determines whether ABAQUS will account for geometric nonlinearity effects from large displacements and deformations. Additionally, whether or not we have nonlinear material, if we want to include the geometry change during the analysis, the NLGEOM setting should be on. In the stress-strain diagram, after a transition from the ultimate strength to the necking region, a sudden drop in stress is witnessed, followed by constant stress with few variations and a strain which keeps increasing. The decrease in stress occurs due to the reduction in cross-sectional area. On the contrary, Figure 5.7 shows constant stress after ultimate strength because the simulation did not consider the change in the cross-sectional since the NLGEOM setting was omitted during the analysis. So, the graph from the simulation presented in Figures 5.6 and 5.7 varies slightly due to the non-linear geometric setting in ABAQUS. Figure 5.7 shows that the results from the static general and dynamic implicit analyses and the experiment are similar and almost identical until the ultimate strength of about 180 MPa with a 4 mm strain [%]. However, it can be seen that the stress from the simulations is a little lower in the strain hardening region. Observing the graph, the static general and dynamic implicit analyses have curves that identically overlap. But after the necking region, the static analysis exceeds the dynamic implicit analysis, as shown in Figure 5.7.

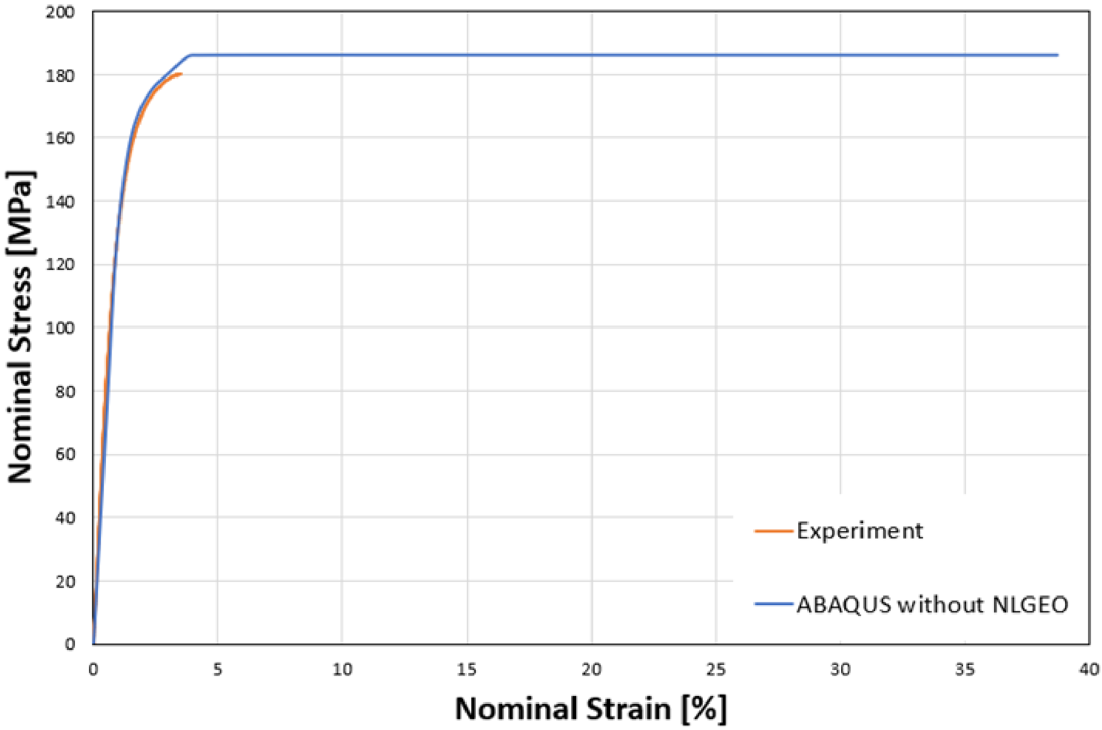

Figure 5.6: The stress-strain simulation and experimental results for dog-bone specimens without weld line and without nonlinear geometry.

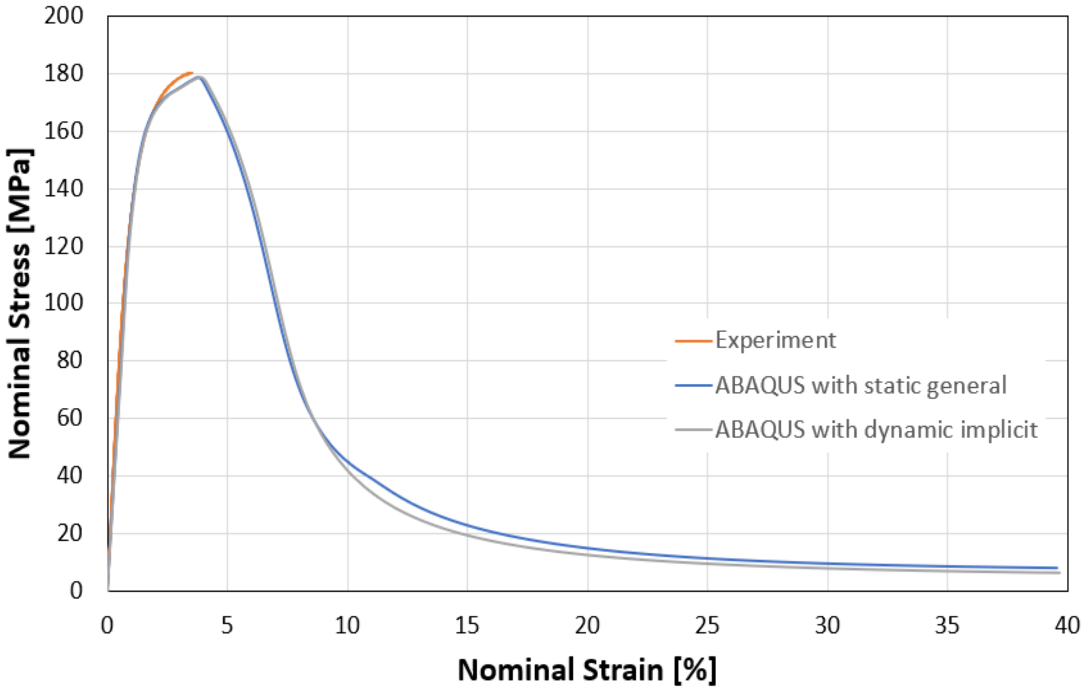

Figure 5.7: The comparison of the curve was compared with the stress-strain curve obtained by static general analysis and the dynamic implicit analysis and experimental results for dog-bone specimens without weld line and with nonlinear geometry.

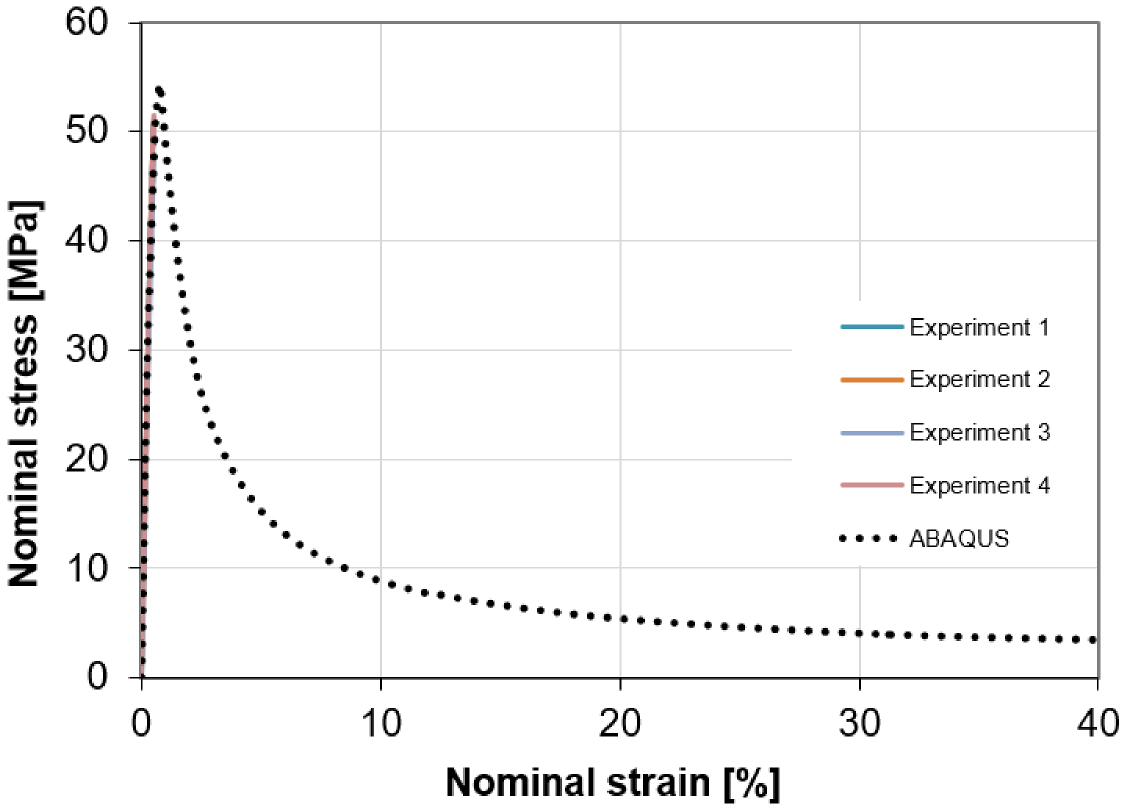

Figure 5.8: The comparison of the stress-strain curve obtained by simulation and experimental results for dog-bone specimens with weld line and with nonlinear geometry.

5.3.5 Damage initiation criteria

Damage progression in the composite is a time-dependent and path-dependent occurrence that includes crack initiation and propagation. The failure or fracture of polymer materials is initiated from the site of a stress raiser. The failure in polymer material can occur from local or distributed material defects, such as structural or geometrical features or damage [126]. The research shows that the polymer materials fail in a brittle manner which means that the material fails instantaneously at the onset of damage. Generally, the fracture in polymer material results from the propagation of the crack. And the cracks in fibre-reinforced polymer material are propagated at a weak interface caused by the fibre orientation, such as weld lines or fibre concentration. The crack propagation in the material is initiated when some local critical condition is met. Therefore, a proper damage criterion describing the failure mechanism is necessary to simulate the material separation accurately. The damage models and failure criteria for orthotropic material, such as Puck's and Hashin's failure criteria are complicated to apply for short fibre composite material. Therefore, damage initiation for isotropic ductile metals is used to define the damage progression of short fibre reinforced polymer.

The damage initiation for ductile metals defines failure based on parameters such as fracture strain, stress triaxiality, and strain rate with damage evolution, presented in the following chapter. These parameters to define damage for specimen with and without weld line are inserted using python scripts in Appendix II and IV. The damage model is determined through the same procedure known as inverse modelling. The damage parameters were calibrated to simulate the failure of both specimens based on the experimental results. Additionally, the value of damage parameters to accurately simulate failure is presented in the Table 5.3. However, the damage parameters and evolution to simulate failure for both specimens will be explained further in the study.

Table 5.3: Summary of damage parameter determined from the experimental calibration for specimen with and without weld line.

Specimen	Fracture strain	Stress triaxiality	Strain rate	Fracture energy
With weld line	0.0820	0.333	0.001	0
Without weld line	0.0255	0.333	0.001	0

Damage parameters

After the yielding process of short fibre composite material, the plastic strain and stress precisely predict the nonlinear material behaviour. However, the material behaviour can no longer be accurately represented with the stress-strain relationship when material damage occurs. The ductile damage criterion in ABAQUS predicts the onset of damage for ductile metals. Generally, ABAQUS simulates the damage to ductile metals caused by nucleation, growth, and coalescence of voids [124]. However, the elongated specimen begins to lose its original cross-section area at the onset of damage. The high strain concentration causes the reduction of area in the place where the cross-sectional area of the specimen is reduced. Generally, the region with non-uniform sections with the reduced area is referred to as a diffuse neck where the maximum load for material is reached. After diffuse necking, the material starts to unload. The plastic deformation occurs in a localised region as necking in the material occurs [127]. The necking phenomenon can be considered by applying approximation methods such as Bridgman correction during the tensile tests.

The traditional quasi-static tensile tests are not able to determine the constitutive parameters beyond the point of maximum load. After the maximum load or necking, the behaviour of the material is unstable, caused by increased strength in the material due to strain hardening. The ductile damage criterion in ABAQUS simulates the damage with an approximation of equivalent plastic strain from the onset of damage $\bar{\varepsilon}_D^{pl}$. At the onset of damage, the plastic strain is referred to as the fracture strain, which indicates the damage initiation of material. The equivalent fracture strain at damage initiation is illustrated in Figure 5.9 where the degradation value $D = 0$. After many simulations, the fracture strain of 0.082 and 0.0255 for specimens with and without weld line was determined to simulate the damage initiation accurately. The obtained fracture strain is significantly higher for elements located at the weld line region. But elements in the weld line region have significantly lower yield stress compared to elements which lie outside the region. The lower yield stress results in earlier degradation of elements during analysis even if the fracture strain is higher.

Furthermore, the ductile criterion predicts the damage at the onset of damage $\bar{\varepsilon}_D^{pl}$ as a function of stress triaxiality and strain rate, which is presented in the equation 5.3.

$$\bar{\varepsilon}_D^{pl}(\beta, \dot{\bar{\varepsilon}}^{pl}) \tag{5.3}$$

The uniaxial stress state assumed at the tensile test changes to triaxial stress during necking. The development of stress triaxiality in the tensile test produces inaccurate stresses from the tensile test. Therefore, the values from the uniaxial test are not valid beyond the onset of necking. The stress triaxiality β can be defined as the ratio between hydrostatic stress and equivalent stress. Thus, stress triaxiality for Von Mises stress can be determined by the equation,

$$\beta = \frac{\sigma_m}{\sigma_{eq,VM}} = \frac{\frac{1}{3}(\sigma_{11} + \sigma_{22} + \sigma_{33})}{\frac{\sqrt{2}}{2}\sqrt{(\sigma_1 - \sigma_2)^2 + (\sigma_2 - \sigma_3)^2 + (\sigma_3 - \sigma_1)^2}} \tag{5.4}$$

Based on the boundary conditions for the uniaxial tensile test, the stresses in perpendicular and cross-section directions are irrelevant. Thus, the stress in $\sigma_{22} = \sigma_{33} = 0$ which gives the stress triaxiality for the tensile test by the following equation,

$$\beta = \frac{\sigma_m}{\sigma_{eq,VM}} = \frac{\frac{1}{3}(\sigma_{11})}{\sigma_{11}} = \frac{1}{3} \tag{5.5}$$

Therefore, a stress triaxiality value of 0.333 was applied for the analysis. In addition, an equivalent plastic strain rate of 0.001 1/s is used to define the change in strain obtained by the material concerning time. The plastic strain rate for the analysis is small since the material is loaded gradually.

The condition for damage initiation is fulfilled in ABAQUS by the criterion when,

$$w_D = \int \frac{d\bar{\varepsilon}^{pl}}{\bar{\varepsilon}_D^{pl}(\beta, \dot{\bar{\varepsilon}}^{pl})} = 0 \tag{5.6}$$

During the material's plastic deformation, the state variable w_D increases monotonically. According to the ABAQUS manual [124], the incremental time increase in w_D at each increment during analysis. It is computed by the equation 5.7.

$$\Delta w_D = \frac{\Delta\bar{\varepsilon}^{pl}}{\bar{\varepsilon}_D^{pl}(\beta, \dot{\bar{\varepsilon}}^{pl})} \geq 0 \tag{5.7}$$

Damage evolution

A damage evolution law controls the following damage propagation when the ductile damage initiation criterion is fulfilled during the analysis. In general terms, the damage evolution model defines the post-damage initiation behaviour of the material. The characteristic stress-strain behaviour process of material undergoing damage from elastic behaviour until final failure is illustrated in the Figure 5.9. The damage in material occurs in two forms, either from softening of the yield stress or degradation of the elasticity. In Figure 5.9, the dashed curve represents the behaviour without damage model, while the solid line indicates the damaged stress-strain behaviour. The yield stress and equivalent plastic strain at the onset of damage are depicted in the Figure 5.9 as σ_{y0} and $\bar{\varepsilon}_0^{pl}$ respectively. While the equivalent plastic strain when the material fails is depicted as $\bar{\varepsilon}_f^{pl}$. The equivalent plastic strain at failure $\bar{\varepsilon}_f^{pl}$ depends on the element's characteristic length. However, the degradation of elements or material is initiated after the onset of damage. Therefore, plastic strain $\bar{\varepsilon}_f^{pl}$ at failure cannot be specified as the material parameter of the damage evolution law [124].

The damage evolution laws applied to govern the condition for initiation and growth of damage parameters are usually written in terms of the strain state in the layer [128]. The damage evolution law specified in ABAQUS is based on the equivalent plastic displacement $\bar{u}^{pl}$ or in terms of fracture energy dissipation G_f. The fracture energy dissipation method is based on the proposed work of Hillerborg, which was published in 1976 [129]. The simulation of the stress-strain relationship after the onset of damage provides inaccurate results. The application of stress-strain response after the onset of damage introduces a strong mesh dependency based on strain localisation [124]. Therefore, Hillerborg proposed an alternative method combining fracture mechanics and finite element analysis based on the strain-softening branch of the material behaviour. The method applies the stress-displacement response instead of the traditional stress-strain response to define the fracture energy. Various application of the approach based on stress-displacement response has resulted in a reduction of mesh dependency after the damage is initiated.

The finite element model requires the definition of a characteristic length L to implement the stress-displacement behaviour. Thus, the fracture energy based on the work of Hillerborg is defined as,

$$G_f = \int_{\bar{\varepsilon}_0^{pl}}^{\bar{\varepsilon}_f^{pl}} L\sigma_y d\bar{\varepsilon}^{pl} = \int_0^{\bar{u}_f^{pl}} \sigma_y d\bar{u}^{pl} \tag{5.8}$$

According to the equation 5.8, the equivalent plastic displacement $\bar{u}^{pl}$ as the fracture work conjugate of the yield stress after damager initiation (work per unit area of the crack) [124]. The damage evolution based on the fracture energy dissipation is efficient to predict the material behaviour. Therefore, in this thesis, the damage evolution law based on the fracture energy dissipation with exponential softening is applied to define the behaviour of material of the short fibre composite material. The fracture energy dissipation method defines the energy required to open a unit area of crack G_f as a material parameter to predict damage after the onset of damage. However, the short fibre reinforced composite material fails instantaneously. The instantaneous failure of material implies that the material does not have damage evolution. Therefore, the fracture energy (G_f) of 0 is applied to define the material damage after the onset of damage. The determined fracture energy will simulate the short fibre reinforced composite as a quasi-brittle material.

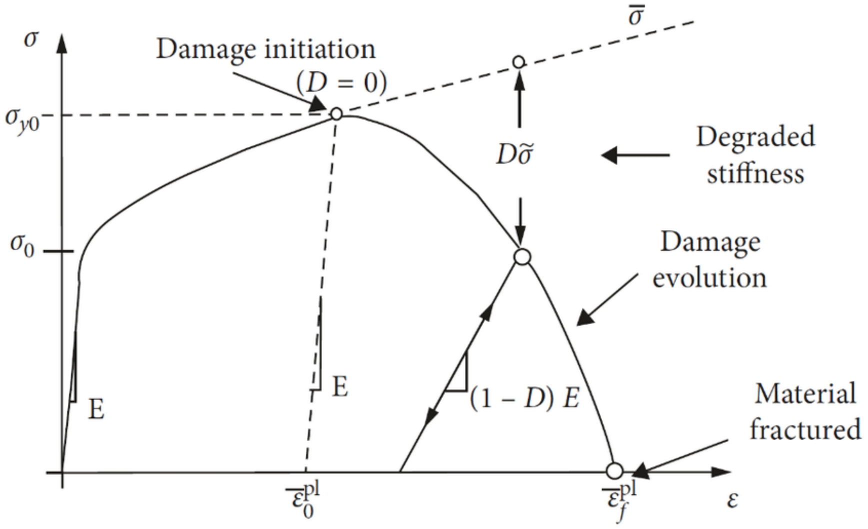

Figure 5.9: The damage model in ABAQUS according to the ductile damage criterion [130].

Comparison of damage model with experiment

The experimental results show that the formation weld line impacts the plasticity behaviour of injection moulded specimens. The specimen with weld line has significantly inferior mechanical properties compared to specimen without weld line. The findings from experiment show that the specimen with weld line fails instantaneously without exhibiting any nonlinear behaviour. The stress-strain diagram for the part that has been simulated with the damage initiation criteria is presented in the Figure 5.10 and 5.11. The figure depicts a comparison of stress-strain curves obtained through simulation and four experimental results. The stress-strain curves for the specimen without weld line simulated in ABAQUS and experiments are shown in the Figure 5.10, with strains ranging from zero to the material fracture. According to the graphs, the elastic limit or yield stress is around 120 MPa for ABAQUS and the experiments. After the yield point, a slight increase in stress causes a significant increase in strain, indicating that the material continues to deform without a substantial increase in stress. According to the graph, the result from the simulation shows a good agreement with the result obtained by the four experiments. However, a minor result can be observed between the elastic region's experimental and simulation results.

Furthermore, the strength of the material can be seen to increase between the yield point and the ultimate strength. The increase in strength is the result of strain hardening. As the deformation progresses, the stress rises due to strain hardening until it reaches the ultimate tensile stress. The ultimate strength, which corresponds to the maximum strength value on the stress-strain diagram, is around 180 MPa with a strain of about 3.1 mm [%]. The necking region extends from the ultimate tensile stress to the fracture point. In this region, the cross-sectional area of the material will be reduced, and the ability of the material to carry a load will decrease. According to the Figure, fracture occurs at a fracture strain of about 3.5 mm for the experiments and the simulation.

The uniaxial tensile test shows that the different specimen samples have different initial yield stress for specimens with weld lines. The specimen sample 1 and 4 with weld line yields at a strain value of 0.006 with a yield stress of 50 MPa. While sample 3 and 2 yields a strain of 0.0052 and 0.0035 respectively. In addition, the results show that sample 3 and 2 has a yield stress of 33 and 48 MPa. However, the results obtained from the ABAQUS show that the result from simulation provides highly accurate results compared with the results from the experiment. The simulation results from ABAQUS have a yield stress of 48 MPa at a strain of 0.0054. Therefore, it is safe to conclude that the ductile plastic and damage model effectively captures the effect of the weld line. In addition, the material model provided in this thesis can certainly predict material behaviour accurately.

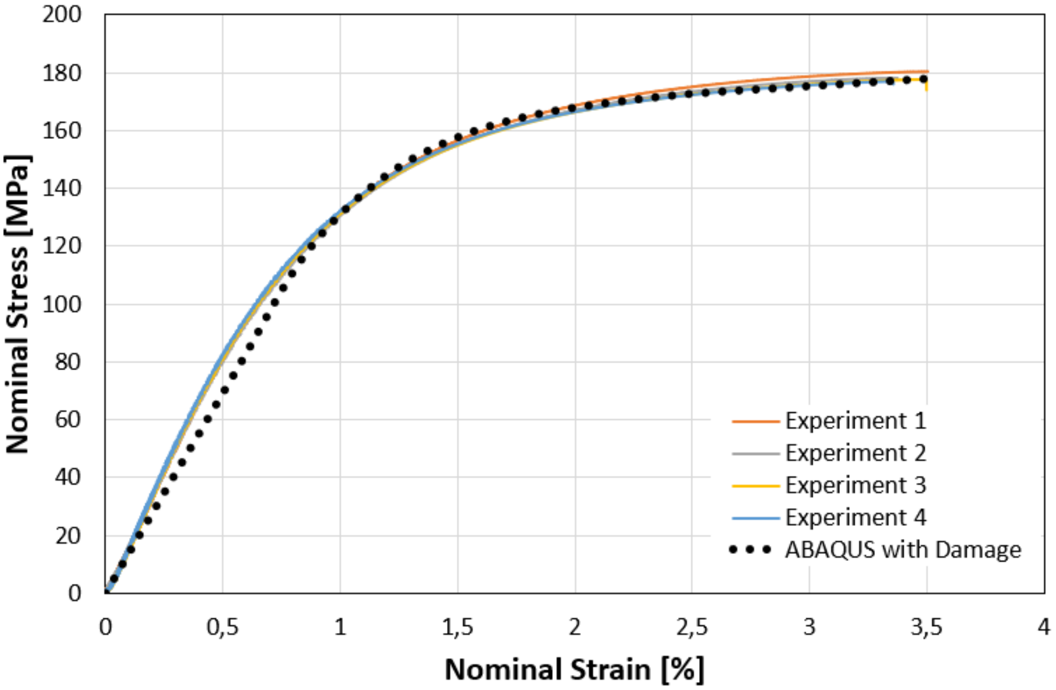

Figure 5.10: The comparison of the stress-strain curve obtained by simulation and experimental results for specimens without weld line and with nonlinear geometry.

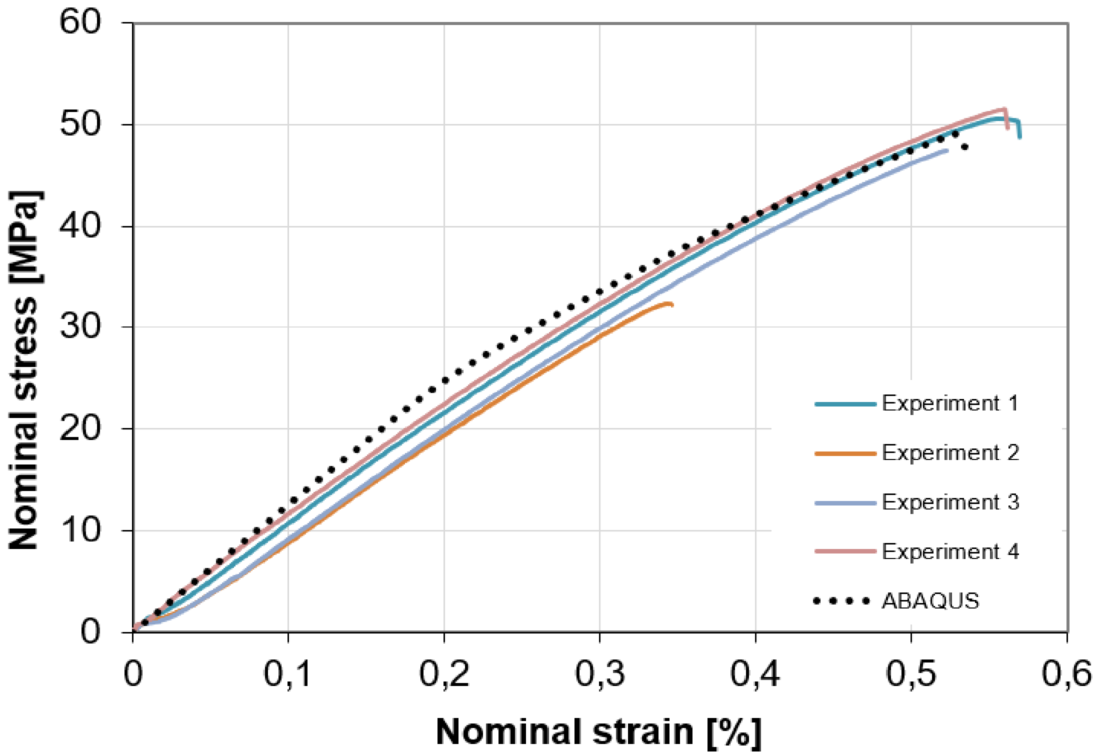

Figure 5.11: The uniaxial tensile test results from experiments and ABAQUS simulation for specimen with weld line.

Stress analysis of specimen

After the simulation of the specimen is complete, the results can be viewed by using contour plots. It is the analysis phase where the results of the analysis are reviewed through graphics. Figure 5.12 shows the longitudinal stress distribution of the specimen without a weld line at an applied displacement of 30 mm. The nominal stress of the gauge section with a cross-section area of 4 mm2 is about 42 MPa. However, the stress distribution result verifies that the stress varies along the gauge length as shown in the Figure 5.12. Furthermore, it can be observed that the stress on the grip section is relatively low. Damage is detected near the grip section where the fixed boundary conditions are applied. According to the Figure 5.12, the necking region is near the grip section, which means a reduction in the cross-sectional area of the specimen occurs in this region and leads to fracture, as shown in the Figure 5.12.

The uniaxial tensile test in ABAQUS shows that the specimen with a weld line fails at the centre of the specimen. Failure location from the obtained simulation results is expected since the weld line region is described at the centre of the specimen. The material properties of the weld line region result in weakness in the specimen. Therefore, the elements at the weld line region are degraded earlier as the elements deletion process is initiated. The results obtained from the ABAQUS are presented in Figure 5.13, which shows stress distribution after the separation of the specimen. The element deletion of the specimen with a weld line is uneven compared to the specimen without the weld line. The observation of element deletion indicates that the mesh elements meet the damage criteria irregularly at the weld line region. And the stresses obtained by the specimen after the material failure are concentrated at the weld line region. While the stresses outside the weld line region falls to the value of 0. In addition, the results show that the specimen with weld lines obtains maximum stress of 84,86 MPa.

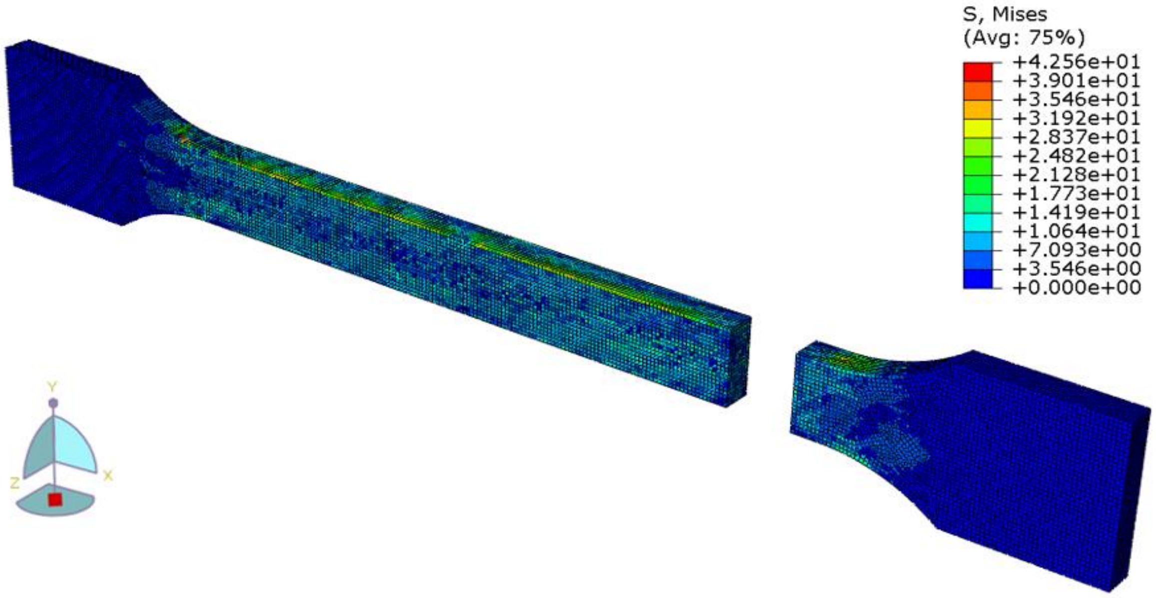

Figure 5.12: Finite elements result of the specimen without weld line to check the stress distribution after material separation in ABAQUS.

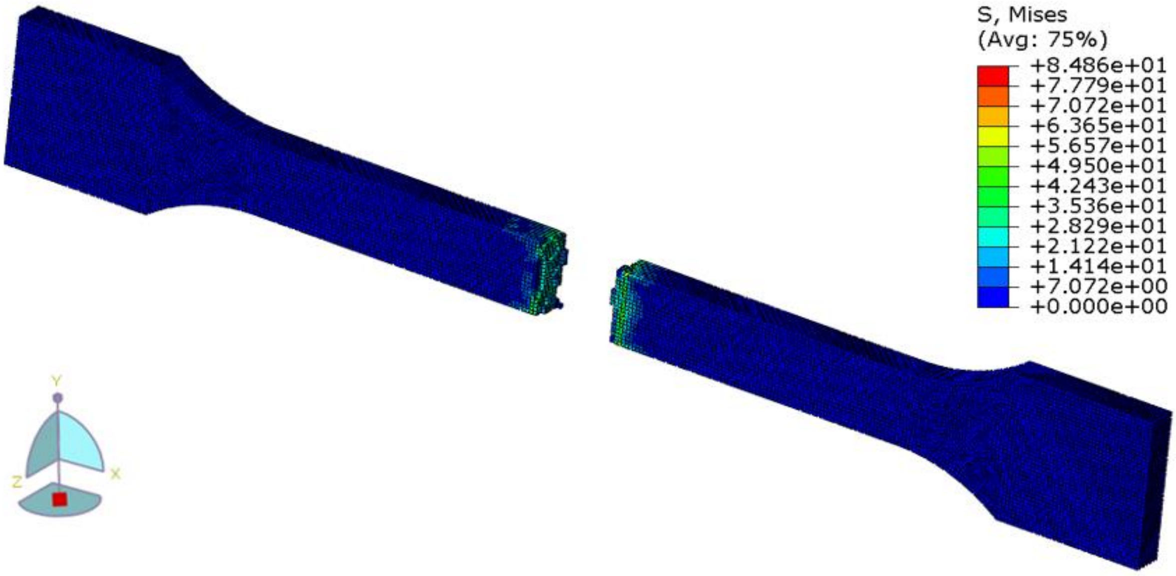

Figure 5.13: The Von Mises stress contour and fracture location for specimen with weld line after material separation in ABAQUS.

6 Discussion

In this thesis, a simulation of thermoplastic injection moulding is conducted. The study reveals that the design of fibre-reinforced thermoplastic parts is hindered by the determination of the various empirical parameters associated with the fibre orientation models. Moldex3D can predict fibre orientation distribution by using different fibre orientation models such as Folgar-Tucker (FT) and improved Anisotropic Rotary Diffusion (iARD) rotary diffusion models with closure approximations such as Invariant Based Optimal Fitting (IBOF). However, the orientation models rely on empirically determined parameters, which must be obtained prior to injection moulding simulations. The orientation models depend on a parameter accounting for the interactions between fibres during the flow, known as the fibre interaction coefficients, such as the fibre-fibre coefficient and fibre-matrix coefficient, and the alpha factor. These coefficients are (C_i, C_m and α) fitting parameters, which affect the distribution of fibre orientation during injection moulding simulation. As far as we know, there is currently no standard test for acquiring these parameters, nor is there a standardised look-up table.

The interaction coefficient must be determined for a particular material since the interaction coefficient differs according to material flow behaviours. A semi-empirical approach suggested by Tseng can be employed to determine the fibre interaction coefficient. Some studies also indicate that the parameters can be determined by optimally fitting the comparison to the experimental orientation tensor component. Since it was pretty challenging to decide on the coefficients empirically in this study. The coefficients were selected based on other studies which have been optimized to be suitable for predicting fibre orientations for a given material. We decided to determine the parameters based on previous studies with similar material corresponding to the material we employed, Grilamid LV-65H (PA12-GF65), with a glass fibre content of 65 %. Materials have a different viscosity depending on their composition. Additionally, the process conditions, such as melt temperature and mould temperature, affect the fibre orientation coefficients. Therefore, it was essential to use a published article based on a similar study to determine the coefficients used in the simulation. Additionally, to validate the accuracy of the fibre orientation models such as Folger-Tucker (FT) and iARD, we could compare the simulation results with an experiment. But due to time limitations, an experiment to validate the fibre orientation of the material could not be conducted.

In this study, the efficiency of the interaction parameters in controlling the predicted patterns of fibre orientation is studied. The values of the fibre-fibre (C_i), matrix-fibre (C_m) interaction coefficients and the alpha-RPR parameter were altered to find how the coefficients influence the fibre distributions. The results prove that the orientation tensor component in the flow direction (a_{11}) is more sensitive to changes in the C_i coefficient, but the flow direction (a_{11}) is also affected by C_m). According to this study, it can be concluded that identifying the accurate fibre orientation parameter is fundamental to obtain reliable results. The different parameters affect the fibre distributions significantly, which affects the mechanical behaviour of the final injection moulded product. To verify how the parameters affect the strength of the material, the material properties such as anisotropic elastic constants, density, and expansion coefficient from the injection moulding process, were directly transferred to structural analysis software ABAQUS. After the analysis, the result indicated that the global stiffness of the material is significantly affected by C_i and C_m. But the slow down factor (α) had an insignificant impact on the strength development of short fibre-reinforced polymer.

During the simulation of short glass fibre-reinforced material in Moldex3D, the process parameters such as aspect ratio were also studied. The study indicates that a higher aspect ratio gives more fibres oriented in the flow direction. The study specifies that the aspect ratio of fibre influence the viscosity of the polymer. The viscosity of typical fibre-reinforced thermoplastic composites increases with an increasing aspect ratio. Because the movement of the polymer molecule is hindered more when the fibre length is longer. Therefore, the complex viscosity of composites increases with an increase in the length of the fibre, which leads to an increase in aspect ratio. So, the viscosity is determined by the nature of interactions between the fibres, which depends mainly on the fibre aspect ratio.

Additionally, the influence of weld lines on fibre orientation is evaluated in this study. The findings indicates that strength is reduced considerable at the weld line region due to a drastic reduction of fibres aligned in the flow direction. At the weld line region, the fountain flow orients polymer fibres perpendicular to flow where the two fronts meet. This is the opposite of what is required for a development of strength of final fibre-reinforced composite part. The stress distribution obtained from ABAQUS simulation shows that a crack propagates at the weld line region. By comparing tensile test results from a specimen without weld lines to one with a weld line, the study has computed the development of stiffness. The result from the study shows that the specimen without a weld line has higher stiffness. So, predicting where weld lines occur and how weak they will be is the key to effective industrial application. The study has shown that weld lines cannot be completely avoided, but they can be moved to a less critical area of the part by changing process settings.

As stated in the literature review, Moldex3D provides two micromechanical models, the Halpin-Tsai model and Mori-Tanaka to predict the mechanical properties of composite material. The result from the analysis implies that the global stiffness calculated with Halpin -Tsai was slightly higher than the stiffness calculated with Mori-Tanaka. It is not fully understood why the two micromechanical models offer different stiffness value. But the study verifies that different micromechanical models provide different results, even though the differences are not significant. Generally, this study shows that fibre orientation is strongly influenced by the process parameters. The mechanical properties of a fibre-reinforced thermoplastic can be quantified and optimised starting from the fibre orientation results.

The short fibre reinforced polymer comprises fibre material embedded inside elastic matrix material. Mainly plastic materials such as thermoplastic are used as a matrix material to manufacture SFRP. Therefore, the reliability of results from the finite element simulation of injection moulded parts is dependent on the obtained results from the injection moulding simulation. The injection moulding simulation provides the field elastic properties based on the fibre orientation distribution. The elastic properties of fibres in a matrix medium are calculated with the homogenisation approach. According to Mori-Tanaka and Eshelby's theory, a computational homogenisation method was applied in this thesis. The homogenisation of the Mori-Tanaka method is derived by calculating the average internal stresses of a matrix in inclusion with transformation strain. However, the original work of Mori and Tanaka with effective field approximation was not developed for composite material. But it was developed to calculate the plastic deformation that occurs in a material with transformation strain. The accuracy of the Mori-Tanaka method in predicting the elastic properties of composite is vital to obtaining reliable results.

The homogenisation of matrix and fibres calculates the elastic constant with density and expansion coefficient. These material properties are distributed throughout the specimen volume, referred to as material cards. However, the plasticity model to simulate the post-yield behaviour of short fibre composite is not available in commercial FEM packages such as ABAQUS. Therefore, the post-yielding behaviour of short fibre composite was based on the classical metal plasticity model, which is available in ABAQUS. The main issue with the application of the ductile plasticity model in ABAQUS is that they were developed for metals. The application of the plasticity model for metal is straightforward and simple regarding the availability and knowledge of authors. But it can oversimplify the complex nonlinear behaviour of composite material, which can provide inaccurate results if used incorrectly for polymers. The application of the plasticity model developed to predict the nonlinear behaviour of composite material might provide more accurate results.

The development of a plastic and damage model that accurately predicts material behaviour can substitute the experimental test, significantly reducing cost and time. The different plasticity data and damage model to simulate the post-yield behaviour of short fibre composite material are presented in this study. The given plasticity data and damage model were determined with inverse modelling and calibration with experimental results until satisfactory results were obtained. The study shows that the final plasticity data provides a good fit to the experimental data for both specimens with and without a weld line. However, the accuracy for simulation was expected because ABAQUS approximates the plastic behaviour of the model with a series of straight lines connecting the given data points. However, the accuracy of plasticity data might be limited to this study or to the specimen's geometry. In addition, the parameters in the ductile damage model are insufficient to simulate the progressive failure behaviour or modulus degradation. Therefore, a study with an industrial product with complex geometry is critical to determine the applicability of the plasticity and damage model even though satisfactory fits of the predicted stress-strain response and failure initiation are achieved in all the studies conducted in this thesis.

The elastic constants in each material cards are based on fibre orientation. Thus, the effect of the weld line from the melt front collision is taken into consideration. The weld line effects in the plastic analysis were simulated by assigning weaker material properties at the weld line region. However, the determined region for the weld line formation was assumed in the study. The properties of the weld line were implemented according to the material cards assigned at the centre of the specimen. The weld line properties at the weld line were assigned with the Python script. However, the weld line region in the script is defined manually. The inadequate assumption of the weld line region can provide inaccurate results during the nonlinear analysis. In addition, the script provided in this thesis has significant limitations since it is only applicable to the specimen in this study. Python script, which can identify the weld line elements based on the elastic constants, can be applied for other studies. Additionally, the scripts which automatically determine the weld line region can provide more accurate results.

Different challenges appeared during the nonlinear finite element analysis in this thesis. However, the major challenge faced during the simulation was regarding the convergence of analysis. The convergence in our analysis occurred when the number of equations became impossible to solve for a static solver in ABAQUS. Generally, the analysis converges due to unreasonable constraints, which may cause conflicts in boundary conditions or improper increment size. The convergence might also occur due to inadequate material data or by using inappropriate mesh elements. In this thesis, the analysis converges due to material data in each material cards, which is distributed throughout the element mesh. ABAQUS requires to find the solution for each mesh element based on the material data at each material card which becomes complex for the static solver. When the analysis converges, the time to solve each increment becomes significantly small due to the high number of degrees of freedom. The number of increments increases while the time step remains constant as the simulation gets aborted. However, the analysis could continue by reducing the minimum increment size, but the simulation's computational time would increase drastically.

The issue with the convergence could be avoided by increasing the size of the element mesh. Increasing the finite element size leads to fewer elements that reduce the model’s nodes. The use of a small mesh size reduces the convergence problem, but this would compensate for the accuracy of the results. Usually, a smaller mesh provides more reliable results, but the computing time also gets significantly high. The selection of an appropriate mesh size to give an accurate and robust result with reasonable computational time is challenging. In this study, a mesh size of 0.5 mm was selected, which provided real results for simulation without weld line, but the analysis converged for the specimen with weld line. Reducing the mesh size again from 0.5 would resolve the convergence issue but would reduce the accuracy of the results. Therefore, we instead opted to use a different solver than static to mitigate the problem with convergence. Generally, the explicit solver is preferred, but it does not allow anisotropic elastic properties with plasticity specification. But the material with anisotropy with the plasticity specification was accepted for an implicit algorithm used for the study. The implicit solver has a higher computational cost than the explicit solver's relatively low cost.

7 Summary and concluding remarks

Short fibre-reinforced composite materials (SFRC) are extensively used due to their superior mechanical properties and low processing costs. However, the manufacturing of short fibre-reinforced polymer with injection moulding is complex. The presence of embedded fibre in the matrix obtains random fibre orientations, which provide anisotropic behaviour in the final injection moulded part. The resulting fibre orientation can be predicted using various fibre orientation models. However, the coefficients for fibre orientation models are empirically determined and varies with the matrix material. In this study, the fibre orientation models, and process parameters are investigated to determine the dependence of the material parameters on the fibre orientation of injection moulded parts. Different fibre orientation models presented in the literature reviews are used to predict the orientation of fibres in Moldex3D simulation.

The findings from the simulation gives us insight into how moulded parts are simulated and affected by different parameters such as fibre orientation parameters (C_i, C_m and α), temperature, viscosity, aspect ratio and fibre concentration etc. Based on the findings from the simulation, it can be concluded that the fibre orientation distribution is affected significantly by the interaction coefficients compared to others. The variation in fibre alignment during injection moulding influences the development of mechanical properties substantially. The findings from the linear structural analysis indicates that the stiffness of the short fibre-reinforced material is substantially affected by the fibre orientation parameters and aspect ratio. According to the study, it can be concluded that these parameters are one of the most important factors which influences the strength development of injection moulded parts. Adjusting process parameters to obtain optimal fibre orientation allows for enhancing the mechanical properties of short fibre-reinforced material.

Finding a constitutive material model for reliably predicting the nonlinear behaviour of short fibre composite is still an on-going work. By utilizing the inverse modelling method, we presented a constitutive plastic model and damage model in this thesis. The performance of these models to predict plastic and progressive damage behaviour of SFRCs was investigated and compared with experimental results. The findings from the study indicates that the developed constitutive material model for nonlinear analysis can accurately predict the behaviour of injection moulded material. However, the model is based on the ductile plasticity model for metal. This can simplify the complex nonlinear behaviour of composite materials, which can predict inaccurate behaviour when applied parts with complex geometry. The study can conclude that it is essential to develop a material model appropriate to reliably predict nonlinear behaviour of short fibre composite materials.

8 Recommendation for further work

During the study, we have examined different parameters which affect the microstructure development during manufacturing particularly fibre orientation. By modifying the parameter during injection moulding simulation, the effect of parameters on mechanical properties is studied with a uniaxial tensile test in FEM software. To further increase the knowledge about how the process parameters affect the fibre orientations, a more detailed study could be made which includes an examination of fibre orientation distribution with the help of X-ray micro-computed-tomography technology. Additionally, the developed constitutive material model needs to be applied to the industrial part with complex geometry. By comparing the simulation results obtained from the material models with experimental results will further validate the applicability of the proposed model in this thesis. There is also a need to optimize the Python script to automatically identify the elements in weld line regions based on the elastic constants. The optimized script will be universally applicable for every industrial part.

Reference

1. Pachauri, R.K., et al., *Climate change 2014: synthesis report. Contribution of Working Groups I, II and III to the fifth assessment report of the Intergovernmental Panel on Climate Change*. 2014: Ipcc.
2. Horowitz, C.A., *Paris Agreement.* International Legal Materials, 2016. **55**(4): p. 740-755.
3. Council, W.G.B., *The building and construction sector can reach net zero carbon emissions by 2050.* 2017.
4. Renfrew, C., C. Frith, and L. Malafouris, *Introduction. The sapient mind: Archaeology meets neuroscience.* Philosophical transactions of the Royal Society of London. Series B, Biological sciences, 2008. **363**: p. 1935-8.
5. de Vries, J., *The Industrial Revolution and the Industrious Revolution.* The Journal of Economic History, 1994. **54**(2): p. 249-270.
6. Dunn, B.D., *Spacecraft Manufacturing—Failure Prevention and the Application of Material Analysis and Metallography*, in *Materials and Processes*. 2016, Springer. p. 115-245.
7. Gandhi, U., et al., *Discontinuous fiber-reinforced composites: fundamentals and applications*. 2020: Carl Hanser Verlag GmbH Co KG.
8. Campbell, F.C., *Structural composite materials*. 2010: ASM international.
9. Perumal, V., et al., *Fiber migration in shear flow: Model predictions and experimental validation.* Polymer Composites, 2019. **40**(9): p. 3573-3581.
10. Callister, W.D. and D.G. Rethwisch, *Materials science and engineering: an introduction*. Vol. 9. 2018: Wiley New York.
11. Shrivastava, A., *2 - Polymerization*, in *Introduction to Plastics Engineering*, A. Shrivastava, Editor. 2018, William Andrew Publishing. p. 17-48.
12. Sajan, S. and D.P. Selvaraj, *A review on polymer matrix composite materials and their applications.* Materials Today: Proceedings, 2021. **47**: p. 5493-5498.
13. Talreja, R. and J. Varna, *Modeling damage, fatigue and failure of composite materials*. 2015: Elsevier.
14. Kessler, M.R., *Polymer matrix composites: A perspective for a special issue of polymer reviews.* Polymer Reviews, 2012. **52**(3): p. 229-233.
15. Campbell, F., *Introduction to composite materials.* Structural composite materials, 2010. **1**: p. 1-29.
16. Park, S.-J. and M.-K. Seo, *Interface science and composites*. Vol. 18. 2011: Academic Press.
17. Arash, B., Q. Wang, and V.K. Varadan, *Mechanical properties of carbon nanotube/polymer composites.* Scientific Reports, 2014. **4**(1): p. 6479.
18. Gandhi, U.N., et al., *1 - Introduction*, in *Discontinuous Fiber-Reinforced Composites*, U.N. Gandhi, et al., Editors. 2020, Hanser. p. 1-27.
19. Pariti, V.N.P.M., *Mechanical Behavior of Carbon and Glass Fiber Reinforced Composite Materials Under Varying Loading Rates*. 2017.
20. Bussetta, P. and N. Correia, *Numerical forming of continuous fibre reinforced composite material: A review.* Composites Part A: Applied Science and Manufacturing, 2018. **113**: p. 12-31.
21. Staab, G.H., *1 - INTRODUCTION TO COMPOSITE MATERIALS*, in *Laminar Composites*, G.H. Staab, Editor. 1999, Butterworth-Heinemann: Woburn. p. 1-16.
22. Koniuszewska, A.G. and J.W. Kaczmar, *Application of polymer based composite materials in transportation.* Progress in Rubber Plastics and Recycling Technology, 2016. **32**(1): p. 1-24.
23. Murat, O., *The use of composite materials in automotive industry*. 2010, M. Sc. Thesis, Institute of Natural and Applied Sciences, Cukurova ….
24. Greene, J.P., *1 - Introduction*, in *Automotive Plastics and Composites*, J.P. Greene, Editor. 2021, William Andrew Publishing. p. 1-15.

25. Ghori, S.W., et al., *The role of advanced polymer materials in aerospace*, in *Sustainable composites for aerospace applications*. 2018, Elsevier. p. 19-34.
26. Cogswell, F., et al., *Woodhead publishing series in composites science and engineering.* Advanced fibrous composite materials for ballistic protection, 2016.
27. Motavalli, M., et al., *Fibre reinforced polymer composite materials for building and construction*, in *Textiles, polymers and composites for buildings*. 2010, Elsevier. p. 69-128.
28. Brahim, B., et al. *Field Durability Study of Vinyl-Ester–Based GFRP Rebars in Concrete Bridge Barriers*. 2018. American Society of Civil Engineers.
29. Ali, H.T., et al., *Fiber reinforced polymer composites in bridge industry.* Structures, 2021. **30**: p. 774-785.
30. Khosravani, M.R., S. Nasiri, and T. Reinicke, *Intelligent knowledge-based system to improve injection molding process.* Journal of Industrial Information Integration, 2021: p. 100275.
31. Mamodiya, U. and P. Sharma, *Review in Controlling Analysis of Injection Molding Machine.* International Journal of Engineering Research, 2014. **3**(6).
32. Osswald, T.A. and J.P. Hernández-Ortiz, *Polymer processing.* Modeling and Simulation. Munich: Hanser, 2006: p. 1-651.
33. Barnes, H.A., J.F. Hutton, and K. Walters, *An introduction to rheology*. Vol. 3. 1989: Elsevier.
34. Papanastasiou, T.C., *Applied Fluid Mechanics* Prentice hall international series in the physical and chemical engineering sciences ed. U.o.H. Neal R. Amundson. 1994, Englewood Cliffs, New Jersey 07632: PTR Prentice Hall. 513.
35. Aho, J., *Rheological characterization of polymer melts in shear and extension: measurement reliability and data for practical processing.* 2011.
36. Osswald, T.A., *3 - Melt Rheology*, in *Understanding Polymer Processing (Second Edition)*, T.A. Osswald, Editor. 2017, Hanser. p. 61-76.
37. Wood-Adams, P.M., et al., *Effect of Molecular Structure on the Linear Viscoelastic Behavior of Polyethylene.* Macromolecules, 2000. **33**(20): p. 7489-7499.
38. Gandhi, K. and R. Burns, *Rheological Properties of Glass Fiber-Reinforced Dough Molding Compounds.* Transactions of the Society of Rheology, 1976. **20**(4): p. 489-502.
39. Sheng, J.J., *Chapter 5 - Polymer Flooding*, in *Modern Chemical Enhanced Oil Recovery*, J.J. Sheng, Editor. 2011, Gulf Professional Publishing: Boston. p. 101-206.
40. Goris, S., et al. *Experimental Study on Fiber Attrition of Long Glass Fiber-Reinforced Thermoplastics under Controlled Conditions in a Couette Flow*. 2017.
41. Fetter, A.L. and C.J. Foot, *Chapter 2 - Bose Gas: Theory and Experiment*, in *Contemporary Concepts of Condensed Matter Science*, K. Levin, A.L. Fetter, and D.M. Stamper-Kurn, Editors. 2012, Elsevier. p. 27-67.
42. Żołek-Tryznowska, Z., *6 - Rheology of Printing Inks*, in *Printing on Polymers*, J. Izdebska and S. Thomas, Editors. 2016, William Andrew Publishing. p. 87-99.
43. Yahia, A., S. Mantellato, and R.J. Flatt, *7 - Concrete rheology: A basis for understanding chemical admixtures*, in *Science and Technology of Concrete Admixtures*, P.-C. Aïtcin and R.J. Flatt, Editors. 2016, Woodhead Publishing. p. 97-127.
44. Ibar, J.P., *7 - Shear-Thinning of Polymeric Melts: The Failure of the Reptation Model*, in *The Physics of Polymer Interactions*, J.P. Ibar, Editor. 2019, Hanser. p. 403-415.
45. Narasimhan, S., *A First Course in Fluid Mechanics*, ed. T.U.o. Virginia. 2007: Universities Press, 2007. 452.
46. Greene, J.P., *5 - Rheology and Plastic Flow*, in *Automotive Plastics and Composites*, J.P. Greene, Editor. 2021, William Andrew Publishing. p. 57-69.
47. Moldex3D, *User Manual and Material Database*. 2015, CoreTech System Hsinchu, Taiwan.
48. Hopmann, C. and J. Onken, *Prediction of part geometry-dependent weld line strength in unreinforced polycarbonate.* Advances in Polymer Technology, 2018. **37**(7): p. 2579-2587.
49. Zhou, H. and D. Li, *Computer evaluation of weld lines in injection-molded parts.* Journal of reinforced plastics and composites, 2005. **24**(3): p. 315-322.

50. Deng, Y.-M., et al., *Injection molding optimization for minimizing the defects of weld lines.* Polymer-Plastics Technology and Engineering, 2008. **47**(9): p. 943-952.
51. Bozzelli, J., *Find the source of visual defects.* Plast. Tech, 2008. **54**(7): p. 55-57.
52. Katariya, P.K. and C.D. Rajput, *Micromechanics analysis of fiber reinforced composite.* Int. J. Eng. Res. Technol., 2015. **4**(5): p. 439-446.
53. Vasiliev, V.V. and E.V. Morozov, *Chapter 2 - FUNDAMENTALS OF MECHANICS OF SOLIDS*, in *Advanced Mechanics of Composite Materials (Second Edition)*, V.V. Vasiliev and E.V. Morozov, Editors. 2007, Elsevier Science Ltd: Oxford. p. 31-56.
54. Zhang, J.J., *Chapter 1 - Stresses and strains*, in *Applied Petroleum Geomechanics*, J.J. Zhang, Editor. 2019, Gulf Professional Publishing. p. 1-27.
55. Bergström, J., *4 - Continuum Mechanics Foundations*, in *Mechanics of Solid Polymers*, J. Bergström, Editor. 2015, William Andrew Publishing. p. 131-207.
56. Belytschko, T., et al., *Nonlinear finite elements for continua and structures*. 2014: John wiley & sons.
57. Zhang, X., Z. Chen, and Y. Liu, *Chapter 2 - Governing Equations*, in *The Material Point Method*, X. Zhang, Z. Chen, and Y. Liu, Editors. 2017, Academic Press: Oxford. p. 11-36.
58. Mitrović, S., *THREE-DIMENSIONAL NONLINEAR DYNAMIC TIME HISTORY ANALYSIS OF SEISMIC SITE AND STRUCTURE RESPONSE*. 2015.
59. Cook, R.D. and W.C. Young, *Advanced mechanics of materials*. Vol. 2. 1999: Prentice Hall Upper Saddle River, NJ.
60. Staab, G.H., *2 - A review of stress–strain and material behavior*, in *Laminar Composites (Second Edition)*, G.H. Staab, Editor. 2015, Butterworth-Heinemann. p. 17-36.
61. Crandall, S.H., N.C. Dahl, and E.H. Dill, *An introduction to the mechanics of solids.* Physics Today, 1960. **13**(8): p. 46.
62. Khan, A.S. and S. Huang, *Continuum theory of plasticity*. 1995: John Wiley & Sons.
63. Wu, H.-C., *Continuum mechanics and plasticity*. 2004: Chapman and Hall/CRC.
64. Yu, M., G. Xia, and V.A. Kolupaev, *Basic characteristics and development of yield criteria for geomaterials.* Journal of Rock Mechanics and Geotechnical Engineering, 2009. **1**(1): p. 71-88.
65. Bai, Q. and Y. Bai, *9 - Thermal Expansion Design*, in *Subsea Pipeline Design, Analysis, and Installation*, Q. Bai and Y. Bai, Editors. 2014, Gulf Professional Publishing: Boston. p. 187-220.
66. Britt, J., R. Labrecque, and K. Murty, *MECHANICAL ANISOTROPY AND CRYSTALLOGRAPHIC TEXTURE IN TiAlMn ALLOY SHEET*, in *Advances in Engineering Plasticity and its Applications*. 1993, Elsevier. p. 563-570.
67. Gdoutos, E.E., *Fracture mechanics: an introduction*. Vol. 263. 2020: Springer Nature.
68. Fink, S., *Simulation of Elastic-Plastic Material Behaviour with Uncertain Material Parameters*, in *Institut für Baumechanik und Numerische Mechanik*. 2015, Gottfried Wilhelm Leibniz Universität Hannover: Germany
69. Laloui, L. and A.F. Rotta Loria, *Chapter 4 - Deformation in the context of energy geostructures*, in *Analysis and Design of Energy Geostructures*, L. Laloui and A.F. Rotta Loria, Editors. 2020, Academic Press. p. 137-205.
70. Moss, D.R. and M. Basic, *8 - High Pressure Vessels*, in *Pressure Vessel Design Manual (Fourth Edition)*, D.R. Moss and M. Basic, Editors. 2013, Butterworth-Heinemann: Oxford. p. 473-556.
71. Zhuang, Z., Z. Liu, and Y. Cui, *Chapter 2 - Fundamental Conventional Concept of Plasticity Constitution*, in *Dislocation Mechanism-Based Crystal Plasticity*, Z. Zhuang, Z. Liu, and Y. Cui, Editors. 2019, Academic Press. p. 29-56.
72. Fu, S.-y., B. Lauke, and Y.-w. Mai, *Chapter 11 - Fracture mechanics*, in *Science and Engineering of Short Fibre-Reinforced Polymer Composites (Second Edition)*, S.-y. Fu, B. Lauke, and Y.-w. Mai, Editors. 2019, Woodhead Publishing. p. 301-409.
73. Judt, P.O., et al., *Anisotropic fracture properties and crack path prediction in glass and cellulose fiber reinforced composites.* Engineering Fracture Mechanics, 2018. **188**: p. 344-360.
74. Jamali, J., et al., *A mechanistic criterion for the mixed-mode fracture of unidirectional polymer matrix composites.* Composites Part B: Engineering, 2019. **176**: p. 107316.

75. Al Kassem, G. and D. Weichert, *Micromechanical material models for polymer composites through advanced numerical simulation techniques.* PAMM, 2009. **9**(1): p. 413-414.

76. Pilvin, P., *3 - Continuum Mechanics*, in *Mechanics - Microstructure - Corrosion Coupling*, C. Blanc and I. Aubert, Editors. 2019, Elsevier. p. 49-63.

77. Schjødt-Thomsen, J. and R. Pyrz, *The Mori–Tanaka stiffness tensor: diagonal symmetry, complex fibre orientations and non-dilute volume fractions.* Mechanics of Materials, 2001. **33**(10): p. 531-544.

78. Vannan, E. and P. Vizhian, *Prediction of the elastic properties of short basalt fiber reinforced al alloy metal matrix composites.* Journal of Minerals and Materials Characterization and Engineering, 2014. **2014**.

79. Silva, L.J.d., et al., *Micromechanical analysis of hybrid composites reinforced with unidirectional natural fibres, silica microparticles and maleic anhydride.* Materials Research, 2012. **15**(6): p. 1003-1012.

80. Kulkarni, A., et al. *Modeling of short fiber reinforced injection moulded composite*. in *IOP Conference Series: Materials Science and Engineering*. 2012. IOP Publishing.

81. Buragohain, M.K., *Composite structures: design, mechanics, analysis, manufacturing, and testing*. 2017: CRC press.

82. Mortazavian, S. and A. Fatemi, *Effects of fiber orientation and anisotropy on tensile strength and elastic modulus of short fiber reinforced polymer composites.* Composites part B: engineering, 2015. **72**: p. 116-129.

83. Sudheer, M., K. Pradyoth, and S. Somayaji, *Analytical and numerical validation of epoxy/glass structural composites for elastic models.* American Journal of Materials Science, 2015. **5**(3C): p. 162-168.

84. Eshelby, J.D., *The Determination of the Elastic Field of an Ellipsoidal Inclusion, and Related Problems.* Proceedings of the Royal Society of London. Series A, Mathematical and Physical Sciences, 1957. **241**(1226): p. 376-396.

85. Weinberger, C., W. Cai, and D. Barnett, *Lecture notes–elasticity of microscopic structures.* ME340–Stanford University, 2005.

86. Thorvaldsen, T., *Modelling the elastic stiffness of nanocomposites using the Mori-Tanaka method.* 2015.

87. Tandon, G.P. and G.J. Weng, *The effect of aspect ratio of inclusions on the elastic properties of unidirectionally aligned composites.* Polymer Composites, 1984. **5**(4): p. 327-333.

88. Mori, T. and K. Tanaka, *Average stress in matrix and average elastic energy of materials with misfitting inclusions.* Acta Metallurgica, 1973. **21**(5): p. 571-574.

89. Fisher, F. and L. Brinson, *Nanomechanics of nanoreinforced polymers*, in *Handbook of theoretical and computational nanoscience*. 2006, American Scientific Publishers. p. 253-360.

90. O'Gara, J., et al., *Fiber Orientation in 3-D Injection Molded Features: Prediction and Experiment.* Int. Polymer Processing, 1999. **14**.

91. Kugler, S.K., et al., *Fiber Orientation Predictions—A Review of Existing Models.* Journal of Composites Science, 2020. **4**(2).

92. Tseng, H.-C., R.-Y. Chang, and C.-H. Hsu, *Comparison of recent fiber orientation models in injection molding simulation of fiber-reinforced composites.* Journal of Thermoplastic Composite Materials, 2018. **33**(1): p. 35-52.

93. Abdelbary, A. and Y.S. Mohamed, *Chapter 4 - Tribological behavior of fiber-reinforced polymer composites*, in *Tribology of Polymer Composites*, S.M. Rangappa, et al., Editors. 2021, Elsevier. p. 63-94.

94. Tseng, H.-C., R.-Y. Chang, and C.-H. Hsu, *Comparison of recent fiber orientation models in injection molding simulation of fiber-reinforced composites.* Journal of Thermoplastic Composite Materials, 2020. **33**(1): p. 35-52.

95. Jeffery, G.B., *The motion of ellipsoidal particles immersed in a viscous fluid.* Proceedings of the Royal Society of London. Series A, Containing papers of a mathematical and physical character, 1922. **102**(715): p. 161-179.

96. Perumal, D.V., *Influence of evolving fibre orientation and fibre concentration distribution on polymer composite viscosity and first normal stress difference*. 2020, RMIT University.
97. Folgar, F. and C.L. Tucker, *Orientation Behavior of Fibers in Concentrated Suspensions.* Journal of Reinforced Plastics and Composites, 1984. **3**(2): p. 98-119.
98. Kugler, S.K., et al., *Fiber Orientation Predictions—A Review of Existing Models.* Journal of Composites Science, 2020. **4**(2): p. 69.
99. Jørgensen, J.K., E. Andreassen, and D. Salaberger, *The effect of fiber concentration on fiber orientation in injection molded film gated rectangular plates.* Polymer Composites, 2019. **40**(2): p. 615-629.
100. Wang, J. and X. Jin. *Comparison of recent fiber orientation models in autodesk moldflow insight simulations with measured fiber orientation data*. in *Polymer Processing Society 26th Annual Meeting*. 2010. Citeseer.
101. Wang, J., J.F. O'Gara, and C.L. Tucker III, *An objective model for slow orientation kinetics in concentrated fiber suspensions: Theory and rheological evidence.* Journal of Rheology, 2008. **52**(5): p. 1179-1200.
102. Wang, J., et al. *Prediction of fiber orientation in injection-molded parts using three-dimensional simulations*. in *AIP conference proceedings*. 2016. AIP Publishing LLC.
103. Phan-Thien, N., et al., *Folgar–Tucker constant for a fibre suspension in a Newtonian fluid.* Journal of Non-Newtonian Fluid Mechanics, 2002. **103**(2-3): p. 251-260.
104. Phelps, J.H. and C.L. Tucker, *An anisotropic rotary diffusion model for fiber orientation in short- and long-fiber thermoplastics.* Journal of Non-Newtonian Fluid Mechanics, 2009. **156**(3): p. 165-176.
105. Tseng, H.-C., R.-Y. Chang, and C.-H. Hsu, *Phenomenological improvements to predictive models of fiber orientation in concentrated suspensions.* Journal of Rheology, 2013. **57**(6): p. 1597-1631.
106. Tseng, H.-C., R.-Y. Chang, and C.-H. Hsu, *Numerical investigations of fiber orientation models for injection molded long fiber composites.* International Polymer Processing, 2018. **33**(4): p. 543-552.
107. Bakharev, A., et al., *Using new anisotropic rotational diffusion model to improve prediction of short fibers in thermoplastic injection molding.* Society of Plastics Engineers: Lubbock, TX, USA, 2018.
108. Hand, G.L., *A theory of anisotropic fluids.* Journal of Fluid Mechanics, 1962. **13**(1): p. 33-46.
109. Cintra, J.S. and C.L. Tucker, *Orthotropic closure approximations for flow-induced fiber orientation.* Journal of Rheology, 1995. **39**(6): p. 1095-1122.
110. Jack, D.A. and D.E. Smith, *The effect of fibre orientation closure approximations on mechanical property predictions.* Composites Part A: Applied Science and Manufacturing, 2007. **38**(3): p. 975-982.
111. Chung, D.H. and T.H. Kwon, *Invariant-based optimal fitting closure approximation for the numerical prediction of flow-induced fiber orientation.* Journal of Rheology, 2002. **46**: p. 169-194.
112. Norge, S., *NS-EN ISO 527-1 Generelle prinsipper*. 2019, Tilgjengelig fra: https://www. standard. no/no/Nettbutikk/produktkatalogen ....
113. Standard, B. and B. ISO, *Plastics—Determination of tensile properties—*. Part, 1996. **1**: p. 527-521.
114. Advani, S.G., *Flow and rheology in polymer composites manufacturing/edited by Suresh G. Advani.* Composite materials series; 10, 1994.
115. Robert D. Cook, D.S.M., Michael E. Plesha, Robert J. Witt, *Concepts and applications of finite element analysis*. 2007: John wiley & sons.
116. Ramirez, W.F., *Chapter 8 - SOLUTION OF PARTIAL DIFFERENTIAL EQUATIONS*, in *Computational Methods in Process Simulation (Second Edition)*, W.F. Ramirez, Editor. 1997, Butterworth-Heinemann: Oxford. p. 353-430.

117. Simulia, D.S., *ABAQUS 6.13 User's manual.* Dassault Systems, Providence, RI, 2013. **305**: p. 306.

118. Pinho-da-Cruz, J., J.A. Oliveira, and F. Teixeira-Dias, *Asymptotic homogenisation in linear elasticity. Part I: Mathematical formulation and finite element modelling.* Computational Materials Science, 2009. **45**(4): p. 1073-1080.

119. Ioannou, I., *A Study on the Numerical Characterisation of Short Fibre Reinforced Composites*, in *Composite System Innovation Centre, Department of Mechanical Engineering*. 2014, The University of Sheffield Sheffield, UK. p. 244.

120. Bowden, A.E. and J. Bergström, *39 - Computer Modeling and Simulation of UHMWPE*, in *UHMWPE Biomaterials Handbook (Third Edition)*, S.M. Kurtz, Editor. 2016, William Andrew Publishing: Oxford. p. 753-771.

121. Vaidya, A. and K. Pathak, *17 - Mechanical stability of dental materials*, in *Applications of Nanocomposite Materials in Dentistry*, A.M. Asiri, Inamuddin, and A. Mohammad, Editors. 2019, Woodhead Publishing. p. 285-305.

122. ?arlo?i, J. and J. Bocko, *Effective Material Moduli for Composites.* American Journal of Mechanical Engineering, 2016. **4**(7): p. 289-292.

123. Geyer, A. and C. Bonten, *Enhancing the weld line strength of injection molded components.* AIP Conference Proceedings, 2019. **2055**(1): p. 070023.

124. Smith, M., *ABAQUS/Standard User's Manual, Version 6.9.* 2009.

125. Bergström, J., *7 - Plasticity Models*, in *Mechanics of Solid Polymers*, J. Bergström, Editor. 2015, William Andrew Publishing. p. 353-369.

126. *7 - Defects and damage and their role in the failure of polymer composites*, in *Failure Analysis and Fractography of Polymer Composites*, E.S. Greenhalgh, Editor. 2009, Woodhead Publishing. p. 356-440.

127. Rajendran, A. and S. Bless, *Determination of tensile flow stress beyond necking at very high strain rate.* Experimental Mechanics, 1986. **26**(4): p. 319-323.

128. Forghani, A., et al., *6 - An overview of continuum damage models used to simulate intralaminar failure mechanisms in advanced composite materials*, in *Numerical Modelling of Failure in Advanced Composite Materials*, P.P. Camanho and S.R. Hallett, Editors. 2015, Woodhead Publishing. p. 151-173.

129. Hillerborg, A., M. Modéer, and P.E. Petersson, *Analysis of crack formation and crack growth in concrete by means of fracture mechanics and finite elements.* Cement and Concrete Research, 1976. **6**(6): p. 773-781.

130. Abedin, M., et al., *Net Section Fracture Assessment of Welded Rectangular Hollow Structural Sections.* Civil Engineering Journal, 2020. **6**: p. 1243-1254.

Appendix I

```python
# -*- coding: mbcs -*-
from part import *
from material import *
from section import *
from assembly import *
from step import *
from interaction import *
from load import *
from mesh import *
from optimization import *
from job import *
from sketch import *
from visualization import *
from connectorBehavior import *

mdb.models['Model-1'].PartFromInputFile(inputFileName='C:/temp/Master_thesis/Damage/Without weldline/without_weldline.inp') #imports only part of the model
mdb.ModelFromInputFile(inputFileName='C:/temp/Master_thesis/Damage/Without weldline/without_weldline.inp', name='Model-1') #imports whole model


for i in range(0,5368):
    mdb.models['Model-1'].materials['MAT%d' %(i+1)].Plastic(table=((134, 0.0), (164, 0.003957654), (175, 0.010245708), (186, 0.02474255)))
```

Appendix II

```python
# -*- coding: mbcs -*-
from part import *
from material import *
from section import *
from assembly import *
from step import *
from interaction import *
from load import *
from mesh import *
from optimization import *
from job import *
from sketch import *
from visualization import *
from connectorBehavior import *

mdb.models['Model-1'].PartFromInputFile(inputFileName='C:/temp/Master_thesis/Damage/Without weldline and damage/without_weldline.inp') #imports only part
mdb.ModelFromInputFile(inputFileName='C:/temp/Master_thesis/Damage/Without weldline and damage/without_weldline.inp', name='Model-1') #imports whole model

for i in range(0,5368):
    mdb.models['Model-1'].materials['MAT%d' %(i+1)].Plastic(table=((134, 0.0), (164, 0.003957654), (175, 0.010245708), (186, 0.02474255)))

for i in range(0,5368):
    mdb.models['Model-1'].materials['MAT%d' %(i+1)].DuctileDamageInitiation(table=((0.0255, 0.33333, 0.001), ))

for i in range(0,5368):
    mdb.models['Model-1'].materials['MAT%d' %(i+1)].ductileDamageInitiation.DamageEvolution(softening=EXPONENTIAL, table=((0, ), ), type=ENERGY)
```

Appendix III

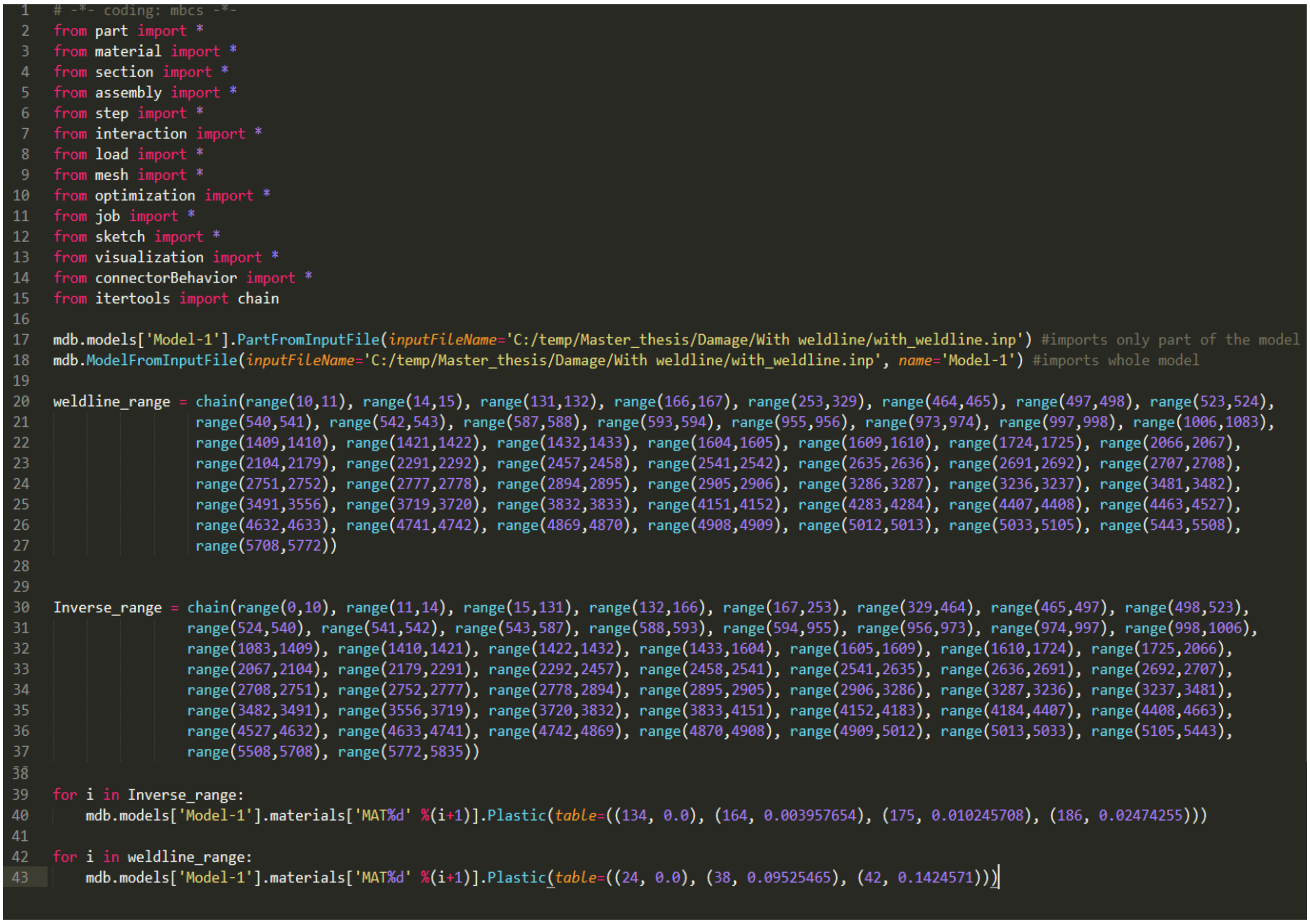

```
# -*- coding: mbcs -*-
from part import *
from material import *
from section import *
from assembly import *
from step import *
from interaction import *
from load import *
from mesh import *
from optimization import *
from job import *
from sketch import *
from visualization import *
from connectorBehavior import *
from itertools import chain

mdb.models['Model-1'].PartFromInputFile(inputFileName='C:/temp/Master_thesis/Damage/With weldline/with_weldline.inp') #imports only part of the model
mdb.ModelFromInputFile(inputFileName='C:/temp/Master_thesis/Damage/With weldline/with_weldline.inp', name='Model-1') #imports whole model

weldline_range = chain(range(10,11), range(14,15), range(131,132), range(166,167), range(253,329), range(464,465), range(497,498), range(523,524),
                       range(540,541), range(542,543), range(587,588), range(593,594), range(955,956), range(973,974), range(997,998), range(1006,1083),
                       range(1409,1410), range(1421,1422), range(1432,1433), range(1604,1605), range(1609,1610), range(1724,1725), range(2066,2067),
                       range(2104,2179), range(2291,2292), range(2457,2458), range(2541,2542), range(2635,2636), range(2691,2692), range(2707,2708),
                       range(2751,2752), range(2777,2778), range(2894,2895), range(2905,2906), range(3286,3287), range(3236,3237), range(3481,3482),
                       range(3491,3556), range(3719,3720), range(3832,3833), range(4151,4152), range(4283,4284), range(4407,4408), range(4463,4527),
                       range(4632,4633), range(4741,4742), range(4869,4870), range(4908,4909), range(5012,5013), range(5033,5105), range(5443,5508),
                       range(5708,5772))


Inverse_range = chain(range(0,10), range(11,14), range(15,131), range(132,166), range(167,253), range(329,464), range(465,497), range(498,523),
                      range(524,540), range(541,542), range(543,587), range(588,593), range(594,955), range(956,973), range(974,997), range(998,1006),
                      range(1083,1409), range(1410,1421), range(1422,1432), range(1433,1604), range(1605,1609), range(1610,1724), range(1725,2066),
                      range(2067,2104), range(2179,2291), range(2292,2457), range(2458,2541), range(2541,2635), range(2636,2691), range(2692,2707),
                      range(2708,2751), range(2752,2777), range(2778,2894), range(2895,2905), range(2906,3286), range(3287,3236), range(3237,3481),
                      range(3482,3491), range(3556,3719), range(3720,3832), range(3833,4151), range(4152,4183), range(4184,4407), range(4408,4663),
                      range(4527,4632), range(4633,4741), range(4742,4869), range(4870,4908), range(4909,5012), range(5013,5033), range(5105,5443),
                      range(5508,5708), range(5772,5835))

for i in Inverse_range:
    mdb.models['Model-1'].materials['MAT%d' %(i+1)].Plastic(table=((134, 0.0), (164, 0.003957654), (175, 0.010245708), (186, 0.02474255)))

for i in weldline_range:
    mdb.models['Model-1'].materials['MAT%d' %(i+1)].Plastic(table=((24, 0.0), (38, 0.09525465), (42, 0.1424571)))
```

Appendix IV

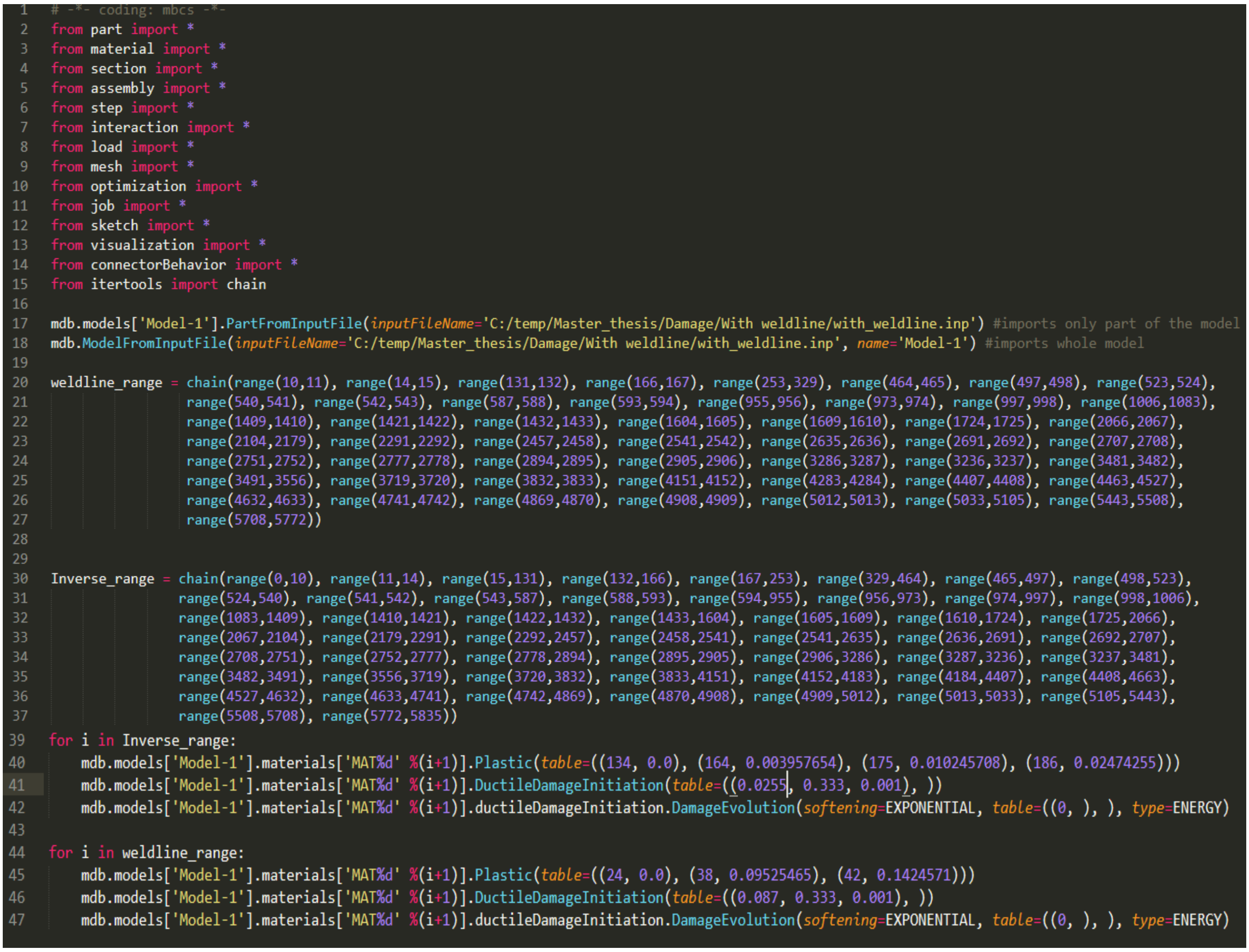

```python
# -*- coding: mbcs -*-
from part import *
from material import *
from section import *
from assembly import *
from step import *
from interaction import *
from load import *
from mesh import *
from optimization import *
from job import *
from sketch import *
from visualization import *
from connectorBehavior import *
from itertools import chain

mdb.models['Model-1'].PartFromInputFile(inputFileName='C:/temp/Master_thesis/Damage/With weldline/with_weldline.inp') #imports only part of the model
mdb.ModelFromInputFile(inputFileName='C:/temp/Master_thesis/Damage/With weldline/with_weldline.inp', name='Model-1') #imports whole model

weldline_range = chain(range(10,11), range(14,15), range(131,132), range(166,167), range(253,329), range(464,465), range(497,498), range(523,524),
                       range(540,541), range(542,543), range(587,588), range(593,594), range(955,956), range(973,974), range(997,998), range(1006,1083),
                       range(1409,1410), range(1421,1422), range(1432,1433), range(1604,1605), range(1609,1610), range(1724,1725), range(2066,2067),
                       range(2104,2179), range(2291,2292), range(2457,2458), range(2541,2542), range(2635,2636), range(2691,2692), range(2707,2708),
                       range(2751,2752), range(2777,2778), range(2894,2895), range(2905,2906), range(3286,3287), range(3236,3237), range(3481,3482),
                       range(3491,3556), range(3719,3720), range(3832,3833), range(4151,4152), range(4283,4284), range(4407,4408), range(4463,4527),
                       range(4632,4633), range(4741,4742), range(4869,4870), range(4908,4909), range(5012,5013), range(5033,5105), range(5443,5508),
                       range(5708,5772))


Inverse_range = chain(range(0,10), range(11,14), range(15,131), range(132,166), range(167,253), range(329,464), range(465,497), range(498,523),
                      range(524,540), range(541,542), range(543,587), range(588,593), range(594,955), range(956,973), range(974,997), range(998,1006),
                      range(1083,1409), range(1410,1421), range(1422,1432), range(1433,1604), range(1605,1609), range(1610,1724), range(1725,2066),
                      range(2067,2104), range(2179,2291), range(2292,2457), range(2458,2541), range(2541,2635), range(2636,2691), range(2692,2707),
                      range(2708,2751), range(2752,2777), range(2778,2894), range(2895,2905), range(2906,3286), range(3287,3236), range(3237,3481),
                      range(3482,3491), range(3556,3719), range(3720,3832), range(3833,4151), range(4152,4183), range(4184,4407), range(4408,4663),
                      range(4527,4632), range(4633,4741), range(4742,4869), range(4870,4908), range(4909,5012), range(5013,5033), range(5105,5443),
                      range(5508,5708), range(5772,5835))
for i in Inverse_range:
    mdb.models['Model-1'].materials['MAT%d' %(i+1)].Plastic(table=((134, 0.0), (164, 0.003957654), (175, 0.010245708), (186, 0.02474255)))
    mdb.models['Model-1'].materials['MAT%d' %(i+1)].DuctileDamageInitiation(table=((0.0255, 0.333, 0.001), ))
    mdb.models['Model-1'].materials['MAT%d' %(i+1)].ductileDamageInitiation.DamageEvolution(softening=EXPONENTIAL, table=((0, ), ), type=ENERGY)

for i in weldline_range:
    mdb.models['Model-1'].materials['MAT%d' %(i+1)].Plastic(table=((24, 0.0), (38, 0.09525465), (42, 0.1424571)))
    mdb.models['Model-1'].materials['MAT%d' %(i+1)].DuctileDamageInitiation(table=((0.087, 0.333, 0.001), ))
    mdb.models['Model-1'].materials['MAT%d' %(i+1)].ductileDamageInitiation.DamageEvolution(softening=EXPONENTIAL, table=((0, ), ), type=ENERGY)
```